Shedding Light on the Tau Lepton:

Measuring photon-induced tau-lepton pairs to constrain the tau electromagnetic moments using $\sqrt{s_{NN}} = 5.02$ TeV lead–lead collision data recorded by the ATLAS detector

Dissertation zur Erlangung des Doktorgrades an der Fakultät für Mathematik, Informatik und Naturwissenschaften, Fachbereich Physik der Universität Hamburg

vorgelegt von

Weronika Stanek-Maslouska

Hamburg

2026

Gutachter/innen der Dissertation:	Dr. Lydia Beresford
	Prof. Dr. Peter Schleper
Zusammensetzung der Prüfungskommission:	Dr. Lydia Beresford
	Prof. Dr. Peter Schleper
	Prof. Dr. Johannes Haller
	Prof. Dr. Elisabetta Gallo
	Prof. Dr. Christophe Grojean
Vorsitzende/r der Prüfungskommission:	Prof. Dr. Johannes Haller
Datum der Disputation:	23.03.2026
Vorsitzender des Fach-Promotionsausschusses PHYSIK:	Prof. Dr. Johannes Haller
Leiter des Fachbereichs PHYSIK:	Prof. Dr. Markus Drescher
Dekan der Fakultät MIN:	Prof. Dr.-Ing. Norbert Ritter

Declaration of oath

I hereby declare and affirm that this doctoral dissertation is my own work and that I have not used any aids and sources other than those indicated.

If electronic resources based on generative artificial intelligence (gAI) were used in the course of writing this dissertation, I confirm that my own work was the main and value-adding contribution and that complete documentation of all resources used is available in accordance with good scientific practice. I am responsible for any erroneous or distorted content, incorrect references, violations of data protection and copyright law or plagiarism that may have been generated by the gAI.

Weronika Stanek-Maslowska

Date: 16.01.2026

Acknowledgements

Success can be seen as continuing to move forward without losing courage, even when facing constant challenges. In terms of this PhD, it would not be possible without the support of many people, to whom I would like to express my gratitude.

First, I would like to thank my supervisor, Lydia Beresford, for her constant support, guidance and for sharing her knowledge. I truly appreciate how available you have always been and how patiently you discussed every detail of the analysis. I would also like to thank Savannah Clawson for all the help with the technical aspects of the AFP and for unravelling the unfolding to me. Your engagement and support throughout my PhD were invaluable. Many thanks also to John Hallford for your input to the analysis and all your effort. I would also like to thank Daniel Werner for helping me with the German translation of the abstract.

I would like to thank the analysis group members from Freiburg, Valerie Lang and Kartik Deepak Bhide. Valerie, thank you for your strong leadership and dedication to ensure that every detail was carefully examined. Kartik, you really pushed this analysis forward and we would not have come this far without all your involvement.

Many thanks as well to Klaudia Maj, Agnieszka Ogrodnik, Mateusz Dyndał, Jakub Kremer, Iwona Grabowska-Bołd, Tomasz Bołd, Qipeng Hu and Peter Steinberg for your help, discussions and valuable advice during the work on the analysis.

From the AFP side, I would like to thank my technical supervisor, Marek Taševský, for your commitment and continuous support. I am also grateful to Yohany Rodriguez Garcia and Gabriela Alejandra Navarro for sharing your knowledge and for guiding me through the alignment framework. Thanks as well to Rafał Staszewski, Maciej Trzebiński and Maciej Lewicki for your contributions and dedication to the project.

I would also like to thank Peter Schleper, my supervisor at Hamburg University and my mentor, Isabell Melzer-Pellmann, for your guidance, discussions and valuable suggestions throughout my studies.

Finally, I acknowledge the use of AI tools developed by OpenAI, which helped me to improve the language and structure of this thesis.

This is all about finding the courage to believe
that the thing we are looking for exists.

— Edward Witten,
Invitation to Black Hole Thermodynamics,
DESY, December 2024

Contents

Abstract

This thesis presents a novel measurement of photon-induced τ-lepton pair production in heavy-ion collisions which advances our understanding of the electromagnetic properties of the τ-lepton. It demonstrates the unique potential of ultra-peripheral lead-lead (Pb+Pb) collisions as a complementary probe of the Standard Model and beyond the Standard Model physics.

The analysis uses $\sqrt{s_{\mathrm{NN}}} = 5.02$ TeV Pb+Pb collision data recorded by the ATLAS detector at the Large Hadron Collider (LHC) in 2015 and 2018. The dataset corresponds to an integrated luminosity of 1.93 nb^{-1}. Strong electromagnetic fields generated in ultra-peripheral Pb+Pb collisions give rise to substantial photon fluxes, providing a unique environment for studying photon-induced processes.

Signal candidates are classified into three exclusive regions according to event topologies in which one τ-lepton decays into a muon and two neutrinos, while the decay of the second τ-lepton is characterised by the presence of either charged-particle track(s) or an electron. A strong suppression of ion breakup is ensured by requiring an absence of forward neutron activity.

Differential cross sections are extracted using an Iterative Bayesian Unfolding approach. The results are compared with leading-order Standard Model predictions and found to be consistent within the measurement uncertainties, which are dominated by limited data statistics. The measurement enables extraction of the anomalous magnetic dipole moment $(g-2)$ and electric dipole moment (EDM) of the τ-lepton. Expected constraints are obtained through a statistical analysis and compared to the existing constraints.

Performance studies of the ATLAS Forward Proton (AFP) detector are also presented. The AFP detector records protons scattered at small angles in photon-induced and diffractive processes, providing kinematic information that can be used to enhance background suppression. The global alignment of the AFP was performed using photon-induced dimuon events, recorded during LHC Run 3 proton-proton collisions at $\sqrt{s} = 13.6$ TeV.

Zusammenfassung

Diese Dissertation präsentiert eine neuartige Messung der photoninduzierten Produktion von τ-Lepton-Paaren in Schwerionenkollisionen und vertieft damit das Verständnis der elektromagnetischen Eigenschaften des τ-Leptons. Sie unterstreicht das besondere Potenzial ultra-peripherer Blei–Blei-(Pb+Pb)-Kollisionen durch ihre komplementären Einblicke in das Standardmodell und die Physik jenseits des Standardmodells.

Die Analyse basiert auf Pb+Pb-Kollisionsdaten bei $\sqrt{s_{\mathrm{NN}}} = 5.02$ TeV, die mit dem ATLAS-Detektor am LHC in den Jahren 2015 und 2018 aufgenommen wurden und einer integrierten Luminosität von 1.93 nb^{-1} entsprechen. Die in ultra-peripheren Pb+Pb-Kollisionen erzeugten starken elektromagnetischen Felder führen zu hohen Photonenströmen und ermöglichen so die Untersuchung photoninduzierter Prozesse.

Signalkandidaten werden in drei exklusive Regionen eingeteilt, in denen ein τ-Lepton in ein Myon und zwei Neutrinos zerfällt, während der Zerfall des zweiten τ-Leptons durch geladene Spur(en) oder ein Elektron gekennzeichnet ist. Ereignisse mit zerbrechenden Ionen werden durch die Forderung nach fehlender Vorwärtsneutronenaktivität wirksam unterdrückt.

Differentielle Wirkungsquerschnitte werden mittels iterativer bayesscher Entfaltung bestimmt und mit Standardmodellvorhersagen führender Ordnung verglichen. Innerhalb der überwiegend statistisch dominierten Unsicherheiten wird eine gute Übereinstimmung beobachtet. Die Messung erlaubt die Extraktion des anomalen magnetischen Dipolmoments $(g-2)$ und des elektrischen Dipolmoments (EDM) des τ-Leptons. Die möglichen Werte dieser Größen werden durch ein statistische Analyse eingegrenzt und mit bestehenden Grenzen verglichen.

Ergänzend werden Leistungsstudien des ATLAS Forward Proton (AFP)-Detektors vorgestellt. Der AFP-Detektor misst bei kleinen Winkeln gestreute Protonen aus photoninduzierten und diffraktiven Prozessen und liefert zusätzliche kinematische Informationen zur Unterdrückung von Untergrundprozessen. Die globale Ausrichtung des Detektors wurde mithilfe photoninduzierter Dimuon-Ereignisse aus LHC Run 3 Proton–Proton-Kollisionen bei $\sqrt{s} = 13.6$ TeV durchgeführt.

Author's contribution

The work presented here has been performed within the ATLAS collaboration as a collaborative effort. The preliminary results for the $\gamma\gamma \to \tau\tau$ differential cross section measurements have been published as an ATLAS conference note [1].

Building upon those results, several improvements have been implemented in the present analysis. These include an improved treatment of the photon flux systematic uncertainty, corrections accounting for spin-correlation effects in $\gamma\gamma \to \tau\tau$ production and decay, a refined modelling of neutron activity in the forward region and the application of a global residual flux factor correction.

The improved results are presented in this thesis together with the expected constraints on the τ-lepton electromagnetic moments, with a focus on the Author's contributions, in Chapters 5 and 6. These contributions include the analysis of neutron activity in the forward region and the derivation of electromagnetic pile-up corrections (Section 5.3), the estimation of the diffractive photonuclear background using a data-driven method (Section 5.7.3) and the detector-level analysis (Section 5.8). In addition, the Author incorporated all systematic uncertainties into the analysis framework (Section 6.2), defined the variables and fiducial regions used in the unfolding procedure and prepared all inputs for the unfolding, which includes the theoretical predictions described in Section 6.4. The Author also served as one of the main editors of the ATLAS internal documentation for this analysis.

The Author also performed technical work on the global alignment of the ATLAS Forward Proton Detector (AFP). It was initially developed as part of the ATLAS Qualification Project and subsequently extended as a contribution to the detector performance studies within the ATLAS Collaboration. The work included the derivation of the global alignment corrections and the corresponding systematic uncertainties using Run 3 data. The resulting global alignment corrections for the 2023 dataset have been published by the ATLAS Collaboration in public plots [2].

Introduction

Our best current theoretical understanding of particle physics is encapsulated in a theory known as the *Standard Model* (SM). It provides a remarkably precise description of the fundamental constituents of matter and the forces acting between them with numerous predictions confirmed experimentally to extraordinary accuracy.

However, despite its success, the SM is known to be incomplete. Several profound questions remain unanswered, for example: What is the nature of dark matter? Why does the universe exhibit a matter–antimatter asymmetry? How can gravity be incorporated into the same theoretical framework as the other fundamental interactions? What is the origin of neutrino masses? These open problems point to physics beyond the Standard Model (BSM).

In fact, current cosmological observations indicate that we have little understanding of approximately 95% of the universe's mass-energy content. The ordinary, baryonic matter from which we, the planets and the stars are made accounts for only about 5%. This constitutes one of the strongest motivations for the existence of yet undiscovered BSM physics. It also highlights why searches for such phenomena are of profound scientific interest.

Searches for BSM can be pursued through two complementary approaches: *direct* and *indirect* searches. At particle colliders, direct searches typically aim to produce BSM particles in high-energy collisions and to detect their signatures in the experimental data. Indirect searches, on the other hand, probe the effects of possible New Physics through precision measurements of known quantities. The work presented in this thesis belongs to the latter category.

In particular, this study focuses on the electromagnetic moments of the τ-lepton. These can be viewed as properties of a particle, which characterise how it interacts with an electromagnetic field. Within the SM, the values of the τ-lepton electromagnetic moments are precisely predicted. Measuring them experimentally and comparing the results to these predictions provides a powerful test of the theory. Any observed deviation could indicate New Physics, requiring either an extension or a reformulation of the SM to account for the discrepancy.

The τ-lepton remains an especially intriguing object of study. Within the lepton family, the electromagnetic moments of the electron and the muon have already

been measured with extraordinary precision - among the most accurately determined quantities in particle physics. The τ-lepton, in contrast, has a much larger mass of about 1.777 GeV, which makes it particularly sensitive to potential effects of New Physics. For this reason, precise studies of the tau's electromagnetic properties provide a unique window into possible BSM contributions.

In practice, however, such measurements are extremely challenging. The τ-lepton has a very short lifetime of approximately 2.9×10^{-13} s (0.3 ps), decaying before it can be directly observed. This makes the experimental reconstruction and precise determination of its properties highly non-trivial.

The results presented in this thesis are based on data collected with the ATLAS detector, located at the Large Hadron Collider (LHC) at CERN. During most of its operation, the LHC collides protons; however, special data-taking periods are dedicated to heavy-ion collisions, such as lead–lead (Pb+Pb) collisions, which typically occur for about one month each data-taking year.

The motivation for studying Pb+Pb collisions lies in the unique physical conditions they provide. At small impact parameters, such collisions allow the study of strongly interacting matter at extreme temperatures and densities, such as the quark–gluon plasma. At large impact parameters, when the nuclei do not physically overlap, they instead interact via their intense electromagnetic fields, leading to so-called *ultra-peripheral collisions* (UPCs).

In UPCs, the nuclei pass by each other without direct contact and only their surrounding electromagnetic fields interact. These strong electromagnetic fields can be effectively described as fluxes of quasi-real photons. In this framework, the electromagnetic fields act as sources of high-energy photons. This opens a rich field of photon-induced studies.

There are several advantages of using UPCs for such studies. The enormous photon flux generated by the highly charged lead nuclei enhances the cross section of photon-induced processes. Furthermore, these collisions allow access to the low-transverse-momentum region, which is otherwise difficult to probe in proton–proton interactions, thus providing complementary kinematic coverage. Another advantage is the cleanliness of the events: since there is no hadronic overlap, the detector typically registers only the products of the photon-induced interaction, resulting in very low background levels.

Among the processes that can occur in photon–photon interactions are the production of lepton pairs: dimuons, dielectrons and ditaus. In the case of τ-lepton pair production, the analysis relies on selecting the visible tau decay products. Events are divided into three mutually exclusive categories based on their topology, requiring one τ-lepton to decay into a muon and two neutrinos, while the decay of the other τ-lepton is identified either through charged-particle track(s) or an electron.

Once the $\gamma\gamma \to \tau\tau$ events are selected, differential $\gamma\gamma \to \tau\tau$ cross sections can be measured after correcting for detector inefficiencies and resolution effects through an *unfolding* procedure. The results presented in this thesis constitute the first measurement of differential $\gamma\gamma \to \tau\tau$ cross sections in Pb+Pb collisions to date.

The electromagnetic moments of the τ-lepton can be extracted from fits to kinematic distributions that are sensitive to their values. Among these observables, the transverse momentum of the muon originating from tau decay (p_{T}^{μ}) is particularly sensitive and variations in the electromagnetic moments modify the shape of the distribution.

This thesis is structured as follows. Chapter 1 provides a general introduction to the SM and establishes the theoretical context for the physics analysis. Chapter 2 presents a more specialised overview of photon-induced processes and describes the specific physics mechanisms investigated in this field. Chapter 3 outlines the experimental setup, including an overview of the LHC and a detailed description of the ATLAS experiment, including particle reconstruction and calibration. Chapter 4 focuses on the ATLAS Forward Proton detectors, with an emphasis on the alignment of the tracking detectors.

The novel measurement of the photon-induced τ-lepton pair production in ultra-peripheral heavy-ion collisions at the LHC, which is the main focus of this thesis, is described in Chapters 5 and 6.

Chapter 1

Theory

Particle physics provides the tools to describe the fundamental laws of nature. It describes elementary particles, which are the fundamental constituents of the Universe, as well as their interactions. The best current theoretical understanding of the particles and their interactions is expressed in the Standard Model (SM). This theory provides the most exact description of all experimental data and it is considered to be one of the most important achievements of science. This chapter provides a broad foundation in particle physics, giving context for the experimental analysis presented in this thesis.

1.1 The Standard Model of Particle Physics

1.1.1 Fundamental particles and forces

Ordinary matter appears to be built from atoms which are bounded states of negatively charged electrons (e^-) and a nucleus composed of neutral neutrons (n) and positively charged protons (p). However, at higher energy, further structure can be observed: protons and neutrons are composed of fundamental particles called quarks and gluons [3].

Elementary constituents of matter described by the SM are called fermions. Fermions have half-integer spin and they are classified in three generations. The first one represents the basic building blocks of the low-energy Universe and it is made up from the electron, electron neutrino (ν_e), up-quark (u) and down-quark (d). Further generations are revealed at the energy scales present in high-energy particle colliders. The second generation is composed of the muon (μ^-), muonic neutrino (ν_μ), strange-quark (s) and charm-quark (c). The tau-lepton (τ^-), tau-neutrino (ν_τ), bottom-quark (b) and top-quark (t) belong to the third generation. The absence of any further generations was proven experimentally [4]. The fermions together with their charge and mass are listed in Table 1.1.1.

For each of the twelve fermions exist an antiparticle, which has an opposite charge and exactly the same mass. This is a consequence of the Dirac equation, which describes the dynamics of fermions. Antiparticles are typically represented by placing a bar over the particle's symbol (e.g., $\bar{d}$ for the anti-down quark) or by explicitly indicating the opposite charge (e.g., e^+ for the positron).

Table 1.1.1: Properties of leptons and quarks in the Standard Model. The charge (Q) is in units of the elementary charge e.

Generation	**Leptons**			**Quarks**		
	Particle	**Q**	**Mass [GeV]**	**Particle**	**Q**	**Mass [GeV]**
First	Electron (e^-)	-1	0.000511	Down (d)	$-\frac{1}{3}$	0.0047
	Neutrino (ν_e)	0	$< 10^{-9}$	Up (u)	$+\frac{2}{3}$	0.0022
Second	Muon (μ^-)	-1	0.1057	Strange (s)	$-\frac{1}{3}$	0.096
	Neutrino (ν_μ)	0	$< 10^{-9}$	Charm (c)	$+\frac{2}{3}$	1.27
Third	Tau (τ^-)	-1	1.776	Bottom (b)	$-\frac{1}{3}$	4.18
	Neutrino (ν_τ)	0	$< 10^{-9}$	Top (t)	$+\frac{2}{3}$	172.9

There are four fundamental forces: the strong force, the electromagnetic force, the weak force and gravity. The strong force is associated with a property analogous to electric charge, known as *colour charge*, which is carried only by quarks and gluons. Consequently, only quarks and gluons undergo strong interactions, distinguishing them from leptons. Due to the phenomenon of confinement, quarks and gluons cannot exist as free particles; instead, they are bound within composite states called hadrons, such as protons and neutrons. The electromagnetic force acts exclusively on charged particles, meaning all fermions except neutrinos experience it. The weak force governs processes such as nuclear β-decay in radioactive isotopes and plays a crucial role in nuclear fusion. It is the only force that interacts with all elementary particles. Gravity is the only force not described by the SM. The gravitational forces between fundamental particles are very small and are neglected when describing particle interactions.

In the SM, each force is described as a Quantum Field Theory (QFT) and elementary particles are quanta of fermion fields. The interactions between particles are mediated by particles of a spin-1, called gauge bosons. The photon (γ) is the massless gauge boson of Quantum Electrodynamics (QED, the theory describing electromagnetic interactions). In Quantum Chromodynamics (QCD, describing the strong interactions), the force is carried by the massless gluon (g). The weak charged-current interactions are mediated by the charged $W^\pm$ bosons and the weak neutral current is carried by a neutral Z boson.

The gravitational force, which is not included in the SM, is hypothesised to be mediated by a force carrier known as the graviton (G). However, no experimental evidence for its existence has been observed to date. The four known forces and their properties are indicated in Table 1.1.2.

Table 1.1.2: Properties of fundamental forces and their gauge bosons. The strengths are relative to the strong interaction. Table adapted from Ref. [3].

Force	**Strength**	**Boson**	**Spin**	**Mass [GeV]**
Strong	1	Gluon (g)	1	0
Electromagnetic	10^{-3}	Photon (γ)	1	0
Weak	10^{-8}	W boson (W)	1	80.4
		Z boson (Z)	1	91.2
Gravity	10^{-37}	Graviton? (G)	2	0

The properties of the strong, electromagnetic and weak interactions are determined by the gauge bosons and the way in which they couple. In the SM, these couplings are described by interaction vertices. The interaction is represented by a three-point vertex of the gauge boson and the incoming and the outgoing fermion. The strength of the each fundamental interaction between the gauge boson and a fermion is given by the coupling constant g, which corresponds to the measure of probability of a fermion emitting or absorbing the boson.

The coupling strength can also be written as a dimensionless constant, $\alpha \propto g^2$, independent of the system of units. The intrinsic strength of the interaction can be then expressed in terms of a single value of α for each interaction vertex. In the case of electromagnetism, $\alpha = 1/137$. For the weak interaction, $\alpha_W \sim 1/30$ (which is greater than for QED, however, due to the large mass of W boson and low-energy scales encountered in particle decays, this interaction is in fact much weaker than QED). The intrinsic strength of the QCD interaction is significantly stronger, with $\alpha_S \sim 1$.

The most recently discovered particle in the SM is the Higgs boson (H), which possesses unique properties distinct from other SM particles. It is the only fundamental scalar particle with spin-0 and has a mass of $m_H \approx 125$ GeV. In terms of QFT, the Higgs boson can be described as an excitation of the Higgs field, which has a non-zero expectation value in the vacuum, unlike any other field in the SM. The other particles acquire their masses via interaction with the non-zero Higgs field in the so-called Higgs mechanism. The discovery of the Higgs boson at the LHC is one of the most important achievements of modern physics and it provides a validation of the theoretical foundations of the SM.

1.1.2 Virtual particles

Virtual particles are an important concept introduced in the SM, as a consequence of its formulation as a QFT. They correspond to intermediate states, typically represented as internal lines in Feynman diagrams. Although they are not directly observable, virtual particles are mathematical representations of quantum fluctuations mediating interactions between real (on-shell) particles. Real particles satisfy the on-shell condition:

$$p^2 = m^2, \tag{1.1.1}$$

where p is the four-momentum and m is the particle mass. In contrast, virtual particles are *off-shell*, meaning that the above relation is not fulfilled. The deviation from the on-shell condition is referred to as the *virtuality*, commonly denoted as q^2:

$$q^2 = p^2 - m^2. \tag{1.1.2}$$

The existence of virtual particles is consistent with the energy-time uncertainty principle, which permits temporary violations of energy conservation within short timescales:

$$\Delta E \, \Delta t \gtrsim \hbar/2. \tag{1.1.3}$$

In high-energy collisions, virtual particles play a fundamental role in mediating interactions. For instance, in photon-induced processes, the distinction between quasi-real ($q^2 \approx 0$) and virtual ($q^2 > 0$) photons is crucial, as it influences the interpretation of observables such as the anomalous magnetic and electric dipole moments.

1.1.3 Gauge group of the Standard Model

Interactions described in the SM emerge from symmetry principles. The fundamental requirement of local gauge invariance means that the Lagrangian of the theory remains unchanged under local transformations of the symmetry group. In terms of the SM, the gauge symmetry group is given by:

$$SU(3)_C \times SU(2)_L \times U(1)_Y. \tag{1.1.4}$$

In the above formulation, $SU(3)_C$ corresponds to the strong interaction (QCD), where C refers to the colour charge. It provides 8 gluons, usually denoted as G^a_μ. $SU(2)_L$ is related to the weak interaction and L refers to the left chiral nature of the $SU(2)$ coupling. It describes 3 weak bosons W^i_μ.

$U(1)_Y$ gauge group corresponds to the hypercharge interaction, which is related to electromagnetism and describes the B-field B_μ, which can be thought of as precursor to the photon. Y denotes the weak hypercharge:

$$Y = 2(Q - T_3), \tag{1.1.5}$$

where Q denotes electric charge and T_3 is the weak isospin. Together, the subgroup $SU(2)_L \times U(1)_Y$ describes the electroweak interactions.

In order to ensure that the SM theory remains locally invariant, the usual derivative ∂_μ (which does not respect local gauge invariance), must be replaced with a covariant derivative:

$$D_\mu = \partial_\mu - igA_\mu, \tag{1.1.6}$$

where A_μ is the gauge field and g denotes the coupling constant. Local gauge invariance allows spontaneous symmetry breaking, leading for instance to the Higgs mechanism and emergence of the electromagnetic force after electroweak symmetry breaking, described in the following sections.

1.1.4 Quantum Electrodynamics

Quantum Electrodynamics (QED) is the QFT of electromagnetism. In the context of the SM, it is a part of electroweak theory (given by $SU(2)_L \times U(1)_Y$) and it appears as a result of the spontaneous symmetry breaking (leaving only $U(1)_{em}$). QED describes interactions between electrically charged particles and photons using quantum fields. It is the first successful QFT and its predictions agree with experimental results at extreme precision (e.g. to order 10^{13} for the electron g-factor [5]).

The QED Lagrangian is given by:

$$\mathcal{L}_{\text{QED}} = \bar{\psi}(i\gamma^\mu D_\mu - m)\psi - \frac{1}{4}F_{\mu\nu}F^{\mu\nu}, \tag{1.1.7}$$

where ψ denotes the Dirac field for the electron (or positron), D_μ is the covariant derivative (allowing gauge invariance) and $F_{\mu\nu}$ is the electromagnetic field tensor:

$$F_{\mu\nu} = \partial_\mu A_\nu - \partial_\nu A_\mu. \tag{1.1.8}$$

Here, the electromagnetic field is represented as a gauge field, A_μ.

In QED, the coupling strength of the electromagnetic interaction and the electron charge are not truly constant but instead vary with the energy scale. This is a consequence of renormalisation - fundamental procedure in every QFT, used in order to handle infinities that arise in calculations of physical observables. This effect, known as the running of the fine-structure constant, necessitates a scale-dependent treatment of the coupling to accurately describe interactions at different energy regimes. Physically, this phenomenon arises due to charge screening, which results from the continuous spontaneous creation and annihilation of virtual fermion-

antifermion pairs in the vacuum. At higher energy scales, these quantum fluctuations become more pronounced, leading to an increase in the effective coupling strength. The QED coupling α_{QED} is defined using an introduced renormalisation scale, μ_R^2:

$$\alpha_{\text{QED}}(q^2) = \frac{e^2(q^2)}{4\pi} = \frac{\alpha_{\text{QED}}(\mu_R^2)}{1 - (\alpha_{\text{QED}}(\mu_R^2)/3\pi)\ln(q^2/\mu_R^2)}, \tag{1.1.9}$$

where q^2 is the squared four-momentum transfer in a scattering process. It defines the energy scale at which the QED coupling is being measured. At low energies, $q^2 \to 0$, $\alpha_{\text{QED}} = 1/137$.

1.1.5 Electroweak Theory

Electroweak theory unifies electromagnetic (QED) and weak interactions. The unification was developed in the 1960s by Glashow, Weinberg and Salam (GWS) [6–8], and it predicted a weak neutral-current mediated by the neutral Z boson. The GWS model was experimentally confirmed by the discovery of W and Z bosons at CERN in 1983 [9–11].

The electroweak sector is based on $SU(2)_L \times U(1)_Y$ symmetry, giving rise to the gauge fields: $W_\mu^{(3)}$, corresponding to $SU(2)_L$ and B_μ, for $U(1)_Y$. The electroweak Lagrangian before the symmetry breaking can be written as:

$$\mathcal{L}_{\text{EW}} = -\frac{1}{4}W_{\mu\nu}^a W^{a,\mu\nu} - \frac{1}{4}B_{\mu\nu}B^{\mu\nu} + i\bar{\psi}\gamma^\mu D_\mu\psi - \bar{\psi}_L Y\Phi\psi_R - V(\Phi). \tag{1.1.10}$$

It includes:

- gauge field kinetic terms with field strength tensors $W_{\mu\nu}^a$ and $B_{\mu\nu}$ for $SU(2)_L$ and for $U(1)_Y$, respectively;
- fermionic term with the covariant derivative D_μ;
- Yukawa term, $\bar{\psi}_L Y\Phi\psi_R$, generating masses of fermions after symmetry breaking;
- Higgs potential, $V(\Phi)$, which causes spontaneous symmetry breaking via the Higgs mechanism.

Due to the gauge invariance requirement in the electroweak symmetry group, all bosons should be massless. The Higgs mechanism describes the spontaneous electroweak symmetry breaking, in which the gauge bosons of the electroweak theory acquire mass, while preserving local gauge invariance.

The Higgs mechanism introduces a complex scalar doublet field Φ:

$$\Phi = \begin{pmatrix} \phi^+ \\ \phi^0 \end{pmatrix} = \frac{1}{\sqrt{2}} \begin{pmatrix} \phi_1 + i\phi_2 \\ \phi_3 + i\phi_4 \end{pmatrix}, \tag{1.1.11}$$

where ϕ^0 denotes the neutral scalar field (needed for neutral gauge bosons, γ and Z^0) and ϕ^+ denotes the charged scalar field (providing longitudinal degrees of freedom of the $W^\pm$ bosons). The corresponding Lagrangian for the given doublet of the complex scalar field can be written as:

$$\mathcal{L}_{\text{Higgs}} = (\partial_\mu \Phi)^\dagger (\partial^\mu \Phi) - V(\Phi), \tag{1.1.12}$$

with a Higgs potential of the form:

$$V(\Phi) = \mu^2 \Phi^\dagger \Phi + \lambda (\phi^\dagger \Phi)^2, \tag{1.1.13}$$

where $\mu^2 < 0$ leads to spontaneous symmetry breaking. In this case, the Higgs field acquires a non-zero vacuum expectation value (v):

$$\langle \Phi \rangle = \frac{1}{\sqrt{2}} \begin{pmatrix} 0 \\ v \end{pmatrix}, \tag{1.1.14}$$

with $v = \sqrt{-\mu^2/\lambda} = 246$ GeV. As a result, the symmetry is broken:

$$SU(2)_L \times U(1)_Y \rightarrow U(1)_{em}. \tag{1.1.15}$$

The mass of the gauge bosons can be then derived from the kinetic term of the Lagrangian 1.1.12 and substituting the v:

$$m_{\text{W}} = \frac{1}{2} g_{\text{W}} v, \quad m_{\text{Z}} = \frac{1}{2} \sqrt{g_{\text{W}}^2 + g'^2}\, v, \quad M_\gamma = 0. \tag{1.1.16}$$

The Higgs mechanism can also be used to generate masses of the fermions via the interaction of the fermion fields with the non-zero expectation value of the Higgs field.

1.1.6 Quantum Chromodynamics

Quantum Chromodynamics (QCD) is a QFT of the strong interaction. It is based on non-Abelian gauge symmetry $SU(3)_C$ and describes the dynamics of quarks and gluons. QCD is mediated by eight massless gluons and the *charge* known from QED is replaced by three conserved *colour* charges: red (r), blue (b) and green (g). Only particles with non-zero colour charge can couple to gluons. The quarks also carry a colour charge and exist in three orthogonal colour states. Similarly to QED, the antiparticles in QCD carry the opposite colour charges, i.e. $\bar{r}$, $\bar{g}$ and $\bar{b}$.

The QCD Lagrangian describes the dynamics of quarks and gluon fields. It can be written as:

$$\mathcal{L}_{\text{QCD}} = -\frac{1}{4} G^a_{\mu\nu} G^{a,\mu\nu} + \sum_f \bar{\psi}_f \left(i\gamma^\mu D_\mu - m_f \right) \psi_f, \tag{1.1.17}$$

where $G^a_{\mu\nu}$ is a strength tensor of the gluon field (with colour index $a = 1, \ldots, 8$), ψ_f denotes the quark field with flavour f, D_μ is a QCD covariant derivative and m_f is the mass of a quark with flavour f. The first term is a gluon kinetic term, describing gluon fields and gluon self-interactions. The second term describes interactions of the quarks with gluons.

One of the fundamental properties of QCD is *colour confinement*, which states that coloured particles cannot be isolated and observed individually; instead, they are always confined within colour-singlet states. As a consequence, free quarks and gluons have never been observed directly in experiments. This phenomenon is connected to the behaviour of the strong coupling constant α_s, which increases at low energy scales. For example, at a typical hadronic scale of $q \sim 1$ GeV, the coupling becomes large, $\alpha_s \sim \mathcal{O}(1)$, causing the strong interaction to be non-perturbative and effectively confining quarks and gluons inside hadrons.

Conversely, the strong coupling decreases at higher energy scales – a property known as *asymptotic freedom*. At energies around $q \sim 100$ GeV, typical of high-energy collider environments, the coupling becomes small, $\alpha_s \sim 0.1$. In this regime, quarks can be approximated as quasi-free particles, allowing perturbative QCD techniques to be applied successfully.

1.2 Limitations of the Standard Model

The SM is one of the most successful theories in modern physics, providing a precise description of a wide range of experimental observations. Its validity up to the electroweak energy scale has been confirmed by numerous precision tests, including the discovery of the Higgs boson. However, the theory is built on several theoretical assumptions designed to reproduce experimental data, and it is not considered a fundamental or ultimate theory of nature.

1.2.1 Parameters of the Standard Model

The SM of particle physics has 26 free parameters (including massive neutrinos), which are not predicted by the theory and must be determined experimentally. These are [3]:

- the masses of the twelve fermions, or equivalently, the twelve Yukawa couplings to the Higgs field, including the neutrino masses,

- the three gauge couplings, which determine the strength of the SM gauge interactions,
- the two parameters of the Higgs potential, corresponding to the Higgs boson mass and the vacuum expectation value,
- the eight flavour-mixing parameters in the quark and lepton sectors, encoded in the Cabibbo–Kobayashi–Maskawa (CKM) [12,13] and Pontecorvo–Maki–Nakagawa–Sakata (PMNS) [14, 15] matrices, respectively (four parameters in each matrix),
- the CP-violating[1] phase in the QCD Lagrangian, associated with strong CP violation.

The SM parameters can be grouped into three categories, excluding the CP-violating phase in the QCD Lagrangian: three are associated with the gauge interactions, eight with the flavour sector, and fourteen with the Higgs sector. Within these groups, certain patterns can be observed (e.g., in the fermion mass spectrum), which may hint at an as-yet unknown underlying symmetry principle.

1.2.2 Open questions

Although the SM is undoubtedly one of the greatest achievements of modern physics, it still leaves several fundamental questions unanswered. There is an active field of current experimental research, addressing these questions. One evident shortcoming of the SM is the lack of explanation for the existence of dark matter [16, 17], which is confirmed by a number of astrophysical and cosmological measurements. Some extensions of the SM explain the cold dark matter in the Universe by weakly interacting massive particles (WIMP) [18]. An extension to the SM is the theory of supersymmetry (SUSY) [19] in which every SM particle has its supersymmetric partner. In this theory some of the SUSY particles may be considered as WIMP candidates for dark matter.

A key goal of modern physics is to formulate a Grand Unified Theory (GUT) that unifies three of the four fundamental forces. The running of the coupling constants suggests that their values may approach each other and potentially converge at a high-energy scale. In the theory proposed by Georgi and Glashow [20], an additional $SU(5)$ symmetry is introduced to the SM, causing the coupling constants of the three gauge interactions to nearly unify at an energy scale of around 10^{15} GeV. However, this framework does not incorporate gravity, and all attempts to include it in such unification schemes have so far been unsuccessful.

[1] CP violation refers to the phenomenon in which the combined charge conjugation C and parity P symmetry is not conserved.

Another active area of research focuses on the nature of the Higgs boson, which is a unique particle within the SM. In order to determine whether the observed particle is indeed the SM Higgs or something more exotic, detailed studies of its properties (e.g. spin, branching ratios, and couplings) are essential. Furthermore, there are numerous open questions in the flavour sector, particularly concerning the origin of CP violation. Although the existence of exactly three generations of fermions and the observed matter–antimatter asymmetry have been experimentally established, the SM does not provide an explanation for these fundamental features.

1.3 Lepton electromagnetic moments

In recent decades, numerous precision tests of the SM have been conducted, which serve as a powerful tool to search for signs of New Physics. A common example of such studies is the measurement of the anomalous magnetic moments of leptons. This section presents a theoretical overview of the electromagnetic moments of leptons. Particular emphasis is placed on the τ-lepton, which constitutes the central focus of this dissertation.

In QED, the quantity that characterises the strength of the magnetic field produced by a magnetic source is known as the magnetic moment vector. At the particle level, charged particles also possess magnetic moments arising from their intrinsic spin. The relation between a particle's spin vector ($\vec{s}$) and its magnetic moment vector ($\vec{\mu}$) is given by the gyromagnetic factor g:

$$\vec{\mu} = g\frac{e}{2m}\vec{s}, \tag{1.3.1}$$

where e and m denote the particle's electric charge and mass, respectively [21]. In Dirac's theory of spin-1/2 particles, $g = 2$; however, loop corrections, such as the emission and absorption of virtual photons, slightly increase this value. The anomalous magnetic moment of a lepton (a_ℓ) is defined as the deviation of g from Dirac's value divided by 2:

$$a_\ell = \frac{g-2}{2}. \tag{1.3.2}$$

Measuring a_ℓ provides a stringent test of QED and can also be sensitive to BSM phenomena, including supersymmetry [22], TeV-scale leptoquarks [23], left-right symmetric models [24] and unparticle physics scenarios [25]. In the case of supersymmetry, the contribution of New Physics to a_ℓ is estimated to be proportional to m_ℓ^2/Λ^2 (where m_ℓ is the mass of the lepton and Λ denotes the scale of the potential New Physics effects). For the muon and electron, this relation gives $(m_\mu/m_e)^2 \sim 4 \times 10^4$ enhancement of the sensitivity to BSM for muon anomalous magnetic moment (a_μ), comparing to the electron (a_e). For the τ-lepton and muon

$(m_\tau/m_\mu)^2 \sim 280$, thus the τ-lepton anomalous magnetic moment (a_τ) is even more sensitive to BSM phenomena.

The values of a_e and a_μ are among the most precisely measured observables in nature, with a precision to 13 [5] and 10 decimal places [26, 27], respectively. The measurement of a_τ still lacks precision, primarily due to the experimental challenges, related to a the very short lifetime of a τ of approximately 0.3 ps [28]. The theoretical value of the a_τ in the SM is predicted to be [21]:

$$a_\tau^{\text{th}} = 0.001177171 \pm 0.000000039. \tag{1.3.3}$$

The interaction of fermions with an electric field is described by their electric dipole moment (EDM or d_ℓ), which is defined through the interaction of the particle's spin $\vec{s}$ with an external electric field $\vec{E}$. The corresponding Hamiltonian is given by:

$$H_{\text{EDM}} = -d_\ell \vec{s} \cdot \vec{E}. \tag{1.3.4}$$

In the SM, the predicted values of d_ℓ are extremely small, e.g. $d_\tau \lesssim 10^{-37}$. Measuring d_ℓ with improved precision is interesting because it provides a direct test of CP-violation in the lepton sector: d_ℓ is aligned with spin while under time reversal, spin reverses direction but the d_ℓ remains unchanged. Thus, the deviation from zero would indicate possible existence of CP-violating phases (assuming CPT is conserved) [29]. Within the SM, the predicted value of d_τ is [30]:

$$|d_\tau^{\text{th}}| \lesssim 10^{-37} e\text{cm}, \tag{1.3.5}$$

which is far beyond the sensitivity of current experimental techniques.

Electromagnetic moments of the τ-lepton can be probed using photon-induced ditau production processes $\gamma\gamma \to \tau\tau$ [31–34]. In the presented thesis, they are probed using the Pb+Pb→Pb($\gamma\gamma \to \tau\tau$)Pb process, illustrated in Figure 1.3.1 for selected τ decay modes. These modes include the *1-prong* channel, where the τ decays into one charged hadron and a neutrino ($\sim$ 46% of all decays); the *3-prong* channel, where the τ decays into three charged hadrons and a neutrino ($\sim$ 19%); and the *leptonic* channel, where the τ decays into an electron or muon accompanied by neutrinos ($\sim$ 35%). In both the 1-prong and 3-prong cases, additional neutral hadrons may also appear in the final state.

In these processes, the presence of $\gamma\tau\tau$ vertices gives sensitivity to electromagnetic couplings of the τ-lepton. This process can arise in so-called ultra-peripheral heavy-ion collisions (UPC) in the ATLAS detector (described in Section 2.2), when the distance between two incoming nuclei is larger than twice the ion radius. The nuclei are surrounded by strong electromagnetic fields which can be viewed as a coherent flux of photons (see Section 2.1).

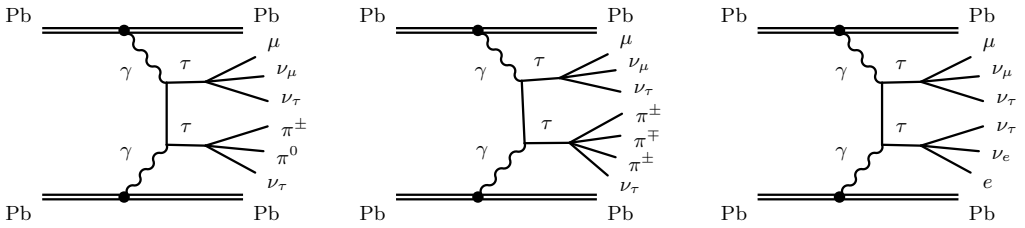

Figure 1.3.1: Illustration of photon-induced τ-lepton pair production in ultra-peripheral lead-lead collisions. Illustrative signatures of τ-lepton decays targeted by the event selection are shown: (left) one muon μ, one charged pion $\pi^{\pm}$, one neutral pion π^0 and neutrinos, (centre) one muon, three charged pions and neutrinos, (right) one muon, one electron e and neutrinos. Figure adapted from Ref. [35].

The photon-lepton vertex $\gamma\tau\tau$ can be parametrised as [36]:

$$i\Gamma_{\mu}^{(\gamma\tau\tau)}(q) = -ie\left[\gamma_{\mu}F_1(q^2) + \frac{i}{2m_{\tau}}\sigma_{\mu\nu}q^{\nu}F_2(q^2) + \frac{1}{2m_{\tau}}\gamma^5\sigma_{\mu\nu}q^{\nu}F_3(q^2)\right], \quad (1.3.6)$$

where q denotes momentum transfer and $\sigma_{\mu\nu} = \frac{i}{2}[\gamma_{\mu}, \gamma_{\nu}]$ represents the spin tensor, proportional to the commutator of the γ matrices. $F_1(q^2)$, $F_2(q^2)$ and $F_3(q^2)$ are the Dirac, Pauli and electric dipole form factors, respectively. The access to electromagnetic moments of the τ-lepton is provided in the limit as $q^2 \to 0$ (i.e. for very small virtualities of the interacting photons):

$$F_1(0) = 1, \quad (1.3.7)$$

$$F_2(0) = a_{\tau}, \quad (1.3.8)$$

$$F_3(0) = d_{\tau}\frac{2m_{\tau}}{e}. \quad (1.3.9)$$

This asymptotic condition is well satisfied in ultra-peripheral heavy-ion collisions at the LHC.

Chapter 2

Physics of photon-induced processes

At the LHC, photon-induced processes are interactions initiated by photons emitted from protons or heavy ions. In the context of heavy-ion collisions, these processes are commonly referred to as ultra-peripheral collisions (UPCs), which occur when the impact parameter exceeds twice the radius of the colliding nuclei, thus suppressing hadronic interactions. Photon-induced interactions can also take place in proton–proton (p+p) and proton–nucleus (p+A) collisions, albeit with lower photon fluxes.

This chapter provides an introduction to ultra-peripheral heavy-ion collisions and the main types of photon-induced processes, including dilepton production and diffractive photonuclear processes, which are directly relevant to the analysis presented in this thesis.

2.1 Equivalent Photon Approximation

The Equivalent Photon Approximation (EPA) is a theoretical framework that simplifies the calculation of electromagnetic processes by treating the electromagnetic field of a fast-moving charged particle as a flux of quasi-real photons. Therefore, the description of the electromagnetic interaction of this particle e.g. with a nucleus is reduced to the interaction of photons with the nucleus. This idea originates from Fermi [37] and it was further developed by Weizsäcker [38] and Williams [39], who included relativistic corrections. The updated procedure is thus also known as the Weizsäcker and Williams method and it is widely used for describing electromagnetic interactions in particle colliders and modelling ultra-peripheral collisions.

In the EPA, the QED process is factorised into a flux of equivalent photons ($n(\omega)$) and the cross section for the photon-induced subprocess. The photon flux

refers to the number of photons emitted by a moving charge per energy unit. In the case of a particle with charge Z, the spectrum is given by:

$$n(\omega) = \frac{2Z^2\alpha}{\pi\omega}\left[\ln\left(\frac{\gamma}{\omega R}\right) - \frac{1}{2}\right], \tag{2.1.1}$$

where α is the fine-structure constant, ω denotes the photon energy, γ is the Lorentz factor of the emitting particle and R refers to the effective cut-off scale (which can be e.g. the nuclear or proton radius).

For hadrons and nuclei, the photon flux is modified by additional form factors. For protons it is usually a dipole form factor, corresponding to an exponential charge distribution. In the case of nuclei, the additional form factor accounts for the nucleon distribution and it is often modelled using a Woods-Saxon distribution or by using a Gaussian form factor for lighter nuclei [40].

The total cross section for a photon-induced process using the EPA is obtained by combining the photon flux $n(\omega)$ with the subprocess cross section $\hat{\sigma}$. The cross section for dilepton production via a two-photon process, $\gamma\gamma \to \ell\ell$, can be written as [41, 42]:

$$\sigma = \int d\omega_1\, d\omega_2\, n_1(\omega_1)\, n_2(\omega_2)\, \hat{\sigma}(\gamma\gamma \to \ell\ell), \tag{2.1.2}$$

and for a single-photon process, e.g. vector meson photonuclear production:

$$\sigma = \int d\omega\, n(\omega)\, \hat{\sigma}(\gamma + A \to X). \tag{2.1.3}$$

One of the key features of the EPA is the assumption that the photons are quasi-real with virtuality $q^2 \lesssim \frac{\omega^2}{\gamma^2} \ll 1$ GeV^2 [43]. Moreover, the EPA is only valid for large enough impact parameters ($b > R_1 + R_2$, where R is the radius of the colliding object) to ensure suppression of hadronic interactions.

2.2 Ultra-peripheral heavy-ion collisions

Ultra-peripheral collisions (UPCs) [43–45] are a class of relativistic heavy-ion interactions in which the impact parameter (b) exceeds the sum of the radii of the colliding nuclei. In such events, no physical overlap of the nuclei occurs, and thus hadronic interactions are strongly suppressed. However, the intense electromagnetic fields generated by the highly charged ions can interact, leading to photon-induced processes. The exchanged photons are quasi-real, with virtualities satisfying $q^2 \lesssim \hbar^2/R^2$, where R denotes the nuclear radius. This justifies the application of the EPA, discussed in more detail in the previous subsection. A schematic illustration of an ultra-peripheral collision is shown in Figure 2.2.1.

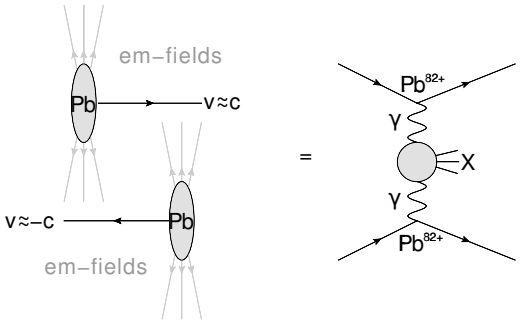

Figure 2.2.1: Illustration of an ultra-peripheral collision. Figure adapted from Ref. [46].

The photon flux in UPCs depends not only on photon energy ω but also on the impact parameter b [45]:

$$n(\omega, b) = \frac{Z^2\alpha}{\pi^2}\frac{1}{b^2\omega}\left[\xi^2 K_1^2(\xi) + \frac{1}{\gamma^2}K_0^2(\xi)\right], \tag{2.2.1}$$

where Z is the charge of the ion, α is the fine-structure constant, γ denotes the Lorentz factor of the ion and $\xi = \omega b/\gamma$. The K_0 and K_1 refer to Bessel functions, arising from the Fourier transform of the electromagnetic field. The total photon flux can then be found by integrating the formula over impact parameters. The integration range in UPC excludes collisions when nuclei interact hadronically by taking the minimum impact parameter of e.g. $2R$ [40].

It is possible that there is more than one photon exchanged between the ions during an individual collision. These photons are usually independent of the main photon-photon or photon-nucleus interaction. They can lead to dissociation of one or both nuclei, which may break up and emit neutrons, boosted along the direction of the beam. In some experiments, forward neutrons are detected by Zero-Degree Calorimeters (ZDC, described in detail in Section 3.3.3 for the ATLAS experiment). Events can then be categorised into three topologies:

- **0n0n**: no neutron emission in either direction,
- **Xn0n or 0nXn**: neutrons emission in one direction,
- **XnXn**: neutrons emission in both directions.

Selection of different ZDC classes is widely used in UPC analyses. It is often utilised to reduce backgrounds. For instance, hadronic contamination is very low in 0n0n, making it a clear signal region. On the other hand, asymmetric classes (Xn0n and 0nXn) can be useful to distinguish incoherent and coherent production (described in more detail in Section 2.3.2) for validation of neutron detection efficiencies.

Neutron topologies are also related to the impact parameter. The 0n0n class corresponds to larger impact parameters ($b > 40$ fm). The Xn0n class selects impact parameters of $b \sim 20$ fm and the XnXn class typically occurs at smaller impact parameters ($b < 15$ fm). The dependence of the impact parameter of the probabilities for different forward neutron topologies is presented in Figure 2.2.2

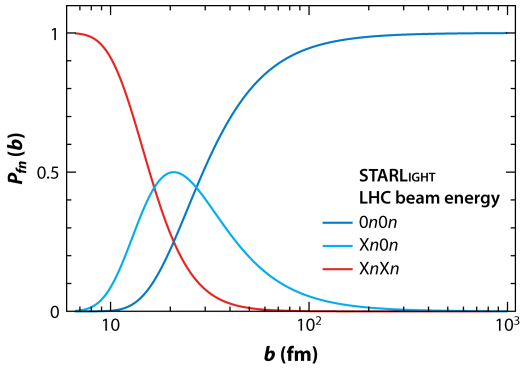

Figure 2.2.2: The dependence of probabilities for different forward neutron topologies versus impact parameter, obtained by STARLIGHT Monte Carlo generator. Figure adapted from Ref. [40].

Another important aspect of UPC analyses is the electromagnetic (EM) pileup, arising from additional soft electromagnetic interactions between the same pair of ions that participate in the hard photon-photon collision. It is caused by the large photon flux at very low photon energies, which can lead to electromagnetic dissociation (EMD) - a process in which one or both nuclei are excited by the electromagnetic field of the other, subsequently breaking up and emitting one or more nucleons, typically neutrons. This in turn can lead to misclassification of the ZDC topology. In UPC analyses, this effect is typically accounted for using correction factors.

UPCs in heavy-ion collisions exhibit several distinctive features compared to photon–photon interactions in proton–proton collisions. Event rates in UPCs depend on photon flux given by Equation 2.2.1, which scales as Z^2 in photonuclear processes and as Z^4 in the case of two-photon interactions. The significantly enhanced cross section in UPCs can be exploited to search for rare processes. Additionally, final states in UPCs have much smaller multiplicity and low pile-up levels. The p_{T} of the photons is small (approximately $p_{\mathrm{T}} \approx \omega/\gamma c$) which leads to low p_{T} of the final state. Low p_{T} thresholds in the trigger and offline reconstruction allows the exploration of regions of phase space that are inaccessible in proton–proton collisions.

2.3 Types of interactions in ultra-peripheral heavy ion collisions

In UPCs, the two common types of interactions are two-photon or photonuclear interactions [40]. The final states of the former are typically lepton or meson pairs, single mesons or two photons (in light-by-light scattering, LbyL). The latter interactions usually involve production of vector mesons or production of dijets. These processes can be classified as *exclusive*, where only the specific final-state particles are produced and the nuclei remain intact, or *inclusive*, where additional particle production occurs beyond the primary final state. Figure 2.3.1 presents diagrams with example interactions which can be measured in UPC. This section provides a general overview of the main physics topics accessible through UPCs.

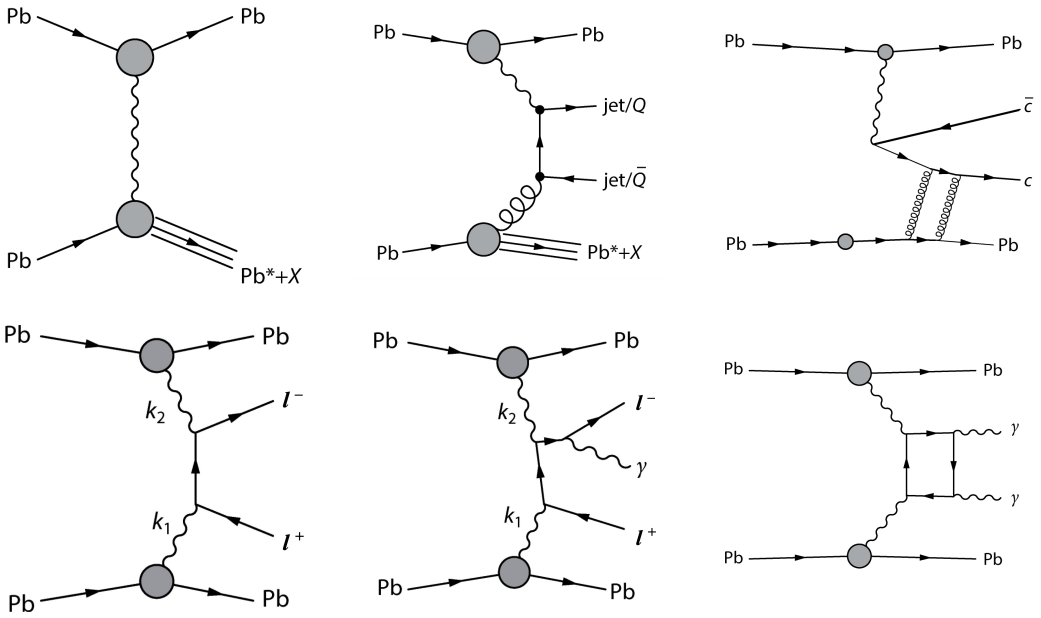

Figure 2.3.1: Illustration of various types of interactions in ultra-peripheral Pb+Pb collisions: (top-left) photonuclear interaction with nuclear dissociation, (top-middle) incoherent photonuclear production of heavy quarks/jets, (top-right) exclusive photonuclear production of a vector meson, (bottom-left) photon-induced dilepton production, (bottom-middle) dilepton production with final state radiation, (bottom-right) light-by-light scattering. Figure adapted from Ref. [40].

2.3.1 Two-photon processes

Interactions of two photons provide a unique environment to study various final states in a wide kinematic range. They couple not only to all charged particles but also to neutral final states through loop diagrams, enabling the production of two-photon final states and, in principle, the Higgs boson (although $\gamma\gamma \to H$ has not been observed yet).

Dilepton production

The most extensively studied two-photon process in heavy-ion collisions is dilepton production, with two oppositely charged leptons in the final state. It is a pure QED process at leading order and leads to very clean final states. The cross section has been well-predicted using the EPA (Equation 2.1.2). This class of interactions can also serve as a benchmark process or a control channel to validate photon flux models, event selection efficiency or detector performance. For example, dimuon and dielectron control regions have been used to validate the analysis strategy for rarer two-photon processes, e.g. $\tau^+\tau^-$ production or light-by-light scattering, respectively.

One of the main features of two-photon processes in UPCs is the very low transverse momentum (p_{T}) of the photons in the initial state. In the case of dilepton production, the p_{T} of the final state system is typically within the range of 20-30 MeV, which is much smaller than in typical hadronic collisions. Alternatively, the p_{T} of a dilepton pair can be estimated using so-called acoplanarity which is the angle between the two leptons in the transverse plane ($A_\phi = 1 - |\Delta\phi|/\pi$, where $\Delta\phi$ is the difference in azimuthal angle between the two leptons). If the leptons are back-to-back, $\Delta\phi = \pi$ and $A_\phi = 0$.

In terms of the analysis presented in this thesis, photon-induced dimuon production is one of the dominant sources of background, as described in Section 5.7.2.

Light-by-light scattering

Light-by-light scattering (LbyL, $\gamma\gamma \to \gamma\gamma$) is forbidden in classical electrodynamics. However, it is allowed via loop diagrams in QED. The process is mediated by virtual charged particles, e.g. electrons, muons or W bosons. LbyL is extremely rare due to the small cross section, nevertheless, it was first observed by ATLAS in Pb+Pb UPCs [47]. The selection criteria rely on diphoton invariant mass, isolation[1] and no additional activity in the detector. For instance, to reduce fake-photon background in the ATLAS measurement, the p_{T} of the diphoton system ($p_{\mathrm{T}}^{\gamma\gamma}$) was required to be below 1 GeV for diphoton invariant mass $m_{\gamma\gamma} < 12$ GeV and below 2 GeV for $m_{\gamma\gamma} > 12$ GeV.

There is still considerable interest in the LbyL scattering process, as it serves as a sensitive probe for BSM physics. It can be affected by various BSM scenarios, including axion-like particles (ALPs), magnetic monopoles and anomalous quartic gauge couplings.

[1] In ATLAS analyses, isolation refers to a requirement that leptons or photons are well separated from other detector activity. It is typically quantified using the scalar sum of transverse momenta of nearby tracks and/or the transverse energy registered by the calorimeter within a cone around the particle direction.

Hadron production

In principle, photon-photon interactions in UPCs can produce hadrons ($\gamma\gamma \to X$), specifically mesons and meson pairs. However, the cross section for these processes is very small, i.e. for mesons with comparable mass, the two-photon cross section is about two orders of magnitude lower than the corresponding cross section for photonuclear production of vector mesons [44]. This difference can be deducted from different coupling strengths of the electromagnetic and strong interactions ($\alpha_{\mathrm{EM}} \approx 1/137$ and $\alpha_{\mathrm{s}} \sim 1$). As a result, measurements become dominated by the large background from photonuclear interactions.

The two-photon production of the neutral pion π^0, the lightest meson, requires photons with relatively high energies, typically $\geq$ 70 MeV, which is significantly larger than the threshold for e.g. dilepton production. As a result, such interactions are more likely to occur at smaller impact parameters (around $2R$), where the probability of emitting hard photons is enhanced. To date, this production channel has not been observed in UPCs at the LHC.

2.3.2 Photonuclear processes

Photonuclear interactions in UPCs occur when a quasi-real photon emitted by one of the colliding nuclei interacts with the other nucleus. These processes provide a powerful probe of the nuclear structure and dynamics at small parton momentum fractions.

Diffractive photonuclear production

Diffractive photonuclear production refers to processes in which a quasi-real photon emitted by one ion scatters diffractively off the target nucleus, producing a hadronic final state while leaving the nucleus either intact or in a low-excitation state. Such interactions are characterised by a small four-momentum transfer and by the presence of a large rapidity gap between the produced system and the remnant nucleus and they are commonly modelled as a Pomeron[2] exchange. The remnants of the Pomeron are usually observed as tracks with low-p_{T}. Diffractive photonuclear production constitutes one of the dominant sources of background in the analysis presented in this thesis, as described in Section 5.7.3.

Low energy photonuclear interactions

The most probable photonuclear processes include low-energy nuclear excitations, as the photon flux scales as $1/\omega$ (Equation 2.2.1). The strong electromagnetic fields can

[2]The Pomeron is a colourless exchange object in QCD that carries vacuum quantum numbers and is used to describe the soft, diffractive interactions between hadrons at high energies.

excite the nuclei to higher energy states, e.g. via a so-called Giant Dipole Resonance (GDR), which is the Coulomb excitation with the highest cross section. In UPCs, the GDR is the dominant mechanism for electromagnetic dissociation, leading to the emission of one or more neutrons. The number of emitted neutrons depends on the energy of the photon and the number of GDR excitations.

Coherent and incoherent photonuclear production of vector mesons

UPC interactions offer a clean and controlled environment to investigate the photonuclear production of vector mesons, such as the ρ^0, ϕ, J/ψ, $\psi(2S)$ and $\Upsilon(nS)$, thereby providing valuable insight into the gluon structure of nuclei at small Bjorken-x (i.e. momentum fraction of a parton in the hadron).

In coherent photonuclear processes, a photon interacts with the entire nucleus as a whole, which remains intact. The produced vector meson typically has very low p_{T} ($\sim$ 60 MeV) [48]. The photon in this kind of interaction probes the average gluon distribution across the nucleus. The cross section scales approximately with the square of the number of nucleons:

$$\sigma_{\mathrm{coh}} \propto A^2. \tag{2.3.1}$$

In incoherent photonuclear processes, a photon interacts with a single nucleon inside the nucleus. In the final state, the nucleus is usually excited and breaks up (in the process of nuclear dissociation). The produced vector meson has a higher p_{T} ($\sim$ 500 MeV), since the effective size of the interaction region is smaller. In this type of photon-nucleon interaction, the photon is able to probe local fluctuations in the nuclear gluon field, which can be used to study nucleon position and substructure fluctuations. The cross section scales approximately with the number of nucleons:

$$\sigma_{\mathrm{incoh}} \propto A. \tag{2.3.2}$$

Both of these processes are relevant for understanding QCD: coherent photonuclear processes give access to the average gluon density, while the incoherent photonuclear processes are sensitive to fluctuations in the gluon field. This can be used for measuring nuclear shadowing (suppression of the nuclear structure functions at small x), constraining nuclear parton distribution functions (nPDFs) as well as studying gluon saturation (a state in which the processes of gluon splitting and recombination reach balance) and possible nonlinear QCD dynamics.

Photonuclear production of jets

UPC processes provide an opportunity to study photonuclear production of jets [49], using two production channels, often referred to as *direct* and *resolved*. In the direct

process, the photon scatters off a nucleon directly and in the resolved process, it virtually fluctuates into a hadronic state and participates in a hard-scattering process with a nucleus. Both production channels are illustrated in Figure 2.3.2.

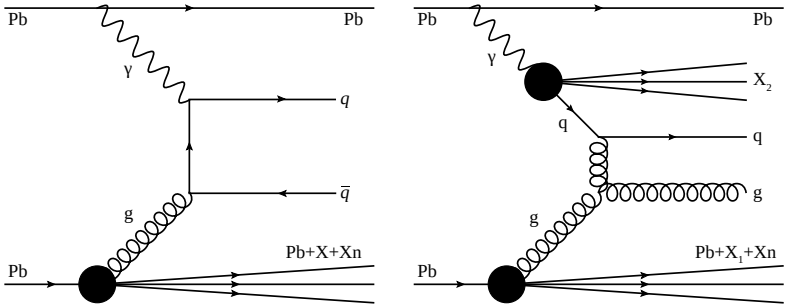

Figure 2.3.2: Feynman diagrams illustrating the leading-order mechanisms of dijet photonuclear production in UPC. Left: the *direct* process, where the photon interacts directly in the hard scattering. Right: the *resolved* process, in which the photon fluctuates into a hadronic state, before one of its constituents participates in the hard interaction. The black circles represent hard QCD scatterings between initial-state partons. Final-state hadronic systems labelled X, X_1, X_2 and X_n arise from the breakup of the nucleus or the remnant of the resolved photon. Figure adapted from [49].

Photonuclear scattering in UPCs can be distinguished from non-UPC hard scattering processes by requiring that the nucleus emitting the photon remains intact. This condition is typically enforced by vetoing neutron activity in one arm of the ZDCs, indicating the absence of nuclear breakup. This cut is combined with a requirement for gaps in the particle rapidity distribution. In the other ZDC direction, at least one neutron must be observed in order to distinguish photonuclear events and suppress backgrounds.

In such photonuclear interactions, the detection of two or more jets allows for the reconstruction of the kinematic properties of the initial-state partons. Dijet or multijet production in UPCs provides a clean and direct probe of nuclear parton distribution functions (nPDFs), free from final-state effects such as jet quenching [50]. These measurements offer access to a broad kinematic range, particularly at small parton momentum fractions x, and extend the reach to higher center-of-mass energies than those achievable in fixed-target experiments. Consequently, UPC jet production serves as a valuable tool to constrain nuclear modifications of parton densities and explore QCD dynamics in the nuclear environment.

Photonuclear production of exotic hadrons

UPCs provide a unique environment for the photonuclear production of exotic hadronic states, such as the so-called XYZ mesons [51] and pentaquarks [52]. These states, many of which contain a heavy $c\bar{c}$ or $b\bar{b}$ quark pair, are generally inaccessi-

ble in traditional fixed-target experiments due to their high production thresholds. Photonuclear production offers sensitivity to the internal structure and quantum numbers of these exotic resonances, thereby contributing to the understanding of their nature.

2.4 Modelling of photon-induced processes in ultra-peripheral heavy-ion collisions

To date, there are two most commonly used Monte Carlo (MC) generators for simulating photon-induced processes in UPC: SuperChic [53] and STARLight [54].

2.4.1 SuperChic Monte Carlo generator

SuperChic is a MC generator for central exclusive and photon-initiated production in proton-proton, proton-ion and ion-ion collisions. The central exclusive production (CEP) refers to a class of processes characterised by the exclusive production of a central system (such as a particle pair), which is isolated from the outgoing beam particles by rapidity gaps. It can be written as:

$$hh \to h + X + h, \tag{2.4.1}$$

where X denotes the final state and h refers to intact outgoing hadrons. System X is usually separated from h by large rapidity gaps, denoted by a + symbol. The CEP may be photon-initiated or QCD-initiated, as presented in Figure 2.4.1. It can also proceed via photonuclear production, which is a combination of both.

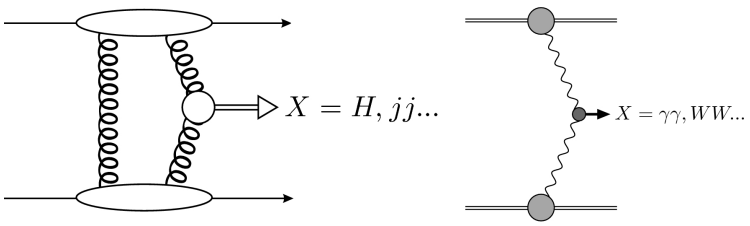

Figure 2.4.1: Illustration of two types of central exclusive production process: (left) QCD and (right) photon initiated [53].

For photon-induced processes in UPC, the total cross section is calculated using the usual EPA-based calculation for the photon flux, combined with the cross section for the simulated process at leading-order. In the photon flux, the ion form factor depends on the proton density in the ion, $\rho_p(r)$, described using the Woods-Saxon distribution:

$$\rho_p(r) = \frac{\rho_0}{1 + \exp[r - R]/d}, \tag{2.4.2}$$

where r is the radial coordinate, R is the radius of the ion ($R \sim A^{1/3}$, where A is a mass number) and d provides the nuclear skin thickness [55], which refers to the difference in the spatial distributions of neutrons and protons within an atomic nucleus ($\sim 0.5 - 0.6$, depending on the ion). The ρ_0 density is calculated using the following requirement (in which Z denotes atomic number):

$$\int \mathrm{d}^3 r \rho_p(r) = Z. \tag{2.4.3}$$

SuperChic also introduces a formalism to compute the probability that no additional interactions spoil the exclusive state. It implements the survival probability $S^2(b)$ as a function of the impact parameter. It is incorporated into the cross section by weighting the process with $S^2(b)$ and the corresponding photon flux at each b. This approach also enables accurate prediction of how the cross section scales with A, depending on the type of process, the kinematics and the centrality of the interaction, which is a measure of the geometric overlap between the two colliding nuclei.

Photon-induced processes which can be generated by SuperChic are W pair and lepton pairs production, $\gamma\gamma$, SM Higgs boson in the $b\bar{b}$ decay channel, LbyL scattering with W-loop contributions, axion-like particles as well as monopole and monopolium production. The newest version [56] additionally enables simulation of non-zero anomalous magnetic moments and electric dipole moments of the τ-lepton.

2.4.2 STARLight Monte Carlo generator

STARLight is a MC generator for UPCs of relativistic ions. It models both two-photon and photonuclear interactions. The cross sections are computed using the EPA calculation, in the impact parameter dependent formalism.

For the simulation of lepton pair production, STARLight uses first order calculations and assumes massless photons. This approach provides results that are generally in good agreement with data, however, in order to improve the kinematic distributions, the addition of higher order corrections from different generators are necessary. In STARLight all three generations of leptons are treated as stable and decays must be implemented externally.

In addition to leptons, the generator can be used for photon-induced single meson production, photonuclear production of vector mesons as well as simulation of coherent and incoherent production with optional breakup. It is also able to handle complex processes with multiple photon exchanges, such as vector meson photonuclear production with mutual Coulomb excitations.

A limitation of the STARLIGHT formalism is the implementation of a sharp cut-off on the nuclear spatial distributions: the impact parameter integrals are evaluated only in the region where $b_1 > R$, $b_2 > R$. This constraint ensures that the interaction occurs outside the spatial extent of both nuclei, consistent with the UPC regime. If the final state were produced inside or near the nuclear volume, the produced particles could undergo strong interactions with the nuclei, potentially leading to nuclear breakup, which is not dynamically modelled in STARLIGHT.

Chapter 3

Experimental setup

The CERN Council approved the Large Hadron Collider (LHC) [57] project in December 1994. The initial plan was to divide the construction of the machine into two stages, beginning with a centre-of-mass energy of 10 TeV and upgrading later to 14 TeV. Two years later, after intense negotiations, CERN Council decided to proceed with a construction of the 14 TeV machine in a single stage.

Economical considerations, such as the cost savings achieved by reusing the LEP tunnel and its injection chain, played a significant role in the decision to construct the LHC at CERN. The tunnel is 26.7 km long and it is composed of eight straight sections and eight arcs. It is located on a plane inclined at 1.4% sloping towards the Leman lake, between 45 m and 170 m underground. Along the LHC tunnel there are four interaction points where the four main experiments are located: ATLAS [58], CMS [59], ALICE [60] and LHCb [61].

3.1 The Large Hadron Collider at CERN

The LHC is a two-ring-superconducting accelerator and collider, designed to operate with centre of mass collision energies of up to 14 TeV. Every second during collisions, the LHC generates a number of events described by:

$$N_{\text{event}} = \mathcal{L} \cdot \sigma_{\text{event}}, \tag{3.1.1}$$

where $\mathcal{L}$ is the machine luminosity and σ_{event} is the cross section for the considered process. The LHC luminosity depends on the parameters of the beam and assuming a Gaussian beam distribution, it is given by:

$$\mathcal{L} = \frac{N_b^2 n_b f_{\text{ref}} \gamma_r}{4\pi \varepsilon_n \beta^*} F. \tag{3.1.2}$$

In the equation above, N_b represents the number of particles per bunch, n_b is the number of bunches per one beam, f_{ref} denotes the revolution frequency, γ_r - the

relativistic factor, ε_n - the normalised transverse beam emittance and β^* is the so-called beta function at the collision point. Both emittance and β^* are key machine parameters - the former quantifies the spread of particle positions in a beam (the nominal value at the LHC is about 3.75 µm) and the latter describes how the beam is focused at the interaction point (IP). A small β^* value indicates that the beam is squeezed strongly and has smaller transverse beam spot size.

The last factor in Equation 3.1.2, F, describes the geometric luminosity reduction, corresponding to the crossing angle at the IP. Assuming round beams with equal beam parameters for both beams, the F factor can be given by:

$$F = \left(1 + \left(\frac{\theta_c \sigma_z}{2\sigma^*}\right)^2\right)^{-\frac{1}{2}}, \tag{3.1.3}$$

where θ_c denotes the full crossing angle at the IP, σ_z is the RMS of the bunch length and σ^* is the transverse RMS of the beam size at the IP. This implies that exploration of rare processes using LHC collisions requires not only high energies of the beams but also high beam intensities.

The integral of the delivered luminosity over time is called the integrated luminosity. It represents the size of the collected dataset and can be written as follows:

$$L = \int \mathcal{L} dt. \tag{3.1.4}$$

The parameters present in the formulas above are optimised in order to reach higher luminosity during data-taking. For example, some of the typical values are: $N_b \sim 10^{11}$, $f_{\text{rev}} \sim 11$ kHz, $\beta^* \sim 0.55$ m and $F = 0.85$.

Another important aspect of operating a collider at high instantaneous luminosities is the occurrence of multiple proton-proton interactions within the same bunch crossing. These additional interactions, known as *pile-up*, overlap with the hard-scatter process of interest and increase detector activity, thereby complicating the reconstruction of physics objects. Dedicated correction techniques are therefore required to mitigate its impact on physics analyses.

3.1.1 Performance goals and machine layout

The LHC hosts two high luminosity experiments, ATLAS and CMS. Their goal is to obtain peak instantaneous luminosities of $L = 10^{34}$ cm^{-2}s^{-1} for proton operation, which is the design value for the LHC. There are also two low luminosity experiments, LHCb (specialising in B-physics) as well as TOTEM [62] (used to detect protons scattered at small angles). Their target peak luminosity is $L = 10^{32}$ cm^{-2}s^{-1} and $L = 10^{29}$ cm^{-2}s^{-1}, respectively. Additionally, the LHC can also operate as an ion collider and a dedicated experiment, ALICE, operates during lead-lead collisions.

ALICE aims at a peak luminosity of $L = 10^{27}$ cm^{-2}s^{-1} for nominal lead-lead operation.

An overview of the CERN accelerator complex is shown in Figure 3.1.1. The LHC machine has eight straight sections and eight arcs. Straight sections are usually referred to as Points with a number from 1 to 8. Each section is approximately 528 m long and is used either for hosting experiments or for housing accelerator infrastructure. The ATLAS and CMS detectors are located at Point 1 and Point 5, respectively, on opposite straight sections. The ALICE and LHCb experiments are located at Point 2 and Point 8, where additionally injection systems for Beam 1 and Beam 2 are located, respectively. The remaining Points 3 and 7 contain two collimation systems and Point 4 additionally contains two Radio-Frequency (RF) systems, which are independent for each beam.

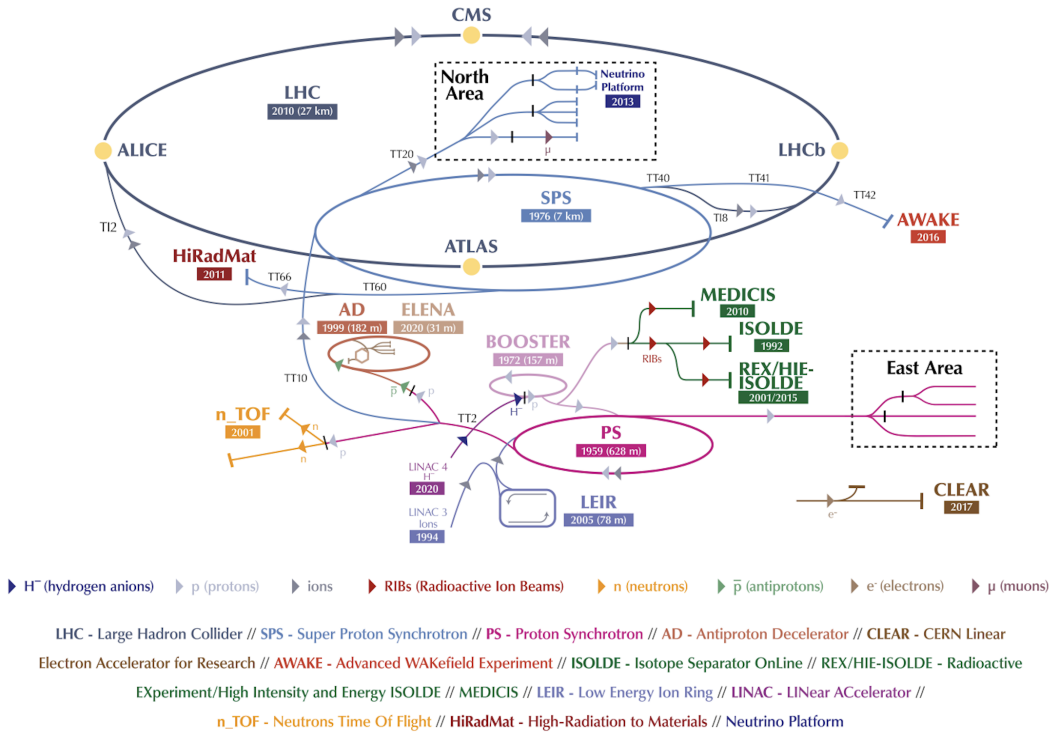

Figure 3.1.1: Schematic view of the CERN accelerator complex [63].

The technology used at the LHC relies on superconducting magnets, which are used to steer and focus the beam. The LHC machine, and circular accelerators in general, use three types of magnets: dipole magnets to create a constant magnetic field to bend the trajectory of particles, quadrupole magnets to focus the particles and prevent them from diverging as well as higher order magnets to refine the beam by correcting for distortions and focus issues introduced by imperfections in the machine or beam. The magnet system at the LHC is cooled down to a temperature below 2 K, using superfluid helium. The magnetic fields are above 8 T.

In order to accelerate the particles, Radio-Frequency (RF) cavities are utilised, which use oscillating electric fields (generated at radio frequencies) that push particles forward each time they pass through a cavity. By synchronising the oscillations with the particle's speed, the cavities can deliver a continuous energy boost as particles circulate. RF cavities also help to group particles into "bunches" and control the spread along the beam path, which improves collision rates and experiment precision.

The LHC uses two primary types of RF cavities: superconducting 400 MHz RF cavities for acceleration (also referred to as ACS - Accelerating System) and 200 MHz RF capture cavities (ACN - Capture System) for initial bunch capture and transfer. In order to achieve maximum efficiency of the ACS, cavities are made from superconducting materials and are cooled to about 1.9 K. This reduces electrical resistance nearly to zero, allowing high power with minimal energy loss, which is crucial at the LHC's high energy levels.

The ACN system is used in earlier stages of the particle injection process to capture, compress, and shape the bunches as they enter the LHC from the injector chain (specifically, from the Super Proton Synchrotron, or SPS). The 200 MHz cavities create an initial grouping of particles into bunches and perform the first longitudinal compression. This is important to ensure each bunch fits within the tighter 400 MHz structure that takes over in the main LHC ring.

3.1.2 Injection Chain

To accelerate the proton beam to relativistic velocities, the process is divided into multiple stages. Protons are sourced from ionised hydrogen gas and directed to the LHC through the injector chain, which includes the LINAC4 linear accelerator (successor of LINAC2), the BOOSTER, the Proton Synchrotron Booster (PSB), the Proton Synchrotron (PS), and finally, the Super Proton Synchrotron (SPS). Each of these accelerators has been upgraded to meet the LHC's requirements, providing a large number of high-intensity proton bunches (up to 2808 per ring in the LHC) with well-defined longitudinal profiles and minimal transverse emittances.

For heavy ions, the process begins at the LINAC3 linear accelerator, followed by beam formation in the Low Energy Ion Ring (LEIR) circular accelerator. Similarly to protons, ions are then injected into the PS and SPS before they reach the LHC.

3.1.3 LHC as an ion collider

The design of the LHC from an early stage included a heavy ion program. Collisions between lead ion beams ($^{208}Pb^{82+}$) are provided not only for the specialised ALICE detector, but also for CMS and ATLAS, which also study heavy ion collisions at similar luminosities. LHCb also records Pb+Pb collisions but at lower luminosity.

The design value for the total centre-of-mass energy per nuclear pair was 2.76 TeV and the design nominal luminosity was $L = 10^{27}$ cm^{-2}s^{-1}. In addition to standard Pb+Pb (and proton-lead collisions, p+Pb) collisions, the heavy-ion program at the LHC also includes collisions of lighter nuclei, i.e. Xenon, Oxygen and Neon.

Although the primary hardware components of the LHC ring are compatible with heavy-ion operations, the beam dynamics and performance limitations for ion beams differ significantly from those of protons in various ways. Heavy-ion running introduces specific challenges; for example, strong electromagnetic interactions in peripheral ion collisions impose constraints on both luminosity and beam lifetime. At the same time, heavy-ion collisions also offer certain advantages: in particular, the instantaneous luminosity is much lower than in proton-proton operation, making the probability of more than one nuclear interaction per bunch crossing negligible.

3.1.4 Timeline of the LHC and ATLAS data-taking

The first period of data collection, which took place between 2009 and 2013, is called Run 1. The first LHC proton beams in 2009 circulated at $\sqrt{s} = 900$ GeV. During this time, the ATLAS detector recorded approximately 9 µb^{-1} of data, which allowed calibration work to be performed. Later that year, the energy of collisions was increased to $\sqrt{s} = 2.36$ TeV, setting a new world record. The next year, proton beams with 3.5 TeV energy successfully circulated in the LHC, resulting in a centre-of-mass energy of $\sqrt{s} = 7$ TeV. This value was maintained by the end of 2011 and in 2012, the centre-of-mass energy was increased up to $\sqrt{s} = 8$ TeV, reaching a maximum peak luminosity of $L = 7.7 \times 10^{23}$ cm^{-2}s^{-1}. During Run 1, ATLAS recorded a total integrated luminosity of around 28 fb^{-1}. The average pileup in Run 1 was $\langle\mu\rangle = 18$.

First collisions of heavy ions occurred in 2010, providing two data-taking periods during Run 1 and resulting in more than 167 µb of total integrated luminosity recorded [64]. The centre-of-mass energy per nuclear pair was 2.76 TeV.

During the first Long Shutdown (LS1) in 2013 and 2014, the superconducting magnets were consolidated and the LHC machine was recommissioned at the collision energy of $\sqrt{s} = 13$ TeV, starting the second data-taking period (Run 2). In 2016, the LHC reached its design luminosity of $L = 1 \times 10^{34}$ cm^{-2}s^{-1} with 2040 bunches and 1.2×10^{11} protons in a bunch. One year later, after optimisation of the beam parameters, a new record of $L = 2.09 \times 10^{34}$ cm^{-2}s^{-1} peak luminosity was set. Due to high pile-up observed in ATLAS and CMS, it was decided to level the instantaneous luminosity to lower values ($L = 1.5 \times 10^{34}$ cm^{-2}s^{-1}). However, in 2018, the LHC achieved an approximately constant peak luminosity of $L = 1.9 \times 10^{34}$ cm^{-2}s^{-1} for most of the data-taking period. During Run 2, ATLAS recorded 147 fb^{-1} of proton-proton data. The average pileup in Run 2 was $\langle\mu\rangle = 34$.

In the case of Pb+Pb collisions, the total integrated luminosity during Run 2 was around 2 nb^{-1}. This corresponds to two heavy ion runs: in 2015 and in 2018 (when ATLAS recorded 548 μb^{-1} and 1.76 nb^{-1} of Pb+Pb data, respectively) [65]. The ions were collided with a centre-of-mass energy of 5.02 TeV per nucleon pair.

After Run 2, the accelerator complex was stopped for 4 years, starting in July 2018. During the so-called second long shutdown (LS2) various maintenance and consolidation work was performed. The LHC Run 3 started in July 2022 and will last until July 2026. The machine was recommissioned at 6.8 TeV, which corresponds to a centre-of-mass energy of 13.6 TeV, setting a new world record. In 2022, the LHC delivered 39.7 fb^{-1} of integrated luminosity, which surpassed initial expectations. The following year was challenging and required an extended repair and recovery period. As a result, the integrated luminosity delivered by the LHC in 2023 was only 31.8 fb^{-1}. So far, the average pileup in Run 3 was $\langle\mu\rangle = 55$.

The comparison of luminosities delivered to ATLAS in years 2011-2025 during p+p collisions is presented in Figure 3.1.2. The comparison of the average numbers of interactions per bunch crossing in years 2011-2025 is shown in Figure 3.1.3.

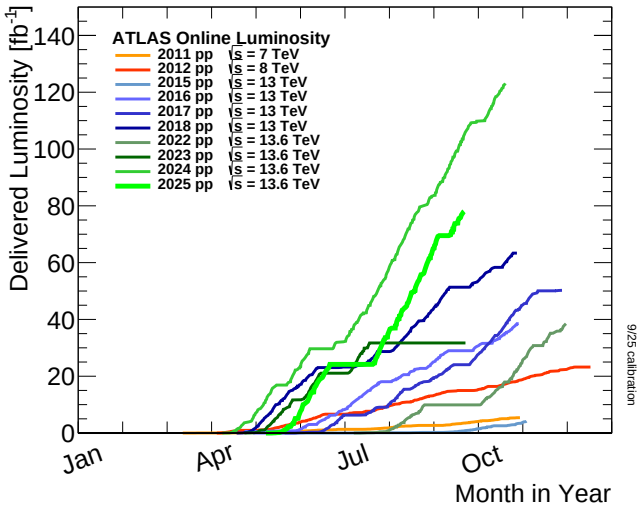

Figure 3.1.2: Delivered luminosity versus time in 2011-2025 delivered to ATLAS during p+p collisions [66].

Heavy ion campaigns in Run 3 at a centre-of-mass energy of 5.36 TeV per nucleon pair took place in 2023, 2024 and 2025. There is also a campaign scheduled for 2026. In 2023 ATLAS recorded 1.75 nb^{-1} of Pb+Pb data, 1.67 nb^{-1} in 2024 and 2.78 nb^{-1} in 2025 [66].

In order to extend the discovery potential of the LHC, there is a major upgrade planned for the next long shutdown (LS3), which will start after Run 3 in 2026 and take 3 years. The upgraded machine, the High-Luminosity LHC (HL-LHC) [67], will be able to increase the luminosity and the collision rate by a factor of five beyond

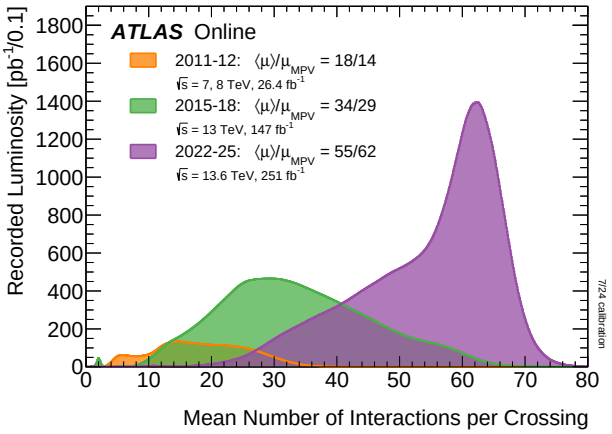

Figure 3.1.3: Average number of simultaneous interactions per bunch crossing $\langle\mu\rangle$ and the most probable values μ_{MPV} in 2011-2025 for data recorded by ATLAS [66].

the design value. The goal is also to increase the integrated luminosity by a factor of ten. The new configuration will rely on a number of cutting-edge technologies, including 11-12 T superconducting magnets, very compact and precise phase control superconducting cavities, new technology of beam collimation as well as long high-power superconducting links with no energy dissipation.

The HL-LHC is approved to operate from 2030 until 2041. It is expected to deliver an instantaneous proton-proton luminosity of up to $L = 7.5 \times 10^{34}$ cm^{-2}s^{-1} and a total integrated luminosity of 3 000 fb^{-1}. This will lead to even higher pileup rates, up to 200 simultaneous inelastic collisions per bunch crossing.

3.2 The ATLAS experiment

The ATLAS (A Toroidal LHC ApparatuS) [58,68] is a general purpose detector, built for probing proton-proton and heavy-ion collisions. By volume, it is the largest detector in the world, with a length of 44 m, a height of 25 m and a mass of about 7000 tonnes. It has a cylindrical geometry around the interaction point and a forward-backward symmetry, which enables coverage of almost the full 4π solid-angle. The detector consists of three main parts, namely the barrel (central cylinder) and two endcaps. The largest subsystem, called the Inner Detector (ID), is located closest to the interaction point. The second layer consists of calorimeters and on the outside of the detector, the Muon Spectrometer (MS) is installed. The cut-away view of the whole ATLAS detector is presented in Figure 3.2.1.

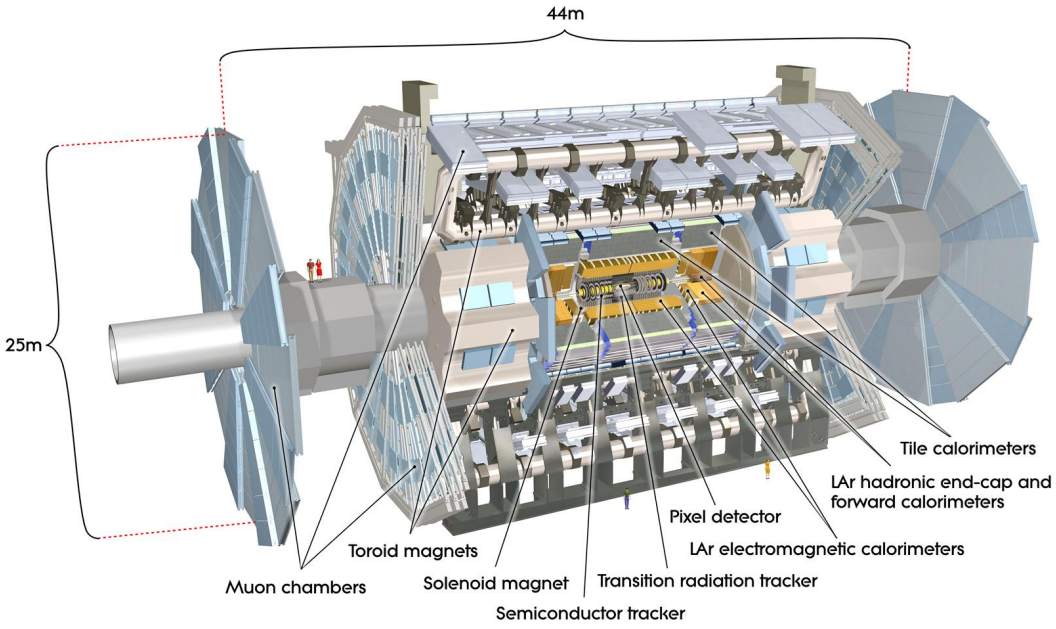

Figure 3.2.1: Schematic view of the ATLAS detector [69].

3.2.1 Coordinate system

The ATLAS detector geometry is described within a coordinate system originating from the interaction point. The z-axis is aligned with the beam direction, while the x-axis points toward the centre of the LHC ring, and the y-axis is oriented vertically upwards from the interaction point. In this framework, side-A of the detector is located in the positive z-axis direction, and side-C in the negative z-axis direction. Using polar coordinates, the azimuthal angle ϕ is measured around the beam axis, and the polar angle θ is measured from the beam axis.

The pseudorapidity η is defined in terms of the polar angle θ as follows:

$$\eta = -\ln\left(\tan\frac{\theta}{2}\right). \tag{3.2.1}$$

For measurements involving massive particles, rapidity y is often preferred over pseudorapidity. The rapidity is given by:

$$y = \frac{1}{2}\ln\left(\frac{1+\beta\cos\theta}{1-\beta\cos\theta}\right), \tag{3.2.2}$$

where β represents the particle's velocity as a fraction of the speed of light.

The radial distance ΔR between two objects in the detector, which characterizes their separation, is defined using the differences in pseudorapidity η and azimuthal angle ϕ:

$$\Delta R = \sqrt{\Delta\eta^2 + \Delta\phi^2}. \tag{3.2.3}$$

3.2.2 Physics requirements and general design concepts

Given the extensive physics potential of the LHC, the requirements for the ATLAS detector were designed around a range of processes anticipated to reveal new phenomena. The high luminosity and large cross-sections provided by the LHC allow for in-depth exploration of Quantum Chromodynamics (QCD), electroweak interactions, and flavour physics, as well as the study of top quark couplings and spin. Key benchmark searches that define the performance of the ATLAS subsystems include an extensive Higgs physics program and numerous exotic searches, such as those for supersymmetry.

To observe the rare processes, the high luminosity and interaction rate of the LHC are essential due to their low cross-sections. At the LHC's design luminosity, the inelastic proton-proton cross-section of 80 mb yields an impressive total rate of 10^9 inelastic events per second. This high event rate presents a significant experimental challenge, as each potential signal for new physics is expected to be accompanied by a large number of simultaneous interactions per bunch crossing.

General requirements for a LHC detector can be summarised in the following list:

- Fast, radiation-hard electronics as well as high detector granularity to operate with high event rates and reduce the impact of overlapping events (pileup),
- Large pseudorapidity acceptance and azimuthal coverage,
- Excellent charged-particle momentum resolution and reconstruction efficiency in the inner tracker,
- Very good electromagnetic calorimetry for identification and measurements of electrons and photons, accompanied with full-coverage hadronic calorimetry for missing transverse energy measurements (used for identifying particles which do not interact with the detector, such as neutrinos or BSM signatures) and jets measurements,
- Accurate muon identification and precise momentum resolution across a broad momentum range, along with the unambiguous determination of the charge for muons with high transverse momentum p_{T},
- Highly efficient triggering for low transverse-momentum objects, complemented with effective background rejection in order to maintain an acceptable trigger rate for the majority of physics processes of interest.

3.2.3 Inner detector

The Inner Detector (ID) is designed to reconstruct the trajectories of charged particles with momenta exceeding a given threshold, while also measuring their charge and identifying both primary and secondary vertices. The ID covers a pseudorapidity range of $|\eta| < 2.5$. It has a cylindrical geometry with a length of 3.512 m and a radius of 1.15 m, and it operates within a solenoidal magnetic field of 2 T.

The ID comprises three complementary sub-detectors: the Pixel Detector (Pixel), the Semiconductor Tracker (SCT) and the Transition Radiation Tracker (TRT). An overview of the ID and its subsystems is shown in Figure 3.2.2.

The Pixel Detector is the innermost subsystem, located closest to the beamline. It consists of silicon sensors, front-end electronics and flex-hybrids, and it spans radial distances between 50.5 mm and 150 mm. It features four layers of highly granular silicon sensors, with the innermost layer, known as the Insertable B-Layer (IBL), added in 2014 during the shutdown to enhance measurement precision, extending coverage down to 33 mm from the interaction point. The Pixel Detector contains approximately 80 million individual sensors, enabling precise three-dimensional reconstruction of particle trajectories.

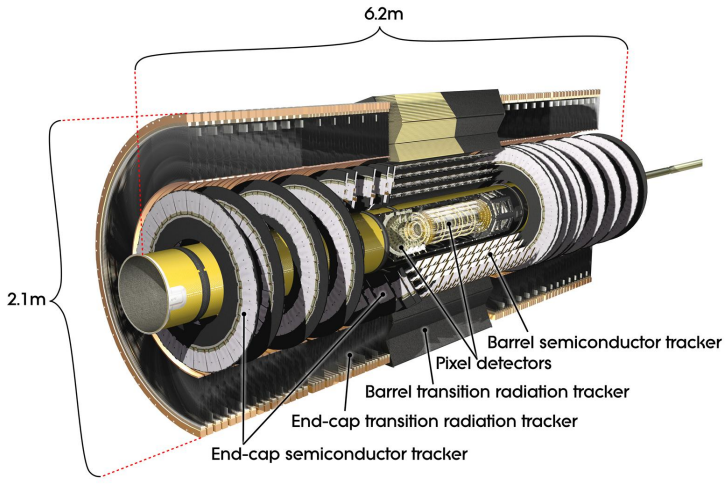

Figure 3.2.2: Schematic view of the ATLAS inner detector [70].

Surrounding the Pixel Detector is the SCT, which covers radial distances from 299 mm to 560 mm. The SCT is composed of silicon strip sensors, or "strips," arranged in four barrel layers and nine disks in the endcap regions. In total, the SCT includes 15 912 microstrips, grouped into 4 088 modules. To enable three-dimensional position measurements, pairs of strips are mounted back-to-back at an angle of 40 mrad.

The TRT forms the outermost layer of the ID, extending radially from 536 mm to 1 066 mm in the barrel region. It primarily consists of gas-filled proportional drift tubes, which facilitate particle tracking and identification by detecting transition radiation. The TRT provides two-dimensional tracking capabilities.

3.2.4 Calorimeters

The ATLAS detector features two primary types of calorimeter systems: electromagnetic (EM) and hadronic. These systems are designed to measure the energy of electromagnetic showers (primarily initiated by photons and electrons) and hadronic showers (produced by hadrons, such as pions). Both calorimeter systems cover a wide pseudorapidity range of $|\eta| < 4.9$. A critical characteristic of the calorimeters is their depth, which is carefully optimised to ensure effective containment of both electromagnetic and hadronic showers while minimising the punch-through of particles into the muon chambers. A cutaway view of the calorimeter system is presented in Figure 3.2.3.

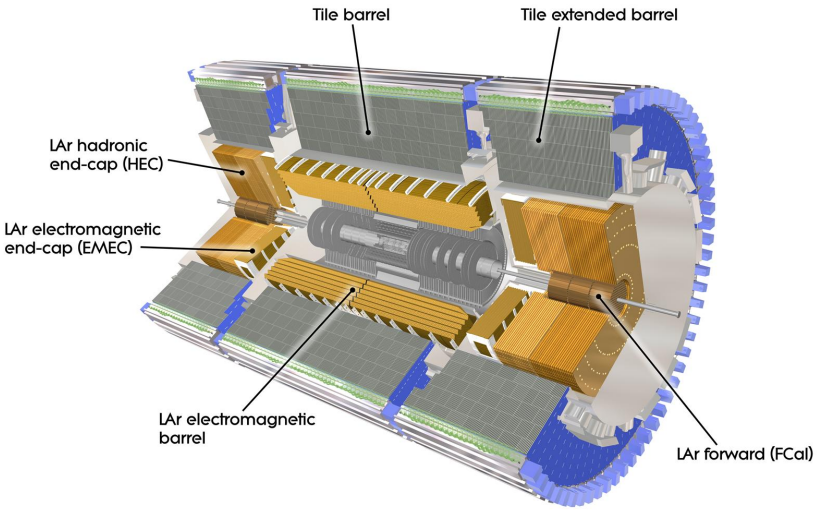

Figure 3.2.3: Schematic view of the ATLAS calorimeters [71].

The Liquid Argon (LAr) calorimeter is dedicated to the measurement of electromagnetic showers. The absorber material is lead, and the active medium is liquid argon. Its thickness is defined in terms of the radiation length (X_0), which represents the average distance over which a high-energy electron loses all but $1/e$ of its energy via bremsstrahlung [72]. In the barrel region, the LAr calorimeter has a depth of 22 X_0 and covers the range up to $|\eta| < 2.5$. For improved energy resolution, there is an additional thin presampler installed, covering the range of $|\eta| < 1.8$. The η range of $1.37 < |\eta| < 1.52$ is called the *transition region* and it is often excluded

in the analyses exploiting electrons and photons, due to decreased reconstruction efficiency. In the endcap region, the depth of the LAr is extended to 24 X_0.

The hadronic calorimeter system is composed of two main components: the Tile Calorimeter and the LAr Calorimeter. The Tile Calorimeter is designed to contain hadronic showers and uses scintillating tiles as the active material, with steel as the absorber. The LAr component includes the Hadronic End-Cap Calorimeter (HEC), which employs liquid argon as the active material and copper as the absorber. Additionally, the Forward Calorimeter (FCal), part of the hadronic system, is capable of measuring both electromagnetic and hadronic showers. The hadronic calorimeter covers the range of $|\eta| < 1.7$ in the barrel and $1.5 < |\eta| < 3.2$ in the end-cap. The FCal operates in the range $3.2 < |\eta| < 4.9$.

3.2.5 Muon system

An overview of the Muon Spectrometer (MS) is shown in Figure 3.2.4. The spectrometer's operation is based on the deflection of muon tracks within the magnetic field of three large superconducting toroid magnets: one in the barrel region and two in the end-cap regions. The toroid configuration generates a magnetic field that is perpendicular to the muon trajectories. In the barrel region, the muon chambers are arranged in three concentric cylindrical layers around the beam axis, while in the end-cap regions, they are positioned in planes perpendicular to the beamline.

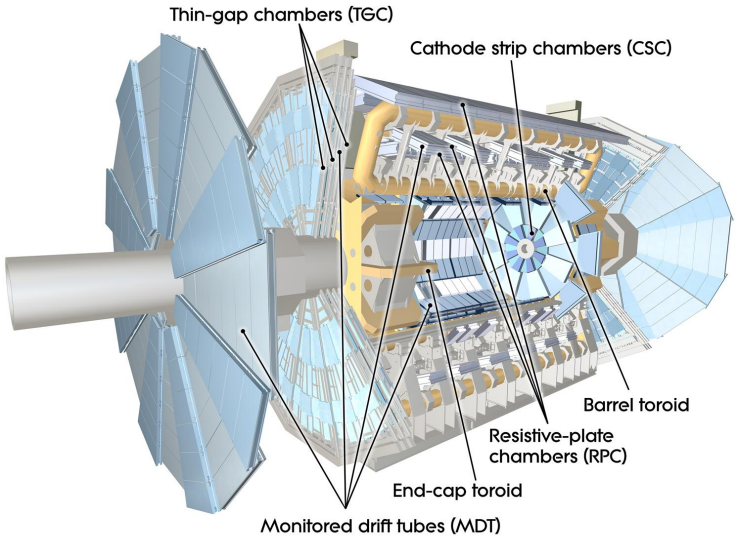

Figure 3.2.4: Schematic view of the ATLAS Muon Spectrometer [73].

The muon subsystem employs four types of chambers: Monitored Drift Tubes (MDT), Cathode Strip Chambers (CSC), Thin Gap Chambers (TGC) and Resistive Plate Chambers (RPC). The MDTs are responsible for precise track coordinate

measurements in the range of $|\eta| < 2.7$. The CSCs, which are multiwire proportional chambers with cathodes segmented into strips, operate in the pseudorapidity range of $2.0 < |\eta| < 2.7$. The TGCs and RPCs are primarily used for bunch crossing identification and coordinate measurements of muons. Both systems are also used for muon triggering: TGCs in the end-cap region and RPCs in the barrel.

3.3 ATLAS forward detectors

In order to provide coverage in the forward region, there are smaller detectors installed along the beam line. The ATLAS forward detector systems, ordered by their distance from the interaction point, begin with the Minimum Bias Trigger Scintillators (MBTS), installed at ±3.6 m from the IP. The next detectors are LUminosity measurement using Cerenkov Integrating Detector (LUCID), placed at ±17 m from the IP and Zero-Degree Calorimeters (ZDCs), positioned at ±140 m from the IP, where the LHC beam-pipe splits into two separate pipes. The last forward system is the ATLAS Forward Proton spectrometer (AFP), located at approximately ±200 m from the ATLAS main detector. Additionally, there used to be a more distant forward system, known as ALFA, however, it completed its planned data-taking period and was decommissioned in 2023.

3.3.1 The MBTS detector

The MBTS detectors [74] are installed at ±3.6 m from the main ATLAS detector, between ECal endcaps and the ID. They cover the forward region with an η range of $2.08 < |\eta| < 3.86$. Each side consists of two concentric rings of plastic scintillator counters, organised into independent sections with different ϕ ranges. Light detected by the scintillators is collected using wavelength-shifting (WLS) fibres and read out by photomultiplier tubes (PMTs).

The MBTS is designed to trigger on and select minimum bias events (with the least possible selection bias) in proton–proton and heavy-ion collisions.

3.3.2 The LUCID detector

Located at ±17 m on either side of the interaction point near the Target Absorber Secondaries (TAS) collimator, LUCID is the primary monitor of relative luminosity for ATLAS. In addition to measuring integrated luminosity, LUCID provides online monitoring of the instantaneous luminosity and beam conditions.

The LUCID detector comprises an array of twenty Cerenkov tubes surrounding the beam pipe and oriented toward the interaction point. Each tube is 1.5 m in length and has a diameter of 15 mm, and they are filled with C_4F_{10} gas at a constant pressure to ensure that traversing particles emit Cerenkov light. This light is then

measured by photomultiplier tubes (PMTs), allowing the system to distinguish the number of particles passing through each tube.

In order to determine the absolute luminosity, a calibration technique called Van Der Meer [75] scans is used. In this method, the two beams are transversely displaced with respect to each other in small, controlled steps in the horizontal and vertical directions. At each step, LUCID measures the interaction rate, which is used to determine the visible cross section. The measured event rates are then converted into the absolute luminosity. The procedure is performed regularly during special LHC fills dedicated to luminosity calibration.

3.3.3 The ZDC detector

The ATLAS ZDC [76] consists of two calorimeter modules designed to detect forward-travelling neutral particles with $|\eta| > 8.3$. This capability is particularly critical for studies of heavy-ion collisions. Positioned symmetrically at ± 140 m from the interaction point, referred to as ZDC-A and ZDC-C, each module is situated between the two beam pipes inside the Target Absorber Neutral (TAN, absorber for neutral particles), ensuring only neutral particles, unaffected by the magnetic fields, can reach the detectors (see Figure 3.3.1). The ZDC system includes both hadronic and electromagnetic calorimeter sections, which are segmented both transversely and longitudinally to provide detailed spatial and energy information for detected particles. Each module is composed of grouped quartz rods connected to photomultipliers.

The ZDC system is instrumental in heavy-ion physics, where it is likely that at least one "spectator" neutron, detached from a colliding nucleus, continues moving forward along the beamline. The ZDC is essential for determining whether the ions break-up or remain intact. This additional information is often used in event selection as it can significantly reduce backgrounds for various processes. The use of ZDC information in ultra-peripheral heavy-ion collisions, which constitute the main topic of this thesis, is discussed in Section 2.2.

3.3.4 The AFP detector

The AFP spectrometer consists of a set of near-beam instruments located in "Roman Pot" (RP) devices that measure protons scattered through very small angles in photon-induced and diffractive processes. The detection of these protons by AFP provides new kinematic information that enables effective background rejection. The AFP stations (called Near and Far) are located at approximately 200 m on both sides of the ATLAS Interaction Point. Both Near and Far stations are equipped with four layers of Silicon Tracker detectors (SiT) and the Far stations additionally contains Time-of-Flight (ToF) devices. The AFP detector is described in detail in Chapter 4.

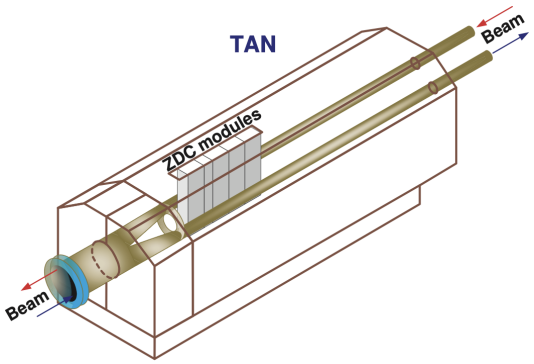

Figure 3.3.1: Illustration of the TAN showing the beam pipe and location of ZDC modules [76].

3.4 ATLAS trigger and data acquisition system

During Run 2 and Run 3 of the LHC, the bunch-crossing interval for proton-proton collisions was 25 ns, corresponding to a collision rate of 40 MHz. The majority of events are soft interactions whereas hard scattering processes are the most interesting for most ATLAS analyses. Moreover, due to the limited capabilities of the data acquisition system, it is impossible to read out and save offline data from all collisions at such a high rate. Therefore, ATLAS uses a dedicated trigger system which reduces the data rate and keeps only physics processes of interest. The ATLAS trigger system consists of two parts: a hardware-based Level-1 (L1) trigger and a software-based High-Level Trigger (HLT).

The L1 trigger [77] processes each collision and reduces the rate of data from 40 MHz to 100 kHz. The L1 consists of the Level-1 Calorimeter (L1Calo), Level-1 Muon (L1Muon) as well as the Level-1 Topological (L1Topo) trigger systems, which analyse information recorded by calorimeters and muon spectrometers, respectively, in order to search for signatures from high-p_{T} muons, electrons, photons, τ-leptons decaying into hadrons, jets and events with large missing transverse energy. The L1 trigger provides a so-called *Region of Interest* (RoI), which specifies the detector region where a signal was detected, indicates whether it passed the energy threshold, and identifies the type of the candidate object. Events accepted by the L1 trigger are then passed to the Central Trigger Processor (CTP) which applies pre-scaling factors in order to reduce the rate of common signatures (e.g. low-p_{T} jets).

Events are then sent to the HLT [78] which uses software processes in order to reconstruct the event in more detail. It reduces the data-rate from 100 kHz to 1 kHz. To provide more precise particle identification as well as better energy and momentum resolution, HLT algorithms use full-granularity information from the calorimeters, muon spectrometers and tracking systems. The HLT performs a

so-called online reconstruction, which is done in real-time during data-taking and uses fast object reconstruction algorithms. The full object reconstruction (offline) is described in Section 3.5.

Reconstruction algorithms are organized into sequential steps, forming what are known as trigger chains. These chains, grouped by their associated physics signatures, are compiled into collections referred to as trigger menus. A trigger menu is a set of selection criteria for both L1 and HLT triggers, which depend on different purposes of data-taking (specific physics analyses, detector calibration, performance measurements).

3.5 Object reconstruction

Object reconstruction in the ATLAS detector refers to the process of identifying and reconstructing the properties of *physics objects* produced during the collision. These objects include particles (electrons, muons, tau leptons, photons), charged particle tracks, jets and missing transverse energy, $E_{\mathrm{T}}^{\mathrm{miss}}$. The raw data collected by the detector consist of electronic signals from various subdetectors and during the process of reconstruction, these raw signals are translated into meaningful physics objects that can be used in physics analyses. Reconstruction of objects used in this thesis is described in the following sections.

Signatures left by traversing particles in different subdetectors are illustrated in Figure 3.5.1. At the level of the ID, the trajectories of charged particles, for example electrons and muons, can be reconstructed. When a high-energy particle enters a calorimeter, it interacts with the absorber material and initiates a cascade of secondary particles, called a shower. Electrons and photons produce electromagnetic (EM) showers through two dominant processes: *bremsstrahlung*, where a high-energy electron emits electromagnetic radiation when deflected by the electric field and *pair production*, in which a high-energy photon converts into an electron–positron pair. Hadrons (e.g. pions) induce *hadronic showers*, which involve nuclear interactions that generate for instance secondary mesons and baryons. Muons typically traverse the calorimeters with little energy loss and are subsequently detected in the MS.

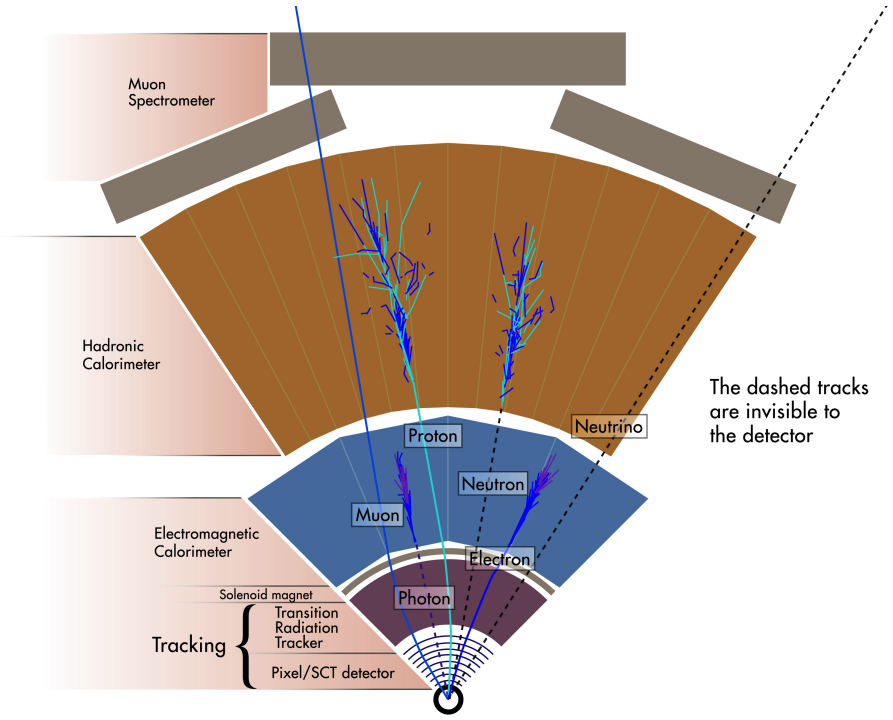

Figure 3.5.1: Illustration of the particle trajectories and their signatures in the transverse plane of the ATLAS detector [79].

3.5.1 Reconstruction of tracks

A track refers to the trajectory of a charged particle passing through the detector. It is described by five parameters and a reference point, as presented in Figure 3.5.2 and Table 3.5.1. The reconstruction of a *primary-track* in the Pixel and SCT detectors begins with cluster creation. A primary track refers to a reconstructed charged-particle trajectory that originates from the primary interaction point of the event, i.e. the location where the proton–proton (or ion–ion) collision occurred. Raw signals from pixels and strips in a given sensor are grouped into a cluster using so-called *connected component analysis* (CCA) [80]. As a result, three-dimensional measurements are obtained, referred to as *space-points*. They correspond to a point (hit) where the charged particle traversed the active material of the detector. Clusters can be created by one passing particle (*single-particle* clusters) or by multiple particles (*merged* clusters).

After cluster creation, the primary-track algorithm proceeds with an iterative track-finding method [81]. It uses track seeds formed from sets of three space-points. A combinatorial Kalman [82] filter is employed to construct track candidates starting from the selected seeds by adding compatible space-points from subsequent layers of the Pixel and SCT detectors. If multiple compatible space-point extensions

are found on the same layer, the filter generates multiple track candidates for the corresponding seed.

In the next step, a stringent ambiguity-solver is used, which compares and rates the track candidates by assigning a track score to each track (the score is largely based on simple measures of track quality, e.g. χ^2 of a track fit). After calculating the track scores, the ambiguity solver deals with clusters assigned to multiple track candidates. The reconstruction efficiency is improved by utilising a neural network (NN), trained to identify merged clusters [83].

In the final step, all track candidates accepted by the ambiguity solver are required to satisfy specific selection criteria, including, for example, the transverse momentum p_{T}, pseudorapidity η, impact parameter ranges, and the number of Pixel and SCT clusters. Track candidates fulfilling the requirements are then fitted using all available information and added to the final track collection. In order to obtain improved resolution, the position with uncertainty is determined by an additional NN, which can predict the position where a charged particle intersected the sensor as well as the number of charged particles which created the cluster.

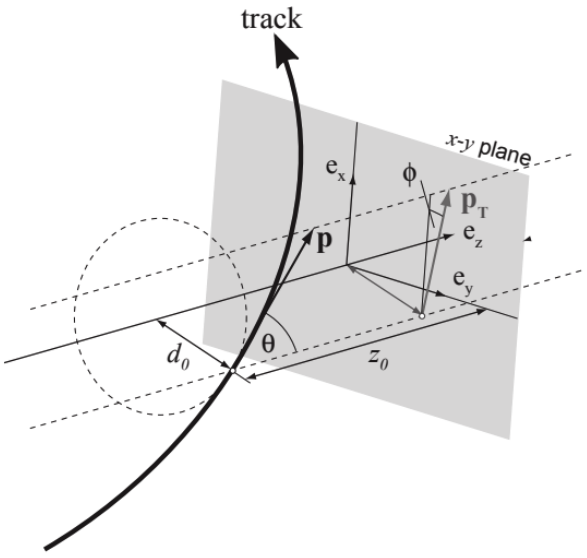

Figure 3.5.2: Schema of the global track parameters $(d_0, z_0, \phi, \theta, \frac{q}{p})$ with respect to the perigee [84].

3.5.2 Reconstruction of topo-clusters

In order to reconstruct calorimeter clusters, the so-called *topological* algorithm [85] is used. In this procedure, clusters are formed from neighbouring calorimeter cells based on the significance of their energy to the noise. The calorimeter clusters obtained in this procedure are also called "topo-clusters". This approach is excellent

Table 3.5.1: Track parameters.

Track Parameter	**Description**
d_0	The transverse impact parameter, defined as the closest approach of the track to the reference point in the transverse plane.
z_0	The longitudinal impact parameter, defined analogously to d_0.
ϕ	The azimuthal angle of the track's momentum in the transverse plane, measured in the range $[-\pi, \pi]$.
θ	The polar angle of the track's momentum in the longitudinal plane, measured in the range $[0, 2\pi]$.
$q/\|p\|$	The ratio of the charge of the reconstructed track to the magnitude of its momentum.

for reconstructing irregular or overlapping energy deposits and reducing noise. Topo-clusters are explicitly used in the analysis presented in this thesis.

Topo-clusters are calibrated using a local hadronic cell weighting (LCW) calibration, in which clusters are classified as electromagnetic or hadronic based on shower-shape variables. The calibration addresses multiple calorimeter signal inefficiencies, including non-compensating calorimeter response (smaller registered signal for hadrons than for electrons and photons at the same energy), signal losses due to intrinsic noise suppression and losses in the inactive material. The calibration procedure provides an improved energy response for particles reconstructed in the calorimeters.

3.5.3 Reconstruction of electrons and photons

In the ATLAS detector, electrons are identified in the central region ($|\eta| < 2.5$) by matching energy deposits in the electromagnetic calorimeter with tracks from the ID [86]. In the forward region ($2.5 < |\eta| < 4.9$), identification relies solely on calorimeter information due to the absence of ID coverage. Photons, on the other hand, are characterised by their energy deposits in the electromagnetic calorimeter without any associated track in the ID, as they have no electric charge. Beyond this distinction, the reconstruction of photons follows a strategy similar to that of electrons.

During Run 2, ATLAS introduced a dynamic cluster size (supercluster) reconstruction [87] to account for energy losses from electromagnetic showering. The

reconstruction algorithm begins by selecting topological clusters to be used in the identification of electrons and photons. Tracks are then refitted using the Gaussian Sum Filter [88] with bremsstrahlung effects taken into account and matched to the selected topo-clusters. The algorithm also reconstructs conversion vertices (points where a photon converts into an electron–positron pair) from the refitted tracks and matches them to the topo-clusters.

After the initial track-cluster matching and conversion building, the electron and photon reconstruction processes proceed separately. For electrons, the algorithm matches tracks to electron superclusters, while for photons, it matches conversion vertices to photon superclusters. Superclusters undergo initial position corrections before this matching step. These corrections are needed in order to account for biases from energy weighting, detector geometry, upstream material, and shower development, ensuring that the reconstructed centroid accurately reflects the particle's true trajectory.

Electrons are defined as objects consisting of a calorimeter supercluster matched to one or more tracks. Converted photons are identified as calorimeter clusters matched to one or more conversion vertices, while unconverted photons are clusters not associated with either tracks or conversion vertices. Since some objects can be classified as both electrons and photons, an ambiguity resolution step is performed to reduce overlap, while maintaining high reconstruction efficiency. Additional variables for quality checks and ambiguity resolution are calculated during the final calibration of the reconstructed electrons and photons.

After the reconstruction, electrons and photons undergo a specific selection in order to distinguish prompt particles and backgrounds [89]. Electrons and photons are identified using dedicated likelihood- and shower–shape–based algorithms designed to suppress backgrounds from non-prompt sources and hadronic activity. Electron identification relies on a multivariate likelihood discriminant that combines tracking and calorimeter observables, such as hit multiplicities, impact parameters, cluster information, with several operating points (called *VeryLoose*, *Loose*, *Medium*, *Tight*) offering different efficiencies and background rejection across transverse momentum and pseudorapidity. Additional background suppression can be achieved through track- and calorimeter-based isolation requirements, defined from the summed activity in a ΔR cone around the candidate after excluding the electron itself; these isolation criteria also provide configurable operating points. Photon identification is based on calorimetric shower-shape variables that exploit the typically narrow electromagnetic showers and low hadronic leakage of prompt photons relative to background photons from jets or neutral pion decays, with several operating points defined analogously to the electron case.

3.5.4 Reconstruction of muons

Reconstruction of muons [90] in the ATLAS detector relies on information from all subdetectors. In the ID, they are reconstructed as any other charged particle, as described in Section 3.5.1. In the calorimeters, they act as minimum ionising particles and deposit a small amount of energy. In the MS, muon reconstruction begins with a search for hits inside each muon chamber to form segments. Muon track candidates are then obtained using a fit, which takes into account hits from segments in different layers. If the χ^2 of the fit satisfies the selection requirements, a muon track is accepted.

The combined ID-MS muon reconstruction is carried out using various algorithms that rely on information from the ID, MS and calorimeters. Four muon types are categorised based on the subdetectors involved in the reconstruction process:

- **Combined (CB) muons**: The reconstruction of the muon track is done independently in the ID and MS. For the global fit, hits from both subdetectors are utilised, however, MS hits may be removed in order to improve the fit quality. The baseline method uses an *outside-in* pattern recognition, in which the reconstruction is firstly done in the MS and then matched to an ID track. In the complementary *inside-out* method, muon tracks are firstly reconstructed in the ID and then extrapolated and matched to MS tracks.

- **Segment tagged (ST) muons**: A track in the ID is identified as a muon if it is successfully extrapolated to the MS and linked to at least one local track segment within the MDT or CSC chambers. This reconstruction approach is primarily employed for muons that traverse only a single layer of MS chambers, either due to their low transverse momentum or because they originate in regions with limited MS coverage.

- **Calorimeter-tagged (CT) muons**: A track in the ID is classified as a muon if it is matched to an energy deposit in the calorimeter consistent with the signature of a minimum-ionising particle. Although this muon type has the lowest purity among all classifications, it extends the acceptance in regions where the MS is partially instrumented due to the presence of cabling and services for the calorimeters and the ID.

- **Extrapolated (ME) muons**: The reconstruction is done using only the MS information and extrapolation to the rest of the detector. At least two hits in the MS chambers and three hits in the forward region are required. This method is used outside of the acceptance of the ID.

In order to resolve the overlap between different muon types, CB muons are given the highest priority, followed by ST muons and finally calorimeter-tagged CT muons.

For overlaps involving ME muons, the track hit content is analysed and the track with better fit quality as well as larger number of hits is selected. After addressing the overlap, the final muon collections used for physics analyses are generated.

After the reconstruction, muon candidates are required to pass identification selections in order to distinguish prompt muons from backgrounds [91]. The identification relies on track–quality and momentum requirements. There are several working points defined (*Loose*, *Medium*, *Tight*, *High-*p_{T}) providing different balances between efficiency and purity. Additional background rejection can be achieved through track- and calorimeter-based isolation variables constructed from the activity in a ΔR cone around the muon, with analogous isolation working points.

Chapter 4

The ATLAS Forward Proton Detector

The ATLAS Forward Proton (AFP) detector [92] is a component of the ATLAS experiment, designed to study processes involving the scattering of protons at very small angles. It enables the detection of photon-induced and diffractive processes where one or both scattered protons remain intact. These protons usually lose a fraction of their initial energy (such that $E_{\text{proton}} < E_{\text{beam}}$) and are effectively separated from the nominal beam, due to the specific magnetic field configuration of the LHC and they can reach the AFP system. The main areas of physics that can be investigated using AFP in proton-proton interactions are various single-diffractive processes (single diffractive production of W, Z bosons and jets), Pomeron structure or photon-induced production of pairs of leptons or W bosons.

The full AFP system, comprising both the A- and C-sides, began recording data during LHC Run 2 in 2017. During this period, the primary AFP physics program focused on studies of diffractive processes accessible with the available detector configuration and luminosity conditions. In particular, AFP participated in the measurement of dilepton production in photon-induced and diffractive processes, providing the first physics results with proton tagging at ATLAS [93]. While several processes such as single diffraction (SD), diffractive jet production and double Pomeron exchange (DPE) remain of strong physics interest, comprehensive analyses of these channels represent important goals for future studies. The experience gained in Run 2 has been instrumental in preparing for Run 3, where the AFP detector is already taking data under higher-luminosity and higher-pileup conditions, further extending its physics reach. The Author contributed to the AFP project by determining the global alignment corrections and corresponding systematic uncertainties using LHC Run 3 data, described in detail in Section 4.4.

4.1 Detector components

The AFP detectors consist of a set of near-beam instruments located in so-called *Roman Pot* (RP) devices, located on both sides of the IP: A-side (towards LHCb at Point 8) and C-side (towards ALICE at Point 2). On each side there are two AFP stations (called NEAR and FAR), placed at approximately 205 m and 217 m on both sides from the ATLAS IP, respectively. Both NEAR and FAR stations are equipped with four layers of Silicon Tracker detectors (SiT) and the FAR stations additionally contain Time-of-Flight (ToF) devices. A schematic of the AFP system in relation to the ATLAS detector is presented in Figure 4.1.1. The specific detectors located in the stations are described in more details in the following sub-sections.

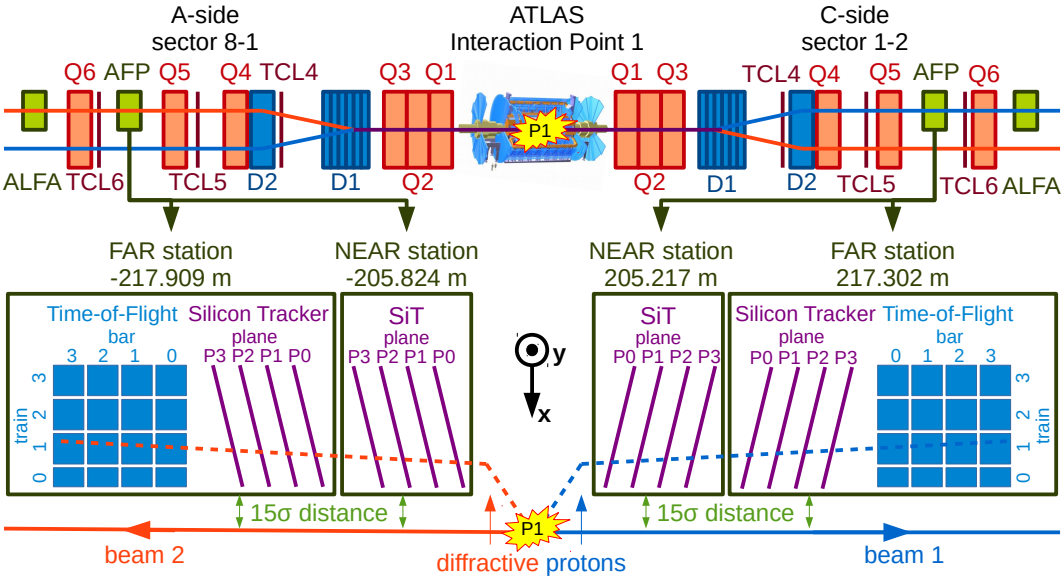

Figure 4.1.1: Schematic of the AFP apparatus and important beam-line elements. The AFP stations are located at approximately 205 m (NEAR) and 217 m (FAR) on both sides of the ATLAS Interaction Point (IP). Each station contains four layers of Silicon Tracking detectors (SiT), labelled 'P0' to 'P3' from the nearest to the furthest from the IP. The FAR stations are also equipped with Time-of-Flight (ToF) devices. The dipole bending (D1, D2) and quadrupole focussing (Q1–Q6) magnets are shown, as well as collimators (TCL5–TCL6) [2].

4.1.1 Roman Pots

AFP detectors are housed in the four RP stations [92]. The RP concept is centred around a detector volume (referred to as the pot) that is isolated from the accelerator's vacuum by a thin window. It is connected with bellows, allowing insertion into the beampipe. The RP are designed to retract the detectors during proton beam injection into the LHC and then they can be inserted to within a few millimetres

from the circulating beam once stable beam conditions are achieved. This technique was initially employed at the Intersecting Storage Rings [94] at CERN, and the RP beam interface has also been adopted by the TOTEM experiment [62].

4.1.2 Silicon tracker planes

The AFP design comprises a high resolution SiT system, providing precise momentum measurement of the scattered protons. Every AFP station accommodates four detector planes, each comprised of a silicon sensor with a thickness of 230 µm. To ensure precise reconstruction of the proton trajectory, the AFP tracking system is designed to achieve a spatial resolution of about 6 µm per station in the horizontal coordinate (x) and 30 µm in the vertical coordinate (y), where x is measured transversely to the beam direction, toward the LHC ring center, and y is measured perpendicular to both the beam and the x-direction, i.e. upward in the detector plane.

Moreover, to measure very small scattering angles, the SiT planes are positioned almost perpendicular to the beam, with a small tilt of 14° that enhances the spatial resolution by promoting charge sharing between adjacent pixel columns and enabling a more precise interpolation of the hit position. The inactive area on the detector side facing the beam is minimised to approximately 100–200 µm, allowing the active edge of the sensor to be positioned as close as 2–3 mm from the beam.

The pixel modules are essential components of the AFP tracking system. The AFP detectors use single-chip 3D pixel modules which are similar to those used in the ATLAS Insertable B-Layer (IBL) [95] with some modifications in order to fulfill the AFP tracking requirements, for example slim edge and resistance to non-uniform irradiation. Sensors are produced with "edge-less" technology, in which the inactive edge area is only about 100 µm. The AFP pixel module consists of 336×80 pixels with a pixel size of 50×250 µm^2. This corresponds to a total active area of 1.68×2.00 cm^2. The 3D sensors used at AFP have undergone beam tests which prove their suitability of operating very close to the beam [96].

In the data collection of Run 2, the SiT detectors demonstrated high efficiency. Near stations exhibited an overall efficiency exceeding 98%, while Far stations had a slightly lower performance ranging from 95% to 98%. One potential reason for this variation could be the radiation-induced degradation of the silicon tracker, particularly in the Far stations, which are positioned approximately 1 mm closer to the beam and thus experience greater exposure to the beam halo. The Far stations are located in the proximity of the TCL6 collimator, which represents a particularly radiation-intense region of the LHC. Furthermore, the efficiency of the Far stations is influenced by showers generated from interactions with detector material in the Near stations [97]. In Run 3, the AFP tracker system continues data-taking with

newly produced SiT modules and new heat exchangers in order to improve cooling capabilities.

4.1.3 Time-of-flight detectors

The main purpose of the AFP Time-of-Flight detectors (ToF) is to reduce the combinatorial background coming from pile-up protons mainly originating from single-diffractive processes. This is especially crucial in high-luminosity data taking with higher levels of pile-up (μ). The aim is to calculate the difference in time of flight of the protons on both A and C sides and compare the signal vertex obtained from proton information with the one measured by the main ATLAS detector from tracking and calorimetry information.

The AFP timing system runs at high instantaneous luminosity, where the pile-up level can exceed $\mu \geq 50$. Thus, it should meet the following requirements: timing resolution of about 10 ps, acceptance fully covering the 16.8 mm $\times$ 20 mm proton tracking detectors, $> 90\%$ efficiency and high rate capability of O(10 MHz/segment), horizontal segmentation for multi proton timing, Level 1 trigger capability as well as radiation hard or suitable for > 100 fb^{-1} integrated run operation. In practice, the best achieved timing resolution was lower, about 25 ps.

AFP comprises two ToF stations, located behind the tracker planes of the Far stations. A visualisation of the ToF detector is presented in Figure 4.1.2. It is composed of L-shaped light-guiding quartz (LQ) bars, photo-sensitive devices as well as a reference timing system to measure the correlation between two stations [98]. The LQ-bar consists of two arms: a radiator arm (exposed to the protons deflected from the beam) and a so-called light guide-arm. They are glued together at 90° angle. The radiator arm is additionally tilted at an angle of 48° (with respect to the beam) in order to optimise the time for light propagation through the bar and to minimise the amount of total reflections. The ends of the radiators extending beyond are trimmed parallel to the beam axis to redirect emitted photons downwards towards the bar. Four bars are arranged consecutively to create a series (trains), with four such series positioned on each side.

The Cherenkov photons emitted as the proton travels within the radiator arm propagate to the light-guide arm and reach the extremities of the bars connected to the micro-channel plate multi-anode photomultiplier (MCP-PMT). The geometry of the bars ensures that the optical path length is uniform across all of them.

In 2017, the resolution of the ToF devices was measured using events from ATLAS physics runs with signals in both stations at pile-up of $\mu \sim 2$. The measured resolution ranged between 20 ps to 50 ps in the individual ToF channels, however, the observed efficiency was below 5% in a major part of the analysed data. The collective time resolution of each ToF detector in that dataset was determined to

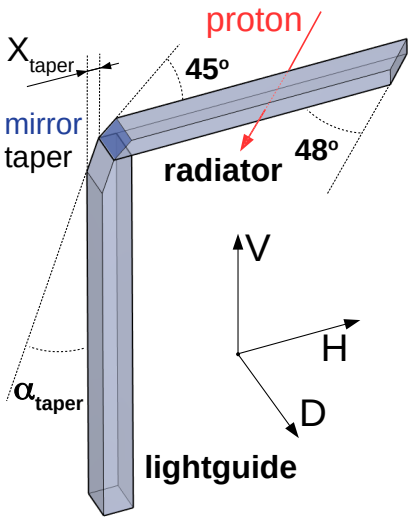

Figure 4.1.2: Visualisation of the LQ bar [2].

be 20 ± 4 ps and 26 ± 5 ps for A-side and C-side, respectively, with systematic uncertainties dominating over the statistical ones [99].

Due to the very low efficiency and several failures of MCP-PMTs during Run 2, the ToF system has undergone a significant upgrade. There was a new design of the detector flange (so called out-of-Vacuum solution) applied, new MCP-PMT back-end electronics and the detector was also equipped with modern glue-less LQ-bars [97]. At the beginning of Run 3 data-taking, the detector efficiencies were very high during the luminosity ramp-up[1] period, when the number of bunches circulating in the LHC was still below the nominal value. Over time, the efficiency gradually degraded as the number of bunches and overall beam intensity increased. The origin of this degradation at high intensities is currently under investigation.

4.2 Reconstruction of forward protons

The objective of forward proton reconstruction is to transform spatial coordinate measurements (x, y, z) into outgoing proton four-vectors (E, p_x, p_y, p_z). The reconstruction of proton four-momentum begins with pixel hits in SiT, which are then clustered together and form tracks. At the end, proton objects are obtained from SiT tracks that passed specific quality requirements. This process is illustrated in Figure 4.2.1.

SiT pixel hits within each plane are clustered using so-called neighbouring functions. They are considered neighbours if they occur in the same SiT plane, in adjacent pixel columns and in the same pixel row. Given the dimensions of the SiT

[1]Ramp-up refers to the gradual increase of the beam energy or the accelerator's operational intensity during a commissioning or restart phase.

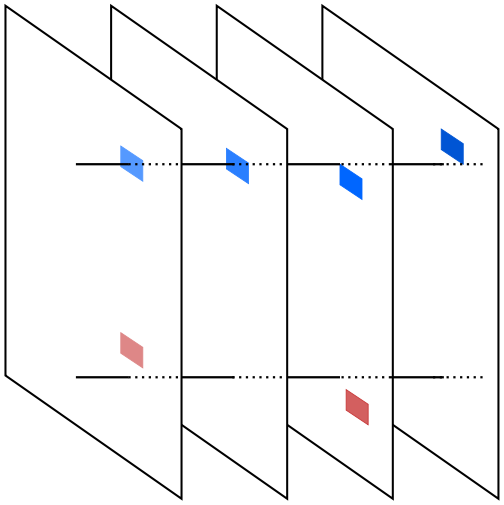

Figure 4.2.1: Illustration of an AFP station, detailing its layers, clusters within layers, and potential SiT tracks. The blue clusters form a track, whereas the red clusters do not, due to the absence of clusters in the second and fourth layers [2].

pixels, a track is more likely to pass through two adjacent pixels in the same column (short-pixel direction) rather than through two adjacent pixels in the same row (long-pixel direction). It should be noted that before further track reconstruction, the positions of the local clusters are additionally corrected for inter-plane misalignment, described in Section 4.3.

The next step is the reconstruction of the tracks by identifying clusters that are within a user-defined maximum separation in the $x - y$ plane ($\sqrt{(\Delta x)^2 + (\Delta y)^2} <$ 0.5 mm, by default). A candidate for a track is then created from each cluster located in the defined region. In the default reconstruction, clusters are required to be present in at least two successive SiT planes. If multiple clusters exist within the track candidate, the optimal track is determined using a linear regression algorithm, which fits a track to the given set of clusters. The goodness of fit is estimated using the χ^2 test. Cluster uncertainties originate from the pixel resolution.

In the last step, forward protons are reconstructed from tracks that meet specific quality criteria. Users can determine the quality of the proton objects by selecting from *loose*, *medium* (default) and *tight* options:

- **Loose**: At least two clusters in the track;
- **Medium**: Meets the Loose criteria, plus a minimum of two SiT planes;
- **Tight**: Meets the Medium criteria, with no more than one cluster hit per SiT plane.

Protons can be reconstructed using tracks detected in both AFP stations or in a single station. The former requires a track in both the NEAR and FAR station with a maximum distance in the transverse plane of $r_{\text{max}} = 2$ mm between the two tracks. In the latter method, there is no such requirement, however, if there are reconstructed tracks in both AFP stations that fail the r_{max} requirement, the proton is reconstructed using only the track from the FAR station.

The kinematics of reconstructed protons in AFP analyses are typically expressed by their fractional energy loss ξ:

$$\xi = 1 - E'_{\text{p}}/E_{\text{p}}, \tag{4.2.1}$$

where E_p and E'_p are the energies of the incoming and scattered protons, respectively. The proton ξ obtained using the above equation can be related to the horizontal position, x, of the proton measured in the AFP. This relation is described by the parametrised transport function, $x = T(\xi)$, which depends on the LHC magnetic optics and is determined from fits to x versus ξ in simulation.

Significant proton fractional energy losses are usually associated with substantial deflections from the beamline, with the strongest correlation being in the x direction due to the D1 and D2 dipole magnets (see Figure 4.1.1). For a fixed ξ, non-zero proton p_x and p_y values primarily influence the spatial positions in the AFP stations along the x and y directions, respectively.

4.3 Inter-plane alignment

Local alignment is the first step of the AFP alignment procedure, which refers to determination of the relative positions of the four SiT planes within each station. It has an impact on track reconstruction and therefore also on the reconstruction of the proton objects. Studies of the local alignment have been initiated during LHC Run 2 using the method described in detail in Ref. [100, 101]. In Run 3, the studies were repeated using new data. This section summarises the used method and the derived corrections.

The derivation of the local alignment corrections rely on minimising the differences between the cluster and the track position within each SiT plane. The expected (true) position of the protons is represented using the track positions as a reference. Each algorithm is initialised by reconstructing track segments[2] within each station using the method discussed in Section 4.2. As a starting point, all planes are assumed to be perfectly aligned and all segments are parallel to the beam-line. The alignment procedure used in Run 2 accounts for off-sets of x and y-coordinates

[2] A track segment is a straight-line trajectory reconstructed within a single AFP station, using hits recorded in the multiple silicon tracking planes of that station.

and rotation of planes around the z-axis. For a track that is parallel to the beam, off-sets in relation to the z-coordinate do not impact track reconstruction. The tilts of the $y-z$ and $x-z$ planes are represented as rotations about the x and y axes and their impact on reconstruction is even smaller and therefore can be neglected. The relation between the position of the track ($\vec{r_t}$) and the position of the clusters ($\vec{r_c}$) can be described with the following formula [101, 102]:

$$\vec{r_t} = R\left(\alpha, \beta, \gamma\right) \vec{r_c} + \delta\vec{r}\left(\delta x, \delta y, \delta z\right) \tag{4.3.1}$$

where $R(\alpha, \beta, \gamma)$ denotes the rotation matrix in three dimensions, which corresponds to the rotation angles around the z, y, x axes, respectively, and $\delta\vec{r}$ is the off-set correction along the x, y, z axes.

Each SiT plane has six degrees of freedom: three rotational and three translational, resulting in 24 free parameters per station. One can use the small-angle approximation for the rotation matrix as shown in Equation 4.3.1 and focus on rotations around the z-axis as well as adjustments in the x and y direction. Additionally, three degrees of freedom are removed by calculating the alignment parameters relative to the SiT plane closest to the collision point, designated as the 0th plane. This approach also eliminates one weak mode (referring to a translation or rotation that does not change the residuals or the χ^2 of a given track), which involves shifting the entire detector. As a result, only nine free parameters need to be determined for each AFP station.

In the method developed during Run 2 [101], in the initial step the values of the alignment parameters are set to zero, assuming no disagreement between the position of a reconstructed track and a cluster in a given plane. Then the alignment algorithm proceeds through iterative calculations until a stable state is reached, indicating that no further correction is needed. The offset along the x-axis before and after local alignment corrections for 2022 data is presented in Figure 4.3.1 for the C-Far station. Before applying all corrections, the average difference between the measured cluster hit position and the reconstructed track position is 29.27 µm, which corresponds to the offset of the 1$^{\text{st}}$ SiT plane in the x-direction. The calculations reach convergence after multiple iterations, resulting in the average distance between the hit and the reconstructed track consistent with zero: 0.01 µm.

Before correcting the plane's rotation, the mean residual $x_{\text{track}} - x_{\text{cluster}}$ (Δx) varies with y, as illustrated in Figure 4.3.2 for the C-Far station using 2022 data. This variation indicates discrepancy between the measured cluster hit position and the reconstructed track position, which increases with y. It indicates the rotation of the considered 1$^{\text{st}}$ SiT plane about the z-axis by an angle of 0.51 mrad. After applying local alignment corrections, Δx dependence on y is considered constant and consistent with zero. Uncertainties are statistical only.

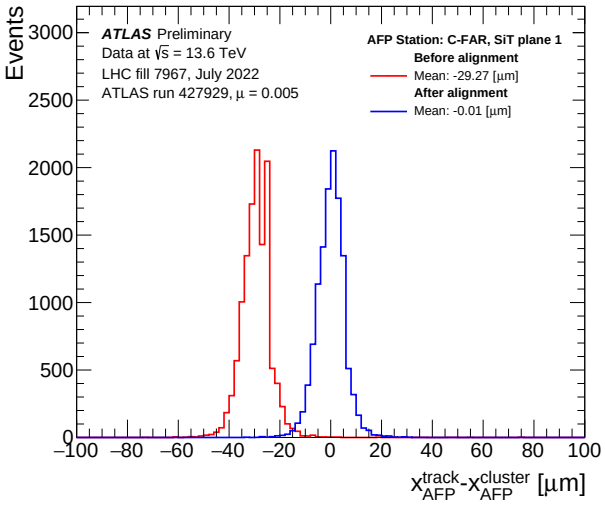

Figure 4.3.1: Comparison of the residual distribution for the x-coordinate in the second plane (plane-1) of the C-Far AFP station, before the alignment (red) and after the alignment (blue). The residuals denote the difference between the measured cluster position in the SiT plane and the reconstructed track position, calculated as $x_{\text{track}} - x_{\text{cluster}}$. The averages of these distributions are displayed as well [2].

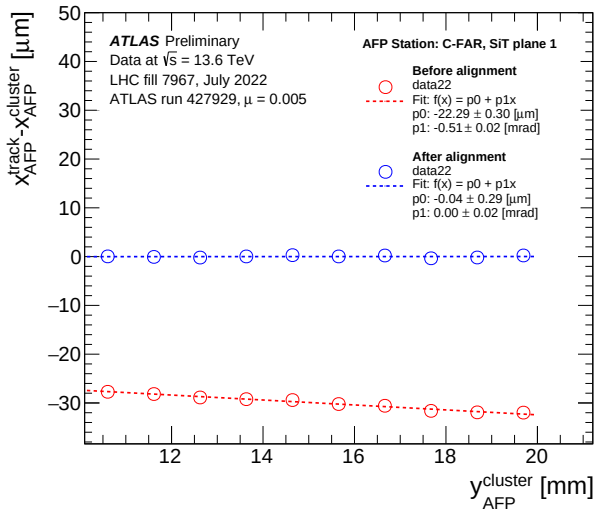

Figure 4.3.2: The mean residual value in x as a function of position in the y-direction, for the second plane of the C-Far station (plane-1), before the alignment (red) and after the alignment (blue). A linear fit to the data points is shown and the parameters of the fits are displayed alongside their respective statistical uncertainties [2].

4.4 Global alignment

The term 'global alignment' pertains to determining the position of each AFP station relative to the beam. The precise calculation of the global alignment corrections is crucial for many analyses relying on AFP, e.g. it was the source of the biggest systematic uncertainty for the Run 2 dilepton + forward proton measurement [93]. Once the relative position of the four SiT planes within a station is known (referred to as 'local alignment', described in Section 4.3), solving the global alignment involves obtaining a single constant that shifts the x-coordinate of reconstructed track segments in each station with respect to the beam. In practice, the position of the nominal origin of the SiT detector relative to the beam is deconstructed into various contributions that explicitly account for run and station dependencies. Given the x-position of the track prior to any alignment other than local, $x_{\text{pre-align}}$, additive alignment parameters dependent on run r and station s are applied to yield the aligned track coordinate $x(r, s)$, as detailed in Ref. [100]:

$$x(r, s) = x_{\text{pre-align}} + x_{\text{tracker}} - x_{\text{beam}}(s) + x_{\text{RP}}(r, s) + \delta x_{\text{corr}}(s) \ . \tag{4.4.1}$$

The tracker position, x_{tracker}, represents the distance between the bottom of the RP and the closest SiT sensor, assumed to be constant across stations and has a fixed value of $-0.5\,\text{mm}$.

The distance between the beam centre and the beam pipe centre ($x_{\text{beam}}(s)$) is determined using standard beam-based alignment (BBA) procedures [103]. These procedures are employed to identify the RP motor positions at which the RP approaches the beam edge, thereby defining the corresponding *safe* motor positions. The RP position ($x_{\text{RP}}(r, s)$) corresponds to the distance between the bottom of the RP and the beam pipe centre and remains constant for long periods. It is also measured from BBA. The distances are depicted in the schema in Figure 4.4.1. The corrections utilised to derive in-situ global alignment constants described in the next sub-section are summarised in Table 4.4.1 [100].

The in-situ corrections, $\delta x_{\text{corr}}(s)$, and the corresponding systematic uncertainties for the 2022 dataset, derived from the analysis of photon-induced dimuon events, were the focus of the Author's ATLAS Qualification Project (AQP). Following the completion of the AQP, the Author continued the work on the global alignment using the datasets collected in 2023 and 2024. The results of the AQP based on 2022 data are elucidated in the subsequent section.

4.4.1 In-situ corrections using dimuon data

The final part of the global alignment corrections, denoted as $\delta x_{\text{corr}}(s)$, is determined from collision data. A tight selection targeting photon-induced dimuon events is

employed to ensure that the intact proton recorded by the AFP and the lepton pair recorded by the central ATLAS detector originate from a common process as frequently as possible. Feynman diagrams illustrating the studied process are depicted in Figure 4.4.2.

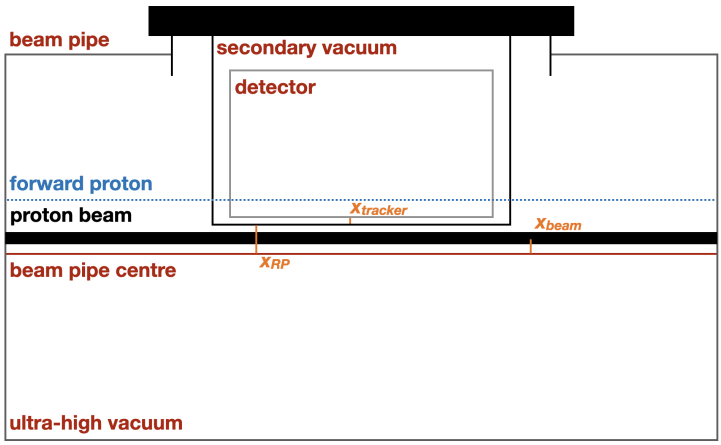

Figure 4.4.1: Schema of an AFP station inside a 'Roman Pot' with respect to the beam pipe. Figure adapted from [104].

Table 4.4.1: Alignment corrections for 2022 data. The parameters dependent on run r and station s, applied to yield the aligned track coordinate $x(r, s)$.

Station	x_{tracker} [mm]	$x_{\text{beam}}(s)$ [mm]	$x_{\text{RP}}(r, s)$ [mm]
0 (A Far)	-0.5	-1.000	-2.47
1 (A Near)	-0.5	-0.782	-3.01
2 (C Near)	-0.5	-0.995	-3.33
3 (C Far)	-0.5	-0.556	-2.08

Using the central ATLAS detector, one can compute the anticipated fractional proton energy loss via the dimuon system ($\xi_{\mu\mu}$). This quantity is dependent on the dimuon invariant mass ($m_{\mu\mu}$), centre-of-mass energy ($\sqrt{s}$) and dimuon rapidity ($y_{\mu\mu}$), as expressed by the equation:

$$\xi_{\mu\mu} = \frac{m_{\mu\mu}}{\sqrt{s}} \mathrm{e}^{\pm y_{\mu\mu}}. \tag{4.4.2}$$

This quantity is correlated to the expected x-coordinate, denoted as $x_{\mu\mu}$, where a proton track segment should be located in each AFP station. In practice, this mapping from ξ to $x_{\mu\mu}$ is accomplished using parametrisation files that offer a description of the LHC magnet configuration. By utilising AFP, one can measure the proton track segment position, denoted as x_{AFP}. In the global alignment process, a

Gaussian distribution is fitted to the $x_{\mathrm{AFP}} - x_{\mu\mu}$ distribution, and its mean value serves as an alignment constant. Thus, the well calibrated dimuon system is used to align the AFP detectors.

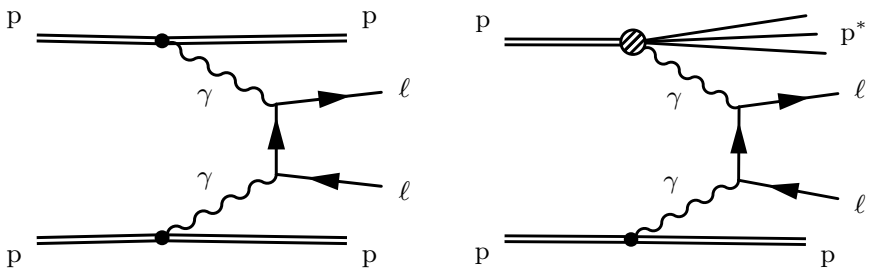

Figure 4.4.2: Feynman diagrams illustrating photon-induced dilepton production in the (left) elastic and (right) single-dissociative process [93].

4.4.2 Analysis framework and event selection

The Author migrated the code originally designed for determining global alignment during Run 2 to the so-called release 22 software, in order be compatible with the Run 3 data. The migration of the analysis framework to release 22 included applying the updated ATLAS and AFP data quality selections (Good Run List, GRL), Run 3 trigger, new recommendations for muons (affecting muon calibration) and updating the beam optics.

The global alignment procedure relies on data corresponding to an integrated luminosity of approximately 25 fb^{-1} [66] recorded in 2022 by AFP (compared to 14.6 fb^{-1} in 2017 [65]), following the application of ATLAS and AFP data quality selections. The first part of the code takes a custom data format designed to select photon-induced processes from 2022 proton-proton collisions at a centre-of-mass energy of $\sqrt{s} = 13.6$ TeV as an input and generates analysis ntuples containing photon-induced dimuon candidates.

Work was also carried out on the global alignment and its associated uncertainties using 2023 and 2024 data, corresponding to an integrated luminosities of approximately 26 fb^{-1} and 110 fb^{-1} recorded by AFP (prior to data-quality requirements) in 2023 and 2024, respectively.

The second part of the code performs the actual global alignment calibration. It utilises events containing dimuon candidates along with all good proton tracks and proton objects. Protons are reconstructed only if a good track is registered in the Far station. However, there is no explicit requirement to have a reconstructed proton object in the event. The x-coordinates are obtained from the reconstructed AFP tracks (rather than proton objects) and signal histograms are generated using

the x-coordinate of the track closest to the dimuon x ($x_{\mu\mu}$) for each station, denoted as x_{AFP}. Consequently, any track can be selected, provided it is sufficiently close to the predicted value.

The code primarily uses double-station reconstruction; however, the reconstructed proton objects are employed only for determining the fractional energy loss of protons, ξ_{AFP}. Therefore, whether single-station reconstruction (with a proton object in the FAR station) or double-station reconstruction (with proton objects in both FAR and NEAR stations) is required makes little practical difference, although minor variations were observed during evaluations due to cuts imposed on ξ_{AFP}. It should be noted that in double-station reconstruction, tracks may also be observed in stations where no proton object is present.

Events are required to pass the dimuon trigger and fulfill the ATLAS and AFP GRLs. The selected muon quality level is set to medium [90] and exactly two muons are required in the event. Further selection criteria include $\xi_{\mu\mu} > 0.02$ and $\xi_{\mathrm{AFP}} > 0.02$, $|\eta_\mu| < 2.4$, $p_{\mathrm{T}}^{\mu} > 14$ GeV. To target photon-induced dimuon production the following requirements are applied: transverse momentum of the dimuon system $p_{\mathrm{T}}^{\mu\mu} < 5$ GeV, acoplanarity $A_{\phi}^{\mu\mu} = 1 - |\Delta\phi_{\mu\mu}|/\pi < 0.01$, distance to the nearest non-μ track $|\Delta z| > 0.5$ mm and dimuon invariant mass ($m_{\mu\mu}$) not in the Z-boson mass window (20 GeV $< m_{\mu\mu} <$ 70 GeV) $\bigcup m_{\mu\mu} > 105$ GeV.

4.4.3 Global alignment correction and systematic uncertainty

The in situ correction relies on event-by-event comparisons between $x_{\mu\mu}$ and x_{AFP}. Distributions of $x_{\mathrm{AFP}} - x_{\mu\mu}$ for A-side and C-side are shown in Figure 4.4.3 and the signal distributions (after subtracting the background) with a fitted Gaussian are depicted in Figure 4.4.4. The peak in these distributions corresponds to genuine correlations between the muons and proton, superimposed on a background resulting from random coincidences. The shift of the peak away from the 0-position indicates the misalignment of the AFP station.

Background estimation is achieved through an event-mixing technique, where $x_{\mu\mu}$ is chosen from a randomly selected event in a dimuon sample before requiring an AFP track segment, and x_{AFP} is selected from a randomly chosen event with an AFP track in the corresponding station. The background is normalised to data in the $(x_{\mathrm{AFP}} - x_{\mu\mu}) < -1$ mm region to avoid signal contamination. The alignment correction value δx_{corr} for a given station is determined from the mean value of a Gaussian fit around the peak region after subtracting the background contribution. For example, in Figure 4.4.4, the Gaussian fit to the distribution before the alignment correction for A-FAR station (top left) yields a mean of 900 ± 46 µm, which is taken as the alignment offset. This procedure is repeated multiple times until it converges at a value consistent with zero.

Alignment corrections for the NEAR stations are further refined during the final 'fine-tuning' step of the global alignment procedure, as illustrated in Figure 4.4.5. This step is motivated by the requirement to centre the x-component of the proton momentum around zero, as protons have an initial transverse momentum of $p_x = 0$ GeV and should exhibit no preferred deviation in the horizontal direction after scattering. In this additional procedure, the background-subtracted $x_{\text{AFP}} - x_{\mu\mu}$ distributions for the NEAR stations are shifted until the mean value of the p_x histogram for the corresponding AFP arm is consistent with zero. For the p_x distribution, events are required to have exactly one good proton track and ξ_{AFP} within the range $0.04 < \xi_{\text{AFP}} < 0.06$. This tight cut on ξ_{AFP} is applied to avoid bias, as the acceptance near the detector edge is not 100%.

The full set of alignment corrections with additional 'fine' tuning step is:

$$\begin{aligned}
\delta x_{\text{corr}}(\text{A FAR}) &= -0.940 \text{ mm};\\
\delta x_{\text{corr}}(\text{A NEAR}) &= -0.703 \text{ mm};\\
\delta x_{\text{corr}}(\text{C NEAR}) &= -0.558 \text{ mm};\\
\delta x_{\text{corr}}(\text{C FAR}) &= -0.350 \text{ mm}.
\end{aligned}$$

In order to evaluate the robustness of the global alignment corrections and to derive the corresponding systematic uncertainties, the in-situ analysis is repeated multiple times with different variations of the selection cuts and other analysis requirements. The considered variations include modifications to the default selection criteria and the application of additional adjustments, such as requiring exactly one track reconstructed in the AFP arm; varying the dimuon pair transverse momentum cut from $p_{\text{T}}^{\mu\mu} < 5$ GeV to $p_{\text{T}}^{\mu\mu} < 4$ GeV and $p_{\text{T}}^{\mu\mu} < 3$ GeV; changing the distance to the nearest non-muon track from $|\Delta z| > 0.5$ mm to $|\Delta z| > 0.3$ mm and $|\Delta z| > 0.7$ mm; varying the acoplanarity cut from $A_\phi^{\mu\mu} < 0.01$ to $A_\phi^{\mu\mu} < 0.02$ and $A_\phi^{\mu\mu} < 0.03$; and changing the $\xi_{\mu\mu}$ requirement from $\xi_{\mu\mu} > 0.02$ to $\xi_{\mu\mu} > 0.015$, $\xi_{\mu\mu} > 0.017$, $\xi_{\mu\mu} > 0.019$, $\xi_{\mu\mu} > 0.021$, $\xi_{\mu\mu} > 0.023$ and $\xi_{\mu\mu} > 0.025$. Additional tests are performed by modifying the binning from 100 bins to 70, 150 and 200 bins and changing the fit range from the default interval of (−1 mm, 1 mm) to (−0.8 mm, 0.8 mm) and (−0.6 mm, 0.6 mm). Furthermore, the procedure is repeated including the region around the Z-boson peak and by performing the analysis without background subtraction.

The comparison of the systematic tests for the AFP stations on the A-side and C-side, obtained from fits to the signal distributions after applying all alignment corrections, is shown in Figures 4.4.6 and 4.4.7, respectively. The applied variations result in shifts of the alignment constants typically below 100 µm for most of the tested modifications.

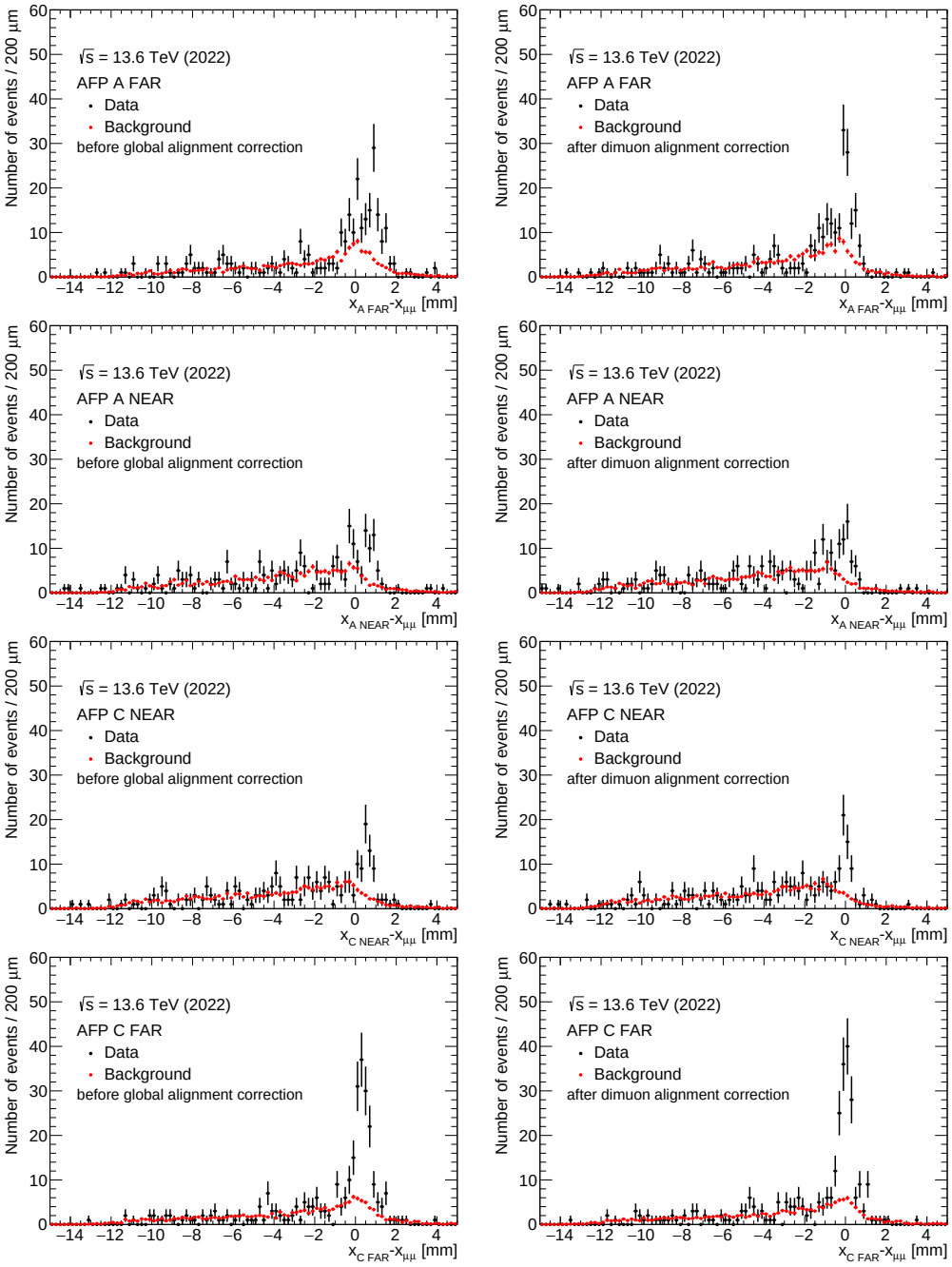

Figure 4.4.3: The distributions show the difference between the track position measured in a given AFP station (first row: A-Far, second row: A-Near, third row: C-Near and last row: C-Far), denoted as x_{AFP}, and the position calculated from the exclusive dimuon candidate system, $x_{\mu\mu}$. The black points represent the selected data events, while the red points correspond to the background estimated from mixed data, where x_{AFP} values are randomly taken from unrelated events. Figures on the left show the distributions before applying the global alignment correction and those on the right show the distributions after the correction.

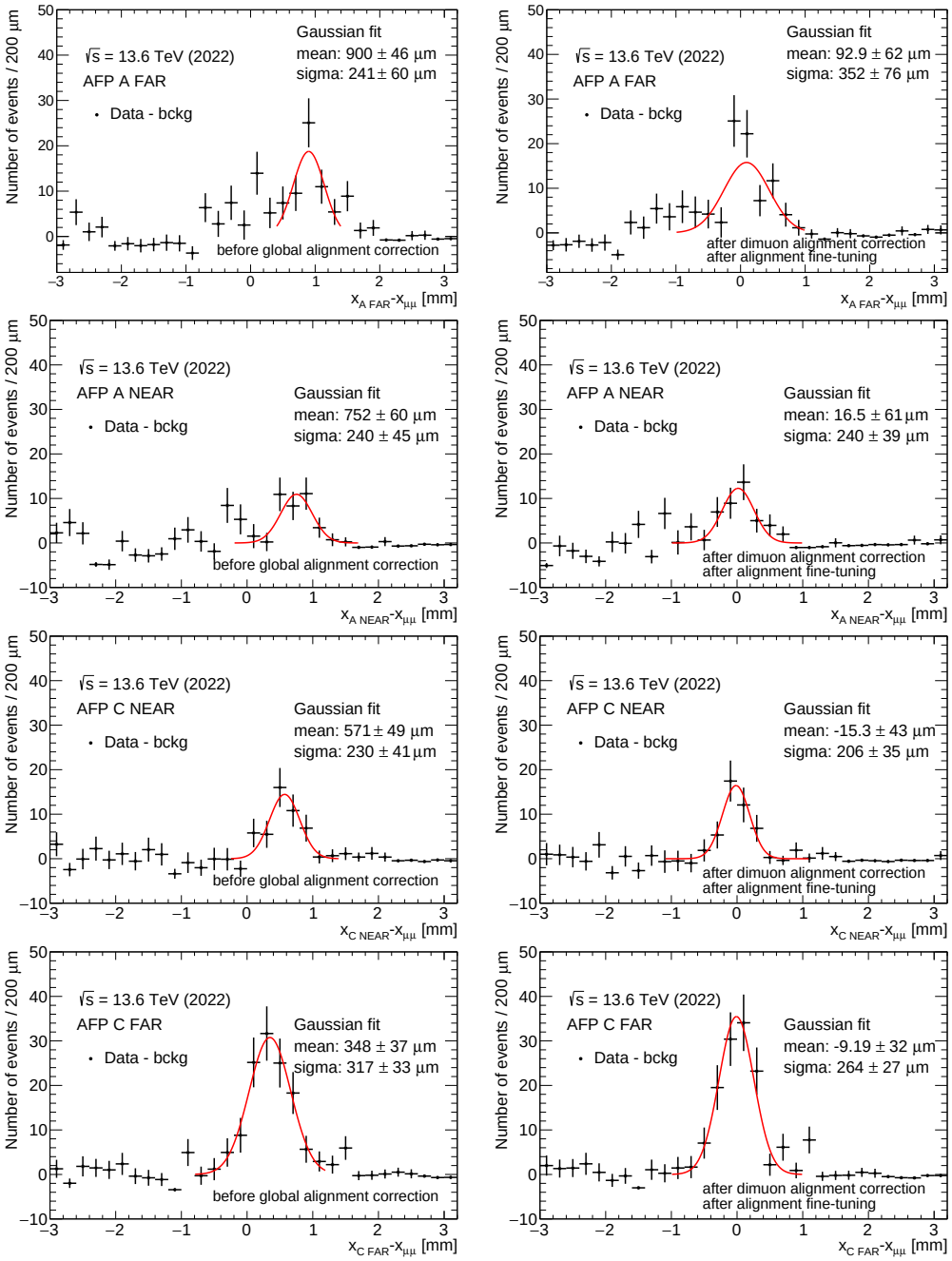

Figure 4.4.4: The distributions depict the difference between the x-position of tracks measured in a given station (first row: A-Far, second row: A-Near, third row: C-Near, and last row: C-Far), denoted as x_{AFP}, and the x-position calculated from the exclusive dimuon candidate system, $x_{\mu\mu}$. Black points represent the background-subtracted distributions where a Gaussian distribution (red line) is fitted to the signal peak. Figures on the left show the distributions before applying the global alignment correction and those on the right show the distributions after the correction.

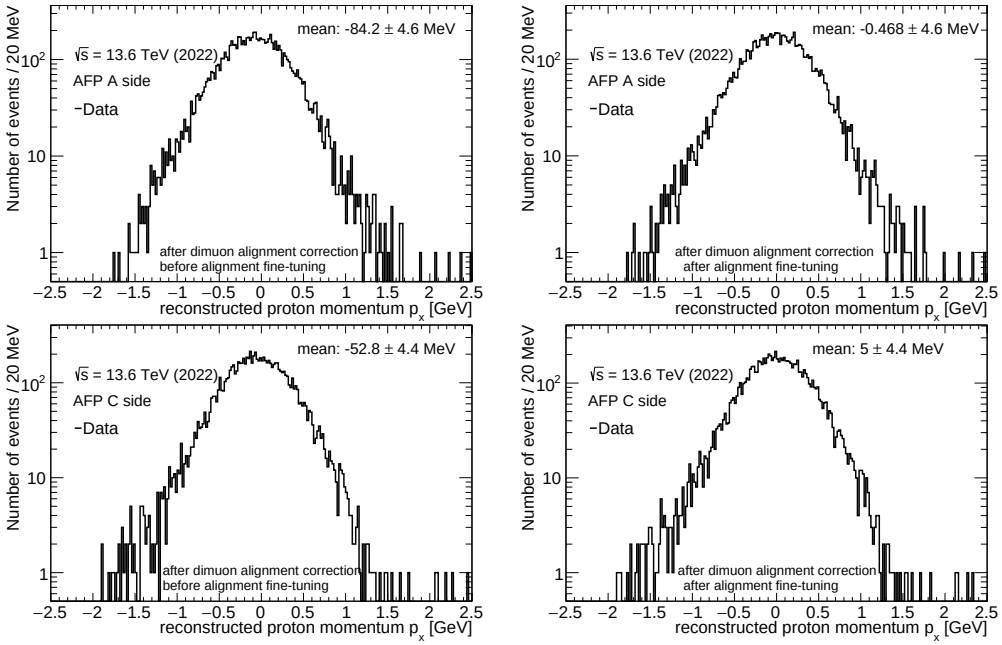

Figure 4.4.5: Distributions of the horizontal component of the momentum of reconstructed protons (p_x), used in the fine-tuning step in the global alignment procedure. The top plots present the A-side and the bottom plots the C-side. The left and right plots corresponds to the distributions before and after the fine-tuning corrections, respectively. The correction is applied to the global position of the A-Near and C-Near stations to make the p_x distribution centred at zero.

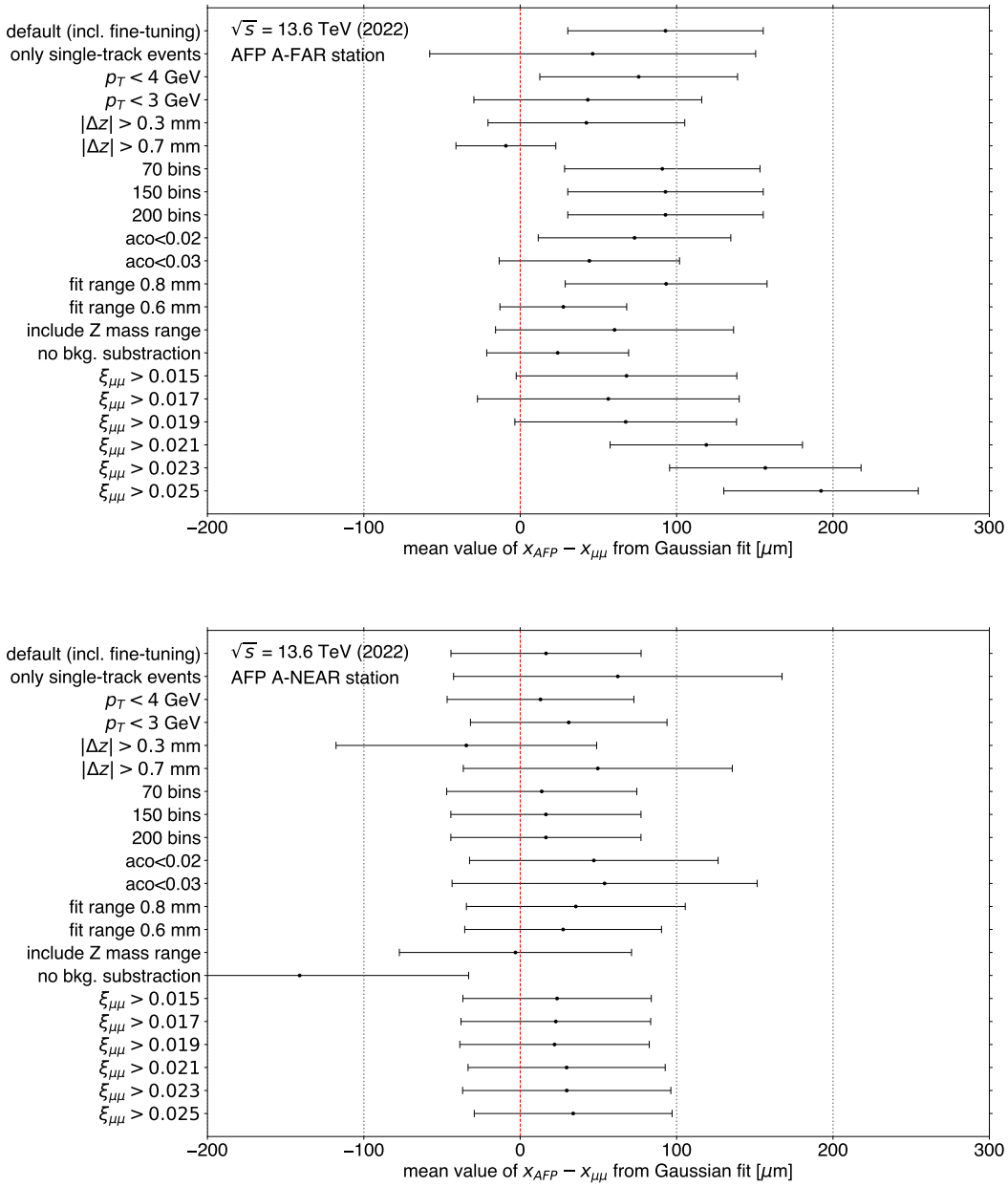

Figure 4.4.6: Comparison of the systematic tests performed on the in-situ global alignment correction for the AFP A-Far (top) and A-Near (bottom) stations. The horizontal axis shows the mean values obtained from Gaussian fits to the $x_{\mathrm{AFP}} - x_{\mu\mu}$ distributions, with error bars indicating the corresponding statistical uncertainties. The vertical axis represents the mean value and its uncertainty from the nominal (default) distribution, including the fine-tuning step, compared with the results from various systematic variations. The considered variations include changes to the default selection criteria or the application of additional adjustments, such as requiring exactly one track reconstructed in the AFP arm, modifying the kinematic selection of the dimuon pair, changing the binning or fit range, including the region around the Z-boson peak and performing the analysis without background subtraction.

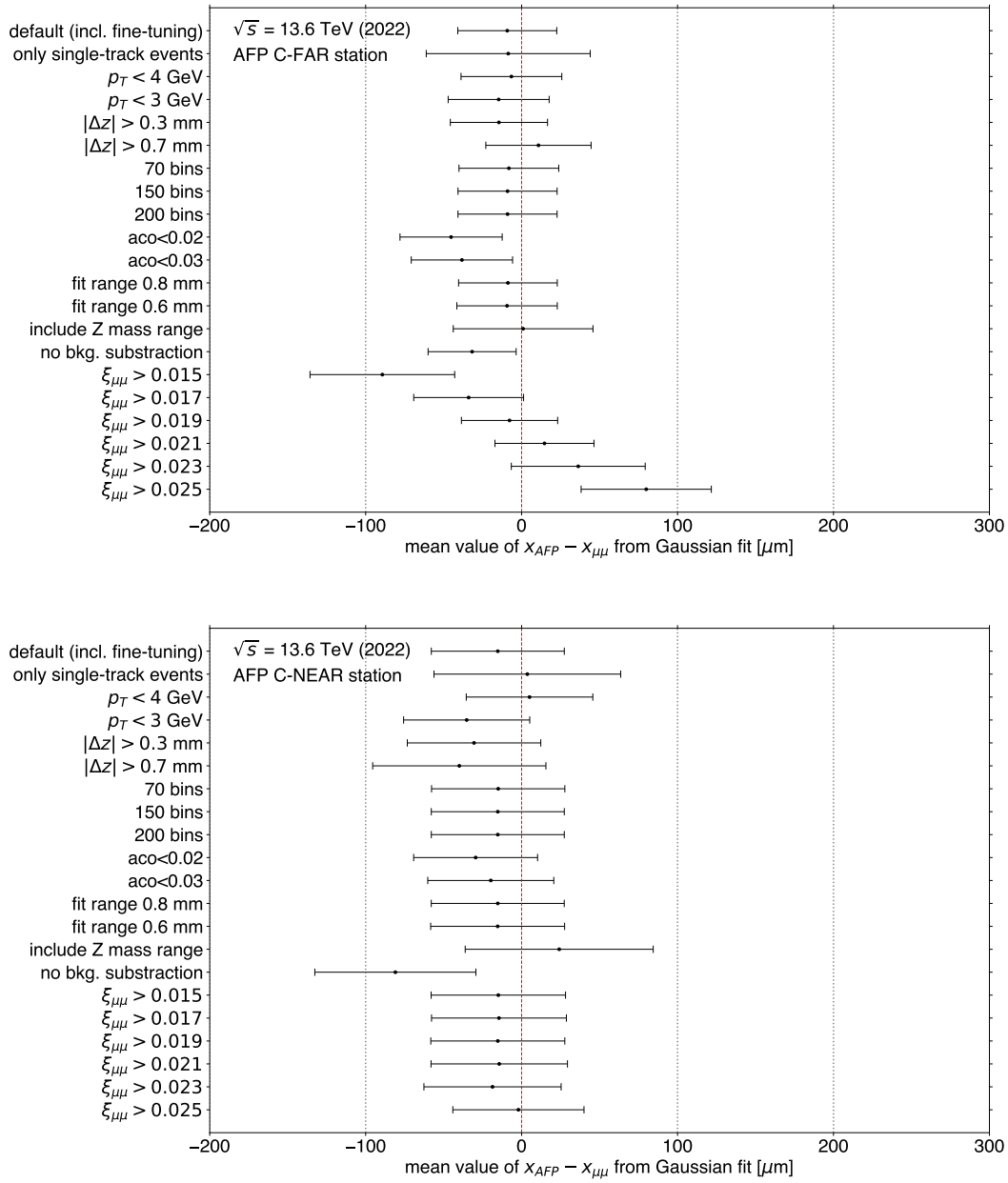

Figure 4.4.7: Comparison of the systematic tests performed on the in-situ global alignment correction for the AFP C-Far (top) and C-Near (bottom) stations. The horizontal axis shows the mean values obtained from Gaussian fits to the $x_{\mathrm{AFP}} - x_{\mu\mu}$ distributions, with error bars indicating the corresponding statistical uncertainties. The vertical axis represents the mean value and its uncertainty from the nominal (default) distribution, including the fine-tuning step, compared with the results from various systematic variations. The considered variations include changes to the default selection criteria or the application of additional adjustments, such as requiring exactly one track reconstructed in the AFP arm, modifying the kinematic selection of the dimuon pair, changing the binning or fit range, including the region around the Z-boson peak and performing the analysis without background subtraction.

Chapter 5

Selection of $\gamma\gamma \to \tau\tau$ candidates in Pb+Pb Collisions

This chapter presents the identification and selection of photon-induced τ-lepton pair production in ultra-peripheral Pb+Pb collisions. This forms the basis for the measurement of the differential $\gamma\gamma \to \tau\tau$ cross sections and the extraction of the constraints on the electromagnetic moments of the τ-lepton, presented in Chapter 6.

The Author's main contributions include the derivation of the ZDC fraction weights and the derivation of electromagnetic pile-up corrections described in Section 5.3, estimation of the backgrounds in Section 5.7 and performing the detector-level analysis discussed in Section 5.8.

5.1 Motivation and analysis strategy

Following the observation of the $\gamma\gamma \to \tau\tau$ process in Pb+Pb collisions by the ATLAS [35] and CMS collaborations [105] and the measurement of the integrated fiducial $\gamma\gamma \to \tau\tau$ cross-section in Pb+Pb collisions by the CMS collaboration [106], a natural next step is to perform differential cross-section measurements. Comparisons between measured differential cross sections and SM or BSM predictions test the theoretical predictions. Furthermore, the measured differential cross-sections can be used to probe the τ-lepton electromagnetic moments.

Precise determinations of the electromagnetic moments of leptons, defined as $a_\ell = \frac{1}{2}(g_\ell - 2)$ for the anomalous magnetic moment and d_τ for the electric dipole moment, provide a stringent test of the SM and a sensitive probe of BSM physics, as discussed in Section 1.3. For the electron and the muon, anomalous magnetic moments belong to the most precisely measured quantities in particle physics [5, 26], offering powerful constraints on BSM scenarios. The τ-lepton, in principle, can be even more sensitive to certain BSM effects; however, its extremely short lifetime makes a direct measurement of a_τ experimentally challenging.

The a_τ was studied at both lepton (e^+e^-) and hadron colliders, using proton-proton ($p+p$) as well as Pb+Pb collision data. To date, the most stringent constraints were set by the CMS Collaboration [107] in $p+p$ collisions. A comparison of the experimental bounds are presented in Table 5.1.1.

Experiment	**Colliding system**	**Limits on a_τ**	**CI**	**Ref.**
OPAL	e^+e^-	$-0.068 < a_\tau < 0.065$	95%	[108]
L3	e^+e^-	$-0.052 < a_\tau < 0.058$	95%	[109]
DELPHI	e^+e^-	$-0.052 < a_\tau < 0.013$	95%	[36]
ATLAS	Pb+Pb	$-0.057 < a_\tau < 0.024$	95%	[35]
		$-0.050 < a_\tau < -0.029$	68%	[35]
CMS	Pb+Pb	$-0.045 < a_\tau < -0.017$	68%	[106]
CMS	$p+p$	$-0.0042 < a_\tau < 0.0062$	95%	[107]
		$-0.0022 < a_\tau < 0.0041$	68%	[107]

Table 5.1.1: Overview of the a_τ measurements. The values for a_τ are indicated, together with the confidence intervals (CIs). Values at the same CI can be directly compared.

The experimental bounds on d_τ were set using e^+e^- as well as $p+p$ collisions. The best constraints to date were also reported by the CMS Collaboration[1]. A comparison of the experimental limits is provided in Table 5.1.2.

Experiment	**Colliding system**	**Limits on d_τ [e·cm]**	**CI**	**Ref.**
OPAL	e^+e^-	$\lvert d_\tau\rvert < 3.7 \times 10^{-16}$	95%	[108]
L3	e^+e^-	$\lvert d_\tau\rvert < 3.1 \times 10^{-16}$	95%	[109]
DELPHI	e^+e^-	$\lvert d_\tau\rvert < 3.7 \times 10^{-16}$	95%	[36]
CMS	$p+p$	$\lvert d_\tau\rvert < 2.9 \times 10^{-17}$	95%	[107]
		$\lvert d_\tau\rvert < 1.7 \times 10^{-17}$	68%	[107]

Table 5.1.2: Overview of the d_τ measurements. The values for $|d_\tau|$ are indicated with the confidence intervals (CIs). Values at the same CI can be directly compared.

The measurement of the $\gamma\gamma \to \tau\tau$ process in heavy-ion collisions provides access to a complementary phase space with respect to $p+p$ collisions, offering sensitivity in the low di-τ mass region, around $\sim$ 50 GeV. This is made possible by lower trigger thresholds in heavy-ion running, which enable more precise cross section measurements (as the cross section decreases with mass). Since the electromagnetic moments of the τ-lepton are formally defined in the limit $q^2 \to 0$, the analysis

[1]The most precise measurement of d_τ to date was performed by the Belle experiment [110] using $ee \to \tau\tau$ events. However, this result corresponds to the kinematic region where $q^2 \neq 0$ and it is not directly comparable to the measurement presented in this thesis.

phase space is restricted to configurations where the photons are quasi-real, i.e. with virtuality $q^2 \sim 0$.

Alternative approaches to constraining the τ electromagnetic moments have been proposed for $p+p$ [111,112] and e^+e^- [113,114] collisions, as well as in fixed-target experiments employing bent crystals [115]. However, some of these approaches probe regions with photons of significantly larger virtuality ($q^2 \gg 0$). While differing in methodology and kinematic coverage, statistically independent determinations of τ-lepton electromagnetic moments open the possibility for future combinations with the results presented here.

5.2 Data and MC Samples

The analysis is based on Pb+Pb collision data recorded by the ATLAS detector during LHC Run 2 at a centre-of-mass energy of 5.02 TeV per nucleon pair. Two datasets were used, collected in 2015 and 2018, corresponding to integrated luminosities of 0.49 nb^{-1} and 1.44 nb^{-1}, respectively, giving a total of 1.93 nb^{-1}. The average number of hadronic interactions per bunch crossing was 0.0022 in 2015 and 0.003 in 2018, which is negligible for this analysis. Nevertheless, the impact of electromagnetic (EM) pile-up must be considered (i.e. multiple simultaneous electromagnetic interactions), in particular its effect on forward neutron production arising from electromagnetic dissociation (EMD) due to the large flux of very low-energy photons.

The nominal Monte Carlo (MC) sample for the signal process ($\gamma\gamma \to \tau\tau$) is simulated at leading order (LO) in QED using the STARLIGHT 2.0 [54] generator, interfaced with TAUOLA [116,117] for τ-lepton decays and PYTHIA 8.245 [118] for simulating final state radiation (FSR) from τ-leptons. The FSR from the charged decay products of τ-leptons is simulated using PHOTOS++ 3.61 [119]. There is also an alternative signal sample used, in which the τ-lepton decays are modelled by PYTHIA 8.245 instead of TAUOLA. It is used to derive the systematic uncertainty on the modelling of τ-lepton decays.

The background from the $\gamma\gamma \to \mu\mu$ process is modelled using MC samples generated with STARLIGHT 2.0 and PYTHIA 8.245 to simulate FSR from the muons. In addition, a next-to-leading-order (NLO) QED sample targeting the $\gamma\gamma \to \mu\mu\gamma$ process is generated with MADGRAPH5_AMC@NLO 2.9 [120], interfaced to PYTHIA 8.245. This sample provides an improved description of events with high-p_{T} photons. It is used instead of STARLIGHT+PYTHIA 8 if a leading photon has $p_{\text{T}} > 2$ GeV to avoid overlap between the two generators.

All MC are passed through a GEANT 4 [121] simulation providing the ATLAS detector geometry. It is a MC toolkit used to model the passage of particles through

matter, including their interactions with detector materials and the resulting detector responses.

5.2.1 Photon flux reweighing

For both the signal and background MC samples, the photon flux is reweighted to that predicted by SuperChic 3.05. As discussed in Section 2.4, STARLight models the photon flux assuming a point-like charge distribution and applies a sharp cut-off at small impact parameters to avoid singularities. In contrast, SuperChic 3 employs a Woods–Saxon nuclear charge distribution, which remains finite at low impact parameters and allows the full kinematic range to be utilised. Consequently, SuperChic 3 is expected to provide a more realistic description of the photon flux.

The reweighting is performed using a two-dimensional histogram of weights, binned in generator-level dimuon invariant mass and rapidity, as presented in Figure 5.2.1. This is motivated by the fact that in the targeted kinematic region, the cross section for the $\gamma\gamma \to \ell\ell$ process depends only on these two variables. The weights are then derived from the ratio of generator-level cross sections predicted by SuperChic 3 to those from STARLight.

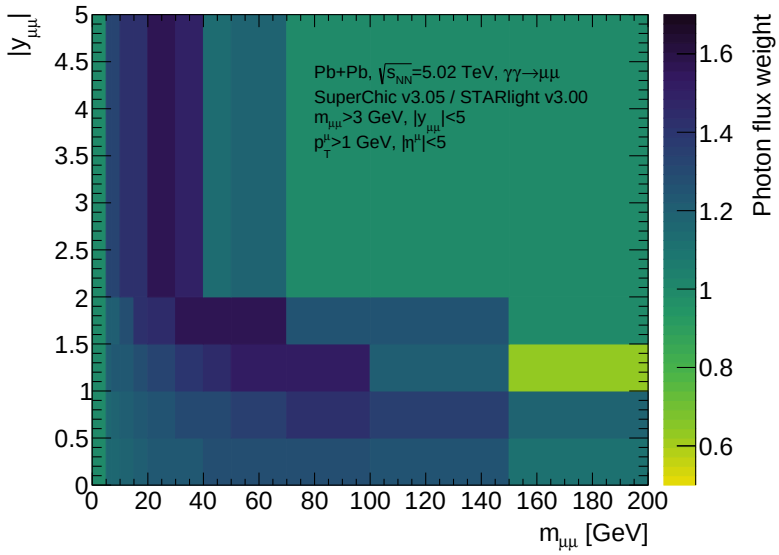

Figure 5.2.1: Ratio of the cross sections for $\gamma\gamma \to \mu\mu$ process between SuperChic 3 (numerator) and STARLight (denominator), as a function of $m_{\mu\mu}$ and $|y_{\mu\mu}|$. The ratio is used to reweight STARLight MC samples. Figure adapted from Ref. [122].

5.2.2 Tau-lepton electromagnetic moments signal parametrisation

The presence of the $\gamma\tau\tau$ vertices provides the sensitivity to the τ-lepton electromagnetic moments. The parametrisation of the vertices follows the procedure used in the original DELPHI measurement [36] and the one used in the previous iteration of the ATLAS measurement [35], as described in detail in Section 1.3.

In order to reweight MC samples with non-zero a_τ and d_τ values, an event-reweighting procedure is employed. The procedure is based on a tree-level QED matrix element calculation of the $\gamma\gamma \to \tau\tau$ process, utilising the four-momenta of the two photons and two τ-leptons, defined at generator-level. The four-vectors are invariant under coordinate transformation in this process, so the kinematic variables can be defined in the centre of mass frame. The virtuality of the photons in the initial state is approximated to zero. The matrix element can be described using:

$$\left|\mathcal{M}\left(\beta, \theta, F_2\left(0\right), F_3\left(0\right)\right)\right|^2 = \sum_{i,j=0}^{4} \left[F_2\left(0\right)\right]^i \left[F_3\left(0\right)\right]^j C_{ij}, \tag{5.2.1}$$

where $\beta = \sqrt{1 - m^2/E^2}$, θ is the longitudinal angle and $F_{2,3}$ denotes form factors corresponding to a_τ and d_τ (i.e. $F_2(0) = a_\tau$ and $F_3(0) = d_\tau \frac{2m_\tau}{e}$, as described in Section 1.3). C_{ij} are coefficients, defined in terms of β and θ. For example, C_{00} corresponds to the a_τ and d_τ values predicted by the SM at tree-level (i.e. $a_\tau = d_\tau = 0$). The non-zero C_{ij} parameters provide BSM predictions.

After calculation of the matrix elements, the final weight used for the BSM $\gamma\gamma \to \tau\tau$ prediction can be calculated as follows:

$$w_i\left(\beta, \theta, F_2\left(0\right) = x, F_3\left(0\right) = y\right) = \frac{\left|\mathcal{M}\left(\beta, \theta, x, y\right)\right|^2}{\left|\mathcal{M}\left(\beta, \theta, 0, 0\right)\right|^2}, \tag{5.2.2}$$

where x and y correspond to the non-zero values of a_τ and d_τ, respectively. The procedure was validated using MC samples from the previous iteration of ATLAS measurement [35], which utilised histogram-based reweighting. The expected event yields as a function of a_τ and the $F_3(0)$ form factor, normalised to the SM prediction is shown in Figure 5.2.2.

5.2.3 Spin correlations

Spin correlation effects in $\gamma\gamma \to \tau\tau$ production and decay were investigated, since τ decays proceed via the weak interaction and are sensitive to spin. These effects cancel in the unfolding procedure as they are applied to both reconstruction and truth-level MC (see Section 6.1). Nevertheless, they can affect the interpretation of the results, particularly for electromagnetic dipole moments, which are inherently related to spin.

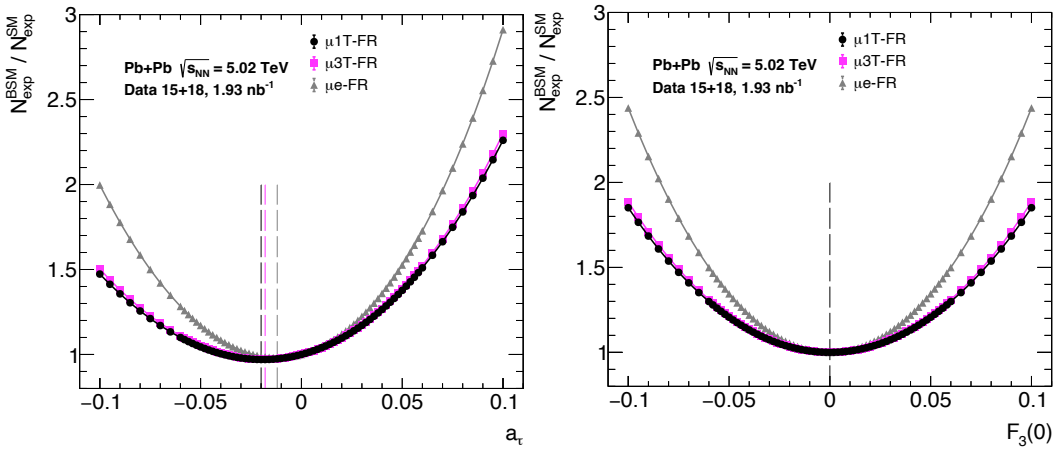

Figure 5.2.2: Event yields as a function of a_τ (left) and $F_3(0)$ form factor (right), normalised to the tree-level SM prediction for the number of events. The three fiducial regions (FR) used in the analysis are shown: μ1T-FR, μ3T-FR and μe-FR (see Section 6.1.1). The points indicate the values of a_τ and $F_3(0)$ for which predictions were obtained using an event-level reweighting procedure, while the lines interpolate between these points. The values of a_τ and $F_3(0)$ corresponding to the minimum predicted number of events in each FR are marked with vertical dashed lines.

A dedicated MC study was performed to quantify the impact of spin–correlation effects. The simulation employs GAMMAUPC [123] for modelling the photon flux from Pb ions, MADGRAPH 5 for the generation of the $\gamma\gamma \to \tau\tau$ hard scattering, TAUOLA for the τ-lepton decays, and TAUSPINNER [124] to incorporate spin information. Ratios of polarised to unpolarised cross-sections were constructed for fiducial regions (FRs, defined in Section 6.1.1). The results show negligible effects in the μ3T-FR and μe-FR, while in the μ1T-FR certain observables (such as muon-track system p_{T} and acoplanarity) display deviations of up to 5–10% in the distribution tails. These effects are therefore included as bin-by-bin corrections in the μ1T-FR.

A further study investigated the interplay between spin correlations and non-zero τ electromagnetic moments using the available TAUSPINNER calculations. For the observables considered, the impact of this interplay was found to be consistent with unity, indicating no significant modification beyond SM spin correlation effects. Thus, SM spin correlation corrections are used for the BSM samples as well.

5.3 Activity in the forward region

In this analysis, one of the dominant background sources arises from diffractive photonuclear processes (see Section 5.7.3), where a photon interacts with a nucleus. Such interactions often cause ion dissociation, in which neutrons from the break up of an ion continue moving in the forward direction. The photonuclear background

can be strongly suppressed using a requirement to have zero neutrons detected by the ZDC in both ion-going directions (the so-called *0n0n topology*). However, additional soft Coulomb exchanges can also lead to neutron emission in the signal process, such that a full neutron veto reduces the cross section of both the signal and the dominant photon-induced dimuon background by about 30–40%. Since the ZDC response is not simulated in the MC samples, the veto is applied only to data by requiring the energy registered on both sides of the ZDC to be $E_{\mathrm{ZDC}}^{\mathrm{A,C}} < 1$ TeV. In simulation, dedicated weights are used to emulate the effect of the ZDC selection.

5.3.1 No neutron topology weights

The signal and dimuon MC samples are generated inclusively in neutron topology and the STARLIGHT generator does not store per-event information on neutron emission. This prevents the application of generator-level cuts to directly select 0n0n events and a reweighting is necessary to restrict to the 0n0n category.

Previous studies using $\gamma\gamma \to \mu\mu$ production [125] have demonstrated that the probability of additional neutron emission in photon-induced interactions depends on the kinematics of the system, which can be parametrised in terms of the invariant mass and rapidity. A comparison of the neutron-emission fractions (0nXn and XnXn) between data and simulation shows that these contributions are overestimated by a few percent by STARLIGHT. For this reason, the 0n0n weights are extracted directly from data in this analysis.

The probability for an event to be in the 0n0n category is measured as the ratio of 0n0n events to the inclusive-ZDC sample (defined without any ZDC requirements) using the $\gamma\gamma \to \mu\mu$ production process. Events are required to satisfy the following criteria:

- Two reconstructed muons,
- Two reconstructed charged-particle tracks,
- Dimuon transverse momentum of $p_{\mathrm{T}}^{\mu\mu} < 1$ GeV,
- Dimuon acoplanarity of $A_{\phi}^{\mu\mu} = 1 - |\Delta\phi(\mu,\mu)|/\pi < 0.01$.

These requirements are motivated by the fact that $\gamma\gamma \to \mu\mu$ events in UPC peak at very small $p_{\mathrm{T}}^{\mu\mu}$ and acoplanarity, reflecting the back-to-back production of the dimuons. The selection effectively suppresses the background contribution from photon-induced dissociative production.

Before deriving the weights using the method described above, an appropriate binning scheme must be defined. The optimal binning in dimuon invariant mass and rapidity is determined by studying the distribution of the 0n0n weights as functions

of these variables. The binning is chosen to accurately preserve the shape information of the distributions. The 0n0n weight distributions as a function of mass and rapidity, with the final binning scheme overlaid in pink, are shown in Figures 5.3.1 and 5.3.2.

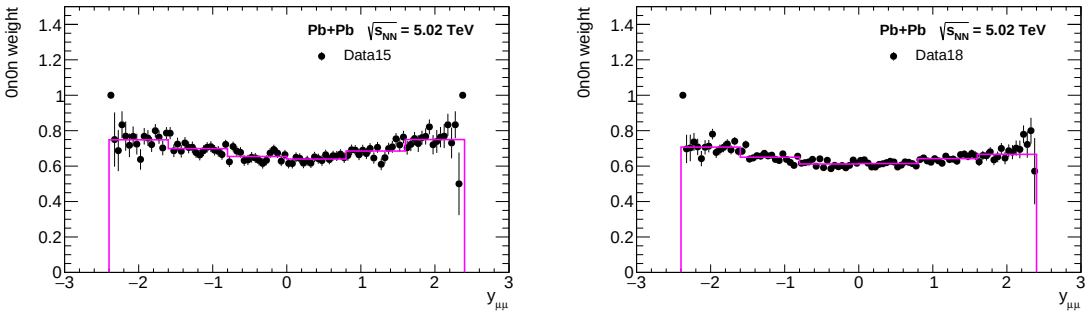

Figure 5.3.1: 0n0n weights as a function of dimuon rapidity, derived using 2015 data (left) and 2018 data (right). The distributions are displayed with fine binning (black points), together with the final binning scheme used for the derivation of the weights (pink histogram). Error bars indicate statistical uncertainties.

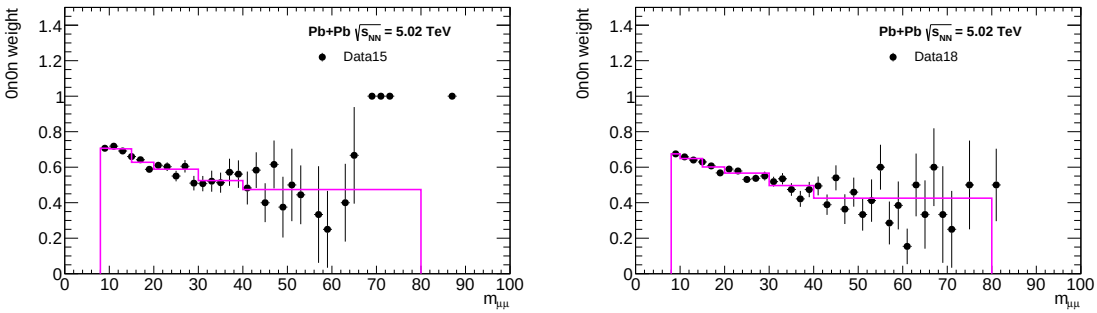

Figure 5.3.2: 0n0n weights as a function of dimuon invariant mass, derived using 2015 data (left) and 2018 data (right). The distributions are displayed with fine binning (black points), together with the final binning scheme used for the derivation of the weights (pink histogram). Error bars indicate statistical uncertainties.

5.3.2 Derivation of the ZDC fractions

The 0n0n weights are to be applied to the generator-level (also referred to as *truth*-level) dimuon or ditau quantities, hence the derived weights must be corrected for migration between measured bins and generator-level bins.

The 0n0n weights corrected for migration effects are obtained using the following procedure. For each bin in truth dimuon invariant mass $m_{\mu\mu}$ and rapidity $y_{\mu\mu}$, a two-dimensional histogram of reconstruction-level $m_{\mu\mu}$ and $y_{\mu\mu}$ is made, as shown in Fig 5.3.3 for selected bins. Then, the measured 0n0n weights are multiplied by the

resulting migration histogram. The final weight for the considered bin is obtained by integrating over the resulting histogram.

The comparison between the measured 0n0n fractions and the 0n0n fractions corrected for migration effects is presented in Figure 5.3.4 as a two-dimensional histogram, separately for 2015 and 2018 data. Additional plots with comparisons as a function of $m_{\mu\mu}$ in four bins of $y_{\mu\mu}$ can be found in Appendix A (Figures A.1 and A.2).

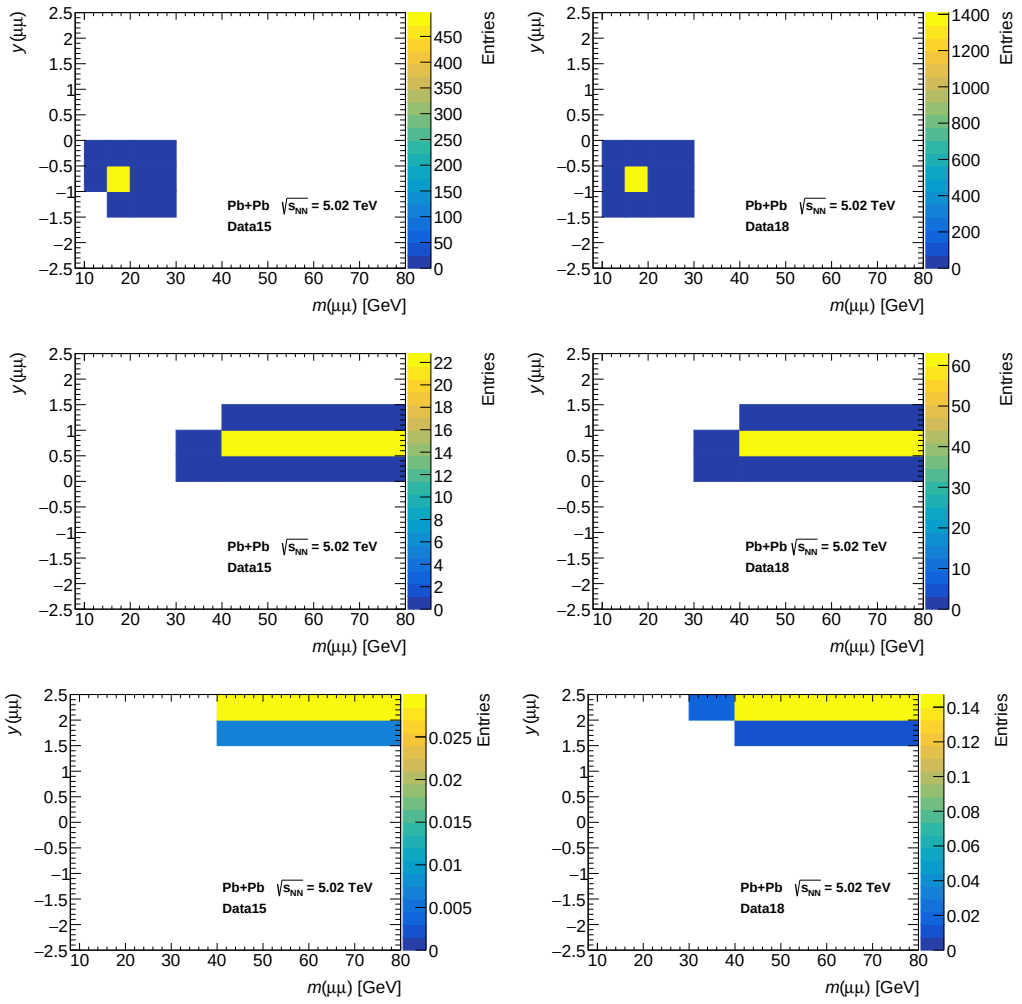

Figure 5.3.3: Two-dimensional histograms of reconstruction-level $m_{\mu\mu}$ and $y_{\mu\mu}$ in selected bins defined at truth-level for 2015 data (left) and 2018 data (right).

A comparison of the 0n0n fractions in 2015 and 2018 data is shown in Figure 5.3.5. To reduce statistical fluctuations, the fractions are fitted with an exponential function. In most bins, the 2015 fractions are slightly higher, reflecting the lower beam intensity in 2015 compared to 2018, which reduces the probability of additional neutron emissions and increases the 0n0n fraction at low $m_{\mu\mu}$.

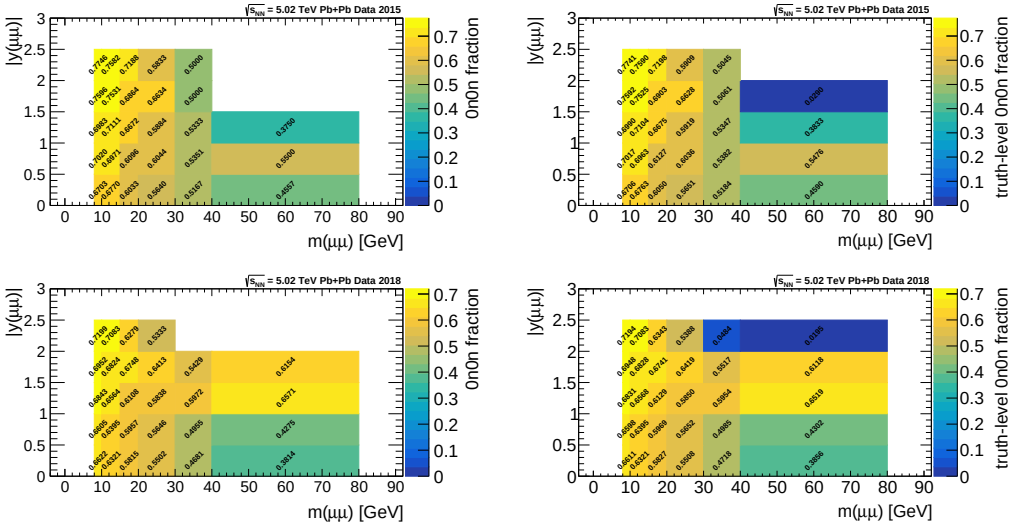

Figure 5.3.4: Comparison of the (left) measured 0n0n fractions and the (right) 0n0n fractions corrected for migration effects between reconstruction-level and truth-level bins. Plots on the top show fractions extracted from 2015 data and below are fractions extracted from 2018 data.

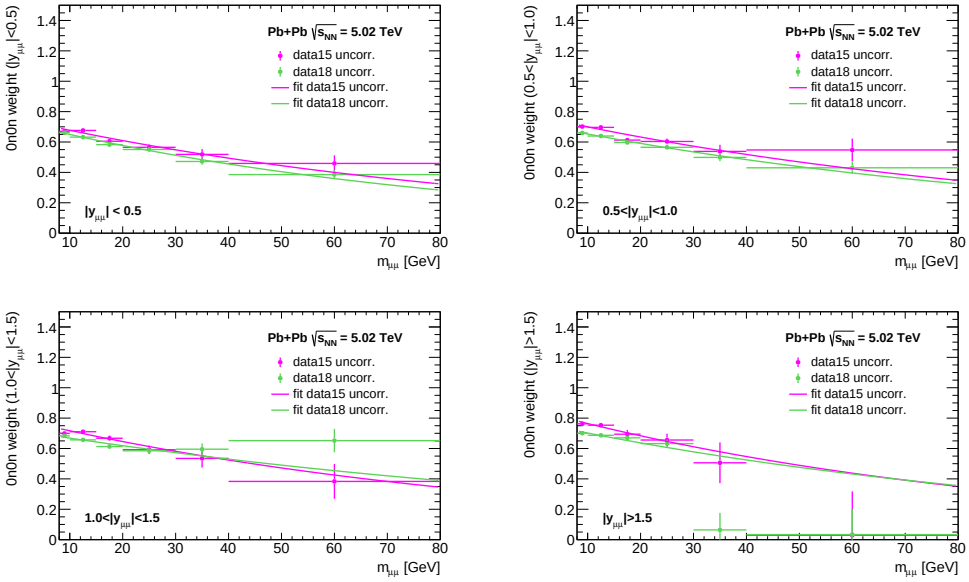

Figure 5.3.5: Comparisons of fractions of 0n0n events corrected for migration effects and uncorrected for EM pileup (see Section 5.3.3), extracted from 2015 data (pink points) and 2018 (green points) using the $\gamma\gamma \to \mu\mu$ process in several dimuon rapidity regions. The fractions are fitted using an exponential function displayed as pink and green lines, corresponding to the 2015 and 2018 fractions, respectively. Error bars indicate statistical uncertainties.

5.3.3 Electromagnetic pileup corrections

As mentioned in Section 5.2, UPC interactions are affected by electromagnetic (EM) pileup, arising from electromagnetic dissociation (EMD) occurring in the same ion bunch crossing as the signal process. This results in the emission of additional neutrons and an increased neutron rate observed in the ZDC. To account for this effect, a correction must be applied to the 0n0n fractions. The correction procedure follows the method described in Ref. [126] and is outlined below.

The cross section for a single EMD (in which one or more neutrons are detected in one ZDC arm) and mutual EMD (where neutrons are detected in both ZDC arms) was only measured by the ALICE experiment [127] at a centre-of-mass energy of 2.76 TeV. The results were compared with the RELDIS model [128], which predicts a 11% increase of the cross section when changing to a higher energy of 5.02 TeV. The extrapolated ALICE measurement yields a cross section of $\mu_{\text{EMD,single}} = 201.2 \pm 0.3\,(\text{stat.})^{+14.2}_{-12.1}\,(\text{syst.})$ b for a single EMD and $\mu_{\text{EMD,mutual}} = 6.0 \pm 0.1\,(\text{stat.}) \pm 0.4\,(\text{syst.})$ b for a mutual EMD.

The EM pileup is calculated by scaling the hadronic pileup (μ_{had}) by the ratio of the single and mutual EMD cross section and the inelastic PbPb cross section (referred to as hadronic interaction cross section):

$$\mu_{\text{EMD,single}} = \mu_{\text{had}} \cdot \frac{\text{cross section for single EMD}}{\text{cross section for hadronic interaction}}, \tag{5.3.1}$$

$$\mu_{\text{EMD,mutual}} = \mu_{\text{had}} \cdot \frac{\text{cross section for mutual EMD}}{\text{cross section for hadronic interaction}}. \tag{5.3.2}$$

The hadronic pileup, μ_{had}, is measured for each luminosity block (a luminosity block corresponds to a time interval of typically 60 s, during which the instantaneous luminosity and data-taking conditions are assumed to remain constant) and it is stored for every ion bunch crossing. The hadronic interaction cross section is predicted by the Glauber model [129] to be 7.7 b.

To evaluate the probability of observing at least one EMD interaction per bunch crossing, Poisson statistics are assumed. For each event, the probability is given by:

$$p_{\text{EMD}} = 1 - \exp(-\mu_{\text{EMD}}), \tag{5.3.3}$$

and the mean value of the resulting distribution is taken. For the 2015 dataset, these probabilities were taken from Ref. [125], while for the 2018 dataset they were derived following the procedure described above. The corresponding distributions of single and mutual EMD probabilities (p_{s} and p_{m}, respectively) are shown in Figure 5.3.6.

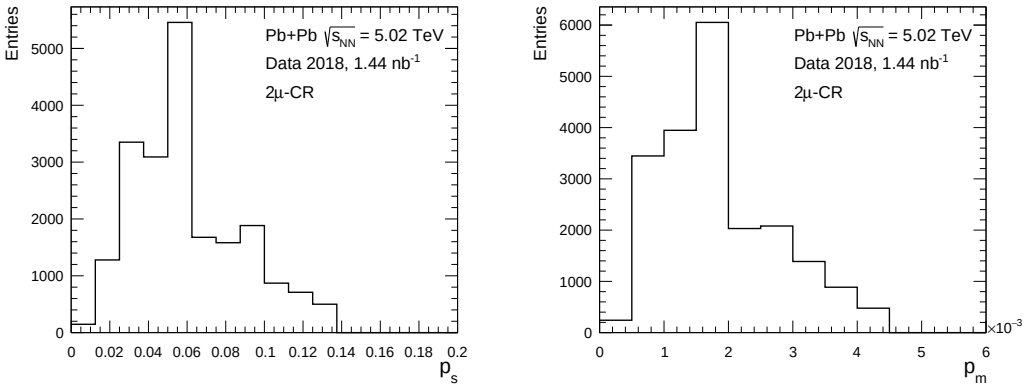

Figure 5.3.6: Probability of single (left) and mutual (right) EMD derived using the 2018 dataset.

The mean values of the single and mutual EMD are:

$$p_s = 5.67^{+0.37}_{-0.32} \times 10^{-2} \text{ (data 2015)}, \quad p_s = 6.066^{+0.412}_{-0.352} \times 10^{-2} \text{ (data 2018)}$$

$$p_m = 1.74 \pm 0.12 \times 10^{-3} \text{ (data 2015)}, \quad p_m = 1.877 \pm 0.129 \times 10^{-3} \text{ (data 2018)}$$

The 0n0n weights are corrected for the EM pileup using the relation [126]:

$$f_{0n0n}^{\text{corrected}} = f_{0n0n}^{\text{uncorrected}} \cdot \Big((1-p_s)^2(1-p_m)\Big)^{-1}. \tag{5.3.4}$$

The two-dimensional histograms of 0n0n fractions corrected for both migration effects and EM pileup as a function of reconstruction-level dimuon mass versus rapidity are shown in Figure 5.3.7.

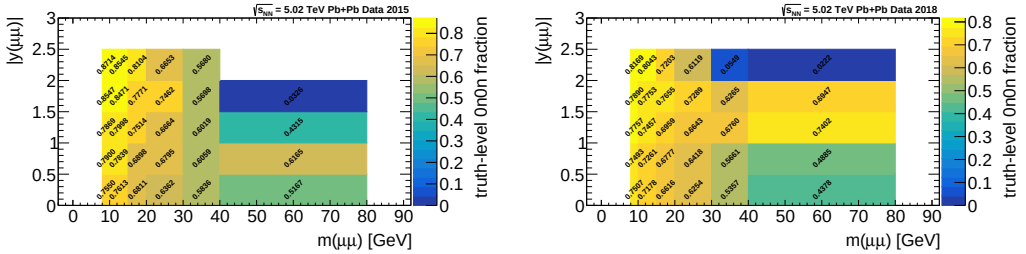

Figure 5.3.7: 0n0n fractions extracted from 2015 data (left) and from 2018 data (right), corrected for migration effects and EM pileup.

5.3.4 Combining 0n0n weights

Since the EM pileup differs between the 2015 and 2018 data-taking periods, the weights cannot be combined before applying the correction for EM pileup. After correcting for EM pileup, the 2015 and 2018 fractions are expected to converge and

can then be combined.

The comparison of 2015 and 2018 fractions after applying the EM pileup correction is shown in Figure 5.3.8. Additional comparisons are shown in Appendix A (Figure A.3). Good agreement is observed between the two datasets and the fractions are therefore combined (indicated in orange) using a weighted average:

$$f_{\text{comb}} = \frac{f_{2015}/\sigma_{2015}^2 + f_{2018}/\sigma_{2018}^2}{1/\sigma_{2015}^2 + 1/\sigma_{2018}^2} \tag{5.3.5}$$

with uncertainty:

$$\sigma_{\text{comb}} = \frac{1}{1/\sigma_{2015}^2 + 1/\sigma_{2018}^2}. \tag{5.3.6}$$

In the above equations, $f_{2015,2018}$ denote the 0n0n probabilities for the respective years and $\sigma_{2015,2018}$ are the corresponding probabilities per bin.

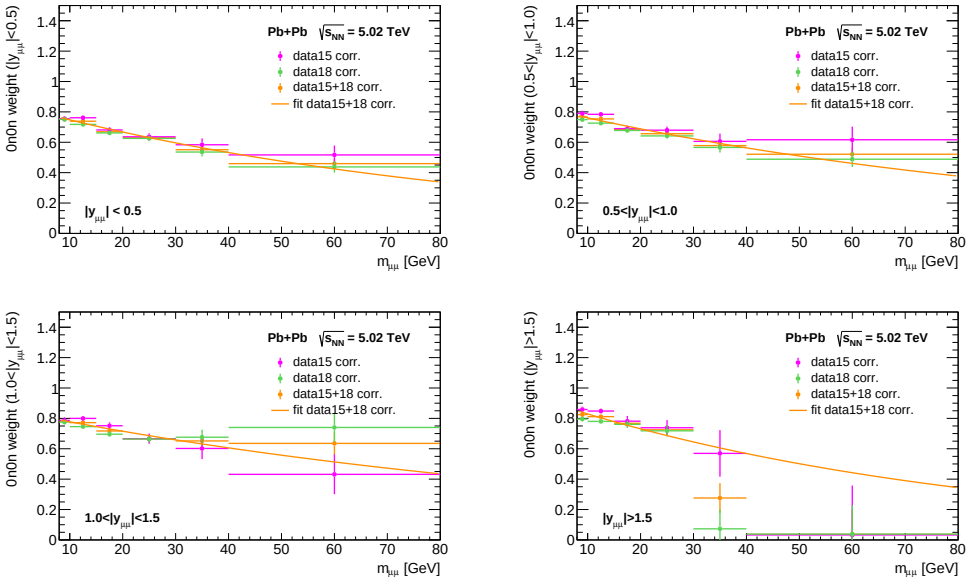

Figure 5.3.8: Comparisons of fractions of 0n0n events corrected for both migration effects and EM pileup, extracted from 2015 data (pink points) and 2018 (green points) using the $\gamma\gamma \to \mu\mu$ process in several dimuon rapidity regions. Orange points denote combined fractions. The combined fractions are fitted using an exponential function (orange line). Error bars indicate statistical uncertainties.

5.3.5 Application of 0n0n weights in the analysis

The derived 0n0n fractions are used to reweight all signal and background MC samples. They are applied as a function of the truth-level dimuon (ditau) invariant mass in the four bins of dimuon (ditau) rapidity:

- Reconstruction-level MC: 0n0n weights corrected for migration effects and un-

corrected for EM pileup, determined separately for 2015 and 2018 data,

- Truth-level MC: 0n0n weights corrected for migration effects and for EM pileup, combined (weighted average of 2015 and 2018 weights).

With this approach, the unfolding procedure (see Section 6.1) effectively extrapolates the data from the 0n0n phase space including EM pileup to the corresponding phase space with the EM pileup contribution removed.

The final 0n0n fractions applied at reconstruction-level are shown in Figure 5.3.9, separately for the 2015 and 2018 data. The combined fractions used at truth-level are presented in Figure 5.3.10.

The fractions are fitted with an exponential function of the form $e^{\mathrm{p0}+\mathrm{p1}\cdot m_{\mu\mu}}$, which is taken as the nominal 0n0n weight. The fit is displayed together with its 68% confidence level (CL) uncertainty, which defines the statistical uncertainty of the 0n0n weight. The uncertainties in the EMD cross sections entering the EM pileup correction are propagated to the corrected weights and included in the fit uncertainty band. In addition, the fractions are fitted with an alternative exponential fit, $\mathrm{p0} + e^{\mathrm{p1}+\mathrm{p2}\cdot m_{\mu\mu}}$, which is used to estimate the systematic uncertainty on the 0n0n fractions.

5.3.6 Systematic uncertainties on the 0n0n weights

Several sources of systematic uncertainty affecting the 0n0n fractions has been examined. In addition to the uncertainty associated with the choice of the fitting function (where an alternative exponential form is used), two further contributions are considered: the ZDC efficiency and the choice of the binning.

The 0n0n fractions are influenced by the finite efficiency of the ZDC and, in principle, should be corrected for this effect. However, Ref. [125] reports an overall ZDC efficiency of about 99%. The residual 1% inefficiency is therefore treated as a systematic uncertainty (see Section 6.2).

An additional uncertainty arises from the choice of the binning in $m_{\mu\mu}$ and $y_{\mu\mu}$. An alternative binning scheme, consisting of three rapidity bins and coarser mass bins, was tested. Comparisons of the fine binning and the alternative binning schemes are provided in Appendix A (Figures A.4 and A.5), demonstrating that the chosen binning adequately preserves the shape information.

The determined fractions using the alternative binning are presented in Figure 5.3.11 for the combined fractions. Figures for the separate 2015 and 2018 datasets used at reconstruction-level are shown in Appendix A (Figure A.6 and A.7). The 68% CL uncertainty bands and alternative function are also included on the figures, but only the nominal fit with the alternative binning is used as systematic uncertainty.

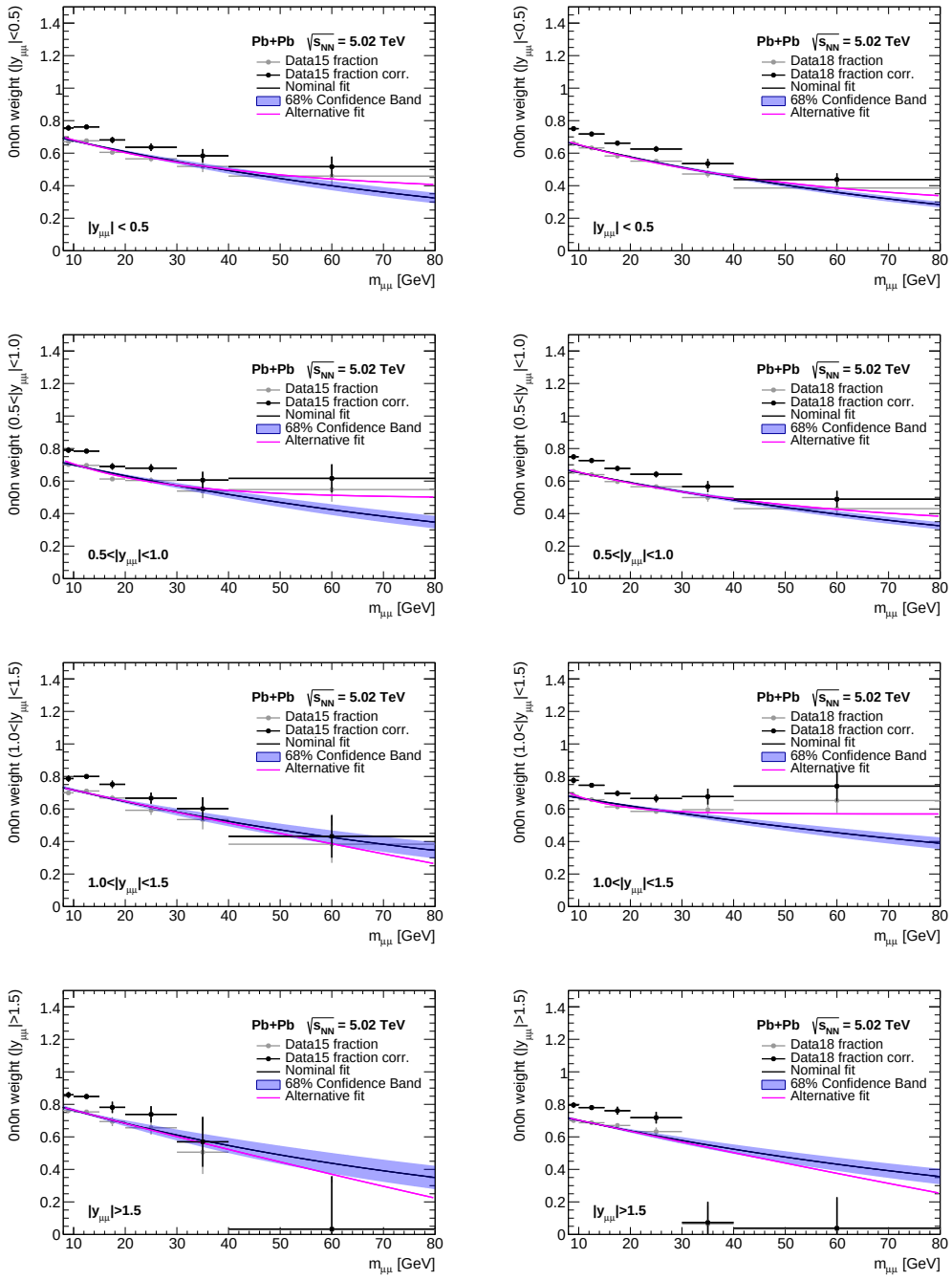

Figure 5.3.9: Fractions of 0n0n events extracted from 2015 data (left column) and 2018 data (right column) using the $\gamma\gamma \to \mu\mu$ process in several dimuon rapidity regions: (first row) $|y| < 0.5$, (second row) $0.5 < |y| < 1.0$, (third row) $1.0 < |y| < 1.5$ and (fourth row) $|y| > 1.5$. Grey points denote fractions uncorrected for EM pileup. To smooth statistical fluctuations, the uncorrected fractions are fitted using an exponential function (black lines) with purple uncertainty band or an exponential function with an additional constant parameter (pink lines). Additionally, fractions corrected for EM pileup are displayed as black points. Error bars indicate statistical uncertainties. Fractions are corrected for migration effects.

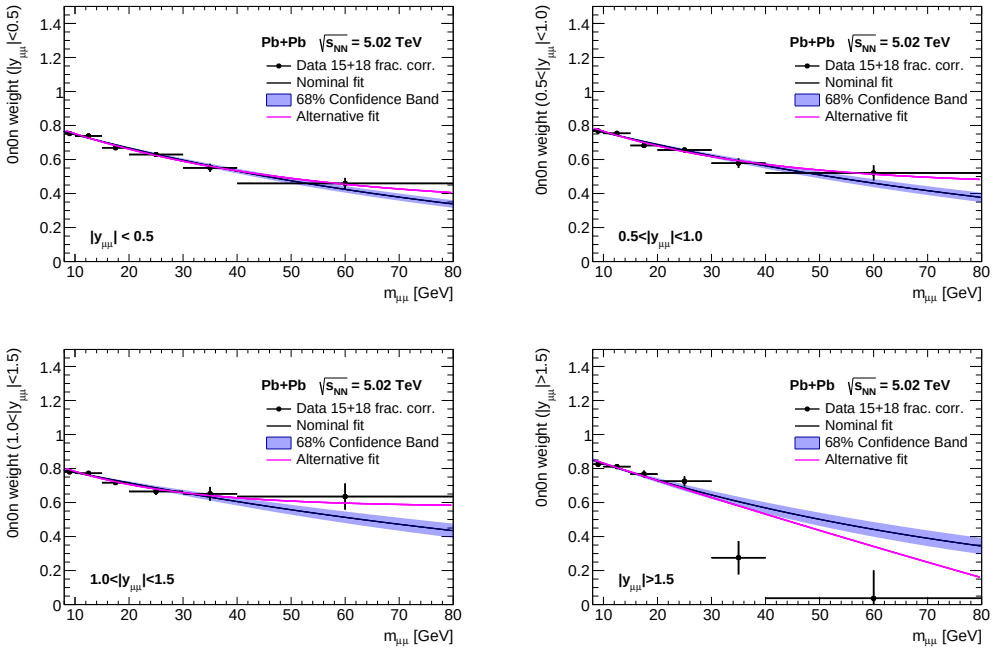

Figure 5.3.10: Combined fractions of 0n0n events extracted from 2015 and 2018 data using the $\gamma\gamma \to \mu\mu$ process in several dimuon rapidity regions: (top-left) $|y| < 0.5$, (top-right) $0.5 < |y| < 1.0$, (bottom-left) $1.0 < |y| < 1.5$ and (bottom-right) $|y| > 1.5$. Black points denote fractions corrected for EM pileup. To smooth statistical fluctuations, the corrected fractions are fitted using an exponential function (black lines) with purple uncertainty band or an exponential function with an additional constant parameter (pink lines). Error bars indicate statistical uncertainties. Fractions are corrected for migration effects.

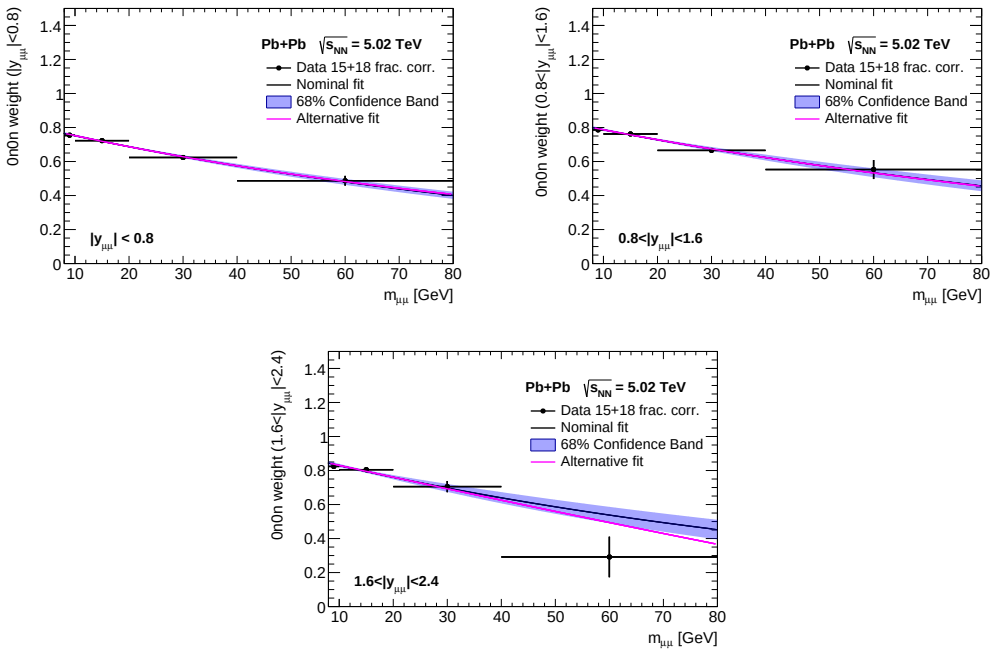

Figure 5.3.11: Combined fractions of 0n0n events extracted from 2015 and 2018 data using the $\gamma\gamma \to \mu\mu$ process using alternative binning in several dimuon rapidity regions: (top-left) $|y| < 0.8$, (top-right) $0.8 < |y| < 1.6$ and (bottom) $1.6 < |y| < 2.4$. Black points denote fractions corrected for EM pileup. To smooth statistical fluctuations, the corrected fractions are fitted using an exponential function (black lines) with purple uncertainty band or an exponential function with an additional constant parameter (pink lines). Error bars indicate statistical uncertainties. Fractions are corrected for migration effects.

5.4 Trigger

The analysis relies on single-muon triggers in both 2015 and 2018 data-taking periods. UPC events typically have very low activity, thus any additional trigger requirements must be specifically designed to retain such topologies. Different triggers are employed for the two datasets, and their corresponding selections are detailed below. In order to correct for differences in efficiency between data and simulation, trigger scale factors (SFs) are applied. They are multiplicative correction factors applied to simulated event samples, ensuring that the MC accurately reflects the detector response observed in real data.

5.4.1 Muon trigger in 2015

During the 2015 data-taking period, events were selected using the following trigger: `HLT_mb_sptrk_vetombts2in_L1MU0_VTE50`. In this trigger, the L1 item is `L1MU0_VTE50` and the HLT item is `HLT_mb_sptrk_vetombts2in`. The trigger chain includes the following set of requirements:

- `L1_MU0`: presence of at least one muon track detected in the MS without any requirements on p_{T},
- `VTE50`: a maximal total transverse energy (E_{T}) of 50 GeV measured by the calorimeter system,
- `vetombts2in`: reject events with more than one hit in the inner MBTS ring, corresponding to the $3.0 < |\eta| < 3.8$ region, in either the forward or backward direction,
- `mb_sptrk`: at least one reconstructed track with $p_{\mathrm{T}} > 200$ MeV

The efficiency of the L1 muon trigger was measured using the Tag-and-Probe method applied to photon-induced dimuon $\gamma\gamma \to \mu\mu$ events. The Tag-and-Probe method is a data-driven technique commonly used to measure detector or trigger efficiencies. It relies on selecting a clean sample of well-identified particle pairs (in this case, dimuons from $\gamma\gamma \to \mu\mu$). One muon in the pair, referred to as the *tag*, is required to pass strict identification and trigger criteria, ensuring that the event is selected with high purity. The other muon, called the *probe*, is then used to test the efficiency of the trigger by checking how often it also satisfies the trigger condition. By comparing the number of probe muons that fire the trigger to the total number of probe candidates, the trigger efficiency can be extracted as a function of kinematic variables such as p_{T} and η.

The overall efficiency of L1 and HLT was found to be dominated by the performance of the `L1_MU0` item, while other components contributed negligible inefficiencies.

Differences between data and simulation were observed at the few-percent level and are corrected by applying SFs for the L1 item. The SFs are derived as the ratio of the trigger efficiency in the data to the trigger efficiency in simulation. They are applied as a function of muon p_{T} and charge–pseudorapidity ($q\eta$). The use of charge–pseudorapidity is motivated by the fact that the trigger efficiency may not be fully charge-symmetric, particularly at large values of $|\eta|$.

In addition to statistical uncertainties, systematic uncertainties on the SFs were evaluated. It was done by varying selection criteria, including impact parameter requirements, track veto conditions, and the tag-muon identification. These effects were propagated into the SFs and found to be small, typically below 1–2% across most kinematic regions. Larger uncertainties, up to about 4%, occur at low p_{T}, while central rapidity and very high-p_{T} bins can reach 6–20%. Overall, statistical uncertainties dominate over systematic ones in the trigger efficiency determination.

5.4.2 Muon trigger in 2018

During the 2018 data-taking period, events were selected using the following trigger: `HLT_mu4_hi_upc_FgapAC3_L1_MU4_VTE50`. In this trigger, the L1 item is `L1_MU4_VTE50` and the HLT item is `HLT_mu4_hi_upc_FgapAC3`. It uses the following set of requirements:

- `HLT_mu4:` require at least one 4 GeV muon at the HLT,
- `FgapAC3`: FCal veto, i.e. reject events with sum of the transverse energy registered by the forward calorimeter $\Sigma E_{\mathrm{T}}^{\mathrm{FCal}} > 3$ GeV,
- `L1_MU4`: require at least one muon with $p_{\mathrm{T}} > 4$ GeV,
- `VTE50`: total transverse energy E_{T} below 50 GeV in the entire calorimeter.

The trigger efficiency was studied with the Tag-and-Probe method using photon-induced dimuon $\gamma\gamma \to \mu\mu$ events. At L1, the efficiency of the `L1_MU4` requirement was measured as a function of muon p_{T} and $q\eta$.

The `L1_VTE50` requirement was validated by checking the L1 E_{T} distribution in both data and simulation. All events had values well below the 50 GeV threshold, confirming that this trigger condition was fully efficient. Cross-checks with signal events and $\gamma\gamma \to \tau\tau$ simulations with muonic decays confirmed that no inefficiency was introduced.

The `HLT_mu4` requirement was also evaluated with the Tag-and-Probe method. Its efficiency reached about 92% (90%) in data (simulation) at $p_{\mathrm{T}} = 4$ GeV and

above 98–99% for $p_{\mathrm{T}} > 10$ GeV. SFs for the HLT item were derived as a function of p_{T}, with values close to unity (1–1.02), and systematic uncertainties were estimated by varying event and matching criteria. Finally, the efficiency of the `FgapAC3` veto was measured in $\gamma\gamma \to ee$ control samples and was found to be $(99.1 \pm 0.6)\%$.

Differences between data and simulation for the L1 item were found to be 5–10% in the barrel region and smaller in the endcap. To correct for these differences, SFs for the L1 item were derived as the ratio of data to simulation efficiencies and applied to simulated events.

In addition to statistical uncertainties, systematic uncertainties were assessed by varying the event selection, impact parameter cuts, identification criteria, track veto, and the use of alternative MC samples. The total deviations in the SFs were typically below 5%, though larger fluctuations occurred at high p_{T} where statistics were limited.

Overall, the 2018 muon trigger was highly efficient, with well-understood systematic uncertainties and SFs applied to correct the simulation.

5.5 Physics objects and calibration

Particles produced in ultra-peripheral Pb+Pb collisions are reconstructed and identified according to the procedures described in this chapter. The τ-leptons produced in $\gamma\gamma \to \tau\tau$ interactions in UPC Pb+Pb collisions typically have low-p_{T}, and the standard ATLAS algorithms used for identifying hadronic decays of τ-leptons cannot be used. Instead, the τ-leptons are identified through their decays to final states with muons, electrons and charged particle tracks. To ensure sensitivity to the presence of neutrinos in the final state, the analysis imposes requirements on the system transverse momentum and on the acoplanarity, allowing for the expected momentum imbalance.

The standard ATLAS Combined Performance (CP) recommendations are followed wherever possible. However, due to the exceptionally clean environment of UPC, not all requirements used in proton–proton collision analyses are necessary. In some cases, these requirements would reduce the signal yield without providing a significant improvement in background rejection. Therefore, looser criteria are adopted when appropriate, for example in the track impact parameter selection.

A summary of the object definitions is provided in Table 5.5.1. Details of the specific reconstruction criteria for each object are given in the following section.

5.5.1 Muons

The reconstruction of muons was introduced in Section 3.5.4. In this analysis, two categories of muons are defined: *Signal* and *Baseline*. The Signal category applies

Property	Requirements	
Muons		
Kinematic	Signal: $p_{\mathrm{T}} > 4$ GeV, $\lvert\eta\rvert < 2.4$ Baseline: $p_{\mathrm{T}} > 2$ GeV, $\lvert\eta\rvert < 2.5$	
Identification	Signal: LowPt	Baseline: –
Impact parameter	Signal: $\lvert d_0\rvert < 0.3$ mm	Baseline: –
Electrons		
Kinematic	$p_{\mathrm{T}} > 4$ GeV, $\lvert\eta\rvert < 2.47$ (excluding $1.37 < \lvert\eta\rvert < 1.52$)	
Identification	LHLoose	
Impact parameter	$\lvert d_0\rvert < 0.5$ mm	
Tracks		
Kinematic	$p_{\mathrm{T}} > 100$ MeV, $\lvert\eta\rvert < 2.5$	
Reconstruction	Loose Primary	
Impact parameter	$\lvert d_0\rvert < 1.5$ mm	
Photons		
Kinematic	$p_{\mathrm{T}} > 1.5$ GeV, $\lvert\eta\rvert < 2.37$ (excluding $1.37 < \lvert\eta\rvert < 1.52$)	
TopoClusters		
Kinematic	$p_{\mathrm{T}} > 1$ GeV for $\lvert\eta\rvert < 2.5$ $p_{\mathrm{T}} > 0.1$ GeV for $2.5 < \lvert\eta\rvert < 4.9$	
Quality	pass HotspotCleaning	

Table 5.5.1: Summary of reconstructed object definitions.

stricter selection requirements, while the Baseline category employs looser criteria. Baseline muons are primarily used to impose a stronger veto than possible with Signal muons, thereby enhancing the suppression of the $\gamma\gamma \to \mu\mu$ background. For all other reconstructed objects, only the Signal category is required. Signal muons used in the analysis must satisfy the following requirements:

- $p_{\mathrm{T}} > 4$ GeV, $\lvert\eta\rvert < 2.4$,
- *LowPt* identification criteria, allowing optimal muon identification down to p_{T} of 3 GeV,
- $\lvert d_0\rvert < 0.3$ mm.

Requirements for baseline muons differ in kinematic cuts, i.e. muons with $p_{\mathrm{T}} > 2$ GeV and $\lvert\eta\rvert < 2.5$ are allowed. In addition, the *LowPt* identification criteria and $\lvert d_0\rvert$ requirement are relaxed.

The muon reconstruction and particle identification (PID) efficiencies used in this analysis are based on previous measurements [35, 125] employing a Tag-and-Probe method with photon-induced $\gamma\gamma \to \mu\mu$ events in 2018 and 2015 Pb+Pb data, respectively. For the Tag-and-Probe analysis, events are required to pass the corresponding data quality and muon trigger selections, contain at most two reconstructed inner-detector tracks and include at least one reconstructed muon.

There are two types of associated efficiencies defined: the Inner Detector (ID) and the Muon Spectrometer (MS). The ID efficiency, $\epsilon(\text{ID}|MS)$, is calculated as the fraction of MS-extrapolated probes matched to ID tracks, while the MS efficiency, $\epsilon(\mu|ID)$, is determined from ID tracks matched to *LowPt* muons. The total efficiency for *LowPt* muons is then given by:

$$\epsilon(\text{LowPt}) = \epsilon(\text{LowPt}|\text{ID})\,\epsilon(\text{ID}|\text{MS}). \tag{5.5.1}$$

For the evaluation of the ID efficiency, the probe is an MS-extrapolated track with $|d_0| < 2$ mm and opposite charge to the tag. The muon pair p_{T} must be less than 2 GeV and acoplanarity of the muon pair is required to be less than 0.02. An ID track is considered as matched to the MS if it fulfils the *LooseMuon* criteria, has $|d_0| < 2$ mm and lies within $\Delta R < 0.1$ of the MS track; the efficiency is then the fraction of probes with a matched ID track.

Similarly, the MS efficiency is obtained by defining the probe as an ID track satisfying the same kinematic and quality selections. A probe is matched to a *LowPt* muon if $\Delta R < 0.01$ and the efficiency is calculated as the fraction of ID probes that have a corresponding matched MS muon.

The ID efficiency is close to 99%–100% across the measured p_{T} and the $q\eta$ ranges, with excellent agreement between data and MC simulation for both 2015 and 2018. Similarly, the MS efficiency shows very good agreement between data and MC across all p_{T} values, confirming the robustness of the reconstruction and PID performance.

For the 2015 dataset, the total muon reconstruction and PID efficiency reaches a plateau of about 93% for $p_{\text{T}} > 4$ GeV and decreases rapidly for $p_{\text{T}} < 3.5$ GeV. At high p_{T} (> 15 GeV), statistical fluctuations increase due to limited event counts. As a function of $q\eta$, the efficiency averages around 93% with some variations.

For the 2018 dataset, the total efficiency is approximately 97% at $p_{\text{T}} = 4$ GeV and approaches nearly 100% at higher p_{T}. The efficiency is around 99% for $|q\eta| > 1.4$ and slightly lower (97–98%) at midrapidity ($|q\eta| < 1.4$). The ratio of efficiency in data to MC simulation remains close to unity across most of the $q\eta$ range. Overall, the data and MC simulation show very good agreement for both years.

Scale factors are applied to correct the muon reconstruction and PID efficiency in MC simulation to match that observed in data, defined as $\text{SF} = \epsilon_{\text{data}}/\epsilon_{\text{MC}}$. The analysis uses SFs derived in Ref. [35] for 2018 and the same methodology is applied

for the 2015 dataset.

Several sources of systematic uncertainties affecting the SFs are considered, including variations in the tag muon identification, acoplanarity and p_{T} requirements, ZDC selection and $|d_0|$. Systematic uncertainties are estimated as the deviation from the nominal SF.

Overall, the SFs are stable across $p_{\mathrm{T}} > 4$ GeV, with total systematic variations generally within the statistical uncertainties. The largest contributions arise from the ZDC selection, while effects from acoplanarity and $|d_0|$ variations are negligible. The maximum SFs deviations are about 1%.

5.5.2 Electrons and photons

The reconstruction of electrons and photons in ATLAS was introduced in Section 3.5.3. They are used in the analysis with the following requirements:

- $E_{\mathrm{T}} > 4.0$ GeV,
- $|\eta| < 2.47$, with the calorimeter transition region $1.37 < |\eta| < 1.52$ excluded,
- $|d_0| < 0.5$ mm,
- *looseLH* identification criteria, based on shower-shape and track-quality variables [130].

This analysis employs SFs, together with their associated uncertainties, to correct the electron reconstruction and identification efficiency. These factors were derived in the Light-by-Light scattering measurement [131] using the 2018 dataset. For the 2015 MC sample, the same SFs as for 2018 are applied, but with an additional $\pm 10\%$ statistical uncertainty. This estimate is motivated by luminosity scaling: the statistical uncertainty on the 2018 SFs is about 5%, which scales by a factor of $\sqrt{1.44/0.49}$ to roughly 8.5%. Assigning a 10% uncertainty thus provides a conservative margin.

The photons are only used in the μ1T-SR selection (see Section 5.6.2) in order to suppress dimuon background contribution with additional FSR. Photons must meet the following criteria:

- $E_{\mathrm{T}} > 1.5$ GeV,
- $|\eta| < 2.37$, excluding the calorimeter transition region $1.37 < |\eta| < 1.52$
- Identification criteria based on shower-shape variables [131].

The efficiency of the photon reconstruction has minimal effect, as photons are only used to identify and suppress dimuon background with FSR emissions (see Section 5.7.2). Therefore, there are no corrections for photon efficiency applied.

5.5.3 Tracks

The reconstruction of tracks was discussed in Section 3.5.1. This analysis uses charged-particle tracks with the following requirements:

- $p_{\mathrm{T}} > 100$ MeV,
- $|\eta| < 2.5$,
- $|d_0| < 1.5$ mm,
- *Loose Primary* track selection.

The *Loose Primary* working point includes the following set of criteria:

- At least seven silicon hits,
- At most one shared module allowed, corresponding to either one shared Pixel hit or two shared SCT hits,
- A maximum of two holes (holes are defined as points where the reconstructed track trajectory crosses a sensitive detector element without producing a corresponding hit [132]) permitted in total in the SCT and Pixel detectors,
- No more than one hole allowed in the Pixel detector,
- Either at least seven silicon hits with no shared silicon hits, or at least ten silicon hits in total,
- A χ^2/ndof requirement, as defined in Ref. [133], with the threshold value depending on the track pseudorapidity.

The efficiency of the track reconstruction for the given working point was studied in the first iteration of the ATLAS measurement [35] using 2018 MC and was found to be in between 80% and 90% for most of the tracks. The are no differences expected between data-taking years.

Since the agreement between data and MC was found to be good, there are no track-related SFs applied to the MC.

5.5.4 Topo-clusters

The reconstruction of topo-clusters was described in Section 3.5.2. They are used in the analysis with the following criteria applied:

- Minimum p_{T} of 0.1 GeV for $2.5 < |\eta| < 4.9$,
- Minimum p_{T} of 1 GeV for $|\eta| < 2.5$,

- Significance criteria for individual cells [134], reducing contributions from electronic noise.

The topo-cluster reconstruction efficiency is studied using hard bremsstrahlung photons from $\gamma\gamma \to ee\gamma$ events, selected with a Tag-and-Probe method. The efficiency is defined as the fraction of events with at least one reconstructed topo-cluster. In data, it reaches about 97% at $E_{\mathrm{T}}^{\gamma} = 1$ GeV and rises to 99% at $E_{\mathrm{T}}^{\gamma} = 3$ GeV. Good agreement between data and simulation is observed and thus no correction factors are applied. Instead, a conservative 2% global systematic uncertainty is assigned to the simulation.

There is also a dedicated procedure used in order to reject topo-clusters from calorimeter 'hotspot' regions. It is described in the following section.

Topo-clusters from calorimeter 'hotspots'

In addition to topo-clusters associated with particles from collisions, the reconstruction of topo-clusters may identify clusters caused by calorimeter noise or malfunctioning cells. In UPC data, however, spurious low-p_{T} activity in specific calorimeter regions, referred to as 'hotspots,' is not always suppressed. Standard procedures only mask calorimeter problems that produce large energy deposits, however, low-p_{T} spurious signals remain below their thresholds and therefore can persist as hotspots in UPC events.

To address this, a dedicated procedure based on η–ϕ maps of low-p_{T} cluster activity is implemented. Maps are constructed from three independent event samples: $\gamma\gamma \to ee$, $\gamma\gamma \to \mu\mu$ and a dedicated 'cosmic' selection, used to capture backgrounds from detector noise and cosmic radiation.

The dilepton selections require exactly two leptons of the same flavour, 0n0n ZDC activity and $\Delta\phi_{\ell\ell} > 3.1$ to suppress FSR contributions. The 'cosmic' selection identifies events with UPC-like signatures in empty bunches. Topo-clusters are considered as 'hotspot' candidates if they satisfy $p_{\mathrm{T}} > 0.2$ GeV, pass cell significance requirements and are not matched to reconstructed leptons. From each calorimeter layer, only the cluster with the highest cell significance is taken.

To ensure robustness against statistical fluctuations, the three channels are combined into a single map per calorimeter layer. A bin is marked as a 'hotspot' if all three event samples contain at least five entries in that bin, each contributing at least 0.1% of the total entries for the channel. The resulting combined maps highlight only the most significant hotspots and are subsequently used in data reprocessing to exclude clusters originating from these regions.

5.6 Event selection

The $\gamma\gamma \to \tau\tau$ events are divided into three signal regions (SRs), defined according to the decay modes of the τ-lepton, as described in Section 1.3.

Based on these decay modes, three statistically independent SRs are defined: μ1T-SR, μ3T-SR and μe-SR. In all SRs, one of the τ leptons is required to decay into a muon, while the other τ is required to decay into a single charged track (1T), three charged tracks (3T), or an electron, respectively. The final state also includes additional neutrinos. The requirement of exactly one muon in the final state significantly suppresses hadronic backgrounds as well as backgrounds from photon-induced dimuon pair production.

In addition to the SRs, a control region (CR) enriched in dimuon events is defined to validate the modelling of the $\gamma\gamma \to \mu\mu$ background and extract photon-flux corrections (see Section 5.7.2). A summary of the selection requirements for the SRs is provided in Table 5.6.1. All SRs are mutually exclusive. For calculation of track-related variables in all regions, a track mass of 140 MeV (the charged pion mass) is assumed, while topo-clusters are considered massless. A detailed discussion of the event selection criteria is presented in the following section.

Observable	Preselection		
GRL & trigger	Pass		
0n0n topology	$E_{\mathrm{ZDC}}^{\mathrm{A,C}} < 1$ TeV for data, 0n0n weights for MC		
Region	**μ1T-SR**	**μ3T-SR**	**μe-SR**
$N_{\mu}^{\mathrm{baseline}}$	$= 1$	$= 1$	—
N_{μ}^{sig}	$= 1$	$= 1$	$= 1$
N_{e}^{sig}	$= 0$	$= 0$	$= 1$
N_{trk} ($\Delta R > 0.1$ from μ^{sig})	$= 1$	$= 3$	—
N_{trk} ($\Delta R > 0.1$ from ℓ^{sig})	—	—	$= 0$
$N_{\mathrm{clust}}^{\mathrm{unmatched}}$	$= 0$	$= 0$	—
$\sum_i q_i$	$= 0$	$= 0$	$= 0$
$p_{\mathrm{T}}^{(\mu,\mathrm{trk})}$	> 1 GeV	—	—
$p_{\mathrm{T}}^{(\mu,\mathrm{trk},\gamma)}$	> 1 GeV	—	—
$p_{\mathrm{T}}^{(\mu,\mathrm{trk,cluster})}$	> 1 GeV	—	—
m_{trks}	—	< 1.7 GeV	—
$A_{\phi}^{\mu,\mathrm{trk(s)}}$	< 0.4	< 0.2	—

Table 5.6.1: Summary of signal region definitions. The 0n0n weights applied for MC for reconstructed distributions include the contribution from EM pileup.

5.6.1 Preselection

At the preselection stage, events are required to pass the so-called Good Run List (GRL). It is an official list of data-taking periods (runs and luminosity blocks) that are certified as suitable for physics analyses. It ensures that only intervals in which all relevant ATLAS subsystems were fully operational are included, thereby guaranteeing high-quality and consistent data for the analysis.

To select events consistent with a 0n0n topology, corresponding to no neutrons emitted in either beam direction, the requirement $E_{\mathrm{ZDC}}^{\mathrm{A,C}} < 1$ TeV is imposed on both sides of the interaction point. This requirement is applied only to data, as the MC samples do not contain ZDC information. In the MC, the 0n0n topology is modelled using data-driven weights, as described in Section 5.3. In addition, events must satisfy dedicated muon triggers, which are detailed in Section 5.4.

5.6.2 Signal Regions

μ1T-SR

For the μ1T-SR selection, exactly one signal muon is required ($N_{\mu}^{\mathrm{sig}} = 1$) and a stricter requirement of exactly one baseline muon is enforced in addition ($N_{\mu}^{\mathrm{baseline}} = 1$). There must be exactly one track separated by a distance of $\Delta R > 0.1$ from the signal muon (N_{trk} ($\Delta R > 0.1$ from μ^{sig}) $= 1$). The contribution from the dielectron background is suppressed by applying an electron veto ($N_{e}^{\mathrm{sig}} = 0$).

Events are required to contain no unmatched topo-clusters ($N_{\mathrm{clust}}^{\mathrm{unmatched}}$=0), defined as topo-clusters that are not associated with either a signal lepton ($\Delta R > 0.3$) or the selected track ($\Delta R > 1.0$). This criterion suppresses photonuclear background contributions, as discussed in Section 5.7.3. Furthermore, the total charge of the lepton and the track is required to be zero ($\sum_i q_i = 0$).

Additional selection criteria are applied on the transverse momentum of different reconstructed systems: the muon–track system ($p_{\mathrm{T}}^{(\mu,\mathrm{trk})}$), the muon–track–photon system ($p_{\mathrm{T}}^{(\mu,\mathrm{trk},\gamma)}$) and the muon–track–cluster system ($p_{\mathrm{T}}^{(\mu,\mathrm{trk,cluster})}$) are required to be above 1 GeV. These requirements effectively retain signal events, which typically have larger transverse momentum, while suppressing dimuon background events. In particular, dimuon events without FSR generally exhibit low pair p_{T}, whereas dimuon events with FSR can be rejected by including low-p_{T} photons or topo-clusters, allowing the reconstruction of a three-body system. These requirements also strongly reduce the p_{T}-balanced backgrounds, while signal events typically are more p_{T}-imbalanced due to the presence of neutrinos.

If a photon is found within $\Delta R < 1$ of the selected track, the three-body p_{T} is computed using the muon, the track and the leading photon. Similarly, if a cluster with $p_{\mathrm{T}} > 2$ GeV is found within $\Delta R < 1$ of the selected track and is not associated

with it, the cluster is used in the three-body p_{T} calculation. A cluster is considered to be associated with the track if it lies within $\Delta R < 0.1$ of the track's extrapolated position in the calorimeter and if the track has $p_{\mathrm{T}} > 0.7$ GeV, since tracks with lower p_{T} are unlikely to reach the calorimeter.

The acoplanarity of the muon–track system is defined as $A_{\phi}^{\mu,\mathrm{trk}} = 1 - |\Delta\phi(\mu, \mathrm{trk})|/\pi$. In order to further reduce the photonuclear backgrounds, it is required to be less than 0.4.

μ3T-SR

For the μ3T-SR selection, events are required to have exactly one signal muon ($N_{\mu}^{\mathrm{sig}} = 1$) with a stricter baseline criterion ($N_{\mu}^{\mathrm{baseline}} = 1$) applied and exactly three track within a distance of $\Delta R > 0.1$ from the signal muon (N_{trk} ($\Delta R > 0.1$ from μ^{sig}) $= 3$). An electron veto is applied in order to suppress the contamination from the dielectron background ($N_{e}^{\mathrm{sig}} = 0$).

The definition of the unmatched clusters follows the one used for the μ1T-SR but requires the cluster to be outside the proximity of all selected tracks ($\Delta R > 1.0$). Signal events are required to contain no unmatched clusters ($N_{\mathrm{clust}}^{\mathrm{unmatched}}$=0). The total sum of the charges of tracks and the muon must be zero ($\sum_i q_i = 0$).

The μ3T-SR selection also includes a dedicated cut on the mass of the three-track system, $m_{\mathrm{trks}} < 1.7$ GeV. This requirement suppresses backgrounds from exclusive ρ meson production that may proceed simultaneously to $\gamma\gamma \to \mu\mu$ process.

In order to reduce the photonuclear background, the acoplanarity between the muon and the three-track system is required to be $A_{\phi}^{\mu,\mathrm{trks}} = 1 - |\Delta\phi(\mu, \mathrm{trks})|/\pi < 0.2$.

μe-SR

For the μe-SR selection, events are required to have exactly one signal muon ($N_{\mu}^{\mathrm{sig}} = 1$) and exactly one electron ($N_{e}^{\mathrm{sig}} = 1$), without any additional tracks within the $\Delta R > 0.1$ from the signal leptons (N_{trk} ($\Delta R > 0.1$ from ℓ^{sig})). The muon and electron must have opposite charges ($\sum_i q_i = 0$).

5.7 Background modelling

After applying the event selection, the dominant background contributions arise from two processes: photon-induced dimuon production ($\gamma\gamma \to \mu\mu(\gamma)$) and diffractive photonuclear interactions, where a photon scatters off a nucleus. These two processes are illustrated in Figure 5.7.1. The diagram of the photon-induced dimuon background additionally includes FSR since $\gamma\gamma \to \mu\mu$ can be accompanied by a hard FSR photon emission. Diffractive photonuclear events are produced via the exchange of a colourless object, referred to as the *Pomeron*. The remnants of the Pomeron typically manifest as low-p_{T} tracks. Such processes are often accompanied by the breakup of the ion.

In the first iteration of the ATLAS measurement [35], additional potential background sources were investigated, including photon-induced dimuon production accompanied by exclusive ρ^0 meson production, photon-induced low-p_{T} jet production ($\gamma\gamma \to q\bar{q}$) and inclusive photonuclear processes. In the present analysis, the impact of simultaneous ρ^0 production was re-evaluated. All of these possible background contributions were found to be negligible and are therefore not considered further in this measurement.

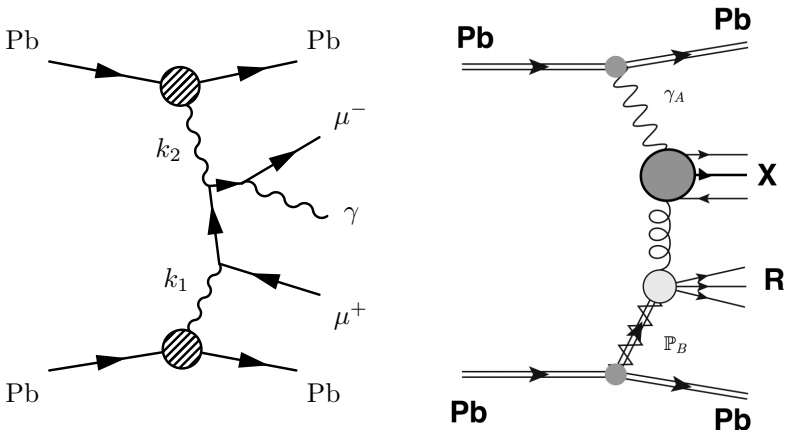

Figure 5.7.1: Illustration of two dominant sources of background: (left) photon-induced dimuon production, (right) diffractive photonuclear particle production, where photon–Pomeron ($\mathbb{P}$) interaction produces system X and R denotes the low-mass dissociation remnant of the Pomeron-emitting nucleus.

The estimation of the dominant dimuon and photonuclear backgrounds was performed by the Author (with the exception of the extraction of the global residual flux factor for the dimuon background). The corresponding studies are presented in the following section. A summary of additional minor background studies is also provided at the end of the section.

5.7.1 Control Regions

For the estimate of the dominant background processes, dedicated control regions (CRs) are defined in order to validate the modelling. For the modelling of the photon-induced dimuon production, a dedicated dimuon CR is constructed (2μ-CR), in which events are required to have exactly two signal muons with a dimuon invariant mass of $m_{\mu\mu} > 11$ GeV, which suppresses the contamination from the exclusive upsilon meson production ($\Upsilon(nS) \to \mu\mu$). There is also a requirement for no tracks with a separation of $\Delta R > 0.1$ from the signal muons (N_{trk} ($\Delta R > 0.1$ from μ^{sig}) $= 0$).

The photonuclear background is estimated using a fully data-driven method, as described in detail in Section 5.7.3. Template distributions are constructed using two CRs, which require an additional soft track with $p_{\text{T}} < 500$ MeV, separated from the signal muon by $\Delta R > 0.1$ (N_{trk} ($\Delta R > 0.1$ from μ^{sig})), as photonuclear events are usually accompanied by extra particle production. The photonuclear CRs are called μ2T-CR (one muon and two tracks) and μ4T-CR (one muon and four tracks). They correspond to the μ1T-SR and μ3T-SR, respectively. In the case of the μe-SR, the photonuclear background was found to be negligible. The selections for μ2T-CR and μ4T-CR are the same as in the corresponding SRs, except the requirements described below.

In the photonuclear CRs, Xn0n or 0nXn forward neutron topologies are accepted in addition to 0n0n, in order to increase the available statistics. This choice is further motivated by the fact that photonuclear interactions are frequently accompanied by the breakup of the Pb nuclei. Unlike in the SRs, events in the CRs are permitted to contain up to eight unmatched topo-clusters ($N_{\text{clust}}^{\text{unmatched}} \leq 8$), rather than requiring none.

To suppress signal contamination, additional requirements are applied. In the μ2T-CR selection, the invariant mass of the two-track system is required to exceed 1 GeV ($m_{\text{trks}} > 1$ GeV) and the acoplanarity between the muon and the leading track (the track with the highest p_{T}) must be greater than 0.2 ($A_{\phi}^{\mu,\ \text{highest-}p_{\text{T}}\ \text{trk}} > 0.2$). For the μ4T-CR selection, the requirement that the sum of charges must be zero is removed ($\sum_i q_i$). A summary of the selection criteria applied in all CRs is provided in Table 5.7.1.

Observable	Preselection		
GRL & trigger	Pass		
Region	2μ-CR	μ2T-CR	μ4T-CR
ZDC requirement	0n0n weights	$E_{\text{ZDC}}^{\text{A or C}} < 1$ TeV	$E_{\text{ZDC}}^{\text{A or C}} < 1$ TeV
$N_{\mu}^{\text{baseline}}$	–	$= 1$	$= 1$
N_{μ}^{sig}	$= 2$	$= 1$	$= 1$
N_{trk} ($\Delta R > 0.1$ from μ^{sig})	$= 0$	$= 2$	$= 4$
p_{T} of lowest-p_{T} trk	–	< 500 MeV	< 500 MeV
$N_{\text{clust}}^{\text{unmatched}}$	–	≤ 8	≤ 8
$\sum_i q_i$	–	$= 0$	–
m_{trks} (or $A_{\phi}^{\mu,\ \text{highest-}p_{\text{T}}\ \text{trk}}$)	–	> 1 GeV (or > 0.2)	< 1.7 GeV
$m_{\mu\mu}$	> 11 GeV	–	–
Purpose	$\gamma\gamma \to \mu\mu$ modelling	photonuclear templates	

Table 5.7.1: Summary of control region definitions used for the modelling of the photon-induced dimuon and diffractive photonuclear background. Table adapted from Ref. [1].

5.7.2 Photon-induced dimuon production

The photon-induced production of dimuons ($\gamma\gamma \to \mu\mu(\gamma)$) is the largest source of background. The emission of an FSR photon can induce a momentum imbalance between the two muons, thereby more closely mimicking the μ1T-SR. In addition, FSR photons may undergo conversions, producing two extra tracks and thus mimicking a μ3T-SR topology, or they may lead to the reconstruction of a fake electron, which is relevant for the μe-SR.

The photon-induced dimuon background is estimated using MC samples produced using the STARLIGHT and MADGRAPH5_aMC@NLO 2.9 MC generators, each interfaced to PYTHIA 8 to model FSR (see Section 5.2). The photon flux for each is reweighted to SUPERCHIC 3 (see Section 5.2.1). The MADGRAPH 5 sample is used to improve the modelling of photon emissions with high-p_{T} in the region where $p_{\text{T}}^{\gamma} \gtrsim p_{\text{T}}^{\mu}$.

Extraction of the Global Residual Flux Factor (GRFF)

The modelling of the photon-induced dimuon background is checked in the 2μ-CR, as shown in Figure 5.7.2 (left). A residual offset remains between the $\gamma\gamma \to \mu\mu(\gamma)$ prediction (after reweighting the photon flux) and the data, attributed to limitations in the photon flux modelling. To correct for this, a data-driven *Global Residual Flux Factor* (GRFF) is extracted in the 2μ-CR and applied as an overall normalisation to both the $\gamma\gamma \to \mu\mu(\gamma)$ background and the $\gamma\gamma \to \tau\tau$ signal.

The GRFF is determined through a profile-likelihood fit. The TRExFitter [135] framework is used, with the leading-muon p_{T} distribution in the 2μ-CR as input. This choice provides improved precision compared to a single-bin fit due to the inclusion of shape information. The post-fit distribution is shown on the right in Figure 5.7.2. The extracted value is:

$$\mathrm{GRFF} = 0.9351^{+0.0349}_{-0.0332}, \tag{5.7.1}$$

with uncertainties corresponding to 68% CL intervals. These uncertainties are propagated as an independent systematic source throughout the analysis (see Section 6.2), including to the cross-section measurements (Section 6.4) and the fits for a_τ and d_τ (Section 6.5 and 6.6), without correlations to other systematics. This conservative treatment ensures robustness of the final results.

The kinematic distributions in the 2μ-CR with the GRFF correction applied are presented in Figure 5.7.3. These include the leading muon p_{T} along with dimuon p_{T} and dimuon invariant mass. Additional plots are included in Appendix B (Fig B.1). The contribution of the signal process was found to be negligible and there is generally good agreement between the data and the prediction.

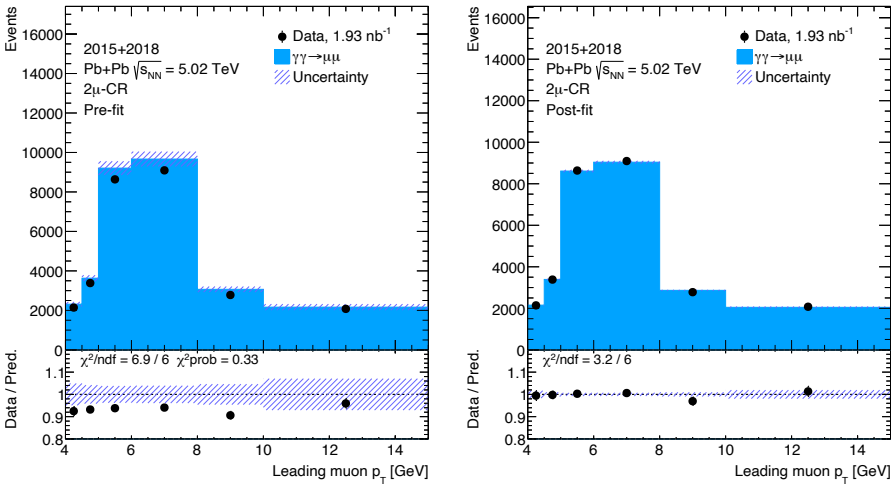

Figure 5.7.2: Pre-fit (left) and post-fit (right) leading muon p_{T} distributions for the GRFF fit in the 2μ-CR with the combined 2015+2018 dataset. The hatched band denotes the total uncertainty.

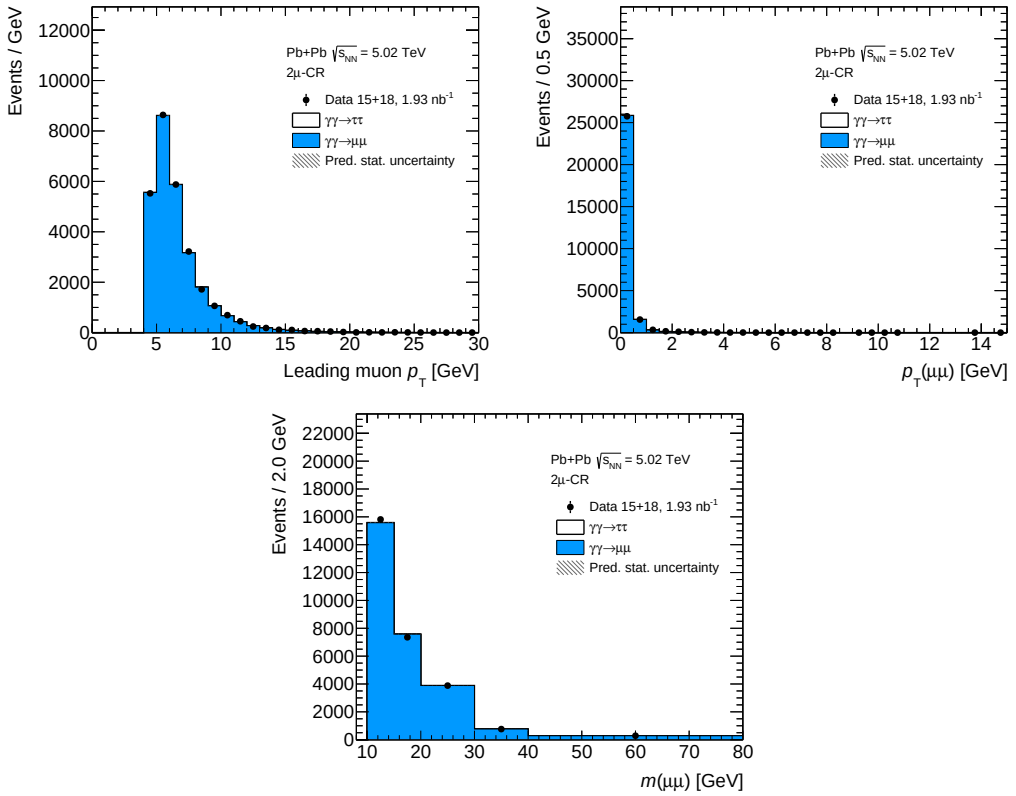

Figure 5.7.3: Control distributions for the combined 2015 + 2018 dataset in the 2μ-CR: (top-left) leading muon transverse momentum, (top-right) dimuon transverse momentum, (below) dimuon invariant mass. Statistical uncertainties on the predictions are shown as hatched bands. The photon flux is reweighted to match the flux from the SuperChic 3 generator. The modelling is improved by applying the GRFF correction.

5.7.3 Photonuclear background

Diffractive photonuclear processes constitute a challenging background source, as they are characterised by low particle activity and topologies with large rapidity gaps. Thus, they are hard to model well using MC. In this analysis, the diffractive photonuclear background is estimated using a fully data-driven method, which exploits the fact that such events are typically accompanied by additional particle production. Template distributions are constructed from dedicated CRs, described in Section 5.7.1.

The templates are normalised using the distribution of unmatched topo-clusters, shown in Figure 5.7.4 for the 2015 and 2018 datasets. The normalisation factor is obtained as the ratio of the integrals of the data and photonuclear template distributions in the region $4 \leq n_{\text{unmatched}}^{\text{topoclusters}} \leq 8$. This region is chosen because it is free from both signal and photon-induced dimuon background contributions.

The beam conditions differed between the two data-taking years, with the 2015 beams being less intense - as can be seen, for example, from the $0n0n$ weights in Figure 5.3.5 in Section 5.3. These different conditions lead to variations in the photonuclear background contribution, motivating the separate treatment of the 2015 and 2018 data. Since no events are observed in the normalisation region for the μ3T-SR in 2015 (Figure 5.7.4, top right), the corresponding background estimate evaluates to zero and the photonuclear background in that region is neglected.

For 2018 data, the photonuclear background is found to be largest in the μ2T-CR, with control plots shown in Figure 5.7.5. These include the muon p_{T} along with muon-leading-track system p_{T} and invariant mass of that system. The remaining distributions, corresponding to the μ2T-CR and the μ4T-CR are provided in Appendix B (Figures B.2 - B.4). Systematic uncertainties related to this background are discussed in Section 5.7.3.

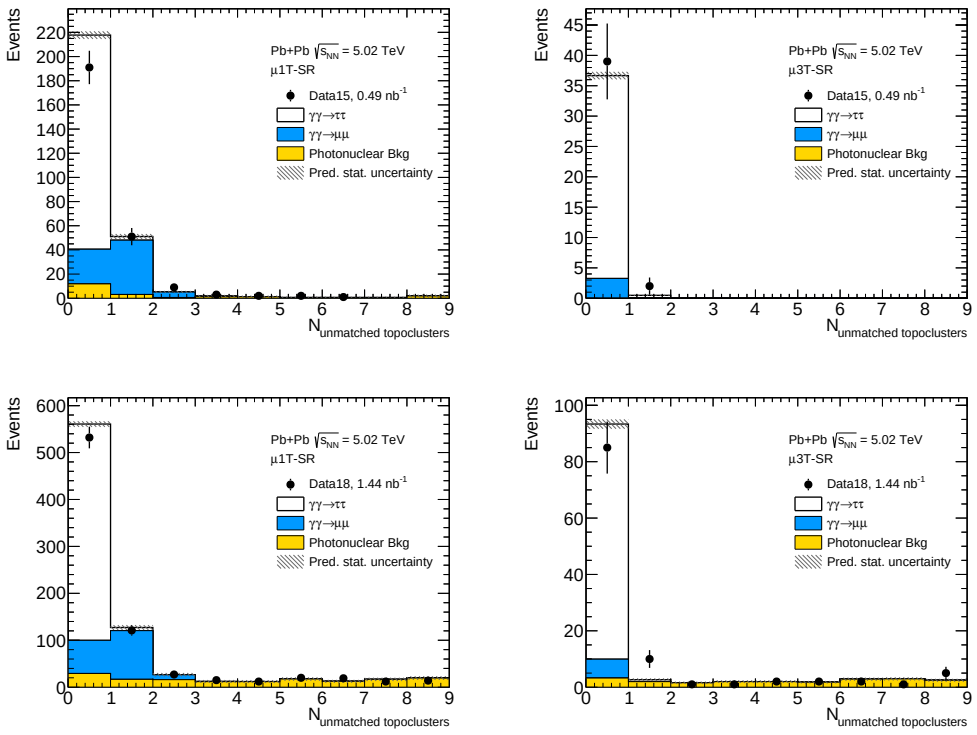

Figure 5.7.4: Distribution of the number of unmatched topoclusters for (left column) μ1T-SR and (right column) μ3T-SR, after relaxing the veto requirement to allow up to 8 extra unmatched topoclusters. Plots on top show 2015 data and plots on the bottom show 2018 data. The photonuclear background estimate (shown as a yellow histogram) is normalised in the $4 \leq n_{\mathrm{unmatched}}^{\mathrm{topoclusters}} \leq 8$ region. The $\gamma\gamma \to \tau\tau$ signal and $\gamma\gamma \to \mu\mu(\gamma)$ background predictions have not been scaled with the GRFF on these figures.

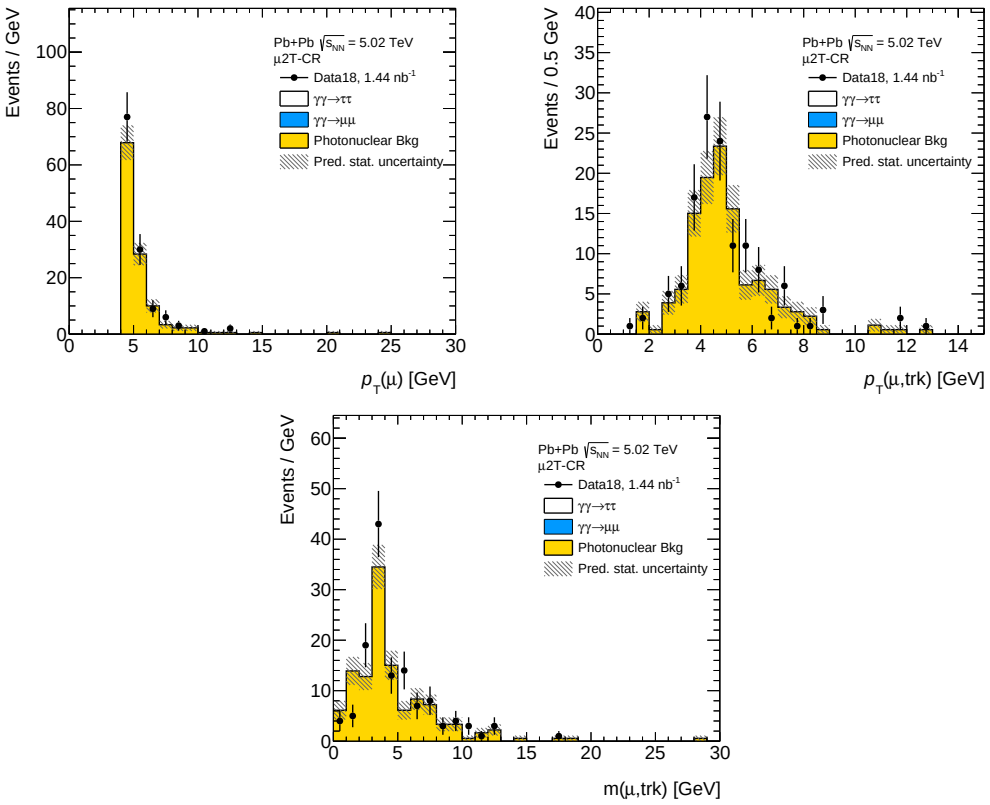

Figure 5.7.5: Control distributions for the 2018 data in the μ2T-CR: (top-left) muon transverse momentum, (top-right) muon–track transverse momentum, (below) muon–track invariant mass.

5.7.4 Other sources of background

Additional potential background sources were investigated. One such contribution arises from simultaneous ρ^0 production in UPC, either through double scattering of photon-induced $\gamma\gamma \to \mu\mu$ and $\gamma P \to \rho^0 \to \pi\pi$ processes (where P is a pomeron), or from ρ^0 production occurring in association with $\gamma\gamma \to \mu\mu$ or $\gamma\gamma \to \tau\tau$. Both scenarios were studied using dedicated control regions and data-driven techniques. In all cases, no significant contribution was observed and these processes are therefore considered negligible.

Another possible background source is $\gamma\gamma \to q\bar{q}$. Simulation studies based on Pythia 8 indicate that its contribution is extremely small (below one event in any SR) and can also be neglected.

The possible impact from inclusive photonuclear background was estimated using additional MC samples, generated with Starlight and DPMJETIII [136]. The background was found to be negligible, as no event passed the selection criteria for any SR.

5.8 Reconstruction-level distributions

The observed data yields, together with the predicted signal and background contributions, are summarised in Table 5.8.1 for each SR. Detector-level distributions of kinematic variables are shown in Figures 5.8.1, 5.8.2 and 5.8.3 for μ1T-SR, μ3T-SR and μe-SR, respectively. These include the muon p_{T} in all SRs, along with transverse momentum and invariant mass of the corresponding system. The system is defined as muon–track in the μ1T-SR, muon–three tracks in the μ3T-SR, and muon–electron in the μe-SR. Additional kinematic variables are shown in Appendix C (Figures C.1 - C.3). The sequential impact of event selection criteria (cutflows) is also included, separately for the 2015 and 2018 datasets, in Tables C.1 - C.6.

The detector-level distributions show a clear $\gamma\gamma \to \tau\tau$ signal, with background contributions remaining very low. The data are in good agreement with the theoretical predictions.

Region	Data	Signal $\gamma\gamma \to \tau\tau$	Background $\gamma\gamma \to \mu\mu(\gamma)$	Background photonuclear	Prediction (Signal + Background)
μ1T-SR	723	598.4 ± 39.2	95.8 ± 8.1	15.9 ± 11.6	710.0 ± 46.2
μ3T-SR	124	109.0 ± 9.2	9.4 ± 1.1	3.2 ± 2.1	121.6 ± 9.8
μe-SR	53	40.6 ± 3.3	3.2 ± 0.5	–	43.8 ± 3.6

Table 5.8.1: Summary of SR yields with a breakdown of the background contributions for the combined 2015+2018 dataset.

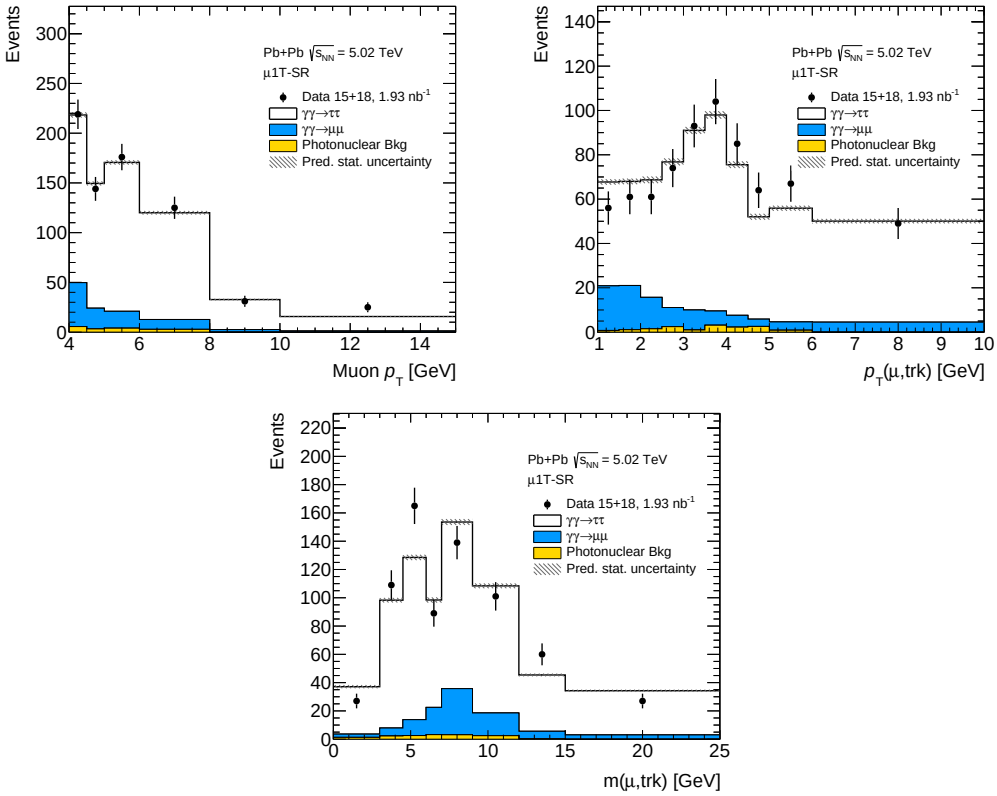

Figure 5.8.1: Control plots for the combined 2015 + 2018 dataset in the μ1T-SR: (top-left) muon transverse momentum, (top-right) muon–track transverse momentum and (below) muon–track invariant mass. Statistical uncertainties on the predictions are shown as hatched bands.

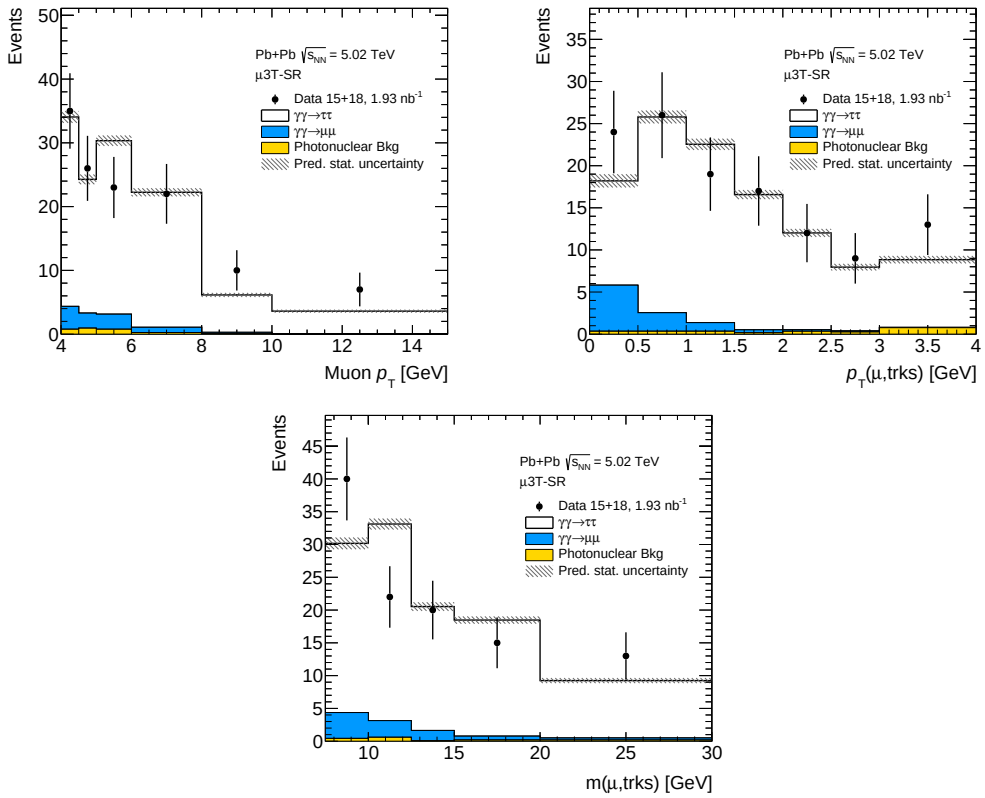

Figure 5.8.2: Control plots for the combined 2015 + 2018 dataset in the μ3T-SR: (top-left) muon transverse momentum, (top-right) muon–3–tracks transverse momentum and (below) muon–3–tracks invariant mass. Statistical uncertainties on the predictions are shown as hatched bands.

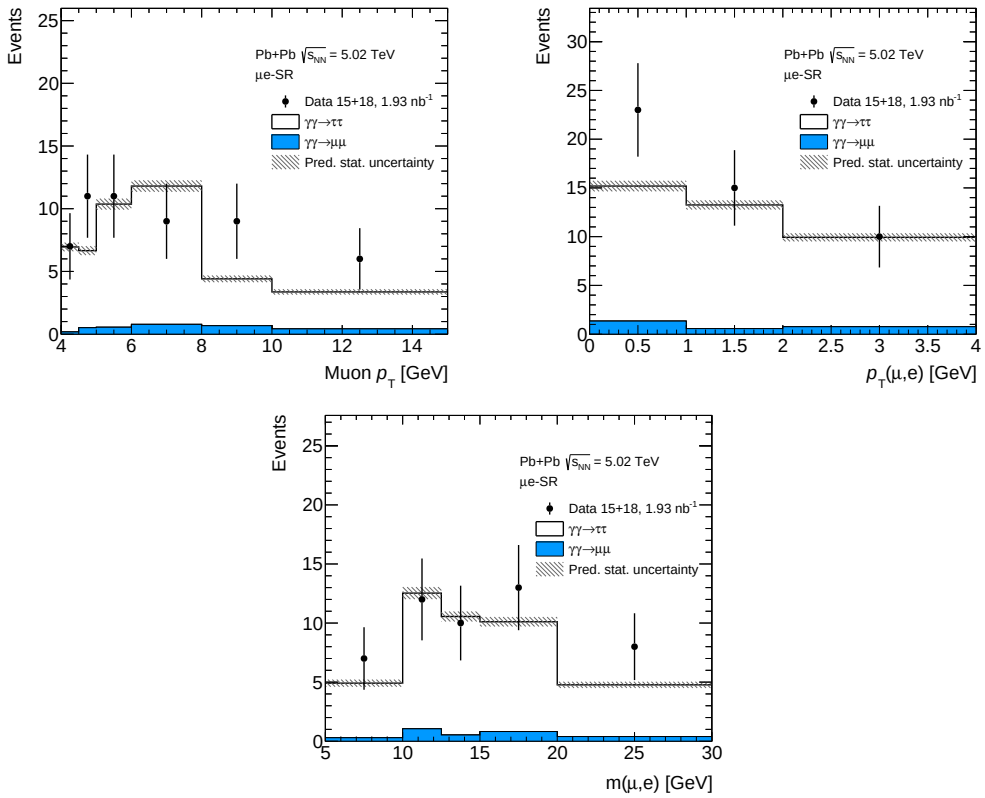

Figure 5.8.3: Control plots for the combined 2015 + 2018 dataset in the μe-SR: (top-left) muon transverse momentum, (top-right) muon–electron transverse momentum and (below) muon–electron invariant mass. Statistical uncertainties on the predictions are shown as hatched bands.

Chapter 6

Differential $\gamma\gamma \to \tau\tau$ cross sections and constraints on τ-lepton electromagnetic moments in Pb+Pb collisions

After selecting $\gamma\gamma \to \tau\tau$ candidate events and subtracting the estimated background contributions, the analysis proceeds with an unfolding procedure to measure this process differentially. This work constitutes the first differential cross-section measurements of this process in heavy-ion collisions at the LHC. These measurements are compared to SM predictions and expected constraints on the electromagnetic moments of the τ-lepton obtained utilising these differential cross-section measurements are also presented.

Unfolding is a statistical technique used to correct the detector-level distributions for effects such as reconstruction inefficiencies and finite detector resolution, thereby enabling a measurement that can be reproduced and reinterpreted by other experiments or theoretical studies. Once the detector effects are removed, an estimate of the true underlying particle-level distributions can be obtained.

The Author's work includes the definition of the fiducial regions (FR) described in Section 6.1.1, definition of kinematic variables to unfold as well as the preparation of all unfolding inputs, as described in Section 6.1.2. The Author generated bootstrap replicas of the data used to estimate the statistical uncertainties and their correlations, described in Section 6.1.3. Furthermore, the Author implemented a major upgrade of the analysis framework to enable a consistent treatment of systematic uncertainties, summarised in Section 6.2. In addition to the nominal inputs, the Author also produced alternative predictions discussed in Section 6.4.

6.1 Unfolding procedure

In general, the goal of the unfolding procedure is to determine the relationship between the measured (reconstructed) distribution R_j and the truth-level distribution T_i. It can be expressed as:

$$R_j = \sum_i M_{ji}\, T_i, \tag{6.1.1}$$

where the detector response is represented by a *response matrix* M_{ji}. It describes the probability that an event generated in bin i of the true distribution is reconstructed in bin j.

In principle, the true distribution could be obtained by directly inverting the above relation:

$$T_j = \sum_i M_{ji}^{-1}\, R_i = \sum_i U_{ji}\, R_i, \tag{6.1.2}$$

where U_{ji} denotes the *unfolding matrix*. However, direct matrix inversion is typically unstable due to statistical fluctuations, which can lead to large variances and unphysical oscillations in the unfolded results. For this reason, regularised unfolding techniques are employed to obtain a stable and physically meaningful estimate of the true distribution.

In this analysis, the *Iterative Bayesian Unfolding* (IBU) method [137,138] is employed. This technique is based on Bayes' theorem, which relates the probability of a true value t_i given a reconstructed observation r_j through the conditional probability $P(t_i|r_j)$. The response matrix, $M_{ji} = P(r_j|t_i)$, encodes the detector response, representing the probability that an event generated in bin i of the true distribution is reconstructed in bin j. The unfolded distribution is obtained iteratively according to:

$$T_i^{(n+1)} = T_i^{(n)} \sum_j \frac{M_{ji}}{\sum_k M_{jk} T_k^{(n)}} R_j, \tag{6.1.3}$$

where $T_i^{(n)}$ is the estimate of the truth-level distribution after n iterations and R_j is the reconstructed (detector-level) distribution. In the denominator, the index k is a summation index running over all truth bins.

The number of iterations acts as a regularisation parameter in the IBU method. A small number of iterations tends to retain some bias from the prior distribution but yields a stable solution with reduced statistical fluctuations. Increasing the number of iterations reduces the bias but amplifies statistical noise, potentially leading to overfitting. In this analysis, the optimal choice of the number of iterations is determined using two criteria:

- The relative statistical uncertainty per unfolded bin should stabilise, increasing only minimally when adding further iterations, and should not fall below the corresponding relative statistical uncertainty of the truth distribution.

- The χ^2 between the unfolded and truth distributions, evaluated using either the unfolded or truth statistical errors, should reach stability. In particular, χ^2_{truth} should no longer change with additional iterations, indicating that the unfolded distribution has converged to the true shape.

Based on these checks, the number of iterations is set to 3 for the μ1T-FR and μe-FR and 2 for the μ3T-FR (for definition of FRs, see Section 6.1.1), for the muon p_{T} variable. The selected number of iterations for all kinematic variables is shown in Table 6.1.1 (unfolded variables are described in detail in Section 6.1.2).

Variable	N_{iter}
Muon p_{T}	3
Track p_{T}	2
$p_{\text{T}}(\mu, \text{trk})$	2
$m(\mu, \text{trk})$	3
$\eta(\mu, \text{trk})$	2
$\Delta\eta(\mu, \text{trk})$	2
$A_{\phi}^{\mu,\text{trk}}$	2

Variable	N_{iter}
Muon p_{T}	2
$p_{\text{T}}(\text{trks})$	2
$p_{\text{T}}(\mu, \text{trks})$	2
$m(\mu, \text{trk}s)$	3
$\eta(\mu, \text{trks})$	2
$\Delta\eta(\mu, \text{trks})$	2
$A_{\phi}^{\mu,\text{trks}}$	2

Variable	N_{iter}
Muon p_{T}	3
Electron p_{T}	3
$p_{\text{T}}(\mu, e)$	4
$m(\mu, e)$	2
$\eta_{(}\mu, e)$	2
$\Delta\eta(\mu, e)$	1
$A_{\phi}^{\mu,e}$	2

Table 6.1.1: The selected number of iterations used for the Iterative Bayesian Unfolding for the kinematic variables in the three FRs: (left) μ1T-FR, (middle) μ3T-FR and (right) μe-FR. Table adapted from Ref. [122].

6.1.1 Fiducial regions definition

The unfolding procedure is performed for three fiducial regions (FRs), which define the specific phase space of the measurements. These regions correspond to areas of the detector with well-understood performance and are defined in terms of truth-level quantities to minimise model dependence. The use of FRs also ensures reproducibility, allowing other experiments and theoretical predictions to be compared directly under the same fiducial selections.

The definitions of truth-level objects used in this analysis are summarised in Table 6.1.2. The objects are then classified into three categories: truth-level muons, truth-level electrons, and a third category encompassing both truth-level hadrons and low-p_{T} leptons (muons and electrons). This third category is defined in this way to remain as consistent as possible with the reconstruction-level definitions, where leptons with p_{T} below standard reconstruction thresholds can occur and not all tracks correspond exclusively to hadrons.

Object	Truth Muons	Truth Electrons	Truth Hadrons	Truth Low-p_{T} Leptons
Kinematic cuts	$p_{\mathrm{T}} > 4$ GeV $\lvert\eta\rvert < 2.5$	$p_{\mathrm{T}} > 4$ GeV $\lvert\eta\rvert < 2.5$	$p_{\mathrm{T}} > 100$ MeV $\lvert\eta\rvert < 2.5$	100 MeV $< p_{\mathrm{T}} < 4$ GeV $\lvert\eta\rvert < 2.5$

Table 6.1.2: Summary of truth object definitions used in the analysis.

There are three FRs defined: μ1T-FR, μ3T-FR and μe-FR, which correspond to the μ1T-SR, μ3T-SR and μe-SR selections, respectively. The definitions of the FRs are provided in Table 6.1.3. Each FR is statistically independent to each other.

The sequential impact of event selection criteria (cutflows) is documented separately for the 2015 and 2018 datasets in Appendix D (Tables D.1 - D.6).

Observable	Preselection		
0n0n topology	0n0n weights for MC		
Region	μ1T-FR	μ3T-FR	μe-FR
N_{μ}^{sig}	$= 1$	$= 1$	$= 1$
N_{e}^{sig}	$= 0$	$= 0$	$= 1$
$N_{\mathrm{trk}}(\Delta R > 0.1$ from $\mu^{\mathrm{sig}})$	$= 1$	$= 3$	—
$N_{\mathrm{trk}}(\Delta R > 0.1$ from $\ell^{\mathrm{sig}})$	—	—	$= 0$
$\sum_i q_i$	$= 0$	$= 0$	$= 0$
$p_{\mathrm{T}}^{(\mu,\mathrm{trk})}$	> 1 GeV	—	—
m_{trks}	—	< 1.7 GeV	—
$A_{\phi}^{\mu,\mathrm{trk(s)}}$	< 0.4	< 0.2	—

Table 6.1.3: Summary of fiducial region definitions. At truth-level, the index 'trk' corresponds to truth hadrons and truth charged leptons with $p_{\mathrm{T}}^{\ell} < 4$ GeV (as defined in Table 6.1.2). The 0n0n weights applied for particle-level MC distributions exclude the contribution from EM pileup.

6.1.2 Inputs for the unfolding

In each FR there are seven variables which are unfolded: the muon p_{T} in all FRs, the leading track p_{T} in the μ1T-FR, the three-track p_{T} in the μ3T-FR and the electron p_{T} in the μe-FR, along with system-level observables: transverse momentum, invariant mass, pseudorapidity difference, pseudorapidity and acoplanarity. The system is defined as muon–track in the μ1T-FR, muon–three tracks in the μ3T-FR and muon–electron in the μe-FR. The definitions of the variables are provided in Table 6.1.4.

Variable	μ1T-FR	μ3T-FR	μe-FR
Muon p_{T}	p_{T}^{μ}	p_{T}^{μ}	p_{T}^{μ}
Track(s)/Electron p_{T}	$p_{\mathrm{T}}^{\mathrm{trk}}$	$p_{\mathrm{T}}(\mathbf{p}_{\mathrm{trks}})$	p_{T}^{e}
p_{T} (μ, trk(s)/e)	$p_{\mathrm{T}}(\mathbf{p}_{\mu}+\mathbf{p}_{\mathrm{trk}})$	$p_{\mathrm{T}}(\mathbf{p}_{\mu}+\mathbf{p}_{\mathrm{trks}})$	$p_{\mathrm{T}}(\mathbf{p}_{\mu}+\mathbf{p}_{e})$
m (μ, trk(s)/e)	$m(\mathbf{p}_{\mu}+\mathbf{p}_{\mathrm{trk}})$	$m(\mathbf{p}_{\mu}+\mathbf{p}_{\mathrm{trks}})$	$m(\mathbf{p}_{\mu}+\mathbf{p}_{e})$
η (μ, trk(s)/e)	$\eta(\mathbf{p}_{\mu}+\mathbf{p}_{\mathrm{trk}})$	$\eta(\mathbf{p}_{\mu}+\mathbf{p}_{\mathrm{trks}})$	$\eta(\mathbf{p}_{\mu}+\mathbf{p}_{e})$
$\Delta\eta$ (μ, trk(s)/e)	$\eta_{\mu}-\eta_{\mathrm{trk}}$	$\eta_{\mu}-\eta(\mathbf{p}_{\mathrm{trks}})$	$\eta_{\mu}-\eta_{e}$
$A_{\phi}^{\mu,\mathrm{trk(s)}/e}$	$1-\lvert\phi_{\mu}-\phi_{\mathrm{trk}}\rvert/\pi$	$1-\lvert\phi_{\mu}-\phi(\mathbf{p}_{\mathrm{trks}})\rvert/\pi$	$1-\lvert\phi_{\mu}-\phi_{e}\rvert/\pi$

Table 6.1.4: Definition of variables measured in each FR. The notation $\mathbf{p}$ indicates the four-vector of the particles. Table adapted from [1].

Comparisons of the simulated $\gamma\gamma \to \tau\tau$ signal process at truth-level and reconstruction-level for chosen kinematic variables in μ1T-FR, μ3T-FR and μe-FR are presented in Figures 6.1.1, 6.1.3 and 6.1.5, respectively. The corresponding response matrices are presented in Figures 6.1.2, 6.1.4 and 6.1.6. These include muon p_{T}, system p_{T} and system invariant mass. The remaining distributions are provided in Appendix D (Figures D.1 - D.6).

6.1.3 Statistical uncertainties and correlations

Statistical uncertainties in the data are propagated through the unfolding using the bootstrap technique with 10,000 replicas of the data histogram. In this technique, statistical variations in the data are simulated by assigning each data event a random weight drawn from a Poisson distribution with a mean of one, instead of the nominal weight of one. This procedure is repeated to generate N_{repl} bootstrap replicas of the data, each of which is unfolded independently. The spread of the unfolded replicas provides an estimate of the statistical uncertainty and the bin-to-bin correlations. Moreover, the bootstrapping method enables the determination of the statistical covariance and correlation between bins of different variables, thereby allowing for the proper combination of multiple unfolded distributions and facilitating a global fit, as described in Section 6.6.

The covariance between two unfolded bins is computed as the average product of deviations from their mean values across all replicas, while the diagonal elements yield the statistical uncertainties. Normalising the covariance defines the correlation matrix. As the method preserves statistical correlations between different observables, bootstrapping enables a consistent propagation of statistical uncertainties and correlations, facilitating combined fits across multiple unfolded distributions.

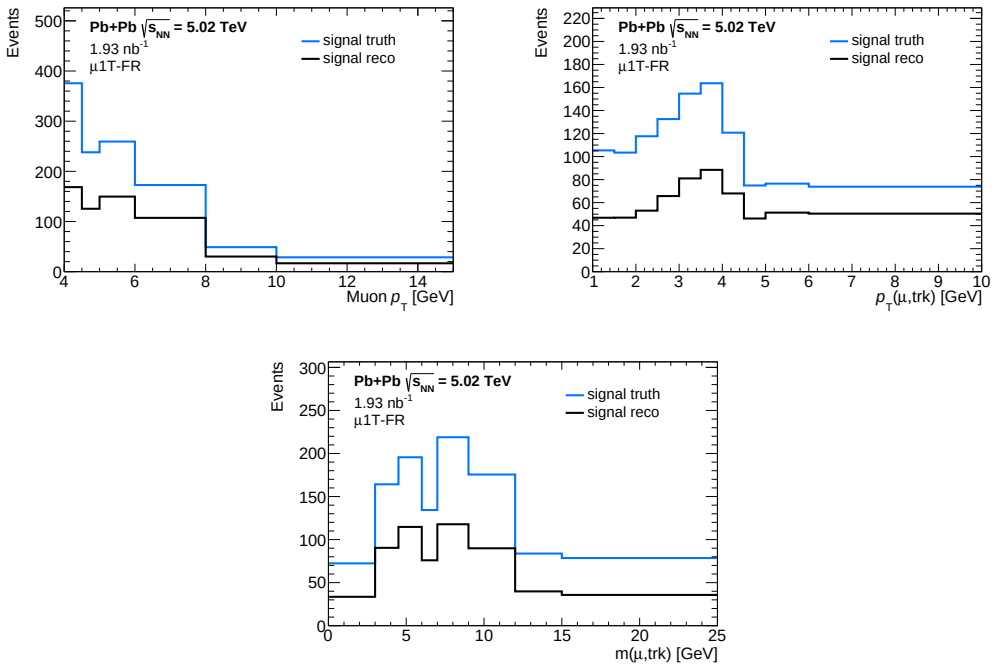

Figure 6.1.1: Signal $\gamma\gamma \to \tau\tau$ histograms at reconstruction-level (black) and truth-level (blue) scaled to the luminosity corresponding to 2015+2018 data in μ1T-FR: (top-left) muon transverse momentum, (top-right) muon–track transverse momentum and (below) muon–track invariant mass.

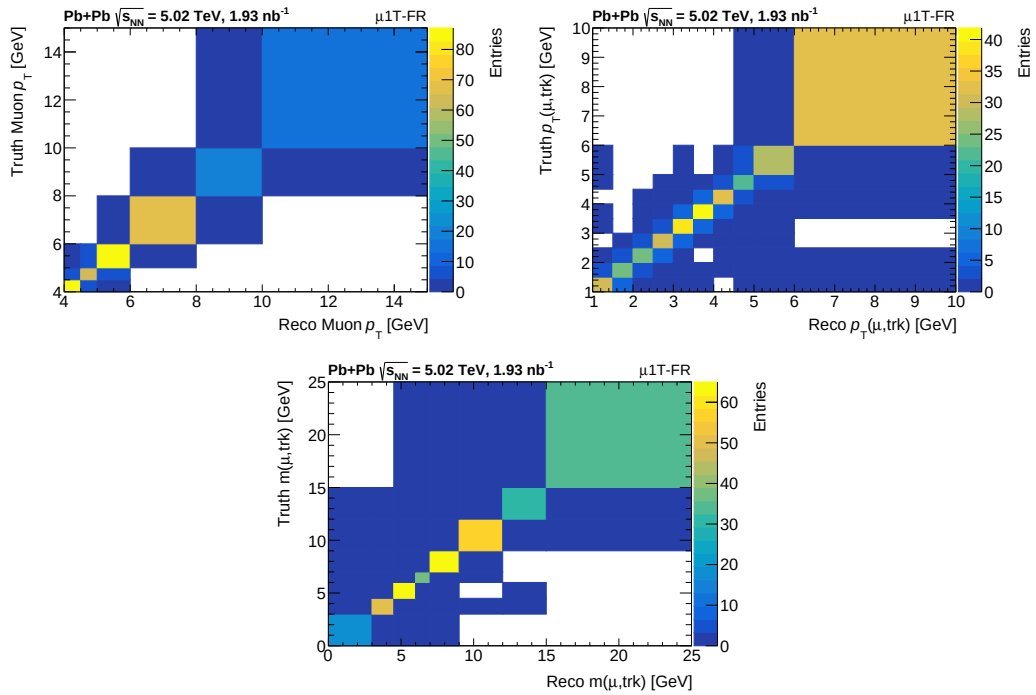

Figure 6.1.2: Response matrices in μ1T-FR: (top-left) muon transverse momentum, (top-right) muon–track transverse momentum and (below) muon–track invariant mass.

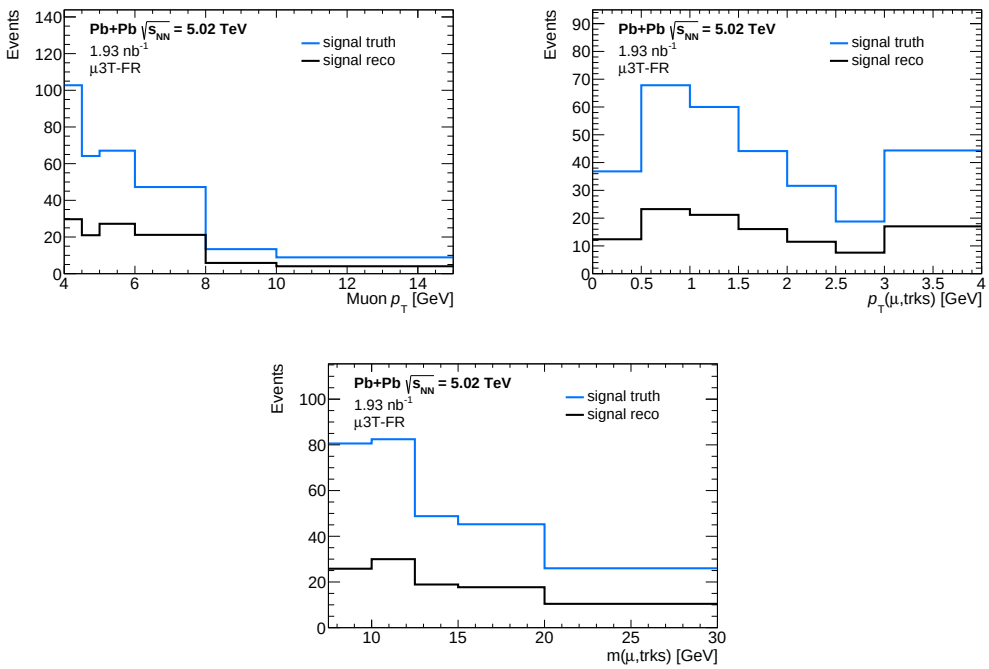

Figure 6.1.3: Signal $\gamma\gamma \to \tau\tau$ histograms at reconstruction-level (black) and truth-level (blue) scaled to the luminosity corresponding to 2015+2018 data in μ3T-FR: (top-left) muon transverse momentum, (top-right) muon–3–track transverse momentum and (below) muon–3–track invariant mass.

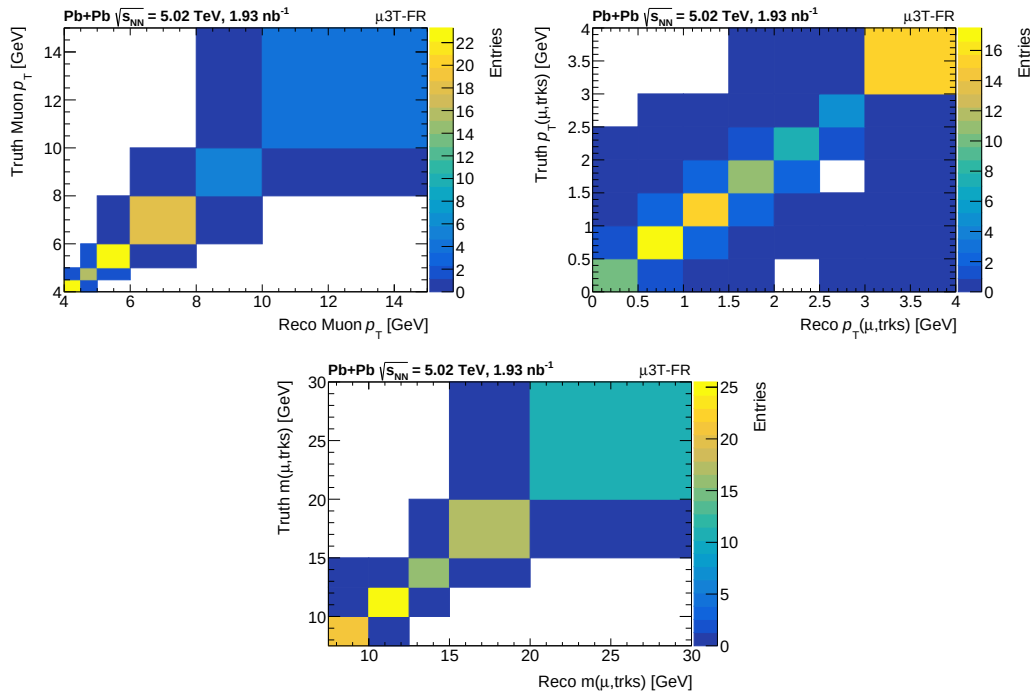

Figure 6.1.4: Response matrices in μ3T-FR: (top-left) muon transverse momentum, (top-right) muon–3–track transverse momentum and (below) muon–3–track invariant mass.

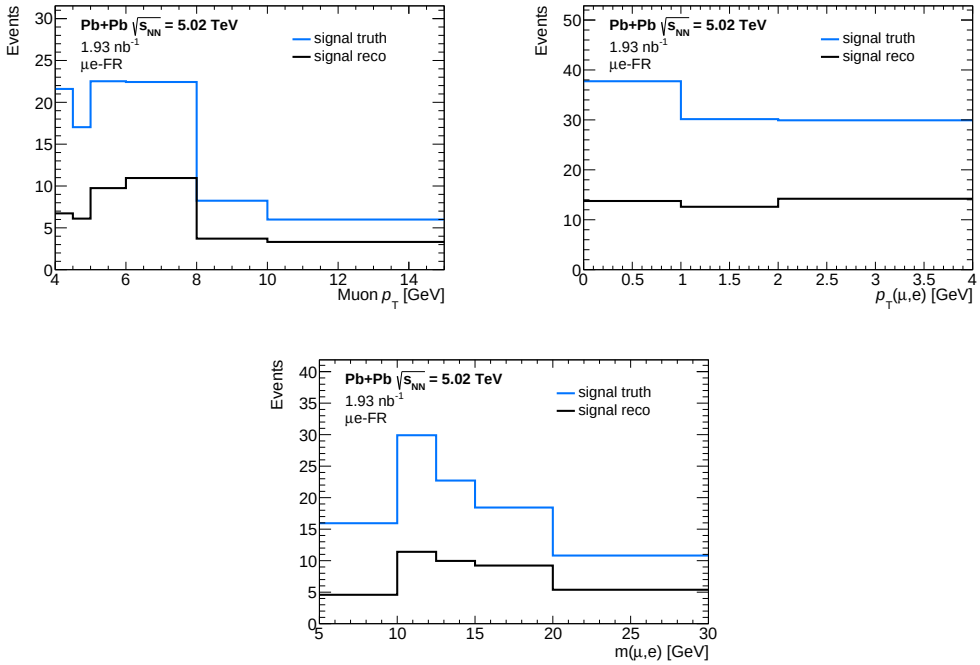

Figure 6.1.5: Signal $\gamma\gamma \to \tau\tau$ histograms at reconstruction-level (black) and truth-level (blue) scaled to the luminosity corresponding to 2015+2018 data in μe-FR: (top-left) muon transverse momentum, (top-right) muon–electron transverse momentum and (below) muon–electron invariant mass.

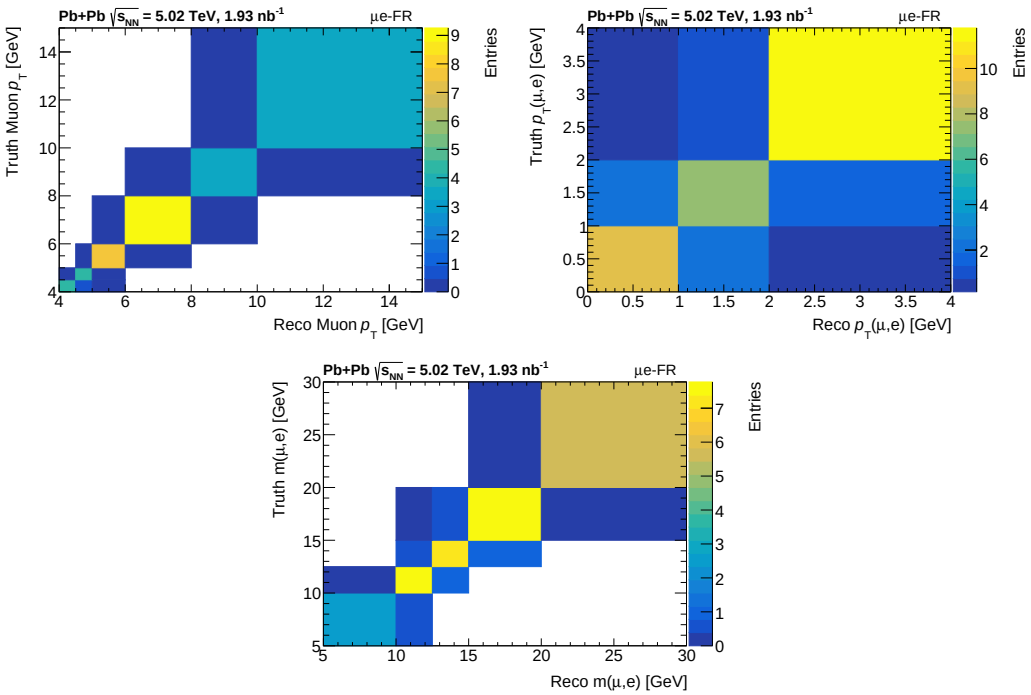

Figure 6.1.6: Response matrices in μe-FR: (top-left) muon transverse momentum, (top-right) muon–electron transverse momentum and (below) muon–electron invariant mass.

The correlation and covariance matrices, obtained using the bootstrap technique in μ1T-FR are shown in Figure 6.1.7. The diagonal elements of the covariance matrix define the statistical uncertainties on the unfolded distributions. They are used under the assumption of a Gaussian likelihood, verified by studying the distributions of unfolded event yields over all bootstrap replicas for each bin. These distributions were well described by Gaussian fits, particularly for bins containing more than approximately 10–20 unfolded events. Statistical uncertainties on the background and signal MC samples used for the unfolding inputs are treated as systematic uncertainties and are propagated separately.

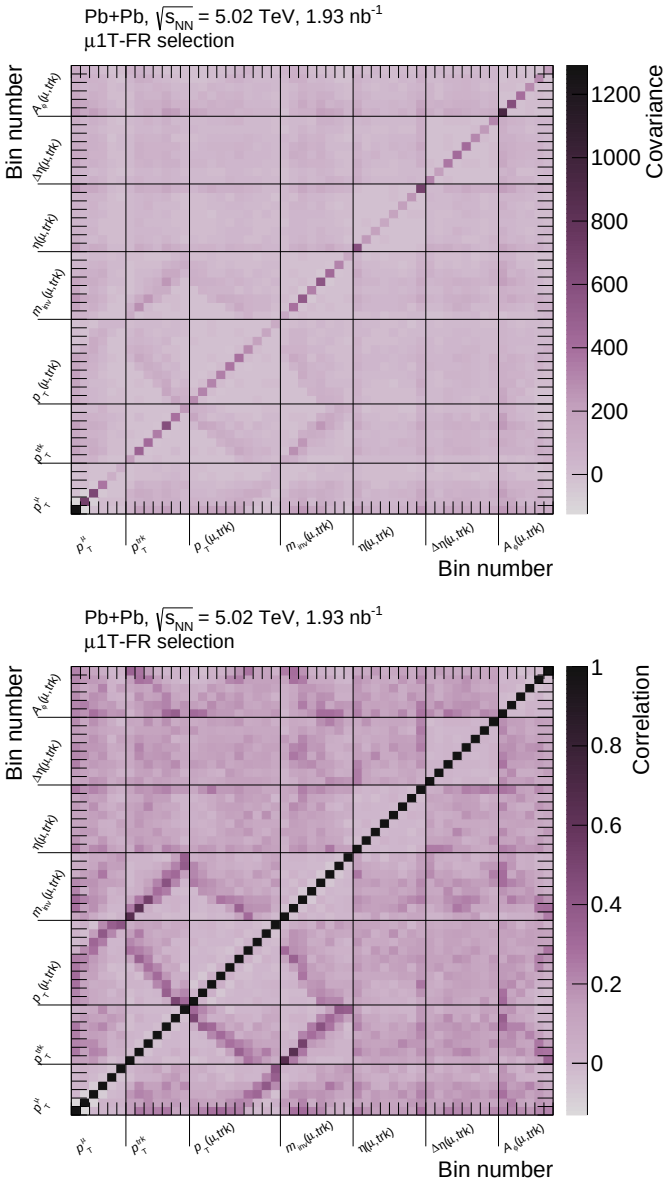

Figure 6.1.7: Covariance (top) and correlation (bottom) between unfolded bins in the 2015+2018 dataset, in μ1T-FR. Figure adapted from [122].

6.2 Systematic uncertainties

The systematic uncertainties affecting the measurement are described in the following section. The Author's work includes the implementation of all systematic uncertainties into the analysis framework and propagation of them through the analysis chain in order to provide inputs for the unfolding and for the extraction of the tau electromagnetic moments, as described in Section 6.5 and 6.6.

Muon systematic uncertainties

Uncertainties related to muon performance arise from trigger, reconstruction and identification efficiencies, as well as from momentum scale and resolution corrections. The uncertainties associated with the trigger and reconstruction/identification efficiencies are derived from the dedicated analyses described in Sections 5.4 and 5.5.1, respectively, and are propagated via their corresponding SFs. For each source, systematic variations are combined into a single uncertainty component, while the statistical uncertainties of the SFs are treated independently. Momentum scale and resolution corrections are applied to align the simulated muon kinematics with those observed in data and to reduce the residual charge-dependent bias between μ^+ and μ^- [91].

Track reconstruction efficiency

The uncertainty associated with the track reconstruction efficiency is evaluated following the procedure in Ref. [35]. The efficiency is measured for all truth-level charged pions, electrons, and muons from τ decays in the signal MC sample, and systematic variations are assessed using alternative MC samples with modified ATLAS detector geometries and GEANT 4 physics models [121]. These variations probe the effects of additional detector material and alternative physics lists[1] on the tracking performance. The resulting variations in tracking efficiency typically range from 5–10% at very low transverse momenta (0.1–0.2 GeV) and decrease to about 1–2% at higher p_{T}. The systematic impact is propagated to the analysis by randomly removing tracks in the nominal MC sample according to the measured efficiency variations, binned in p_{T} and $|\eta|$, which reduces the sensitivity to statistical fluctuations in the simulation.

[1] A *physics list* provides a predefined configuration of physics models used in the GEANT 4 detector simulation. It specifies the set of electromagnetic, hadronic, and decay processes, along with their corresponding models and parameters, that govern how particles interact with the detector material.

Electron and photon systematic uncertainties

Uncertainties related to electron performance arise from reconstruction and identification efficiencies, as well as from energy scale and resolution corrections. The efficiency SFs and their uncertainties are taken from the Light-by-Light scattering measurement [47]. The calibration corrections for electrons and photons are applied following the ATLAS recommendations [89], optimised for $\mu = 0$. Since the analysis primarily relies on muon-based selections with limited sensitivity to electron/photon calibrations, there is a single nuisance parameter utilised for energy scale and resolution of both electrons and photons.

Topo-cluster reconstruction and calibration

The uncertainty on the topo-cluster reconstruction efficiency corresponds to a conservative relative uncertainty of 2% (see Section 5.5.4). This uncertainty is propagated by randomly removing 2% of topo-clusters in the MC samples, with the resulting yield variations symmetrised around the nominal values. Additional uncertainties in the topo-cluster energy calibration are evaluated by applying p_{T}-dependent shifts to account for small data-to-MC discrepancies.

Photonuclear background estimate

The photonuclear background is discussed in detail in Section 5.7.3. There are two sources of related uncertainties considered: the statistical uncertainty arising from the limited number of data events in the photonuclear background normalisation region ($4 \leq n_{\mathrm{unmatched}}^{\mathrm{topoclusters}} \leq 8$) as well as the systematic uncertainty, which is estimated by applying variations in selections for the photonuclear background templates. As a systematic variation in the μ2T-CR, the same charge of the leading track and the muon is allowed. In the μ4T-CR systematic variation template, only events with non-zero net electric charge are allowed. Other selection criteria remain the same as for the nominal templates.

ZDC selection

As discussed in Section 5.3.6, there are three sources of systematic uncertainties affecting the 0n0n selection: uncertainty arising from the ZDC inefficiency, the choice of the fitting function for the 0n0n weights and the choice of the associated binning scheme.

The efficiency of the ZDC was estimated to be over 99% [125]. The corresponding uncertainty is derived using 0n0n fractions and varying them by $\pm 1\%$.

The systematic uncertainty associated with the choice of fit function for the 0n0n weights is evaluated by repeating the fit using an alternative function and taking the

difference in the resulting weights as the uncertainty. In addition, the impact of the binning choice is assessed by repeating the fit with alternative binning configuration and treating the variation in the extracted fractions as a systematic uncertainty.

Photon flux modelling

The uncertainty on the photon flux modelling is evaluated using the SuperChic3 generator, which employs a Woods–Saxon parametrisation of the nuclear charge density (see Section 2.4.1). Variations of the proton and neutron radius ($R_{p,n}$) and skin thickness ($a_{p,n}$) within their experimental uncertainties [55, 139, 140] are propagated to the predicted $\gamma\gamma \to \mu\mu$ cross-section to estimate the photon flux uncertainty. The resulting deviations, symmetrised between the largest up and down variations, are computed as functions of $m_{\mu\mu}$ and $|y_{\mu\mu}|$ and are applied to the $\gamma\gamma \to \mu\mu$ and $\gamma\gamma \to \tau\tau$ events. The uncertainty increases with both variables and reaches about 0.5% in the kinematic region most relevant for this analysis.

In addition, a flat 2.5% uncertainty is assigned to account for the theoretical modelling of the survival factor, reflecting conservative assumptions relative to recent studies [141].

Global Residual Flux Factor

In order to improve the modelling of the photon flux, a data-driven Global Residual Flux Factor (GRFF) is derived using the 2μ-CR, as described in Section 5.7.2. It is applied to signal and dimuon background MC samples with an associated uncertainty. The calculated GRFF value is $0.9351^{+0.0349}_{-0.0332}$.

Modelling of τ-lepton decays

The uncertainties on the modelling of the τ-lepton decays are estimated using an alternative signal sample, in which the modelling of the τ-lepton decays is handled by Pythia 8 instead of Tauola (see Section 5.2).

Spin correlation correction

The spin correlation corrections are only applied in the μ1T-FR, as described in Section 5.2.3. The related uncertainty is defined as the size of the correction factor in each bin (i.e. 100%), at both reconstruction and truth-level.

Luminosity

The luminosity uncertainty provided by the ATLAS recommendations for the combined 2015+2018 dataset is 1.5%. It takes into account the correlations of the luminosity uncertainties between the 2015 and 2018 datasets.

Unfolding systematics

There are three main sources of uncertainties related to the unfolding procedure described in Section 6.1:

- Potential biases in the unfolding method, arising from the choice of the number of iterations in the IBU method, the binning scheme, or discrepancies between the shapes of data and the prediction. These biases are covered by the *data closure test*, which is used to verify whether the unfolding can correctly reproduce truth-level distributions when the MC simulation is reweighted to resemble data;
- Statistical uncertainties on the background estimates, evaluated through pseudo-experiments on the background templates;
- Statistical uncertainties on the response matrix.

The pseudo-experiments referred to in this section follow a similar concept to the bootstrapping method described in Section 6.1.3 but the fluctuations are applied to the bin contents using Gaussian variations based on their statistical uncertainties, rather than to individual event weights drawn from a Poisson distribution. This method can be used to propagate statistical uncertainties through the unfolding where bootstrapping is considered to be too extensive.

The resulting unfolding systematic uncertainties are generally at the level of a few percent in the μ1T-FR and slightly larger in the μ3T-FR and μe-FR due to limited statistics. In the unfolding procedure, they are all treated as systematic uncertainties.

6.2.1 Impact on unfolded distributions

Each source of systematic uncertainty can affect the background, reconstructed signal, or truth-level signal distributions used in the unfolding. The corresponding varied histograms (including the response matrix) are employed consistently in the unfolding procedure. The impact of each uncertainty per unfolded bin is quantified as the difference between the varied and nominal results, and the total systematic uncertainty is obtained by summing the individual contributions in quadrature, separately for up and down variations.

The impact of relative systematic uncertainties on the unfolded muon p_{T} distributions in the three FRs is presented in Figure 6.2.1. For clarity, systematic uncertainties are grouped into the following categories:

- **Muon:** uncertainties related to muon reconstruction, identification and calibration;

- **Muon trigger:** muon trigger SFs uncertainties;
- **Egamma:** uncertainties related to electron and photon reconstruction, identification, energy scale and resolution uncertainties;
- **Track:** uncertainties related to track reconstruction efficiency;
- **Modelling:** including photon flux, 0n0n systematics, GRFF, spin correlation and tau decay modelling uncertainties;
- **Other:** including topo-cluster, luminosity, background and unfolding uncertainties.

To simplify the extraction of a_τ and d_τ from the unfolded cross sections, all systematic variations are symmetrised. The leading contributions to the total systematic uncertainty originate from the trigger and modelling components.

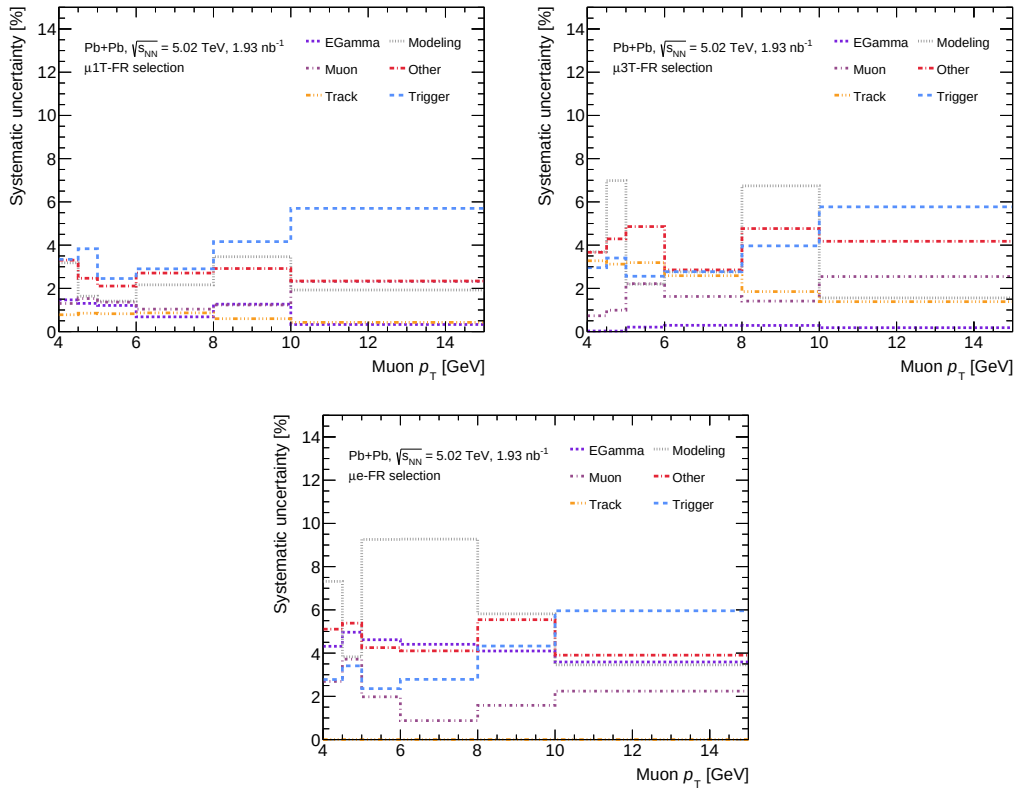

Figure 6.2.1: Impact of the grouped systematic uncertainties on the unfolded muon p_{T} distributions in (top-left) μ1T-FR, (top-right) μ3T-FR and (below) μe-FR. Figure adapted from Ref. [122].

6.3 Unfolded distributions

Unfolded distribution of the muon p_{T} in the three FRs are shown in Figure 6.3.1. The error bands represent the statistical and systematic uncertainties. Statistical errors are computed as the square roots of the diagonal elements of the corresponding covariance matrix obtained through the bootstrapping procedure. The unfolded results are compared to the nominal signal prediction, simulated using STARLIGHT interfaced with PYTHIA 8 and TAUOLA, with the photon flux reweighted to SUPERCHIC 3 (see Section 5.2). Within the total uncertainty, good agreement is observed.

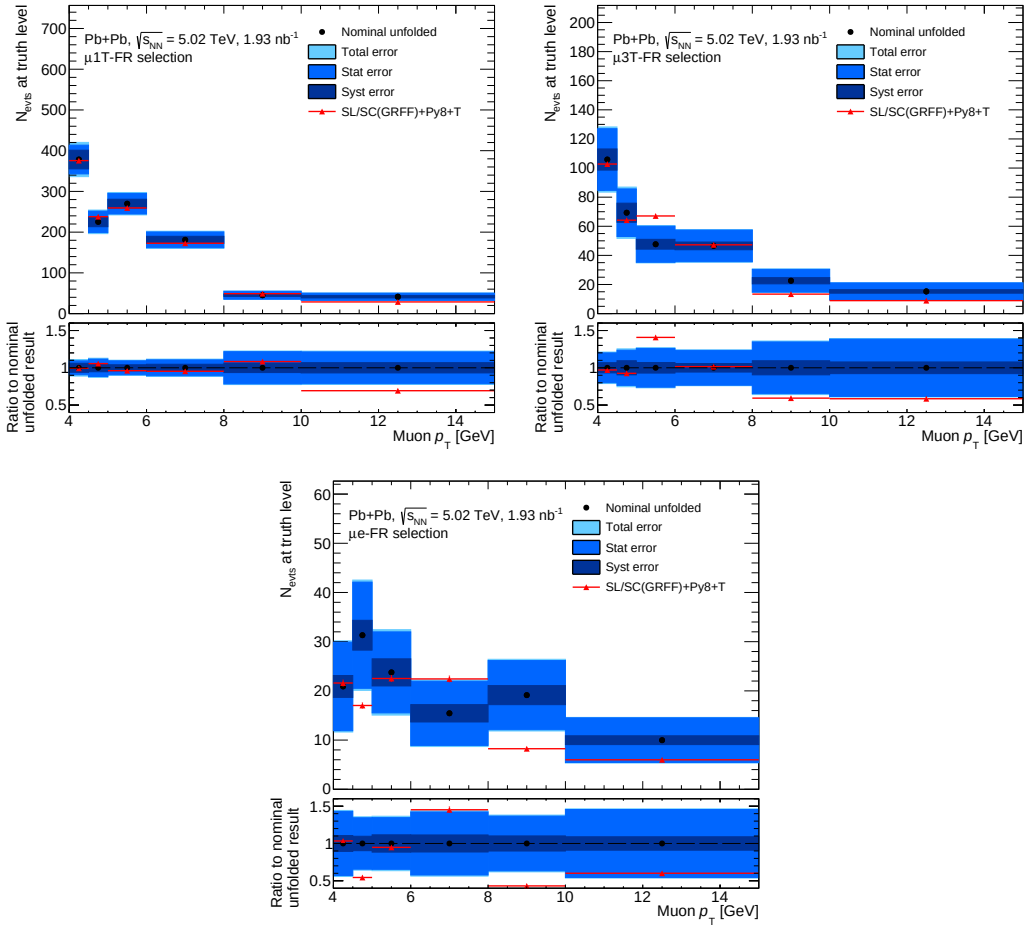

Figure 6.3.1: Number of unfolded events as a function of the muon p_{T} in (top-left) μ1T-FR, (top-right) μ3T-FR and (below) μe-FR. Figure adapted from Ref. [122].

6.4 Differential cross section results

The differential cross sections at particle level for the $\gamma\gamma \to \tau\tau$ process are calculated for seven unfolded variables in each FR. The cross section as a function of a variable v is estimated by:

$$\frac{d\sigma}{dv} = \frac{1}{\mathcal{L}} \cdot \frac{N_i}{\Delta v_i}, \tag{6.4.1}$$

where $\mathcal{L}$ denotes the central value of the 2015+2018 luminosity, N_i is the number of unfolded events in bin i and Δv_i is the width of the corresponding bin.

The measured differential cross sections as a function of muon p_{T}, system p_{T} and system invariant mass in μ1T-FR, μ3T-FR and μe-FR are presented in Figures 6.4.1, 6.4.2 and 6.4.3, respectively. The remaining cross sections are shown in Appendix E (Figures E.1 - E.3). The statistical uncertainties are shown as black error bars and the systematic uncertainties are denoted with grey hatched bands. The measured cross sections are compared to several SM $\gamma\gamma \to \tau\tau$ predictions:

- **SL + Py8 + T**: MC sample simulated with StarLight and interfaced to Pythia 8 for FRS from τ-leptons and to Tauola for modelling of the τ-lepton decays and FSR from the charged decay products;
- **SL/SC + Py8 + T**: similar to the above prediction but with the photon flux reweighed to SuperChic;
- **SL/SC(GRFF) + Py8 + T**: similar to the above prediction but with an additional photon flux normalisation factor (GRFF) applied to the truth signal prediction (see Section 5.7.2);
- **SL/SC(GRFF) + Py8 + T + S-corr**: similar to the above prediction but with an additional correction for spin correlations applied in μ1T-FR (see Section 5.2.3). This sample provides the nominal prediction;
- **SL/SC(GRFF) + Py8**: MC sample simulated with StarLight with the photon flux reweighted to SuperChic and the GRFF correction applied. The sample is interfaced to Pythia 8 for FRS from τ-leptons. The modelling of the τ-lepton decay and FSR from the charged decay products is also simulated with Pythia 8, instead of Tauola.

There is reasonable agreement between the measured differential cross sections and the SM predictions. The measurement is limited by statistical uncertainties.

Reweighting the photon flux to SuperChic leads to a significantly better agreement with the measured data for most bins compared to the prediction without reweighting, i.e., using the StarLight flux, SL + Py8 + T. Overall, the choice of

photon flux has the largest impact on the predictions, typically affecting the results at the 10–30% level.

The variation from the τ-lepton decay modelling by Pythia 8 and Tauola is considerably smaller than the variation induced by the choice of photon flux. It affects the result at the sub-percent level.

Applying the residual photon flux normalisation factor (GRFF) improves the agreement between the prediction and the measured data for most bins by a few percent.

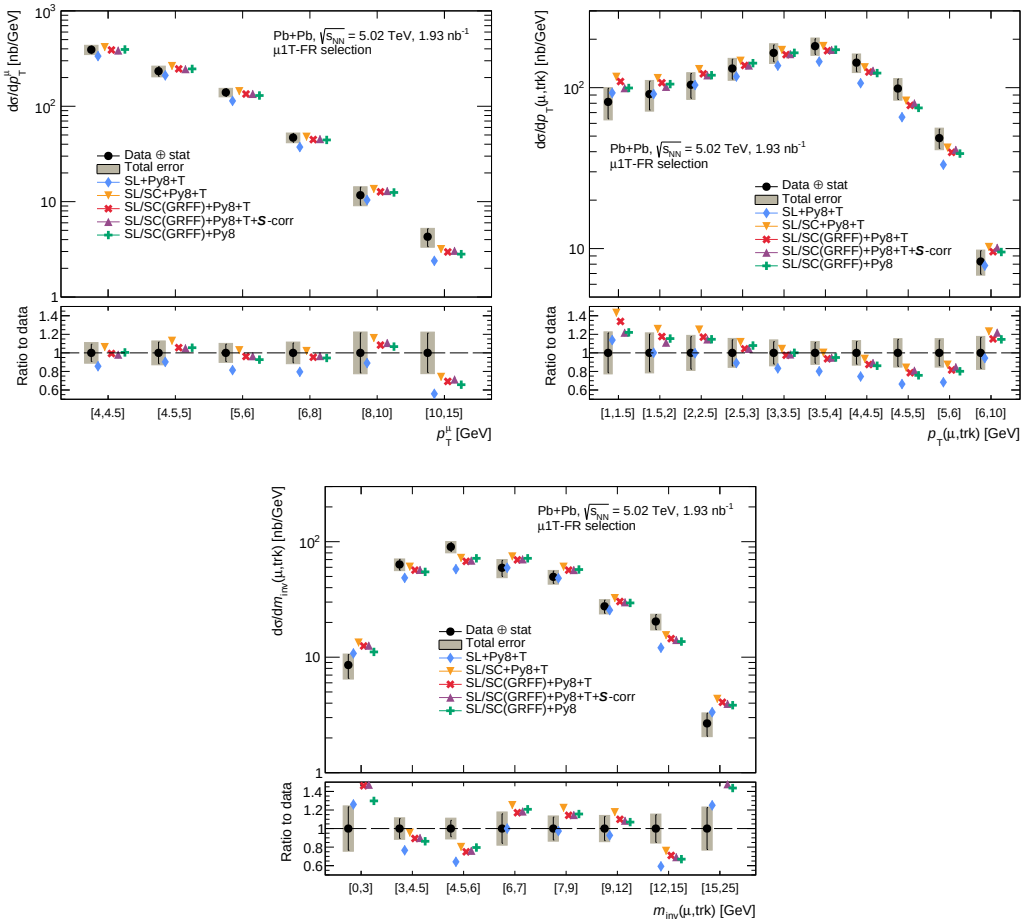

Figure 6.4.1: Differential fiducial cross sections at particle-level in the μ1T-FR: (top-left) muon transverse momentum, (top-right) muon–track transverse momentum and (bottom) muon–track invariant mass. Statistical uncertainties on the unfolded data are shown as black bars and the systematic uncertainties are shown as grey hatched bands. The cross sections are compared to predictions described in text. Figures adapted from Ref. [122].

A small mis-modelling is visible for example in the ratio panel of the muon–track system p_{T} distribution: at low p_{T} the SL/SC(GRFF) + Py8 + T prediction tends to overestimate the data, while at high p_{T} it underestimates it. This discrepancy is reduced by applying spin correlation corrections. The fully corrected prediction (SL/SC(GRFF) + Py8 + T + S-corr) generally lies closer to the measured data and agrees within the experimental uncertainties.

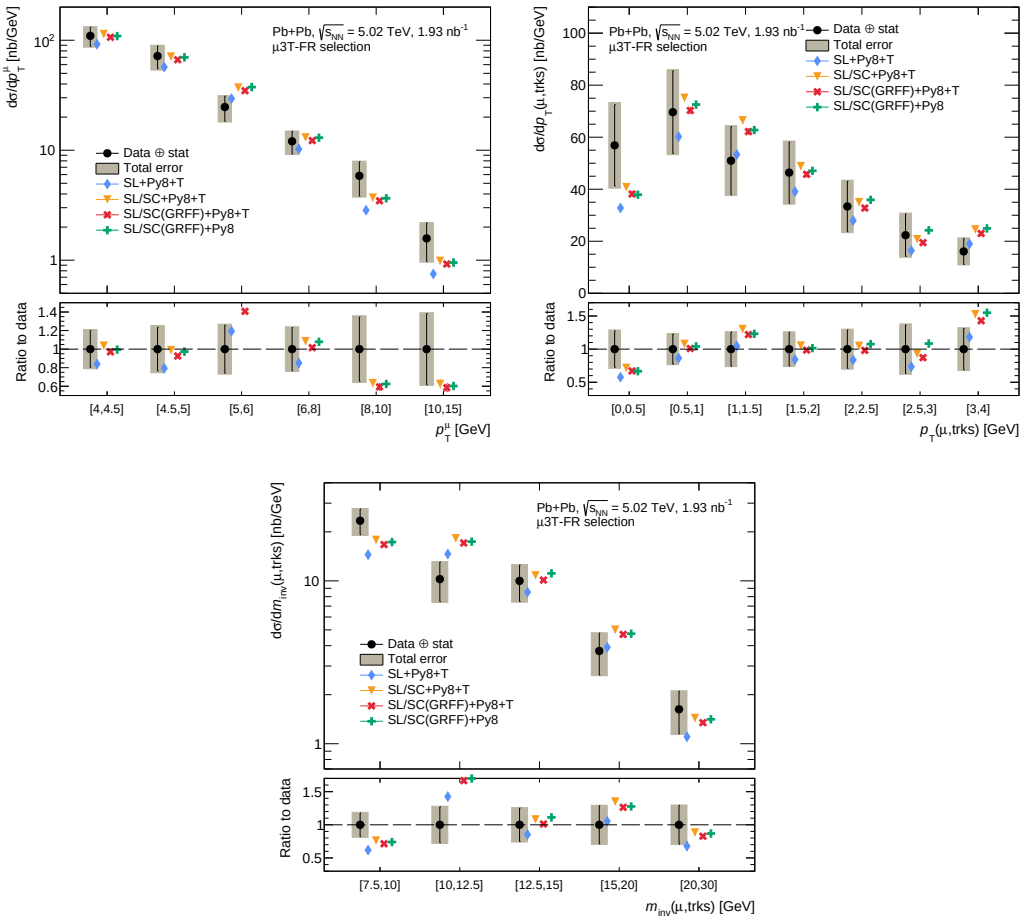

Figure 6.4.2: Differential fiducial cross sections at particle-level in the μ3T-FR: (top-left) muon transverse momentum, (top-right) muon–3–track transverse momentum and (bottom) muon–3–track invariant mass. Statistical uncertainties on the unfolded data are shown as black bars and the systematic uncertainties are shown as grey hatched bands. The cross sections are compared to predictions described in text. Figures adapted from Ref. [122].

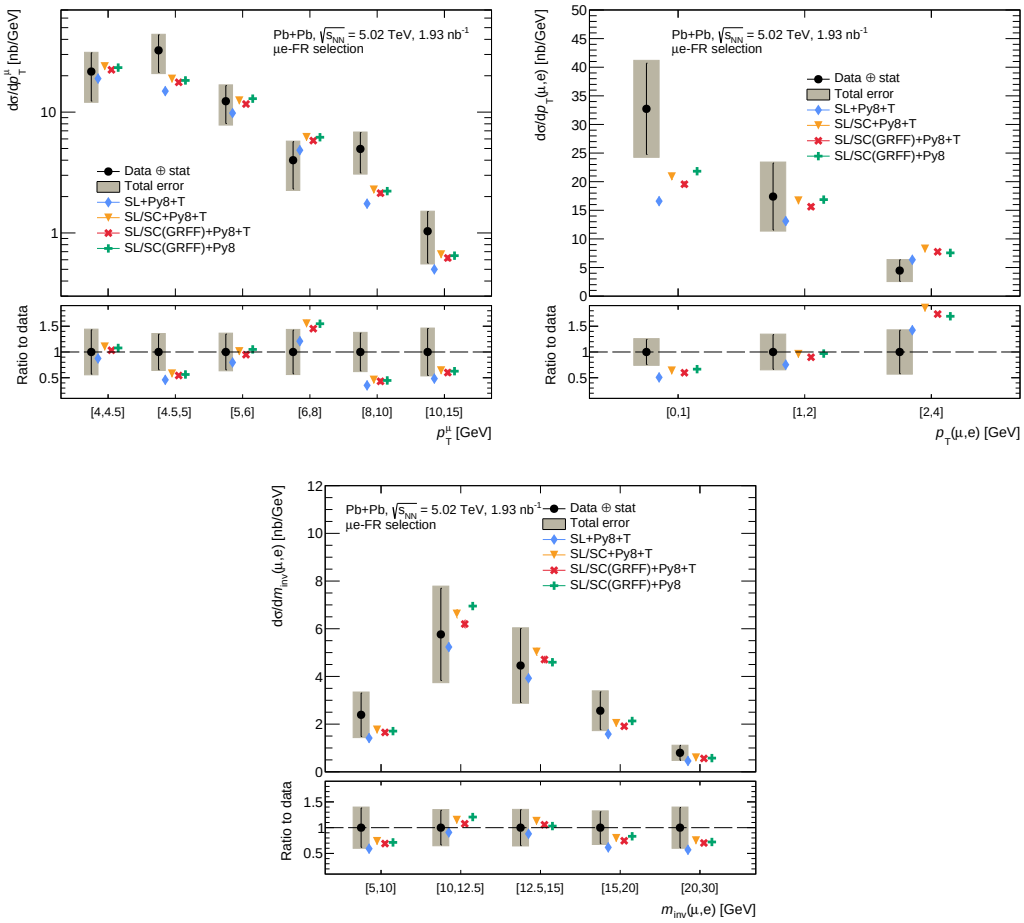

Figure 6.4.3: Differential fiducial cross sections at particle-level in the μe-FR: (top-left) muon transverse momentum, (top-right) muon–electron transverse momentum and (bottom) muon–electron invariant mass. Statistical uncertainties on the unfolded data are shown as black bars and the systematic uncertainties are shown as grey hatched bands. The cross sections are compared to predictions described in text. Figures adapted from Ref. [122].

6.5 Fitting tau-lepton electromagnetic moments using reconstruction-level information

Before obtaining constraints on a_τ and d_τ using truth-level information (Section 6.6), values of a_τ and d_τ are extracted using detector-level information in a profile likelihood fit implemented in TRExFitter. Fits are performed independently, assuming the tree-level SM value of d_τ in the a_τ fits and the tree-level SM value of a_τ in the d_τ fits. For a single variable fit, sensitivity is maximised using the muon p_{T} distribution, which is consistent with previous studies [35]. Therefore, at reconstruction-level, only this variable is used for fitting. The likelihood function incorporates all

measurement bins and fit parameters, with the Parameter of Interest (POI), β (a_τ or d_τ), and systematic uncertainties as nuisance parameters, θ:

$$L(n|\beta,\theta) = \prod_{i\in\text{bins}} P(n_i|\beta(\theta)) \times \prod_{j\in\text{NPs}} G(\theta_j), \tag{6.5.1}$$

where P is a Poisson term for the observed data events n_i in each bin, and G represents Gaussian priors for systematics. Templates for non-zero a_τ and d_τ values are generated via an analytical event-level reweighting of the signal MC (see Section 5.2.2), producing 76 independent histograms per POI, which serve as inputs to the fit. Fits are performed in six bins of muon p_T in the defined signal regions, and results are reported both per region and combined.

Distributions of the muon p_T in μ1T-SR are presented in Figure 6.5.1. The left panel compares the distribution obtained for the nominal value $a_\tau = 0$ with several representative non-zero variations, while the right panel shows the corresponding distributions for the nominal value $d_\tau = 0$ together with selected non-zero variations.

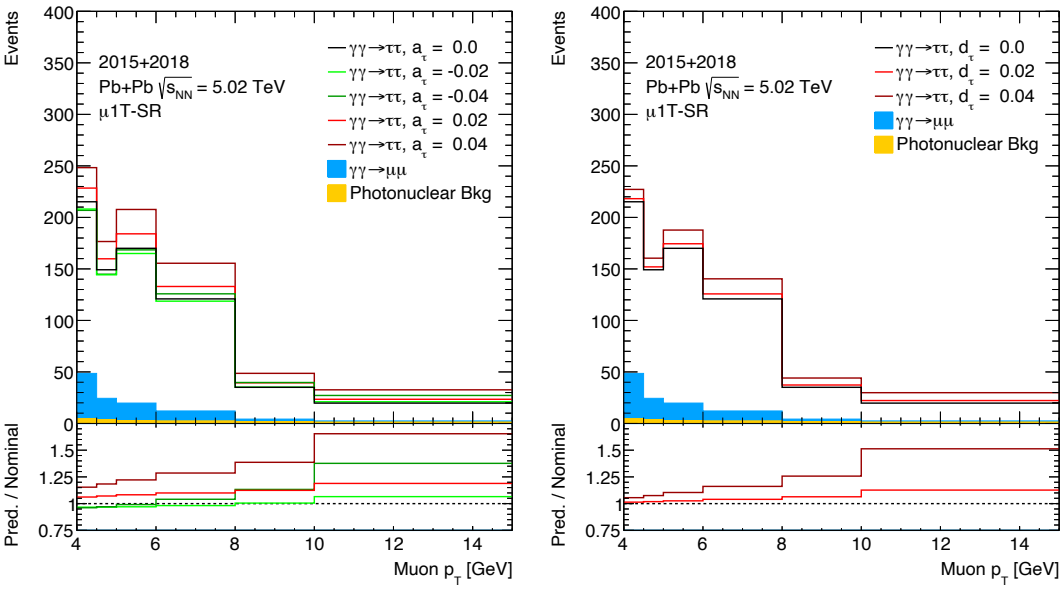

Figure 6.5.1: Distributions of muon p_T in μ1T-SR, including selected variations on a_τ (left) and d_τ (right). The variations are stacked on top of the background and the lower panel shows the ratio of the varied distributions with respect to a_τ and d_τ of zero.

The limits on a_τ obtained using reconstruction-level information were cross-checked with the previous ATLAS measurement [35] and the results are compatible. Both a_τ and d_τ limits were additionally cross-checked with fits based on truth-level muon p_{T} and they are very consistent. After completing these cross-checks, the analysis proceeds to fits based on truth-level information, where higher sensitivity is achieved through the combination of all 21 variables, corresponding to seven observables in each FR. These results are described in the following section.

6.6 Fitting tau-lepton electromagnetic moments using truth-level information

An unconventional statistical procedure is used to extract limits on the τ lepton electromagnetic dipole moments from the measured fiducial cross sections. Unlike the standard ATLAS likelihood approach, which models uncorrelated Poisson counts in each bin, this analysis accounts for correlations between measurements by modelling the data with a multivariate Gaussian likelihood:

$$\mathcal{L}\left(\vec{\mu},\vec{b}\right) = \exp\left[-\frac{1}{2}\sum_{i,k=1}^{N_{\mathrm{bins}}}\Delta_i\left(V^{-1}\right)_{ik}\Delta_k\right]\prod_{j=1}^{N_{\mathrm{syst}}}e^{-\frac{b_j^2}{2}}, \tag{6.6.1}$$

where $\vec{\mu} = \{\mu_1,\ldots,\mu_{\mathrm{N_{POI}}}\}$ is the set of physical parameters of interest (POIs), N_{syst} is the number of systematic uncertainties and $\vec{b} = \{b_1,\ldots,b_{N_{\mathrm{syst}}}\}$ are the corresponding nuisance parameters. The matrix V^{-1} is the inverse of the statistical covariance matrix of the measured cross sections, obtained using a bootstrap method, as discussed in Section 6.1.3.

The quantities Δ_i represent the difference between the measured and predicted cross sections in the i^{th} bin and are defined as:

$$\Delta_i = n_i\left(1-\sum_{j=1}^{N_{\mathrm{syst}}}\gamma_{ij}b_j\right) - T_i\left(\vec{\mu}\right)\left(1-\sum_{m=1}^{N_{\mathrm{syst}}}\tilde{\gamma}_{im}b_m\right). \tag{6.6.2}$$

In the equation above, $T_i(\vec{\mu})$ denotes the predicted fiducial cross section in bin i for a given set of POIs. The coefficients γ_{ij} quantify the relative change of the measured cross section in bin i induced by the j^{th} experimental systematic uncertainty, while $\tilde{\gamma}_{im}$ represent the corresponding relative variations of the theoretical or modelling predictions. The same set of nuisance parameters b_j is used to encode correlated systematic effects across all bins. By construction, $\tilde{\gamma}_{im} = 0$ for systematics that do not affect the modelling uncertainty.

This likelihood formulation allows for correlations of systematic uncertainties between bins through the nuisance parameters, while uncorrelated systematic effects

are incorporated as diagonal contributions to the covariance matrix V. In this measurement, statistical uncertainties from background estimates, response matrices, and model predictions $T_i(\vec{\mu})$ are treated as uncorrelated.

The likelihood is maximised (equivalently, $-2\log\mathcal{L}$ minimised) using a `Minuit` routine [142], yielding the best-fit parameters. Confidence intervals are derived from the $\Delta\chi^2$ profile, where 68% and 95% confidence levels correspond to $\Delta\chi^2 = 1$ and 3.92, respectively.

Similarly to the detector-level fits, templates for non-zero a_τ and d_τ values are generated via analytical event-level reweighting of the signal MC, as described in Section 5.2.2. There are 76 independent histograms per parameter, serving as an input to the fit.

The parameters of interests in the fit are $F_2(0)$ and $F_3(0)$, which are dimensionless. The details about the parametrisation are included in Section 1.3. The form factor $F_2(0)$ is numerically equal a_τ. The form factor $F_3(0) = d_\tau \frac{2m_\tau}{e}$ and d_τ is expressed in units of electric charge times centimetre [e·cm]. Consequently, d_τ limits are placed in the range of $10^{-16} - 10^{-17}$ [e·cm]. In order to avoid numerical issues in the fitting procedure, $F_3(0)$ is fitted and then converted to d_τ using the following relation:

$$d_\tau = 5.5925 \times 10^{-15} F_3(0) \quad [\mathrm{e}\cdot\mathrm{cm}]. \tag{6.6.3}$$

The results presented here are preliminary and therefore *blinded*, i.e. the tree-level SM prediction of a_τ and d_τ equal to zero are used instead of measured fiducial cross sections ($T_i(a_\tau = 0; d_\tau = 0)$ in Equation 6.6.2). The statistical and systematic uncertainties are taken from the measurement (V, γ_{im} and $\tilde{\gamma}_{im}$). In this setup, the best-fit values and nuisance parameters are equal to zero. As a result, the constraints on a_τ and d_τ obtained in this procedure refer to *expected* limits.

The $\Delta\chi^2$ curves from fits to $F_2(0)$ and $F_3(0)$ form factors are presented in Figure 6.6.1. In these fits, combined information from 7 fiducial cross sections in each FR is used. The likelihood curves obtained from the global fits, which use all 21 fiducial cross sections is also shown.

The $\Delta\chi^2$ curves for $F_2(0)$ have a parabolic shape with a minimum at zero. They are shifted towards the negative values of $F_2(0)$. This is a consequence of the $\gamma\gamma \to \tau\tau$ cross section dependence on a_τ, which has a minimum at a negative value around -0.002 (see Figure 5.2.2). The likelihood curves for $F_3(0)$ have a similar, parabolic shape with a minimum at zero. They are symmetric with respect to zero, which is expected, as the measurement is only sensitive to the magnitude of $F_3(0)$.

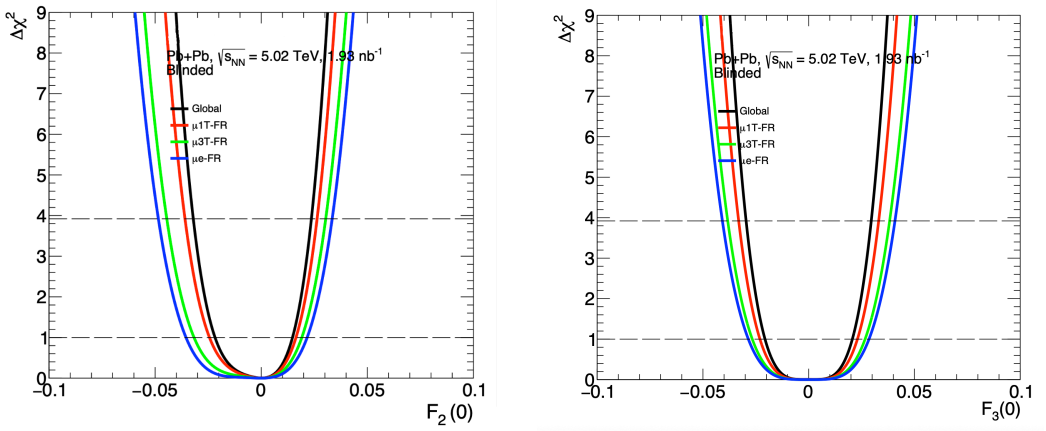

Figure 6.6.1: $\Delta\chi^2$ curves from the fits to (left) $F_2(0)$ and (right) $F_3(0)$ form factors, related to a_τ and d_τ, respectively. The fits are performed to 7 fiducial cross sections in μ1T-FR (red curve), μ3T-FR (green curve) and μe-FR (blue curve). The likelihood curve obtained from the global fit, combining information from all 21 fiducial cross sections, is displayed in black. The results are preliminary and thus blinded, i.e. a_τ and d_τ values are set to 0. Figure adapted from Ref. [122].

6.6.1 Constraints on tau electromagnetic moments

From the likelihood curves, the expected 68% and 95% confidence level intervals (CIs) are derived. The resulting expected limits on a_τ and d_τ are compared with the most recent experimental constraints, as shown in Figures 6.6.2 and 6.6.3. The SM prediction is indicated by the dashed vertical line.

For both a_τ and d_τ, the limits exhibit a clear improvement with increasing statistical power in the corresponding FR. The intervals are the widest in the μe-FR, where the available statistics are the lowest and become progressively narrower in regions with higher event yields, reaching their tightest constraints in the global fits that exploit the full available dataset.

For a_τ, the expected limits obtained from the global fits improve with respect to the previous ATLAS [35] and CMS [106] measurements in Pb+Pb collisions, both of which are based on reconstruction-level analyses of the 2018 dataset. The results presented here also surpass the precision of the DELPHI [36] measurement obtained in e^+e^- collisions. In contrast, the CMS result derived from $p+p$ collision data [107] remains the most stringent constraint to date, exceeding the sensitivity of the present analysis by approximately an order of magnitude.

For d_τ, the results are compared with the constraints provided by the DELPHI experiment in e^+e^- collisions [36] and by CMS in $p+p$ collisions [107]. The expected limits obtained from the global fits improve upon the DELPHI result but remain approximately an order of magnitude weaker than the current CMS constraints.

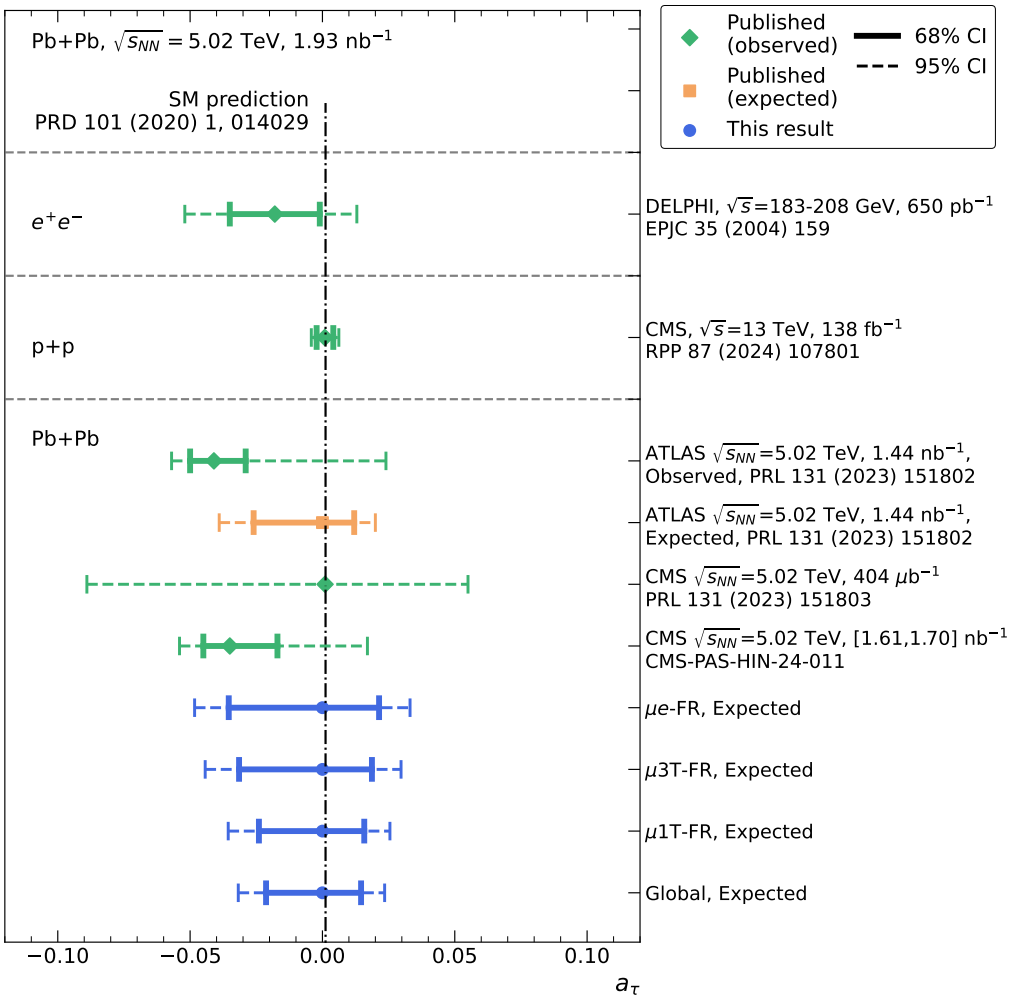

Figure 6.6.2: Comparison of the expected 68% and 95% confidence intervals (CIs) for a_τ obtained in the presented analysis (blue) with the existing published observed (green) and expected (orange) results. The SM prediction is indicated by the dashed vertical line. Figure adapted from Ref. [122].

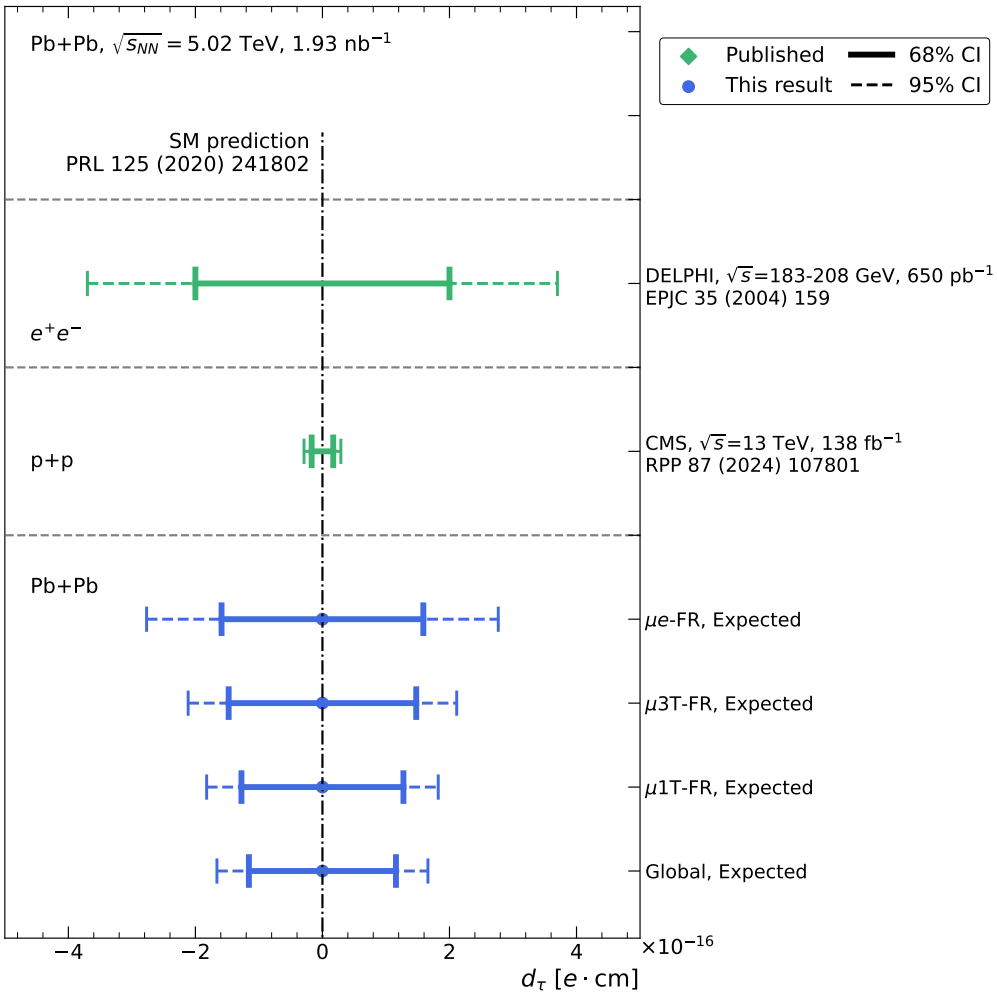

Figure 6.6.3: Comparison of the expected 68% and 95% confidence intervals (CIs) for d_τ obtained in the presented analysis (blue) with the existing published observed results (green). The SM prediction is indicated by the dashed vertical line. Figure adapted from Ref. [122].

Chapter 7

Conclusions and outlook

The work presented in this thesis reports the measurement of the $\gamma\gamma \to \tau\tau$ process in ultraperipheral heavy-ion collisions. The substantial photon flux generated in these interactions provides an ideal environment for studying photon-induced processes. The analysis is based on $\sqrt{s_{\mathrm{NN}}} = 5.02$ TeV Pb+Pb collision data recorded in 2015 and 2018, corresponding to an integrated luminosity of 1.93 nb^{-1}.

Signal candidates are classified into three mutually exclusive regions according to event topologies in which one τ-lepton decays into a muon and two neutrinos, and the decay of the second τ-lepton is characterised by a charged-particle track(s) or an electron. The measurement is performed in a phase space defined by the absence of forward neutron activity, which suppresses photonuclear and dissociative backgrounds. Combined with a veto on additional detector activity beyond the τ-pair, this selection helps ensure that the reconstructed pairs originate from photon-induced interactions.

To obtain differential cross sections, an unfolding procedure based on Iterative Bayesian Unfolding is employed. This results in 21 differential measurements that capture a wide range of accessible τ-pair kinematics. The cross sections are corrected for detector effects and compared with several leading-order Standard Model predictions. Overall, the results are found to be compatible with these predictions within the experimental uncertainties, which are dominated by limited data statistics.

The study of photon-induced τ-lepton pair production enables constraints to be set on the anomalous magnetic dipole moment $(g-2)$ and the electric dipole moment (EDM) of the τ-lepton. The analysis benefits from a combined global fit that incorporates information from all fiducial regions and all unfolded observables. This approach is made possible by the use of a bootstrap method, which provides full access to the bin-to-bin and inter-variable statistical correlations. Although the resulting expected constraints are preliminary, they exhibit a moderate improvement over the expected constraints from the previous ATLAS analysis for a_τ and they are the first ATLAS results for d_τ. The measurement probes a low-mass region that

complements the phase space accessible in proton-proton collisions. While higher masses offer increased sensitivity to some potential BSM effects, the falling cross sections render Pb+Pb collisions particularly advantageous for precise cross-section measurements.

This work constitutes the first measurement of its kind in Pb+Pb collisions and represents a significant step forward in studying photon-induced τ-lepton pair production. It provides new insight into the electromagnetic properties of the τ-lepton and demonstrates the potential of heavy-ion collisions as a complementary probe of its fundamental interactions. In the future, additional improvements are expected from the inclusion of the full Run 3 Pb+Pb dataset and the expansion of the analysis to additional signal regions, potentially incorporating fully hadronic τ decays for both τ-leptons.

In addition to the measurement of the $\gamma\gamma \to \tau\tau$ process, this thesis also presents performance studies of the ATLAS Forward Proton (AFP) detector. AFP is a dedicated subsystem of the ATLAS experiment designed to detect protons that scatter at very small angles and remain intact in photon-induced and diffractive interactions. The detection of such protons provides valuable kinematic constraints that significantly enhance the rejection of background processes. Achieving optimal detector performance requires highly accurate alignment. For Run 3, the global alignment of AFP was determined using a data-driven approach based on photon-induced dimuon events.

Bibliography

[1] ATLAS Collaboration, "Differential measurements of $\gamma\gamma \to \tau\tau$ using $\sqrt{s_{\mathrm{NN}}} =$ 5.02 TeV Pb+Pb collisions with the ATLAS detector," tech. rep., CERN, Geneva, 2025. https://cds.cern.ch/record/2929691.

[2] Public Forward Detector Plots for Collision Data, 2023. https://twiki.cern.ch/twiki/bin/view/AtlasPublic/ForwardDetPublicResults.

[3] M. Thomson, *Modern particle physics*. Cambridge University Press, 2013.

[4] ALEPH and DELPHI and L3 and OPAL and LEP Electroweak Working Group, "Precision Electroweak Measurements on the Z Resonance," *Phys. Rep.*, vol. 427, pp. 257–454, 2006. DOI: 10.1016/j.physrep.2005.12.00.

[5] X. Fan, T. G. Myers, B. A. D. Sukra, and G. Gabrielse, "Measurement of the Electron Magnetic Moment," *Phys. Rev. Lett.*, vol. 130, Feb 2023. DOI: 10.1103/physrevlett.130.071801.

[6] S. Glashow, "Partial-symmetries of weak interactions," *Nucl. Phys.*, vol. 22, pp. 579–588, 1961. DOI: 10.1016/0029-5582(61)90469-2.

[7] S. Weinberg, "A Model of Leptons," *Phys. Rev. Lett.*, vol. 19, pp. 1264–1266, 1967. DOI: 10.1103/PhysRevLett.19.1264.

[8] A. Salam, "Weak and Electromagnetic Interactions," in *Elementary Particle Theory: Relativistic Groups and Analyticity, N. Svartholm (ed.)*, p. 367, Almqvist and Wiksell, 1968. DOI: 10.1142/9789812795915_0034.

[9] UA1 Collaboration, "Experimental Observation of Isolated Large Transverse Energy Electrons with Associated Missing Energy at $\sqrt{s} = 540$ GeV," *Phys. Lett. B*, vol. 122, pp. 103–116, 1983. DOI: 10.1016/0370-2693(83)91177-2.

[10] UA1 Collaboration, "Observation of Single Isolated Electrons of High Transverse Momentum in Events with Missing Transverse Energy at the CERN pp Collider," *Phys. Lett. B*, vol. 122, pp. 476–485, 1983. DOI: 10.1016/0370-2693(83)91605-2.

[11] UA1 Collaboration, "Experimental Observation of Lepton Pairs of Invariant Mass Around 95 GeV/c^2 at the CERN SPS Collider," *Phys. Lett. B*, vol. 126, pp. 398–410, 1983. DOI: 10.1016/0370-2693(83)90188-0.

[12] N. Cabibbo, "Unitary Symmetry and Leptonic Decays," *Phys. Rev. Lett.*, vol. 10, pp. 531–533, Jun 1963. DOI: 10.1103/PhysRevLett.10.531.

[13] M. Kobayashi and T. Maskawa, "CP Violation in the Renormalizable Theory of Weak Interaction," *Prog. Theor. Phys.*, vol. 49, pp. 652–657, 1973. DOI: 10.1143/PTP.49.652.

[14] B. Pontecorvo, "Mesonium and Antimesonium," *Sov. Phys. JETP*, vol. 6, pp. 429–431, 1958.

[15] Z. Maki, M. Nakagawa, and S. Sakata, "Remarks on the Unified Model of Elementary Particles," *Progress of Theoretical Physics*, vol. 28, pp. 870–880, Nov 1962. DOI: 10.1143/PTP.28.870.

[16] F. Zwicky, "On the masses of nebulae and of clusters of nebulae," *Astrophys. J.*, vol. 86, pp. 217–246, 1937. DOI: 10.1086/143864.

[17] V. C. Rubin and W. K. J. Ford, "Rotation of the Andromeda Nebula from a Spectroscopic Survey of Emission Regions," *Astrophys. J.*, vol. 159, pp. 379–403, 1970. DOI: 10.1086/150317.

[18] J. L. Feng, "Dark Matter Candidates from Particle Physics and Methods of Detection," *Annual Review of Astronomy and Astrophysics*, vol. 48, no. Volume 48, 2010, pp. 495–545, 2010. DOI: 10.1146/annurev-astro-082708-101659.

[19] P. Fayet, "Supersymmetry and weak, electromagnetic and strong interactions," *Phys. Lett. B*, vol. 64, no. 2, pp. 159–162, 1976. DOI: 10.1016/0370-2693(76)90319-1.

[20] H. Georgi and S. L. Glashow, "Unity of All Elementary-Particle Forces," *Phys. Rev. Lett.*, vol. 32, pp. 438–441, Feb 1974. DOI: 10.1103/PhysRevLett.32.438.

[21] S. Eidelman and M. Passera, "Theory of the τ lepton anomalous magnetic moment," *Modern Physics Letters A*, vol. 22, no. 03, pp. 159–179, 2007. DOI: 10.1142/S0217732307022694.

[22] S. P. Martin and J. D. Wells, "Muon Anomalous Magnetic Dipole Moment in Supersymmetric Theories," *Phys. Rev.*, vol. D64, p. 035003, 2001. DOI: 10.1103/PhysRevD.64.035003.

[23] F. Feruglio, P. Paradisi, and O. Sumensari, "Implications of scalar and

tensor explanations of $R_{D^{(*)}}$," *JHEP*, vol. 11, p. 191, 2018. DOI: 10.1007/JHEP11(2018)191.

[24] A. Gutierrez-Rodriguez, M. A. Hernandez-Ruiz, and L. N. Luis-Noriega, "Limits on the dipole moments of the tau lepton via the process $e^+e^- \to \tau^+\tau^-\gamma$ in a left right symmetric model," *Mod. Phys. Lett.*, vol. A19, p. 2227, 2004. DOI: 10.1142/S0217732304014689.

[25] A. Moyotl and G. Tavares-Velasco, "Weak properties of the tau lepton via a spin-0 unparticle," *Phys. Rev.*, vol. D86, p. 013014, 2012. DOI: 10.1103/PhysRevD.86.013014.

[26] T. Aoyama *et al.*, "The anomalous magnetic moment of the muon in the Standard Model," *Phys. Rep.*, vol. 887, p. 1–166, Dec 2020. DOI: 10.1016/j.physrep.2020.07.006.

[27] Muon $g-2$ Collaboration, "Measurement of the Positive Muon Anomalous Magnetic Moment to 127 ppb," 2025. https://arxiv.org/abs/2506.03069.

[28] Belle Collaboration, "Measurement of the $\tau-$lepton lifetime at Belle," *Phys. Rev. Lett.*, vol. 112, Jan 2014. DOI: 10.1103/physrevlett.112.031801.

[29] Shu-Min Zhao *et al.*, "The study of lepton EDM in CP violating BLMSSM," *JHEP*, vol. 07, p. 124, 2015. DOI: 10.1007/JHEP07(2015)124.

[30] Y. Yamaguchi and N. Yamanaka, "Large Long-Distance Contributions to the Electric Dipole Moments of Charged Leptons in the Standard Model," *Phys. Rev. Lett.*, vol. 125, p. 241802, Dec 2020. DOI: 10.1103/PhysRevLett.125.241802.

[31] F. del Aguila, F. Cornet, and J. Illana, "The possibility of using a large heavy-ion collider for measuring the electromagnetic properties of the tau lepton," *Phys. Lett. B*, vol. 271, no. 1, pp. 256–260, 1991. DOI: 10.1016/0370-2693(91)91309-J.

[32] L. Beresford and J. Liu, "New physics and tau $g-2$ using LHC heavy ion collisions," *Phys. Rev. D*, vol. 102, p. 113008, Dec 2020. DOI: 10.1103/PhysRevD.102.113008.

[33] M. Dyndał, M. Kłusek-Gawenda, A. Szczurek, and M. Schott, "Anomalous electromagnetic moments of τ lepton in $\gamma\gamma \to \tau^+\tau^-$ reaction in Pb+Pb collisions at the LHC," *Phys. Lett. B*, vol. 809, p. 135682, 2020. DOI: 10.1016/j.physletb.2020.135682.

[34] L. Beresford, S. Clawson, and J. Liu, "Strategy to measure tau $g-2$ via photon fusion in LHC proton collisions," *Phys. Rev. D*, vol. 110, Nov 2024. DOI: 10.1103/physrevd.110.092016.

[35] ATLAS Collaboration, "Observation of the $\gamma\gamma \to \tau\tau$ Process in Pb + Pb Collisions and Constraints on the τ-Lepton Anomalous Magnetic Moment with the ATLAS Detector," *Phys. Rev. Lett.*, vol. 131, p. 151802, Oct 2023. DOI: 10.1103/PhysRevLett.131.151802.

[36] DELPHI Collaboration, "Study of tau-pair production in photon-photon collisions at LEP and limits on the anomalous electromagnetic moments of the tau lepton," *Eur. Phys. J. C*, vol. 35, p. 159–170, 2004. DOI: 10.1140/epjc/s2004-01852-y.

[37] E. Fermi, "On the Theory of the impact between atoms and electrically charged particles," *Z. Phys.*, vol. 29, pp. 315–327, 1924. DOI: 10.1007/BF03184853.

[38] C. F. von Weizsäcker, "Radiation emitted in collisions of very fast electrons," *Z. Phys.*, vol. 88, pp. 612–625, 1934. DOI: 10.1007/BF01333110.

[39] E. J. Williams, "Nature of the high-energy particles of penetrating radiation and status of ionization and radiation formulae," *Phys. Rev.*, vol. 45, pp. 729–730, 1934. DOI: 10.1103/PhysRev.45.729.

[40] S. R. Klein and P. Steinberg, "Photonuclear and Two-Photon Interactions at High-Energy Nuclear Colliders," *Annual Review of Nuclear and Particle Science*, vol. 70, p. 323–354, Oct 2020. DOI: 10.1146/annurev-nucl-030320-033923.

[41] V. Budnev, I. Ginzburg, G. Meledin, and V. Serbo, "The two-photon particle production mechanism. Physical problems. Applications. Equivalent photon approximation," *Phys. Rep.*, vol. 15, no. 4, pp. 181–282, 1975. DOI: 10.1016/0370-1573(75)90009-5.

[42] C. A. Bertulani, "Photon exchange in nucleus-nucleus collisions," *International Journal of Modern Physics A*, vol. 18, no. 05, pp. 685–723, 2003. DOI: 10.1142/S0217751X03012357.

[43] G. Baur, K. Hencken, and D. Trautmann, "Photon photon physics in very peripheral collisions of relativistic heavy ions," *J. Phys. G*, vol. 24, pp. 1657–1692, 1998. DOI: 10.1088/0954-3899/24/9/003.

[44] C. A. Bertulani, S. R. Klein, and J. Nystrand, "Physics of ultraperipheral nuclear collisions," *Ann. Rev. Nucl. Part. Sci.*, vol. 55, pp. 271–310, 2005. DOI: 10.1146/annurev.nucl.55.090704.151526.

[45] A. J. Baltz *et al.*, "The Physics of Ultraperipheral Collisions at the LHC," *Phys. Rept.*, vol. 458, pp. 1–171, 2008. DOI: 10.1016/j.physrep.2007.12.001.

[46] ATLAS Collaboration, "Evidence for light-by-light scattering in heavy-ion collisions with the ATLAS detector at the LHC," *Nature Physics*, vol. 13, p. 852–858, Aug 2017. DOI: 10.1038/nphys4208.

[47] ATLAS Collaboration, "Observation of Light-by-Light Scattering in Ultraperipheral Pb + Pb Collisions with the ATLAS Detector," *Phys. Rev. Lett.*, vol. 123, p. 052001, Jul 2019. DOI: 10.1103/PhysRevLett.123.052001.

[48] ALICE Collaboration, "Coherent J/ψ and ψ' photoproduction at midrapidity in ultra-peripheral Pb–Pb collisions at $\sqrt{s_{\rm NN}} = 5.02$ TeV," *The European Physical Journal C*, vol. 81, pp. 1434–6052, 2021. DOI: 10.1140/epjc/s10052-021-09437-6.

[49] ATLAS Collaboration, "Measurement of photonuclear jet production in ultraperipheral Pb+Pb collisions at $\sqrt{s_{\rm NN}} = 5.02$ TeV with the ATLAS detector," *Phys. Rev. D*, vol. 111, p. 052006, Mar 2025. DOI: 10.1103/PhysRevD.111.052006.

[50] A. Majumder and M. van Leeuwen, "The theory and phenomenology of perturbative QCD based jet quenching," *Progress in Particle and Nuclear Physics*, vol. 66, p. 41–92, Jan 2011. DOI: 10.1016/j.ppnp.2010.09.001.

[51] N. Brambilla *et al.*, "The XYZ states: Experimental and theoretical status and perspectives," *Phys. Rep.*, vol. 873, pp. 1–154, 2020. DOI: 10.1016/j.physrep.2020.05.001.

[52] GlueX Collaboration, "First Measurement of Near-Threshold J/ψ Exclusive Photoproduction off the Proton," *Phys. Rev. Lett.*, vol. 123, p. 072001, Aug 2019. DOI: 10.1103/PhysRevLett.123.072001.

[53] L. A. Harland-Lang, V. A. Khoze, and M. G. Ryskin, "Exclusive LHC physics with heavy ions: SuperChic 3," *The European Physical Journal C*, vol. 79, Jan 2019. DOI: 10.1140/epjc/s10052-018-6530-5.

[54] S. R. Klein, J. Nystrand, J. Seger, Y. Gorbunov, and J. Butterworth, "STARlight: A Monte Carlo simulation program for ultra-peripheral collisions of relativistic ions," *Computer Physics Communications*, vol. 212, p. 258–268, Mar 2017. DOI: 10.1016/j.cpc.2016.10.016.

[55] C. M. Tarbert *et al.*, "Neutron skin of ^{208}Pb from Coherent Pion Photoproduction," *Phys. Rev. Lett.*, vol. 112, no. 24, p. 242502, 2014. DOI: 10.1103/PhysRevLett.112.242502.

[56] L. A. Harland-Lang, "Higher precision constraints on the tau g–2 in LHC photon-initiated production: a full account of hadron dissociation and soft survival effects," *Eur. Phys. J. C*, vol. 84, no. 12, p. 1332, 2024. DOI: 10.1140/epjc/s10052-024-13685-7.

[57] L. R. Evans and P. Bryant, "LHC Machine," *JINST*, vol. 3, p. S08001. 164 p, 2008. DOI: 10.1088/1748-0221/3/08/S08001.

[58] ATLAS Collaboration, "The ATLAS Experiment at the CERN Large Hadron Collider," *JINST*, vol. 3, pp. S08003–S08003, Aug 2008. DOI: 10.1088/1748-0221/3/08/s08003.

[59] CMS Collaboration, "The CMS Experiment at the CERN LHC," *JINST*, vol. 3, p. S08004, 2008. DOI: 10.1088/1748-0221/3/08/S08004.

[60] ALICE Collaboration, "The ALICE experiment at the CERN LHC," *JINST*, vol. 3, p. S08002, Aug 2008. DOI: 10.1088/1748-0221/3/08/S08002.

[61] LHCb Collaboration, "The LHCb Detector at the LHC," *JINST*, vol. 3, p. S08005, Aug 2008. DOI: 10.1088/1748-0221/3/08/S08005.

[62] TOTEM Collaboration, "The TOTEM Experiment at the CERN Large Hadron Collider," *JINST*, vol. 3, p. S08007, Aug 2008. DOI: 10.1088/1748-0221/3/08/S08007.

[63] CERN Document Server, "The CERN accelerator complex." https://cds.cern.ch/record/2813716/.

[64] ATLAS Collaboration, "ATLAS experiment public results: ATLAS luminosity measurements in Run-1." https://twiki.cern.ch/twiki/bin/view/AtlasPublic/LuminosityPublicResultsRun1.

[65] ATLAS Collaboration, "ATLAS experiment public results: ATLAS luminosity measurements in Run-2." https://twiki.cern.ch/twiki/bin/view/AtlasPublic/LuminosityPublicResultsRun2.

[66] ATLAS Collaboration, "ATLAS experiment public results: ATLAS luminosity measurements in Run-3." https://twiki.cern.ch/twiki/bin/view/AtlasPublic/LuminosityPublicResultsRun3.

[67] G. Apollinari, O. Brüning, T. Nakamoto, and L. Rossi, "High Luminosity Large Hadron Collider HL-LHC," tech. rep., CERN, 2015. DOI: 10.5170/CERN-2015-005.1.

[68] ATLAS Collaboration, "The ATLAS experiment at the CERN Large Hadron

Collider: a description of the detector configuration for Run 3," *JINST*, vol. 19, p. P05063, May 2024. DOI: 10.1088/1748-0221/19/05/P05063.

[69] CERN Document Server, "Computer generated image of the whole ATLAS detector." https://cds.cern.ch/record/1095924.

[70] CERN Document Server, "Computer generated image of the ATLAS inner detector." https://cds.cern.ch/record/1095926.

[71] CERN Document Server, "Computer Generated image of the ATLAS calorimeter." https://cds.cern.ch/record/1095927.

[72] ATLAS Collaboration, "Study of the material of the ATLAS inner detector for Run 2 of the LHC," *JINST*, vol. 12, p. P12009. 71 p, Jul 2017. DOI: 10.1088/1748-0221/12/12/P12009.

[73] CERN Document Server, "Computer generated image of the ATLAS Muons subsystem." https://cds.cern.ch/record/1095929.

[74] A. Sidoti, "Minimum Bias Trigger Scintillators in ATLAS Run II," *JINST*, vol. 9, p. C10020, Oct 2014. DOI: 10.1088/1748-0221/9/10/C10020.

[75] V. Balagura, "Van der Meer scan luminosity measurement and beam–beam correction," *The European Physical Journal C*, vol. 81, Jan 2021. DOI: 10.1140/epjc/s10052-021-08837-y.

[76] M. Leite, "Performance of the ATLAS Zero Degree Calorimeter," tech. rep., CERN, Geneva, Nov 2013. http://cds.cern.ch/record/1628749.

[77] ATLAS Collaboration, "ATLAS level-1 trigger: Technical Design Report," 1998. https://cds.cern.ch/record/381429.

[78] ATLAS Collaboration, "ATLAS high-level trigger, data-acquisition and controls: Technical Design Report," 2003. https://cds.cern.ch/record/616089.

[79] CERN Document Server, "How ATLAS detects particles: diagram of particle paths in the detector." https://cds.cern.ch/record/1505342.

[80] A. Rosenfeld and J. L. Pfaltz, "Sequential Operations in Digital Picture Processing," *J. ACM*, vol. 13, p. 471–494, Oct 1966. DOI: 10.1145/321356.321357.

[81] ATLAS Collaboration, "Performance of the ATLAS track reconstruction algorithms in dense environments in LHC Run 2," *The European Physical Journal C*, vol. 77, Oct 2017. DOI: 10.1140/epjc/s10052-017-5225-7.

[82] R. Frühwirth, "Application of Kalman filtering to track and vertex fitting," *Nuclear Instruments and Methods in Physics Research Section A: Accelerators, Spectrometers, Detectors and Associated Equipment*, vol. 262, no. 2, pp. 444–450, 1987. DOI: 10.1016/0168-9002(87)90887-4.

[83] ATLAS Collaboration, "A neural network clustering algorithm for the ATLAS silicon pixel detector," *JINST*, vol. 9, p. P09009–P09009, Sep 2014. DOI: 10.1088/1748-0221/9/09/p09009.

[84] ATLAS Tracking Software Tutorial, "ATLAS Track Reconstruction – General Overview. Global track parameters." https://atlassoftwaredocs.web.cern.ch/internal-links/tracking-tutorial.

[85] ATLAS Collaboration, "Topological cell clustering in the ATLAS calorimeters and its performance in LHC Run 1," *The European Physical Journal C*, vol. 77, Jul 2017. DOI: 10.1140/epjc/s10052-017-5004-5.

[86] ATLAS Collaboration, "Electron and photon energy calibration with the ATLAS detector using 2015–2016 LHC proton-proton collision data," *JINST*, vol. 14, p. P03017–P03017, Mar 2019. DOI: 10.1088/1748-0221/14/03/p03017.

[87] ATLAS Collaboration, "Electron and photon reconstruction and performance in ATLAS using a dynamical, topological cell clustering-based approach," tech. rep., CERN, Geneva, 2017. https://cds.cern.ch/record/2298955.

[88] ATLAS Collaboration, "Improved electron reconstruction in ATLAS using the Gaussian Sum Filter-based model for bremsstrahlung," tech. rep., CERN, Geneva, 2012. https://cds.cern.ch/record/1449796.

[89] ATLAS Collaboration, "Electron and photon energy calibration with the ATLAS detector using LHC Run 2 data," *JINST*, vol. 19, p. P02009, Feb. 2024. DOI: 10.1088/1748-0221/19/02/p02009.

[90] ATLAS Collaboration, "Muon reconstruction performance of the ATLAS detector in proton–proton collision data at $\sqrt{s} = 13$ TeV," *The European Physical Journal C*, vol. 76, p. 292, May 2016. DOI: 10.1140/epjc/s10052-016-4120-y.

[91] ATLAS Collaboration, "Studies of the muon momentum calibration and performance of the ATLAS detector with pp collisions at $\sqrt{s} = 13$ TeV," *The European Physical Journal C*, vol. 83, Aug. 2023. DOI: 10.1140/epjc/s10052-023-11584-x.

[92] ATLAS Collaboration, "Technical Design Report for the ATLAS Forward

Proton Detector," tech. rep., CERN, 2015. https://cds.cern.ch/record/2017378.

[93] ATLAS Collaboration, "Observation and Measurement of Forward Proton Scattering in Association with Lepton Pairs Produced via the Photon Fusion Mechanism at ATLAS," *Phys. Rev. Lett.*, vol. 125, p. 261801, Dec 2020. DOI: 10.1103/PhysRevLett.125.261801.

[94] U. Amaldi *et al.*, "The energy dependence of the proton-proton total cross-section for centre-of-mass energies between 23 and 53 GeV," *Phys. Lett. B*, vol. 44, no. 1, pp. 112–118, 1973. DOI: 10.1016/0370-2693(73)90315-8.

[95] C. Da Via *et al.*, "3D silicon sensors: Design, large area production and quality assurance for the ATLAS IBL pixel detector upgrade," *Nuclear Instruments and Methods in Physics Research Section A: Accelerators, Spectrometers, Detectors and Associated Equipment*, vol. 694, pp. 321–330, 2012. DOI: 10.1016/j.nima.2012.07.058.

[96] J. Lange *et al.*, "3D silicon pixel detectors for the ATLAS Forward Physics experiment," *JINST*, vol. 10, p. C03031, Mar 2015. DOI: 10.1088/1748-0221/10/03/C03031.

[97] M. Trzebiński on behalf of the ATLAS Collaboration, "Overview of ATLAS forward proton detectors for LHC Run 3 and plans for the HL-LHC," *Nuclear Instruments and Methods in Physics Research Section A: Accelerators, Spectrometers, Detectors and Associated Equipment*, vol. 1050, p. 168187, 2023. DOI: 10.1016/j.nima.2023.168187.

[98] L. Nozka *et al.*, "Design of Cherenkov bars for the optical part of the time-of-flight detector in Geant4," *Opt. Express*, vol. 22, pp. 28984–28996, Nov 2014. DOI: 10.1364/OE.22.028984.

[99] ATLAS Collaboration, "Performance of the ATLAS Forward Proton Time-of-Flight Detector in 2017," tech. rep., CERN, Geneva, 2021. https://cds.cern.ch/record/2749821.

[100] ATLAS Collaboration, "Performance of the ATLAS Forward Proton Spectrometer during High Luminosity 2017 Data Taking," tech. rep., CERN, Geneva, 2024. https://cds.cern.ch/record/2890974.

[101] S. Clawson, "The light at the end of the tunnel gets weaker: Observation and measurement of photon-induced W^+W^- production at the ATLAS Experiment," *University of Manchester*, 2022. https://cds.cern.ch/record/2851404. Presented 2022.

[102] F. Ozturk, on behalf of the ATLAS Collaboration, "Alignment of the ATLAS-AFP Detectors," Tech. Rep. ATL-FWD-PROC-2024-005, CERN, 2024. https://cds.cern.ch/record/2894034.

[103] G. Valentino *et al.*, "Semiautomatic beam-based LHC collimator alignment," *Phys. Rev. ST Accel. Beams*, vol. 15, p. 051002, May 2012. DOI: 10.1103/PhysRevSTAB.15.051002.

[104] R. Staszewski on behalf of the ATLAS Collaboration, "ATLAS Roman Pots at LHC Run 3 - Detector Status," 2022. https://cds.cern.ch/record/2810084.

[105] CMS Collaboration, "Observation of τ Lepton Pair Production in Ultraperipheral Pb+Pb Collisions at $\sqrt{s_{\mathrm{NN}}} = 5.02$ TeV," *Phys. Rev. Lett.*, vol. 131, p. 151803, Oct 2023. DOI: 10.1103/PhysRevLett.131.151803.

[106] CMS Collaboration, "Measurement of the tau g-2 factor in ultraperipheral PbPb collisions recorded by the CMS experiment," tech. rep., CERN, Geneva, 2024. https://cds.cern.ch/record/2912969.

[107] CMS Collaboration, "Observation of $\gamma\gamma \to \tau\tau$ in proton–proton collisions and limits on the anomalous electromagnetic moments of the τ lepton," *Reports on Progress in Physics*, vol. 87, p. 107801, Sep 2024. DOI: 10.1088/1361-6633/ad6fcb.

[108] OPAL Collaboration, "An upper limit on the anomalous magnetic moment of the τ lepton," *Phys. Lett. B*, vol. 431, p. 188–198, Jul 1998. DOI: 10.1016/s0370-2693(98)00520-6.

[109] L3 Collaboration, "Measurement of the anomalous magnetic and electric dipole moments of the tau lepton," *Phys. Lett. B*, vol. 434, no. 1, pp. 169–179, 1998. DOI: 10.1016/S0370-2693(98)00736-9.

[110] Belle Collaboration, "An improved search for the electric dipole moment of the τ lepton," *JHEP*, vol. 2022, Apr 2022. DOI: 10.1007/jhep04(2022)110.

[111] U. Haisch, L. Schnell, and J. Weiss, "LHC tau-pair production constraints on a_τ and d_τ," *SciPost Physics*, vol. 16, Feb 2024. DOI: 10.21468/scipostphys.16.2.048.

[112] I. Galon, A. Rajaraman, and T. M. Tait, "$H \to \tau\tau$ as a probe of the τ magnetic dipole moment," *JHEP*, vol. 2016, Dec 2016. DOI: 10.1007/jhep12(2016)111.

[113] J. Bernabéu, G. González-Sprinberg, J. Papavassiliou, and J. Vidal,

"Tau anomalous magnetic moment form factor at super B/flavor factories," *Nuclear Physics B*, vol. 790, no. 1, pp. 160–174, 2008. DOI: 10.1016/j.nuclphysb.2007.09.001.

[114] S. Eidelman, D. Epifanov, M. Fael, L. Mercolli, and M. Passera, "τ dipole moments via radiative leptonic τ decays," *JHEP*, vol. 2016, Mar 2016. DOI: 10.1007/jhep03(2016)140.

[115] A. S. Fomin, A. Y. Korchin, A. Stocchi, S. Barsuk, and P. Robbe, "Feasibility of τ-lepton electromagnetic dipole moments measurement using bent crystal at the LHC," *JHEP*, vol. 2019, Mar 2019. DOI: 10.1007/jhep03(2019)156.

[116] S. Jadach, Z. Was, R. Decker, and J. Kuhn, "The τ decay library TAUOLA, version 2.4," *Computer Physics Communications*, vol. 76, no. 3, pp. 361–380, 1993. DOI: 10.1016/0010-4655(93)90061-G.

[117] N. Davidson, G. Nanava, T. Przedzinski, E. Richter-Was, and Z. Was, "Universal interface of TAUOLA: Technical and physics documentation," *Computer Physics Communications*, vol. 183, no. 3, pp. 821–843, 2012. DOI: 10.1016/j.cpc.2011.12.009.

[118] T. Sjöstrand, S. Ask, J. R. Christiansen, R. Corke, N. Desai, P. Ilten, S. Mrenna, S. Prestel, C. O. Rasmussen, and P. Z. Skands, "An introduction to PYTHIA 8.2," *Computer Physics Communications*, vol. 191, p. 159–177, Jun 2015. DOI: 10.1016/j.cpc.2015.01.024.

[119] N. Davidson, T. Przedzinski, and Z. Was, "PHOTOS interface in C++: Technical and physics documentation," *Computer Physics Communications*, vol. 199, pp. 86–101, 2016. DOI: 10.1016/j.cpc.2015.09.013.

[120] J. Alwall *et al.*, "The automated computation of tree-level and next-to-leading order differential cross sections, and their matching to parton shower simulations," *JHEP*, vol. 07, p. 079, 2014. DOI: 10.1007/JHEP07(2014)079.

[121] S. Agostinelli *et al.*, "Geant4 - a simulation toolkit," *Nuclear Instruments and Methods in Physics Research Section A: Accelerators, Spectrometers, Detectors and Associated Equipment*, vol. 506, no. 3, pp. 250–303, 2003. DOI: 10.1016/S0168-9002(03)01368-8.

[122] K. Deepak Bhide, "Illuminating the tau lepton with the ATLAS detector: A study of $\gamma\gamma \to \tau\tau$ scattering in ultra-peripheral Pb+Pb collisions, and constraints on the tau lepton electromagnetic dipole moments," *University of Freiburg*, 2025. https://repository.cern/records/k6c00-82t92. Presented 2025.

[123] H.-S. Shao and D. d'Enterria, "gamma-UPC: automated generation of exclusive photon-photon processes in ultraperipheral proton and nuclear collisions with varying form factors," *JHEP*, vol. 2022, Sep 2022. DOI: 10.1007/jhep09(2022)248.

[124] Z. Czyczula, T. Przedzinski, and Z. Was, "TauSpinner Program for Studies on Spin Effect in tau Production at the LHC," *Eur. Phys. J. C*, vol. 72, p. 1988, 2012. DOI: 10.1140/epjc/s10052-012-1988-z.

[125] ATLAS Collaboration, "Exclusive dimuon production in ultraperipheral Pb+Pb collisions at $\sqrt{s} = 5.02$ TeV with ATLAS," *Phys. Rev. C*, vol. 104, Aug 2021. DOI: 10.1103/physrevc.104.024906.

[126] ATLAS Collaboration, "Exclusive dielectron production in ultraperipheral Pb+Pb collisions at $\sqrt{s_{\mathrm{NN}}} = 5.02\,\mathrm{TeV}$ with ATLAS," *JHEP*, vol. 06, p. 182, 2023. DOI: 10.1007/JHEP06(2023)182.

[127] ALICE Collaboration, "Measurement of the Cross Section for Electromagnetic Dissociation with Neutron Emission in Pb-Pb Collisions at $\sqrt{s_{\mathrm{NN}}}$=2.76 TeV," *Phys. Rev. Lett.*, vol. 109, p. 252302, Dec 2012. DOI: 10.1103/PhysRevLett.109.252302.

[128] I. A. Pshenichnov, J. P. Bondorf, I. N. Mishustin, A. Ventura, and S. Masetti, "Mutual heavy ion dissociation in peripheral collisions at ultrarelativistic energies," *Phys. Rev. C*, vol. 64, p. 024903, Jul 2001. DOI: 10.1103/PhysRevC.64.024903.

[129] M. L. Miller, K. Reygers, S. J. Sanders, and P. Steinberg, "Glauber Modeling in High-Energy Nuclear Collisions," *Annual Review of Nuclear and Particle Science*, vol. 57, p. 205–243, Nov 2007. DOI: 10.1146/annurev.nucl.57.090506.123020.

[130] ATLAS Collaboration, "Electron and photon performance measurements with the ATLAS detector using the 2015–2017 LHC proton–proton collision data," *JINST*, vol. 14, p. P12006, 2019. DOI: 10.1088/1748-0221/14/12/P12006.

[131] ATLAS Collaboration, "Measurement of light-by-light scattering and search for axion-like particles with $2.2\,\mathrm{nb}^{-1}$ of Pb+Pb data with the ATLAS detector," *JHEP*, vol. 03, p. 243, 2021. DOI: 10.1007/JHEP03(2021)243.

[132] ATLAS Collaboration, "Track Reconstruction Performance of the ATLAS Inner Detector at $\sqrt{s} = 13$ TeV." ATL-PHYS-PUB-2015-018, 2015. https://cds.cern.ch/record/2037683.

[133] A. Wharton, W. Yao, and R. Jansky, "ATLAS Inner Detector Track Quality Cuts for Run 2," tech. rep., CERN, Geneva, Aug 2014.

[134] ATLAS Collaboration, "Rapidity gap cross sections measured with the ATLAS detector in pp collisions at $\sqrt{s} = 7\,\text{TeV}$," *Eur. Phys. J. C*, vol. 72, p. 1926, 2012. DOI: 10.1140/epjc/s10052-012-1926-0.

[135] "TRExFitter documentation." https://trexfitter-docs.web.cern.ch.

[136] S. Roesler, R. Engel, and J. Ranft, *The Monte Carlo Event Generator DPMJET-III*, p. 1033–1038. Springer Berlin Heidelberg, 2001. DOI: 10.1007/978-3-642-18211-2_166.

[137] G. D'Agostini, "A multidimensional unfolding method based on Bayes' theorem," *Nuclear Instruments and Methods in Physics Research Section A: Accelerators, Spectrometers, Detectors and Associated Equipment*, vol. 362, no. 2, pp. 487–498, 1995. DOI: 10.1016/0168-9002(95)00274-X.

[138] G. D'Agostini, "Improved iterative Bayesian unfolding," 2010. arXiv:1010.0632.

[139] C. Loizides, J. Kamin, and D. d'Enterria, "Improved Monte Carlo Glauber predictions at present and future nuclear colliders," *Phys. Rev. C*, vol. 97, no. 5, p. 054910, 2018. [Erratum: Phys.Rev.C 99, 019901 (2019)]. DOI: 10.1103/PhysRevC.97.054910.

[140] B. Klos *et al.*, "Neutron density distributions from antiprotonic Pb-208 and Bi-209 atoms," *Phys. Rev. C*, vol. 76, p. 014311, 2007. DOI: 10.1103/PhysRevC.76.014311.

[141] L. A. Harland-Lang, V. A. Khoze, and M. G. Ryskin, "Elastic photon-initiated production at the LHC: the role of hadron-hadron interactions," *SciPost Phys.*, vol. 11, p. 064, 2021. DOI: 10.21468/SciPostPhys.11.3.064.

[142] F. James, "MINUIT Function Minimization and Error Analysis: Reference Manual Version 94.1," 1994. https://cds.cern.ch/record/2296388/files/minuit.pdf.

Appendix A

0n0n figures

Figures A.1 and A.2 compare the measured 0n0n weights (black points) and 0n0n weights corrected for migration effects between measured and truth-level bins (red points) in four dimuon rapidity bins for the 2015 and 2018 data, respectively. At this stage, the weights are not corrected for the effect of EM pileup. The close agreement between the black and red points indicates that migrations between reconstruction- and truth-level bins are small. The 0n0n fractions used in the analysis are corrected for migration effects.

A direct comparison of the 0n0n fractions in 2015 and 2018 data is shown in Figure A.3. The 2015 results, including the fits and uncertainty bands, are displayed in shades of blue, while the 2018 results are shown in shades of red. The two datasets are found to be in good agreement, allowing the weights to be combined.

Figures A.4 and A.5 show the 0n0n weights as functions of the dimuon rapidity and invariant mass, respectively. The distributions are displayed with fine binning (black), together with the alternative binning scheme (orange) used to define the systematic uncertainty arising from the binning choice.

The 0n0n fractions derived using the alternative binning scheme for the 2015 and 2018 datasets are shown in Figure A.6 and Figure A.7, respectively. The nominal fit to fractions uncorrected for EM pileup is used as a systematic uncertainty arising from the choice of the binning scheme and it is applied to the reconstruction-level MC. Additionally, the uncertainty band and the alternative fit is shown, however, they are not used in the analysis.

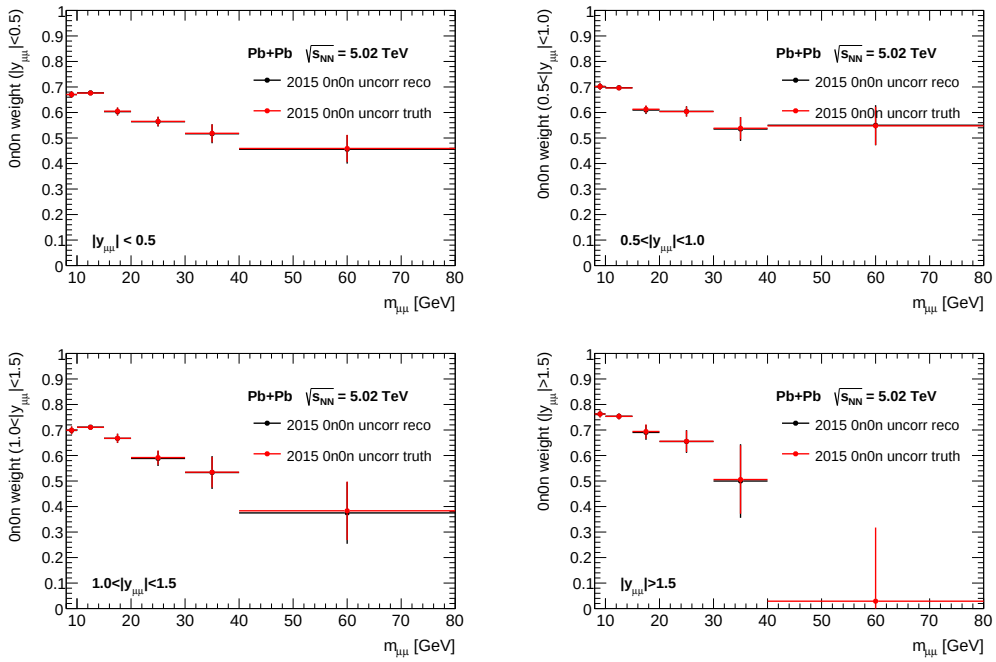

Figure A.1: Comparison of the measured 0n0n weights (black) and the 0n0n weights corrected for migration effects (red), extracted from 2015 data fractions in several dimuon rapidity regions: (top-left) $|y| < 0.5$, (top-right) $0.5 < |y| < 1.0$, (bottom-left) $1.0 < |y| < 1.5$ and (bottom-right) $|y| > 1.5$. Error bars indicate statistical uncertainties.

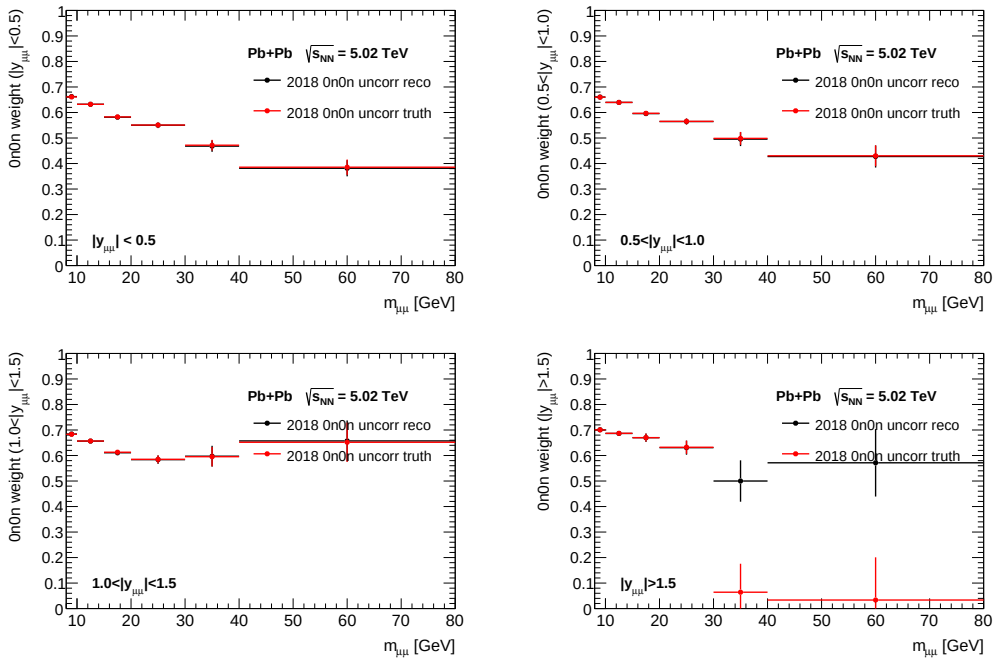

Figure A.2: Comparison of the measured 0n0n weights (black) and the 0n0n weights corrected for migration effects (red), extracted from 2018 data fractions in several dimuon rapidity regions: (top-left) $|y| < 0.5$, (top-right) $0.5 < |y| < 1.0$, (bottom-left) $1.0 < |y| < 1.5$ and (bottom-right) $|y| > 1.5$. Error bars indicate statistical uncertainties.

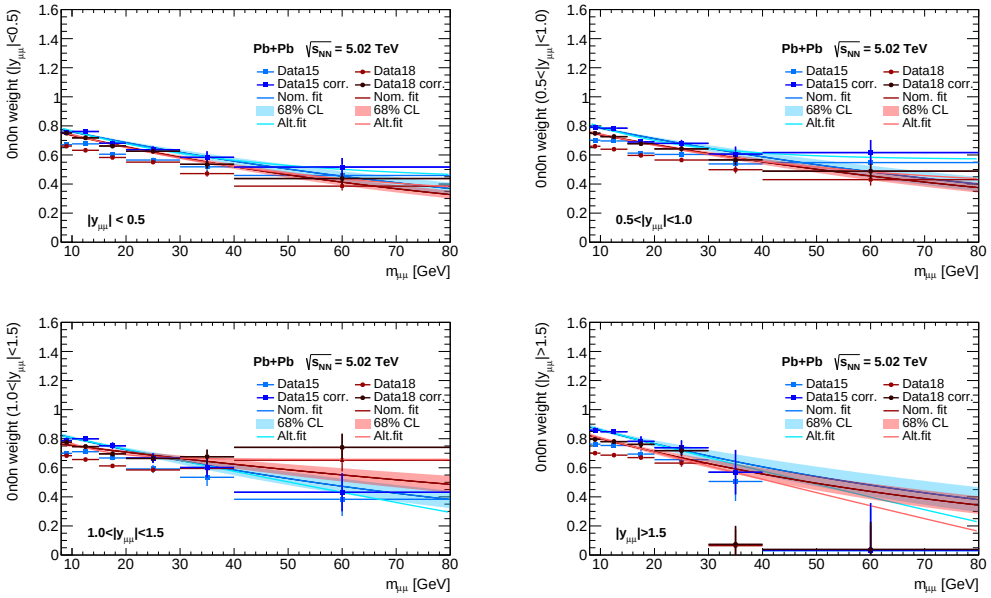

Figure A.3: Comparisons of fractions of 0n0n events extracted from 2015 data (displayed using shades of blue) and 2018 (displayed using shades of red) using the $\gamma\gamma \to \mu\mu$ process in several dimuon rapidity regions: (top-left) $|y| < 0.5$, (top-right) $0.5 < |y| < 1.0$, (bottom-left) $1.0 < |y| < 1.5$ and (bottom-right) $|y| > 1.5$. The points denote fractions corrected (darker colour) and uncorrected (lighter colour) for EM pileup. Corrected fractions are fitted using an exponential function with an uncertainty band and an alternative exponential function with an additional constant parameter (no uncertainty band). Error bars indicate statistical uncertainties. Fractions are corrected for migration effects.

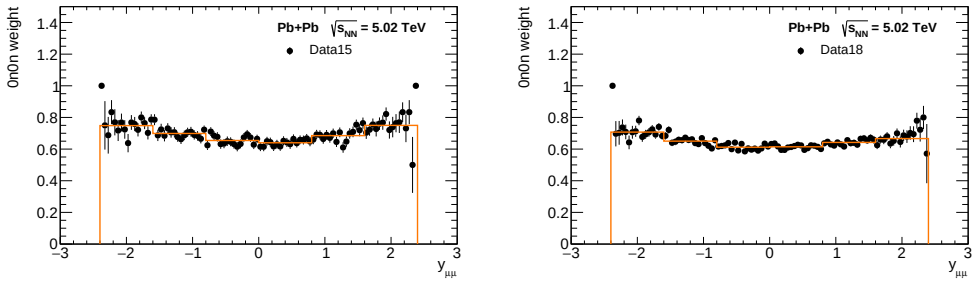

Figure A.4: 0n0n weights as a function of dimuon rapidity, derived using 2015 data (left) and 2018 data (right). The distributions are displayed with fine binning (black points), together with the final binning scheme used for the derivation of the weights (orange histogram). Error bars indicate statistical uncertainties.

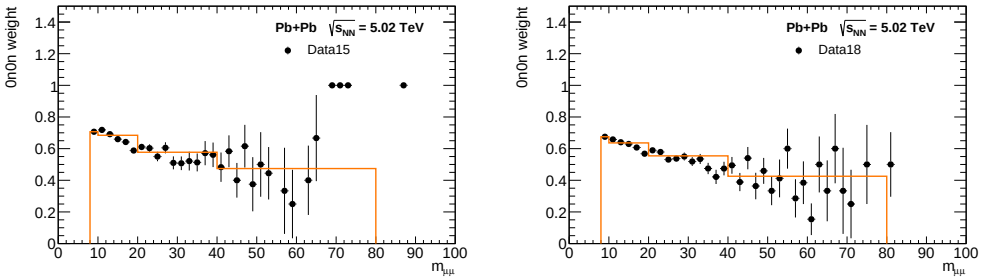

Figure A.5: 0n0n weights as a function of dimuon invariant mass, derived using 2015 data (left) and 2018 data (right). The distributions are displayed with fine binning (black points), together with the final binning scheme used for the derivation of the weights (orange histogram). Error bars indicate statistical uncertainties.

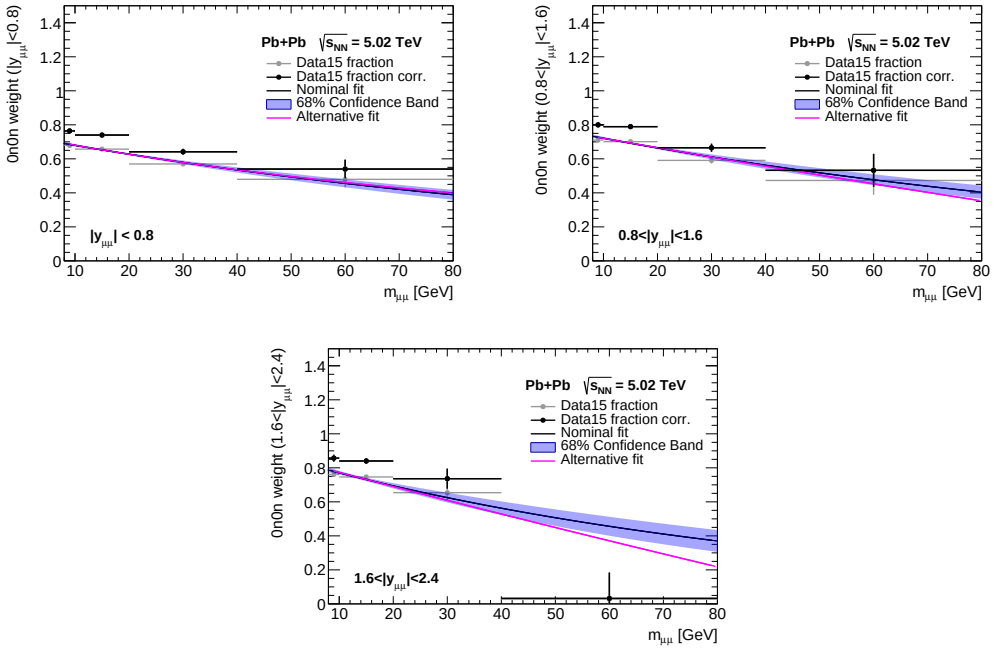

Figure A.6: Fractions of 0n0n events extracted from 2015 data using the $\gamma\gamma \to \mu\mu$ process with alternative binning in several dimuon rapidity regions: (top-left) $|y| < 0.8$, (top-right) $0.8 < |y| < 1.6$ and (bottom) $1.6 < |y| < 2.4$. Black points denote fractions corrected for EM pileup. To smooth statistical fluctuations, the uncorrected fractions are fitted using an exponential function (black lines) with purple uncertainty band or an exponential function with an additional constant parameter (pink lines). Error bars indicate statistical uncertainties. Fractions are corrected for migration effects.

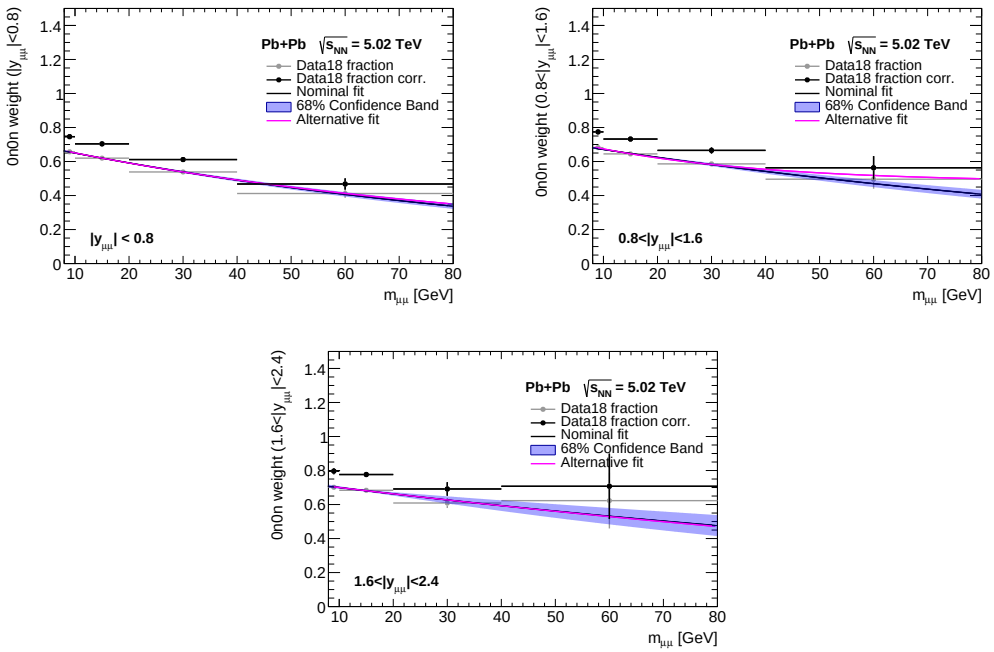

Figure A.7: Fractions of 0n0n events extracted from 2018 data using the $\gamma\gamma \to \mu\mu$ process with alternative binning in several dimuon rapidity regions: (top-left) $|y| < 0.8$, (top-right) $0.8 < |y| < 1.6$ and (bottom) $1.6 < |y| < 2.4$. Black points denote fractions corrected for EM pileup. To smooth statistical fluctuations, the uncorrected fractions are fitted using an exponential function (black lines) with purple uncertainty band or an exponential function with additional constant parameter (pink lines). Error bars indicate statistical uncertainties. Fractions are corrected for migration effects.

Appendix B

Backgrounds

This appendix presents supplementary plots related to the modelling of the two dominant background sources for the $\gamma\gamma \to \tau\tau$ process: photon-induced dimuon production and diffractive photonuclear interactions. Figure B.1 presents kinematic distributions in the 2μ-CR with the GRFF correction applied. Figures B.2 and B.3 present distributions of kinematic variables in the μ2T-CR for the 2015 and 2018 datasets, respectively. Figure B.4 shows the kinematic distributions in the μ4T-CR for the 2018 dataset. In the 2015 data, the photonuclear contribution in the μ4T-CR is found to be negligible.

All the CRs have negligible signal contamination. The CRs for the diffractive photonuclear production also have negligible contamination from the photon-induced dimuon process. The results confirm reliable modelling of the dimuon as well as photonuclear background.

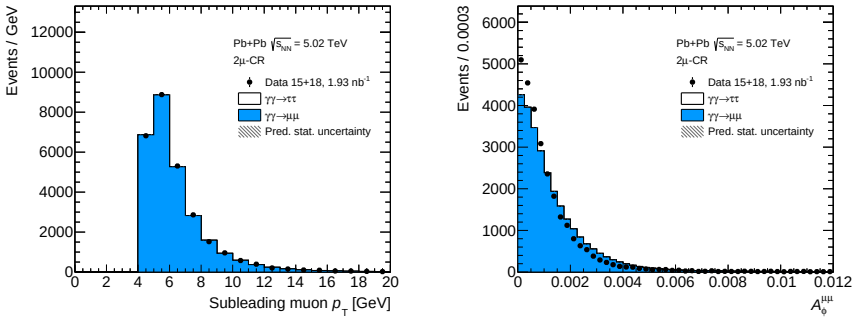

(a)

(b)

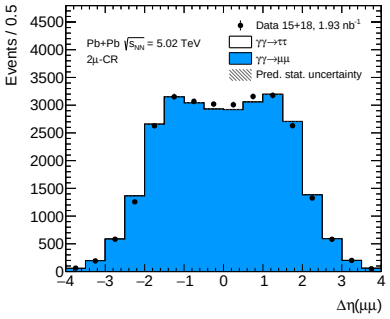

(c)

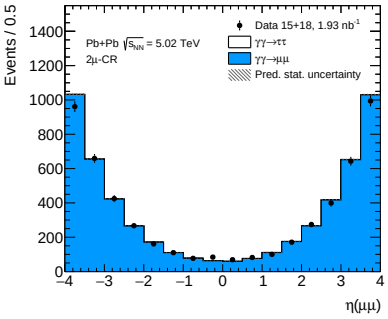

(d)

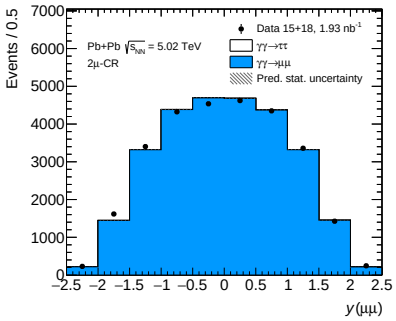

(e)

Figure B.1: Additional control distributions for the combined 2015 + 2018 dataset in the 2μ-CR: (a) sub-leading muon transverse momentum, (b) dimuon acoplanarity, (c) difference in pseudorapidity of the two muons, (d) dimuon pseudorapidity and (e) dimuon rapidity. Statistical uncertainties on the predictions are shown as hatched bands. The photon flux is reweighted to match the flux from the SuperChic 3 generator. The modelling is improved by applying the GRFF correction.

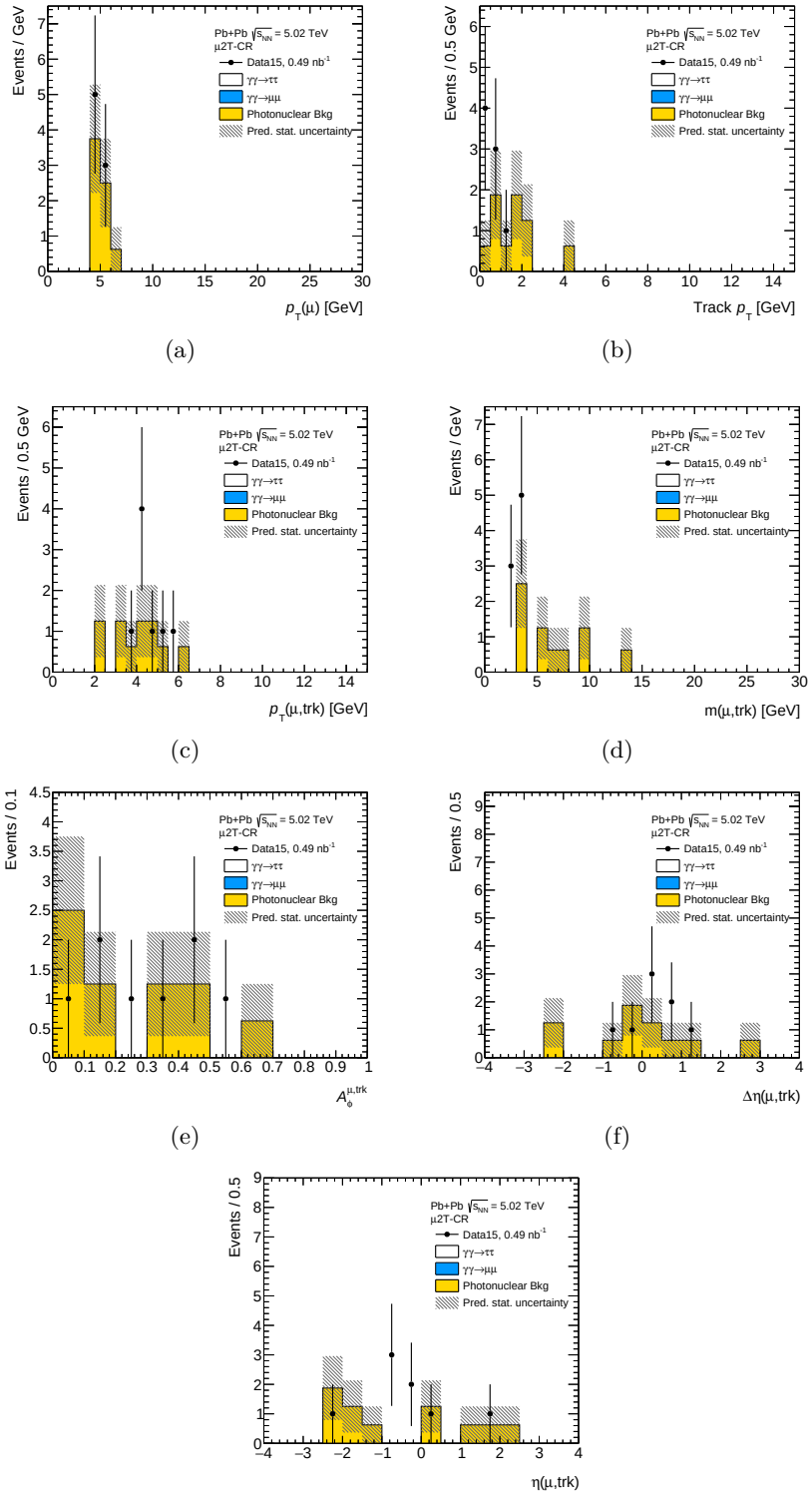

Figure B.2: Control distributions for the 2015 data in the μ2T-CR: (a) muon transverse momentum, (b) leading track transverse momentum, (c) muon–track transverse momentum, (d) muon–track invariant mass, (e) muon–track acoplanarity, (f) muon–track pseudorapidity difference, (g) muon–track pseudorapidity.

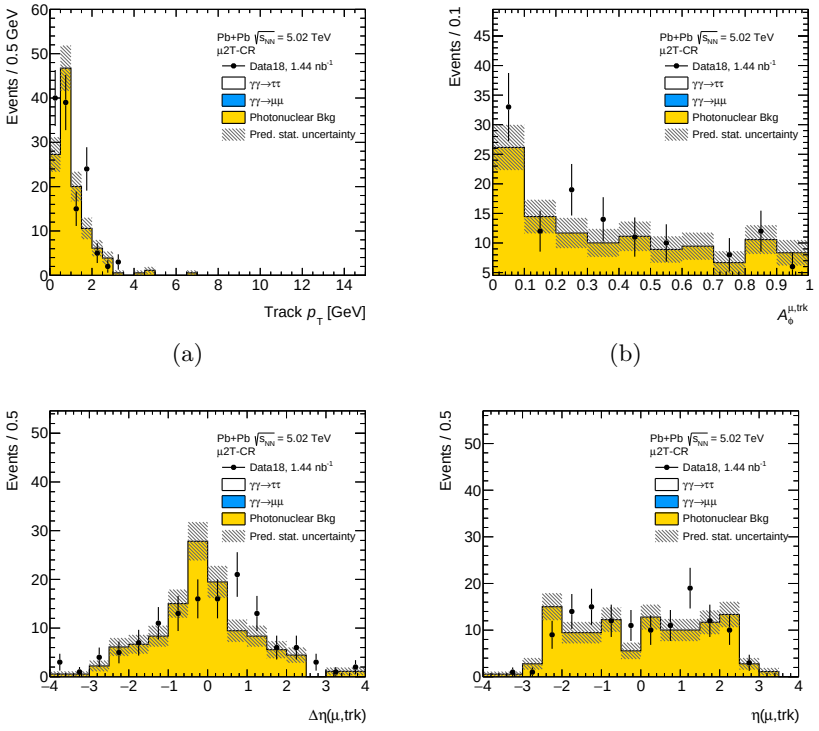

Figure B.3: Control distributions for the 2018 data in the μ2T-CR: (a) leading track transverse momentum, (b) muon–track acoplanarity, (c) muon–track pseudorapidity difference, (d) muon–track pseudorapidity.

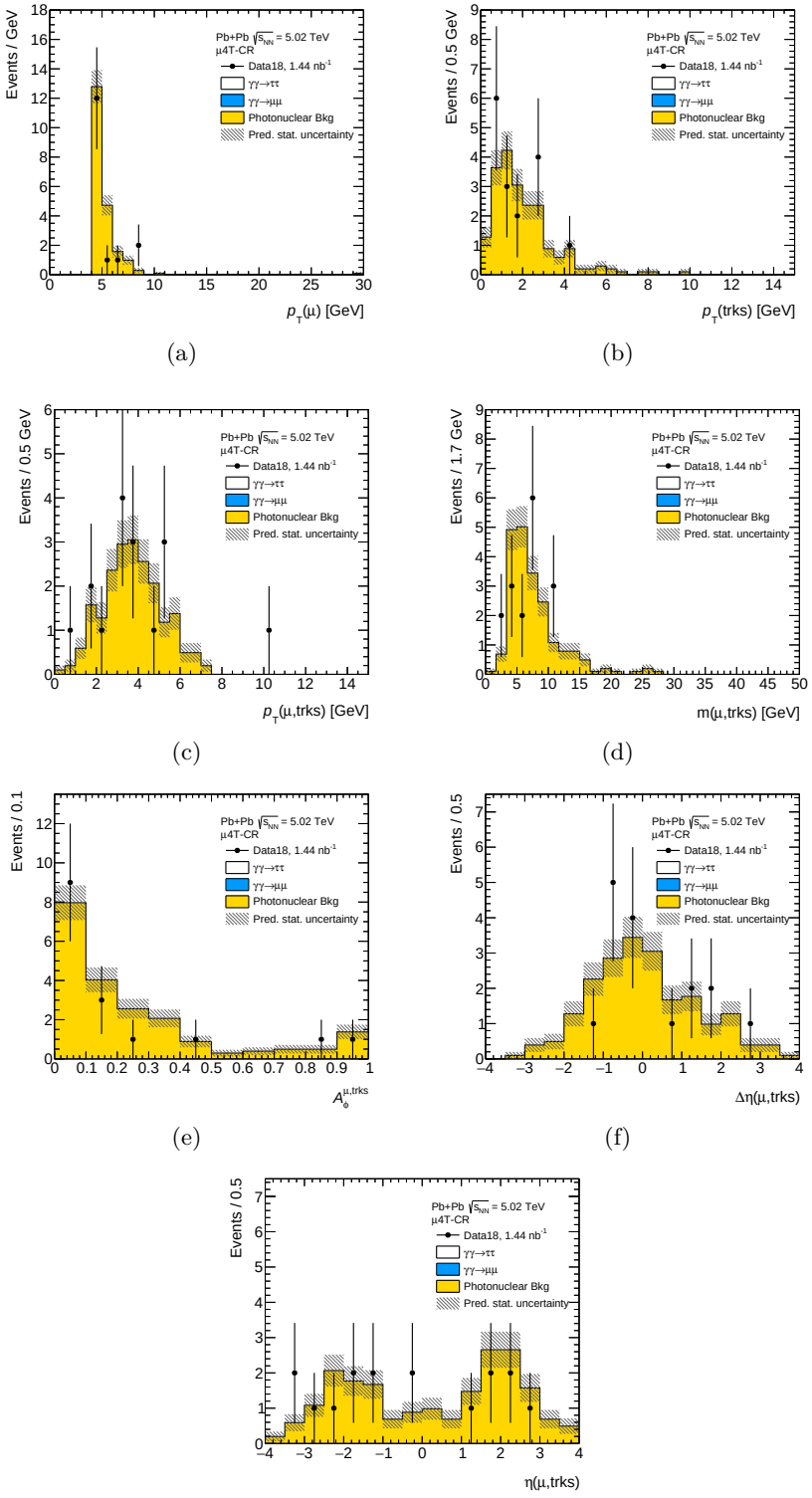

Figure B.4: Control distributions for the 2018 data in the μ4T-CR: (a) muon transverse momentum, (b) 3-tracks transverse momentum, (c) muon–3-tracks transverse momentum, (d) muon–3-tracks invariant mass, (e) muon–3-tracks acoplanarity, (f) muon–3-tracks pseudorapidity difference, (g) muon–3-tracks pseudorapidity.

Appendix C

Detector-level distributions

This appendix provides details on the detector-level analysis of the $\gamma\gamma \to \tau\tau$ process. Additional kinematic distributions are shown in Figures C.1, C.2 and C.3 for μ1T-SR, μ3T-SR and μe-SR, respectively.

The sequential impact of event selection criteria (cutflows) separately for the 2015 and 2018 datasets is provided in Tables C.1 and C.2 for μ1T-SR, Tables C.3 and C.4 for μ3T-SR and in Tables C.5, C.6 for μe-SR. The photon-induced dimuon samples are simulated for two ranges of dimuon invariant mass: $7 < m_{\mu\mu} < 20$ GeV and $m_{\mu\mu} > 20$ GeV. In tables they are denoted as *7M20* and *20M*, respectively.

μ1T Signal Region

Requirement	Data 15	$\gamma\gamma \to \tau\tau$	$\gamma\gamma \to \mu\mu$ 7M20	$\gamma\gamma \to \mu\mu$ 20M	$\gamma\gamma \to \mu\mu\gamma$	Diffractive photonuclear
pass GRL	191487.0	11261.4	42801.8	4162.5	860.4	–
HLT mb trigger	191487.0	1152.0	33849.4	3535.4	564.0	–
$E_{\mathrm{ZDC}}^{A,C} < 1$ TeV (data) / 0n0n topology (MC)	110041.0	758.0	23891.0	2082.4	375.7	–
$N_{\mu}^{\mathrm{baseline}} = 1$	34931.0	688.1	3394.0	438.2	255.0	–
$N_{\mu}^{\mathrm{sig}} = 1$	3388.0	316.6	1760.3	360.3	170.0	–
$N_{e}^{\mathrm{sig}} = 0$	3369.0	305.4	1760.0	360.2	168.1	–
N_{trk} ($\Delta R > 0.1$ from μ) $= 1$	647.0	209.3	260.1	8.3	129.8	–
Veto unmatched clusters	527.0	200.5	250.8	7.8	57.7	–
$\sum$ charge $= 0$	517.0	198.9	250.6	7.7	56.9	–
$p_{\mathrm{T}}^{(\mu,\mathrm{trk})} > 1$ GeV	286.0	182.4	40.0	2.1	56.7	–
$p_{\mathrm{T}}^{(\mu,\mathrm{trk},\gamma)} > 1$ GeV	227.0	174.4	24.6	1.1	20.3	–
$p_{\mathrm{T}}^{(\mu,\mathrm{trk,cluster})} > 1$ GeV	194.0	167.1	17.1	0.9	9.5	–
$A_{\phi}^{\mu,\mathrm{trk}} < 0.4$	191.0	166.2	17.0	0.8	9.5	–
Including photonuclear bkg	191.0	166.2	17.0	0.8	9.5	2.1

Table C.1: Cutflow of 2015 yields in μ1T-SR after each requirement applied sequentially, normalised to $\mathcal{L} = 0.49$ nb^{-1} for the simulated samples.

Requirement	Data 18	$\gamma\gamma \to \tau\tau$	$\gamma\gamma \to \mu\mu$ 7M20	$\gamma\gamma \to \mu\mu$ 20M	$\gamma\gamma \to \mu\mu\gamma$	Diffractive photonuclear
pass GRL	4335070.0	33086.2	124580.2	12136.8	2501.0	–
HLT mu4 trigger	171566.0	1720.1	67570.6	9718.6	1236.2	–
$E_{\mathrm{ZDC}}^{A,C} < 1$ TeV (data) / 0n0n topology (MC)	60313.0	1029.4	44258.6	5405.1	763.4	–
$N_{\mu}^{\mathrm{baseline}} = 1$	13806.0	945.3	5286.7	1062.4	478.9	–
$N_{\mu}^{\mathrm{sig}} = 1$	11218.0	842.6	4328.2	1002.9	416.8	–
$N_{e}^{\mathrm{sig}} = 0$	11145.0	812.7	4326.9	1002.5	411.7	–
N_{trk} ($\Delta R > 0.1$ from μ) $= 1$	1846.0	539.6	605.7	22.6	312.5	–
Veto unmatched clusters	1367.0	518.4	586.2	21.7	142.7	–
$\sum$ charge $= 0$	1351.0	513.0	584.6	20.9	141.0	–
$p_{\mathrm{T}}^{(\mu,\mathrm{trk})} > 1$ GeV	722.0	472.2	95.1	6.3	140.8	–
$p_{\mathrm{T}}^{(\mu,\mathrm{trk},\gamma)} > 1$ GeV	608.0	452.7	57.4	3.3	52.0	–
$p_{\mathrm{T}}^{(\mu,\mathrm{trk,cluster})} > 1$ GeV	549.0	434.0	40.7	2.6	26.6	–
$A_{\phi}^{\mu,\mathrm{trk}} < 0.4$	532.0	431.6	39.9	2.1	26.4	–
Including photonuclear bkg	532.0	431.6	39.9	2.1	26.4	13.5

Table C.2: Cutflow of 2018 yields in μ1T-SR after each requirement applied sequentially, normalised to $\mathcal{L} = 1.44$ nb^{-1} for the simulated samples.

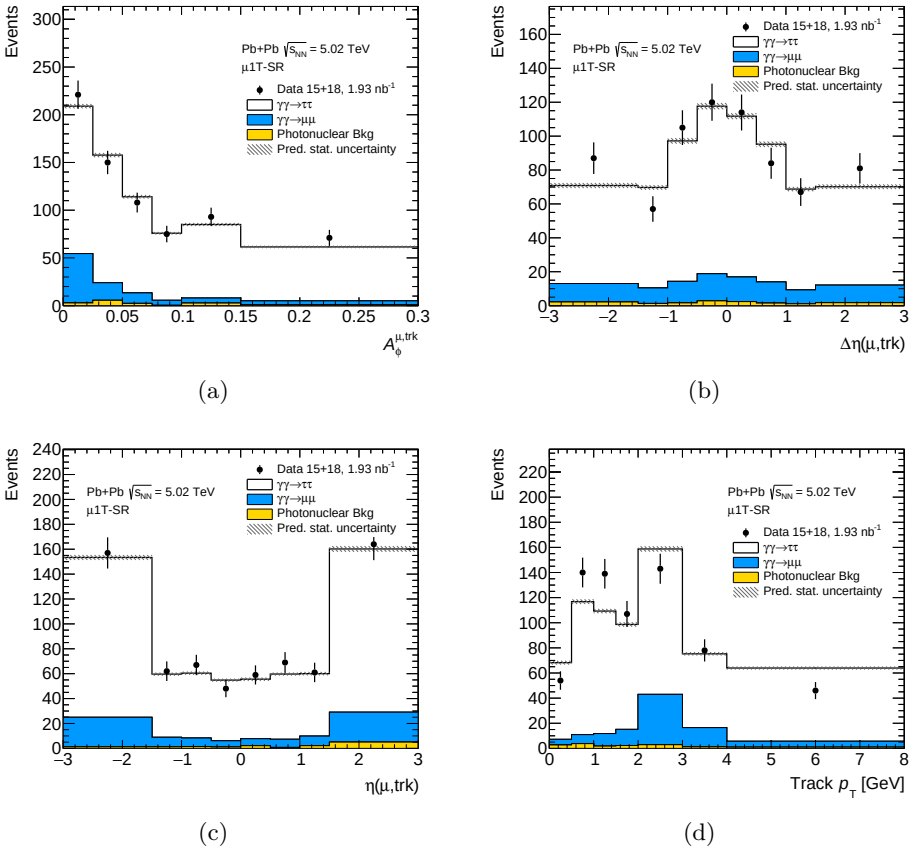

Figure C.1: Control plots for the combined 2015 + 2018 dataset in the μ1T-SR: (a) muon–track acoplanarity, (b) muon–track pseudorapidity difference, (c) muon–track pseudorapidity and (d) track transverse momentum. Statistical uncertainties on the predictions are shown as hatched bands.

μ3T Signal Region

Requirement	Data 15	$\gamma\gamma \to \tau\tau$	$\gamma\gamma \to \mu\mu$ 7M20	$\gamma\gamma \to \mu\mu$ 20M	$\gamma\gamma \to \mu\mu\gamma$
pass GRL	191487.0	11261.4	42801.8	4162.5	860.4
HLT mb trigger	191487.0	1152.0	33849.4	3535.4	564.0
$E_{\text{ZDC}}^{A,C} < 1$ TeV (data) / 0n0n topology (MC)	110041.0	758.0	23891.0	2082.4	375.7
$N_{\mu}^{\text{baseline}} = 1$	34931.0	688.1	3394.0	438.2	255.0
$N_{\mu}^{\text{sig}} = 1$	3388.0	316.6	1760.3	360.3	170.0
$N_{e}^{\text{sig}} = 0$	3369.0	305.4	1760.0	360.2	168.1
N_{trk} ($\Delta R > 0.1$ from μ) $= 3$	75.0	33.2	1.8	0.1	3.9
Veto unmatched clusters	62.0	32.0	1.7	0.1	3.7
$\sum$ charge $= 0$	58.0	31.6	1.7	0.1	3.7
$m_{\text{trks}} < 1.7$ GeV	39.0	31.3	1.3	0.1	1.7
$A_{\phi}^{\mu,\text{trks}} < 0.2$	39.0	31.3	1.3	0.1	1.7

Table C.3: Cutflow of 2015 yields in μ3T-SR after each requirement applied sequentially, normalised to $\mathcal{L} = 0.49$ nb^{-1} for the simulated samples.

Requirement	Data 18	$\gamma\gamma \to \tau\tau$	$\gamma\gamma \to \mu\mu$ 7M20	$\gamma\gamma \to \mu\mu$ 20M	$\gamma\gamma \to \mu\mu\gamma$	Diffractive photonuclear
pass GRL	4335070.0	33086.2	124580.2	12136.8	2501.0	–
HLT mu4 trigger	171566.0	1720.1	67570.6	9718.6	1236.2	–
$E_{\text{ZDC}}^{A,C} < 1$ TeV (data) / 0n0n topology (MC)	60313.0	1029.4	44258.6	5405.1	763.4	–
$N_{\mu}^{\text{baseline}} = 1$	13806.0	945.3	5286.7	1062.4	478.9	–
$N_{\mu}^{\text{sig}} = 1$	11218.0	842.6	4328.2	1002.9	416.8	–
$N_{e}^{\text{sig}} = 0$	11145.0	812.7	4326.9	1002.5	411.7	–
N_{trk} ($\Delta R > 0.1$ from μ) $= 3$	331.0	82.1	3.7	0.2	8.7	–
Veto unmatched clusters	145.0	79.4	3.6	0.2	8.3	–
$\sum$ charge $= 0$	130.0	78.4	3.6	0.2	7.9	–
$m_{\text{trks}} < 1.7$ GeV	85.0	77.7	2.8	0.2	3.4	–
$A_{\phi}^{\mu,\text{trks}} < 0.2$	85.0	77.7	2.8	0.2	3.4	–
Including photonuclear bkg	85.0	77.7	2.8	0.2	3.4	2.8

Table C.4: Cutflow of 2018 yields in μ3T-SR after each requirement applied sequentially, normalised to $\mathcal{L} = 1.44$ nb^{-1} for the simulated samples.

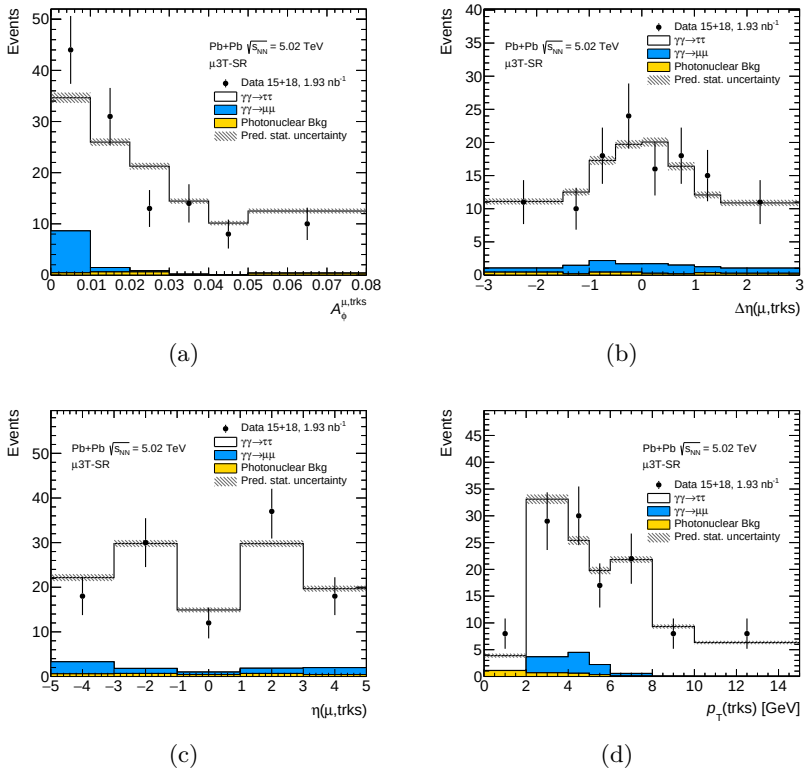

Figure C.2: Control plots for the combined 2015 + 2018 dataset in the μ3T-SR: (a) muon–3–tracks acoplanarity, (b) muon–3–tracks pseudorapidity difference, (c) muon–3–tracks pseudorapidity and (d) 3–tracks transverse momentum. Statistical uncertainties on the predictions are shown as hatched bands.

μe Signal Region

Requirement	Data 15	$\gamma\gamma \to \tau\tau$	$\gamma\gamma \to \mu\mu$ 7M20	$\gamma\gamma \to \mu\mu$ 20M	$\gamma\gamma \to \mu\mu\gamma$
pass GRL	191487.0	11261.4	42801.8	4162.5	860.4
HLT mb trigger	191487.0	1152.0	33849.4	3535.4	564.0
$E_{\mathrm{ZDC}}^{A,C} < 1$ TeV (data) / 0n0n topology (MC)	110041.0	758.0	23891.0	2082.4	375.7
$N_\mu^{\mathrm{sig}} = 1$	6727.0	339.5	4738.2	583.9	231.2
$N_e^{\mathrm{sig}} = 1$	20.0	11.4	0.4	0.4	2.3
N_{trk} ($\Delta R > 0.1$ from μ/e) $= 0$	16.0	11.2	0.3	0.3	0.3
$\sum$ charge $= 0$	14.0	11.1	0.3	0.2	0.2

Table C.5: Cutflow of 2015 yields in μe-SR after each requirement applied sequentially, normalised to $\mathcal{L} = 0.49$ nb^{-1} for the simulated samples.

Requirement	Data 18	$\gamma\gamma \to \tau\tau$	$\gamma\gamma \to \mu\mu$ 7M20	$\gamma\gamma \to \mu\mu$ 20M	$\gamma\gamma \to \mu\mu\gamma$
pass GRL	4335070.0	33086.2	124580.2	12136.8	2501.0
HLT mu4 trigger	171566.0	1720.1	67570.6	9718.6	1236.2
$E_{\mathrm{ZDC}}^{A,C} < 1$ TeV (data) / 0n0n topology (MC)	60313.0	1029.4	44258.6	5405.1	763.4
$N_{\mu}^{\mathrm{sig}} = 1$	19404.0	896.2	11177.0	1590.9	566.2
$N_{e}^{\mathrm{sig}} = 1$	75.0	31.0	2.0	1.2	6.1
N_{trk} ($\Delta R > 0.1$ from μ/e) $= 0$	41.0	29.8	1.6	0.8	0.8
$\sum$ charge $= 0$	39.0	29.7	1.4	0.7	0.4

Table C.6: Cutflow of 2018 yields in μe-SR after each requirement applied sequentially, normalised to $\mathcal{L} = 1.44$ nb^{-1} for the simulated samples.

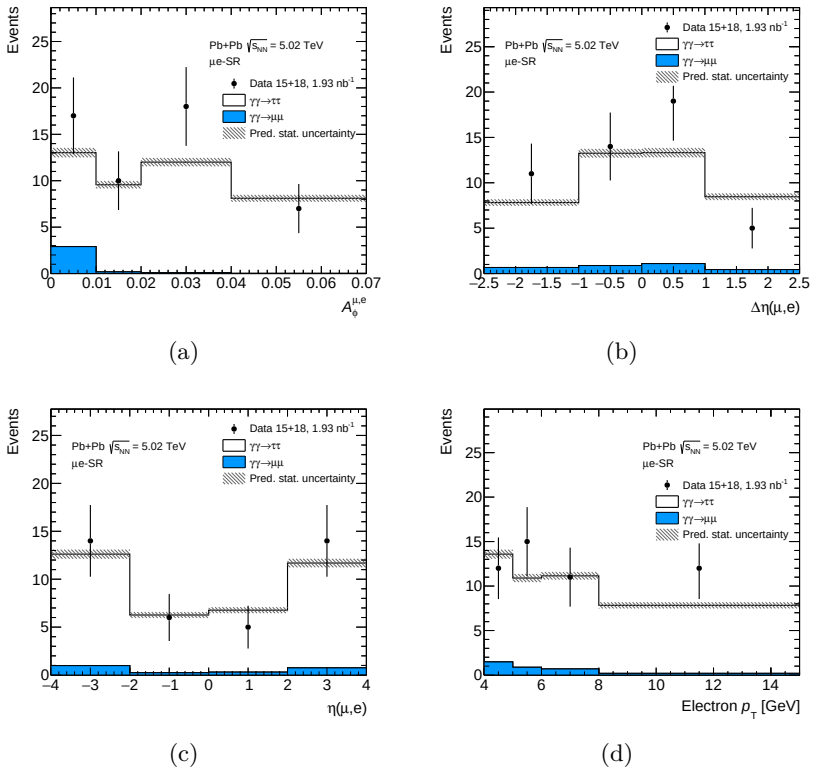

Figure C.3: Control plots for the combined 2015 + 2018 dataset in the μe-SR: (a) muon–electron acoplanarity, (b) muon–electron pseudorapidity difference, (c) muon–electron pseudorapidity and (d) electron transverse momentum. Statistical uncertainties on the predictions are shown as hatched bands.

Appendix D

Unfolding inputs

The sequential impact of event selection criteria (cutflows) in the FRs is shown separately for the 2015 and 2018 datasets in Tables D.1 and D.2 for μ1T-FR, Tables D.3 and D.4 for μ3T-FR and Tables D.5 and D.6 for μe-FR.

The comparison of signal $\gamma\gamma \to \tau\tau$ histograms at reconstruction- and truth-level are provided in Figure D.1 for μ1T-FR, Figure D.3 for μ3T-FR and Figure D.5 for μe-FR. The corresponding response matrices are shown in Figures D.2, D.4 and D.6, respectively.

μ1T Fiducial Region

Requirement	truth-level $\gamma\gamma \to \tau\tau$
0n0n topology	8260
$N_{\mu}^{\text{sig}} = 1$	583.3
$N_{e}^{\text{sig}} = 0$	558.4
N_{trk} ($\Delta R > 0.1$ from μ) $= 1$	435.7
$\sum$ charge $= 0$	434.9
$dR_{\mu,\text{trk}}$	434.9
$p_{\text{T}}^{(\mu,\text{trk})} > 1$ GeV	396.8
$A_{\phi}^{\mu,\text{trk}} < 0.4$	393
$p_{\text{T}}^{\ell} < 4.0$ GeV	285

Table D.1: Cutflow of 2015 yields in μ1T-FR after each requirement applied sequentially, normalised to $\mathcal{L} = 0.49$ nb^{-1} for the simulated samples.

Requirement	truth-level $\gamma\gamma \to \tau\tau$
0n0n topology	$2.428e+04$
$N_{\mu}^{\text{sig}} = 1$	1715
$N_{e}^{\text{sig}} = 0$	1642
N_{trk} ($\Delta R > 0.1$ from μ) $= 1$	1281
$\sum$ charge $= 0$	1279
$dR_{\mu,\text{trk}}$	1279
$p_{\text{T}}^{(\mu,\text{trk})} > 1$ GeV	1167
$A_{\phi}^{\mu,\text{trk}} < 0.4$	1155
$p_{\text{T}}^{\ell} < 4.0$ GeV	838.3

Table D.2: Cutflow of 2018 yields in μ1T-FR after each requirement applied sequentially, normalised to $\mathcal{L} = 1.44$ nb^{-1} for the simulated samples.

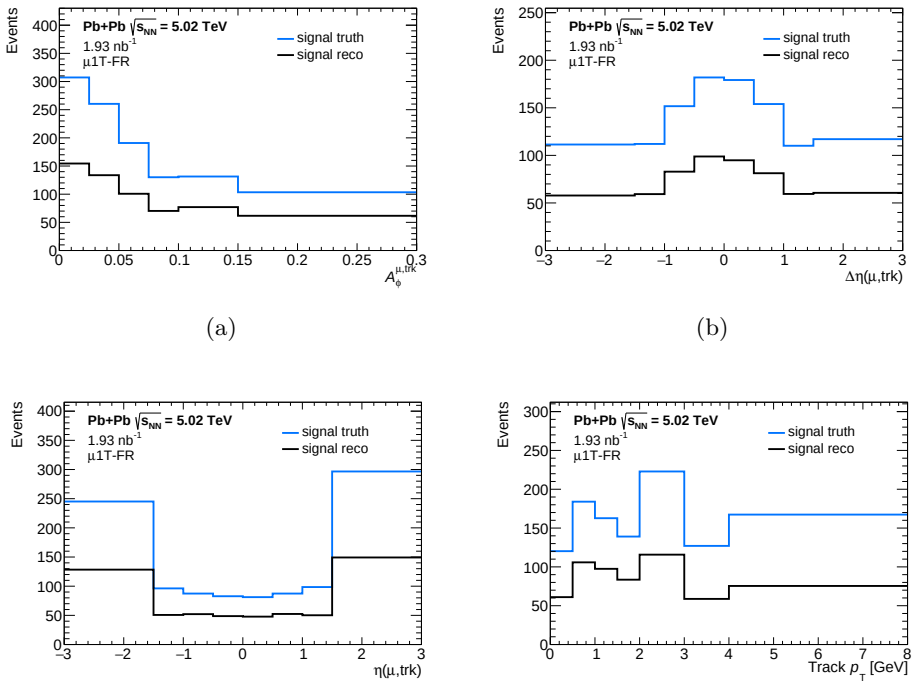

Figure D.1: Signal $\gamma\gamma \to \tau\tau$ histograms at reconstruction-level (black) and truth-level (blue) scaled to the luminosity corresponding to 2015+2018 data in μ1T-FR: (a) muon–track acoplanarity, (b) muon–track pseudorapidity difference, (c) muon–track pseudorapidity, (d) track transverse momentum.

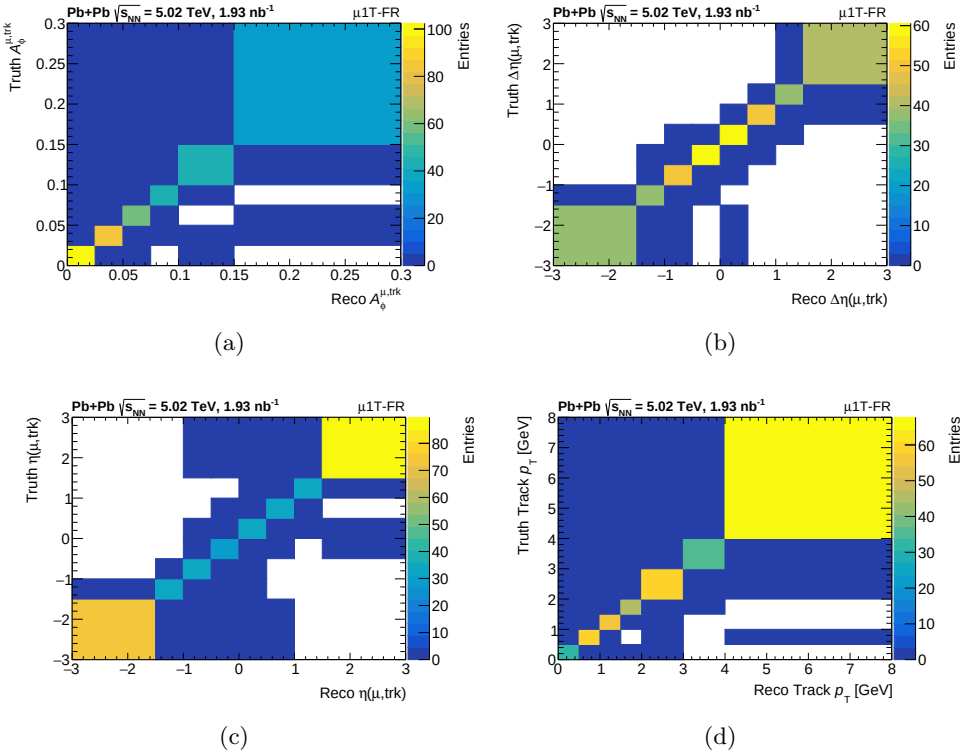

Figure D.2: Response matrices in μ1T-FR: (a) muon–track acoplanarity, (b) muon–track pseudorapidity difference, (c) muon–track pseudorapidity, (d) track transverse momentum.

μ3T Fiducial Region

Requirement	truth-level $\gamma\gamma \to \tau\tau$
0n0n topology	8260
$N_\mu^{\text{sig}} = 1$	583.3
$N_e^{\text{sig}} = 0$	558.4
N_{trk} ($\Delta R > 0.1$ from μ) $= 3$	77.09
$\sum$ charge $= 0$	77.09
$m_{\text{trks}} < 1.7$ GeV	77.02
$dR_{\mu,\text{trks}}$	77.02
$A_\phi^{\mu,\text{trks}} < 0.2$	76.94

Table D.3: Cutflow of 2015 yields in μ3T-FR after each requirement applied sequentially, normalised to $\mathcal{L} = 0.49$ nb^{-1} for the simulated samples.

Requirement	truth-level $\gamma\gamma \to \tau\tau$
0n0n topology	$2.428e+04$
$N_{\mu}^{\text{sig}} = 1$	1715
$N_{e}^{\text{sig}} = 0$	1642
N_{trk} ($\Delta R > 0.1$ from μ) $= 3$	227.1
$\sum$ charge $= 0$	227.1
$m_{\text{trks}} < 1.7$ GeV	226.9
$dR_{\mu,\text{trks}}$	226.9
$A_{\phi}^{\mu,\text{trks}} < 0.2$	226.6

Table D.4: Cutflow of 2018 yields in μ3T-FR after each requirement applied sequentially, normalised to $\mathcal{L} = 1.44$ nb^{-1} for the simulated samples.

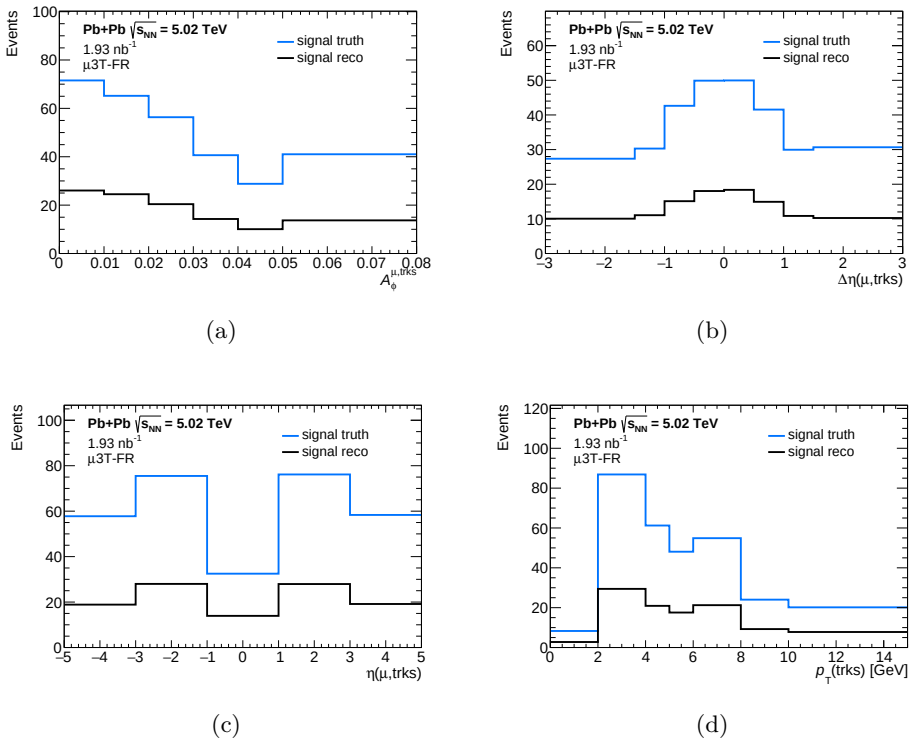

Figure D.3: Signal $\gamma\gamma \to \tau\tau$ histograms at reconstruction-level (black) and truth-level (blue) scaled to the luminosity corresponding to 2015+2018 data in μ3T-FR: (a) muon–3–tracks acoplanarity, (b) muon–3–tracks pseudorapidity difference, (c) muon–3–tracks pseudorapidity, (d) 3–tracks transverse momentum.

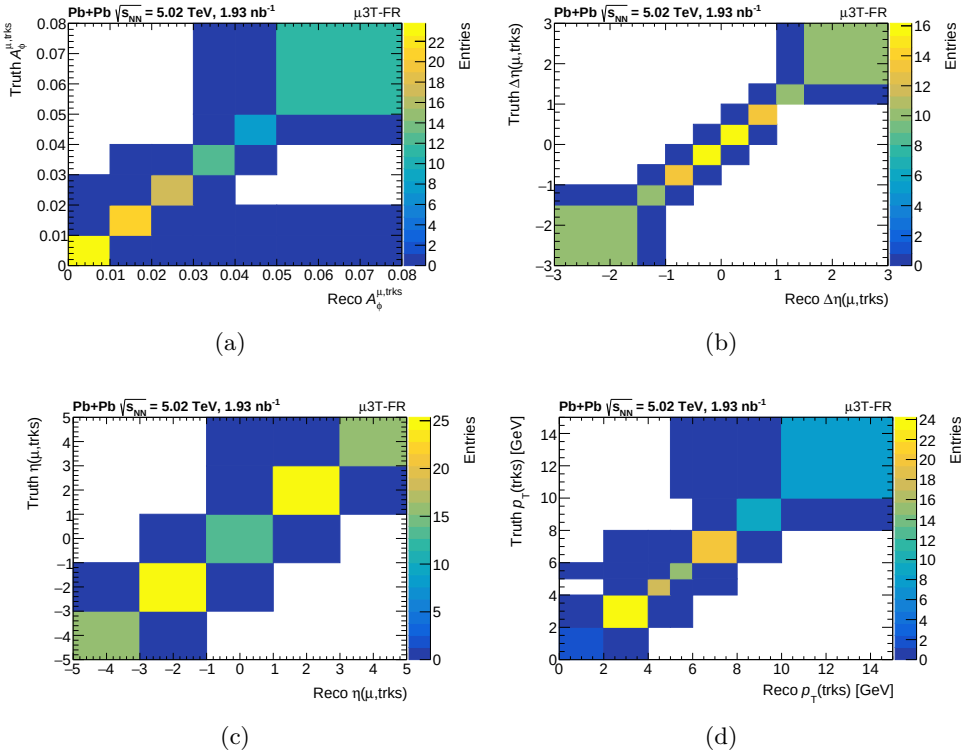

Figure D.4: Response matrices in μ3-FR: (a) muon–3-tracks acoplanarity, (b) muon–3–tracks pseudorapidity difference, (c) muon–3–tracks pseudorapidity, (d) 3–tracks transverse momentum.

μe Fiducial Region

Requirement	truth-level $\gamma\gamma \to \tau\tau$
0n0n topology	8260
$N_\mu^{\text{sig}} = 1$	583.3
$N_e^{\text{sig}} = 1$	24.9
N_{trk} ($\Delta R > 0.1$ from μ/e) $= 0$	24.87
$\sum$ charge $= 0$	24.86

Table D.5: Cutflow of 2015 yields in μe-FR after each requirement applied sequentially, normalised to $\mathcal{L} = 0.49$ nb^{-1} for the simulated samples.

Requirement	truth-level $\gamma\gamma \to \tau\tau$
0n0n topology	$2.428e+04$
$N_{\mu}^{\text{sig}} = 1$	1715
$N_{e}^{\text{sig}} = 1$	73.07
N_{trk} ($\Delta R > 0.1$ from μ/e) $= 0$	72.97
$\sum$ charge $= 0$	72.95

Table D.6: Cutflow of 2018 yields in μe-FR after each requirement applied sequentially, normalised to $\mathcal{L} = 1.44$ nb^{-1} for the simulated samples.

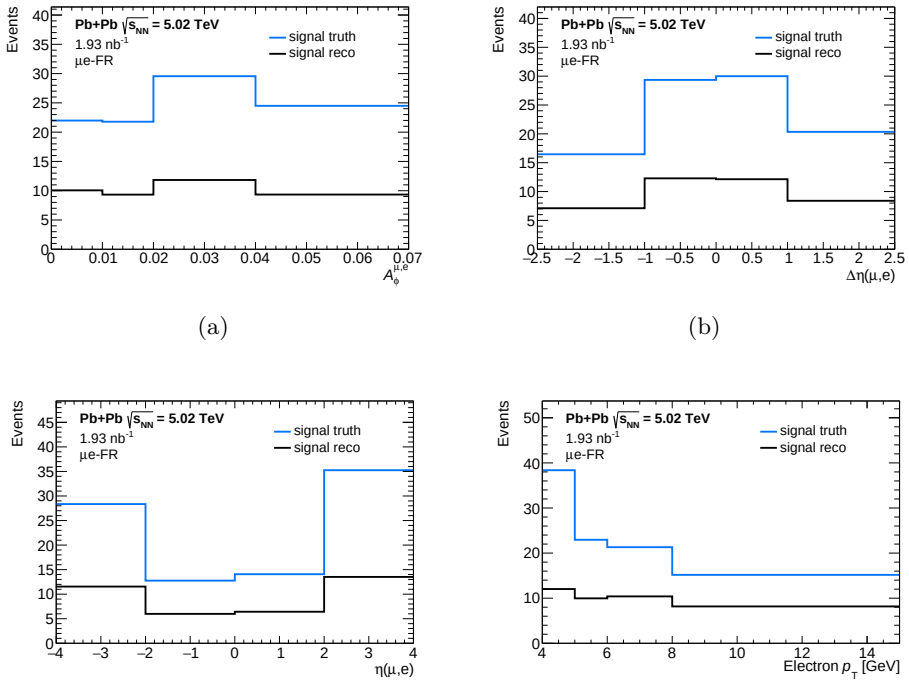

Figure D.5: Signal $\gamma\gamma \to \tau\tau$ histograms at reconstruction-level (black) and truth-level (blue) scaled to the luminosity corresponding to 2015+2018 data in μe-FR: (a) muon–electron acoplanarity, (b) muon–electron pseudorapidity difference, (c) muon–electron pseudorapidity, (d) electron transverse momentum.

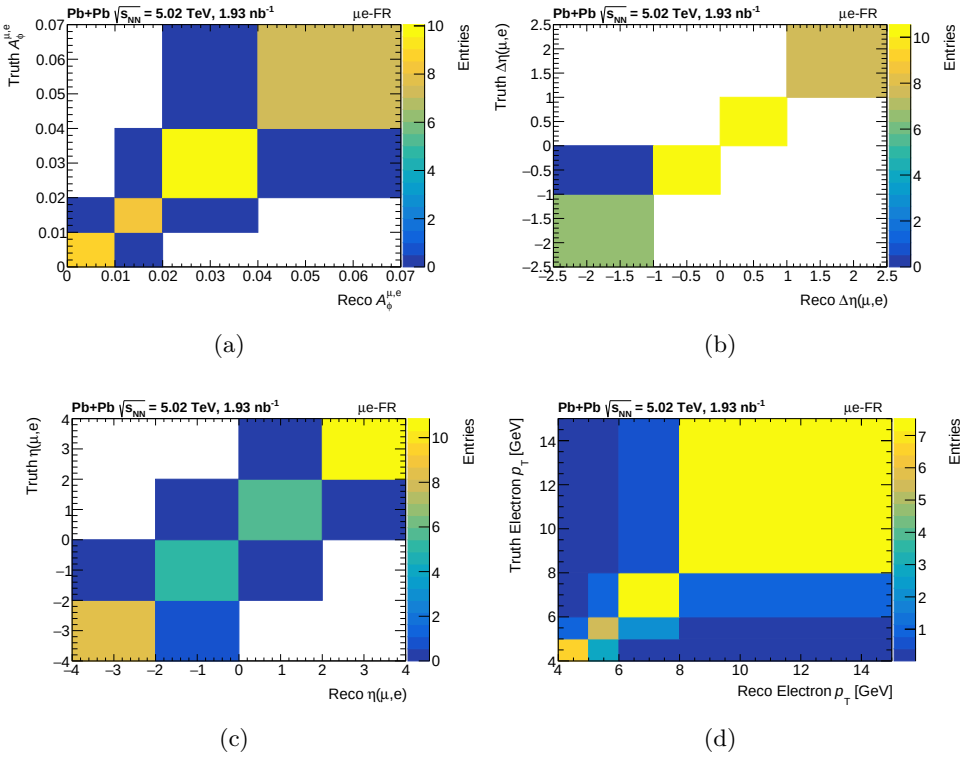

Figure D.6: Response matrices in μe-FR: (a) muon–electron acoplanarity, (b) muon–electron pseudorapidity difference, (c) muon–electron pseudorapidity, (d) electron transverse momentum.

Appendix E

Differential cross sections

The differential cross sections at particle level for the $\gamma\gamma \to \tau\tau$ process in μ1T-FR, μ3T-FR and μe-FR are shown in Figures E.1, E.2 and E.3, respectively.

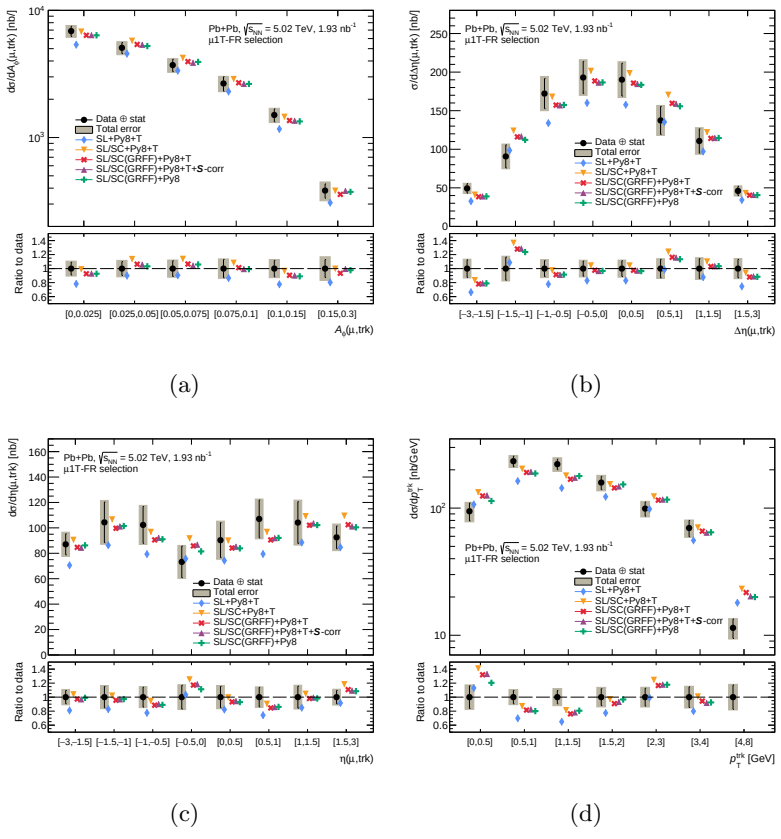

Figure E.1: Differential fiducial cross sections at particle-level in the μ1T-FR: (a) muon–track acoplanarity, (b) muon–track pseudorapidity difference, (c) muon–track pseudorapidity and (d) track transverse momentum. Statistical uncertainties on the unfolded data are shown as black bars and the systematic uncertainties as shown as grey hatched bands. The cross sections are compared to predictions described in Section 6.4. Figures adapted from [122].

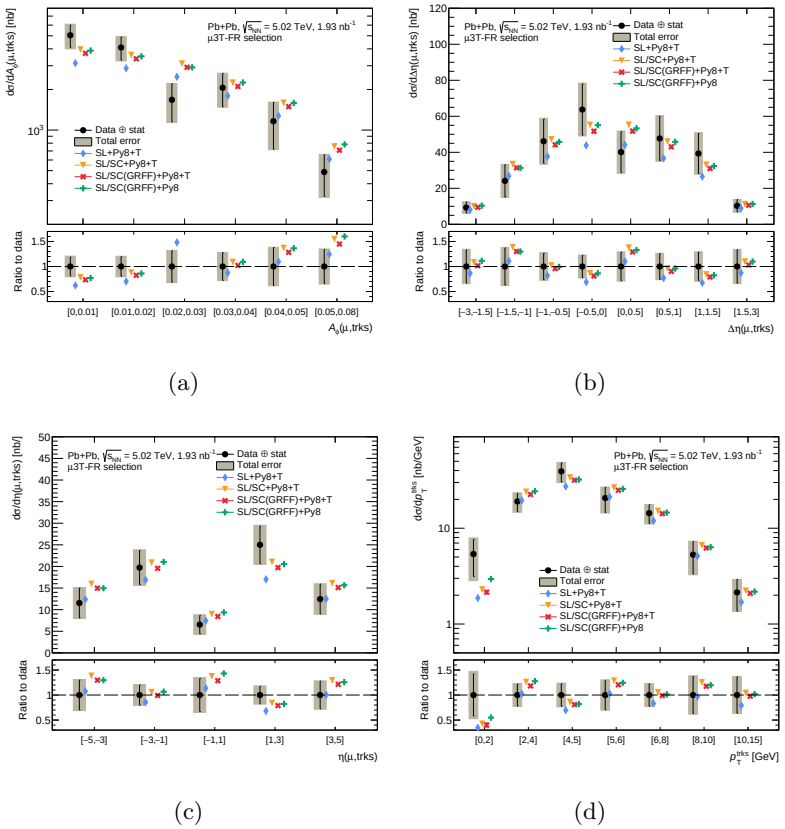

Figure E.2: Differential fiducial cross sections at particle-level in the μ3T-FR: (a) muon–3–tracks acoplanarity, (b) muon–3–tracks pseudorapidity difference, (c) muon–3–tracks pseudorapidity, (d) 3–tracks transverse momentum. Statistical uncertainties on the unfolded data are shown as black bars and the systematic uncertainties as shown as grey hatched bands. The cross sections are compared to predictions described in Section 6.4. Figures adapted from [122].

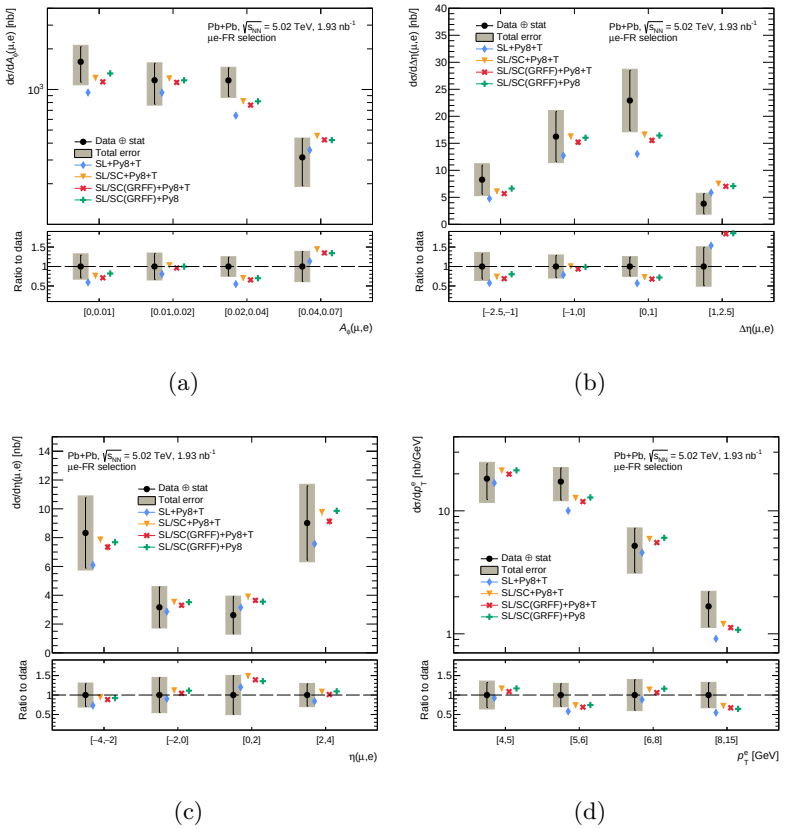

Figure E.3: Differential fiducial cross sections at particle-level in the μe-FR: (a) muon–electron acoplanarity, (b) muon–electron pseudorapidity difference, (c) muon–electron pseudorapidity, (d) electron transverse momentum. Statistical uncertainties on the unfolded data are shown as black bars and the systematic uncertainties as shown as grey hatched bands. The cross sections are compared to predictions described in Section 6.4. Figures adapted from [122].